2015

The electronic structure of oxide perovskites and related materials

Philip S. Lavers
University of Wollongong, ppl02@uowmail.edu.au

The Electronic Structure of Oxide Perovskites and Related Materials

Philip S. Lavers

Submitted as the Major Thesis recording review and original theoretical research to fulfill requirements for the degree of Doctor of Philosophy.

Department of Engineering Physics. University of Wollongong

6th June 2015

CERTIFICATION

I, Philip Sydney Lavers, declare that this thesis, submitted in partial fulfilment of the requirements for the award of Doctor of Philosophy, in the Department of Engineering Physics, University of Wollongong, is wholly my own work unless otherwise referenced or acknowledged. The document has not been submitted for qualifications at any other academic institution.

Philip Sydney Lavers
6th June 2015

Abstract

The purpose of the study was to gain insight into how the electronic charge density distribution (measured or calculated) relates to the spectacular range of macroscopic properties associated with the distortion, but not destruction, of the distinctive perovskite crystal structure. This report on the study in terms of two paradigms: In discourse, the *chemical bond* is taken to be that concept about which, in Roald Hoffman's words, "Chemists have built up a great deal of understanding, in the intuitive language of simple covalent or ionic bonding, of the structure of solids .... " [1]; but the theoretical calculations and conclusions have been been in terms of the precisely defined quantum mechanical observable *bond path*.

The electronic structure of 22 $\mathrm{ABO_3}$ perovskite oxide materials was studied by ab initio density functional methods, employing the CRYSTAL06 set of programmes. Calculated charge density from modern self-consistent methods are accurate to within 2-5% of the total charge density at any point in space [8], page 41. The calculated models used in this paper can thus be regarded as reasonable simulation of what can be measured experimentally.

The concepts of topological atoms and bond paths connecting them, introduced by Bader and and further developed by Tsirelson and others, were employed. Following the ideas of London and Feynman the bond path between these topological atoms is regarded as a bridge between them. This bridge is created by the "bunching" or "corralling" of electronic charge density along the bond path between them. This quantum mechanical effect, acting on a limited availability of non core electrons, is analysed in terms of pairwise bond strength to explain how and why the perovskite structure distorts but persists.

The idea of the *Bridge Index* is introduced and defined for a pair of Bader topological atoms within a crystalline material as a simple characterisation of the London bridge that connects them and from which an ordinal quantification of the pair-wise bond strength can be assessed.

The CRYSTAL06 programme is employed to map out the topological atoms in the perovskites and a variety of other materials to illustrate these ideas. The CRYSTAL06 output was further processed to profile (usually along the bond path between the nuclei of adjoining atoms) the electronic charge density, the Laplacian of this, the kinetic energy density, the ELF, and the LOL.

The study concentrates on the $\mathrm{O_6}$ octahedra that contain the B cations of the $\mathrm{ABO_3}$ oxide perovskites. These octahedra are used as a standard object of description for both structure and dynamics under the so-called Glazer notation. It is the robustness of these octahedra that intrigues the author.

It is concluded that these materials and properties are best understood in the Bader scheme - one of atomic cores surrounded by a rather sparse cloud of valence/conduction electrons in coalescent bundles defined by common surfaces of zero flux in the electronic charge density. The simple picture is that without thermal agitation of the ionic cores, the strongest pairwise interaction will form by "bunching" of the electrons between cores to the extent that Coulombic repulsion and Pauli exclusion will permit. Since there are only a fixed number of non-core electrons, the remaining bonds cannot be as strong, so asymmetry of the electronic charge density distribution, hence also polarisability, tends to prevail. The uneven bond strength results in distortion of the octahedral "cages" but not so much as to interfere with their corner connected character.

Although these effects happen in a sparse "cloud" of valence/conduction electrons that surround the denser complete shells of the atomic core, Bader showed that this core is layered around the nucleus, and some hard polarisation effects will be attributable to the core.

It is found that:

(i) There is a duality between the overlapping wave function picture of bonding and the electronic charge density picture. The Bridge Index is a reasonable proxy for the overlap integral in

gauging the degree of co-valency. A quasi-logarithmic relationship exists between the Bridge Index and calculated pairwise bond strength and also between the Bridge index and published bulk density.

(ii) The free atomic Hartree-Fock estimation of outer orbital energies, coupled with the electronic charge density picture provides a good fundamental explanation of the variety of properties of oxide perovskites. It is demonstrated that a degree of co-valency in bonds forms more readily when the outer orbital energies of the precursor anion and cation atoms are close in value.

(iii) The results of the study reveal that the BO_6 octahedra are robust because the $B-O$ bonds are very strong.

(iv) High electronegativity contrast between the A and B elements favours rotationally distorted phases: low electronegativity contrast between the A and B elements favours axially polarised phases.

Acknowledgements

The author has returned to an education in Physics as a mature age student. He has at one time or another been helped, advised or tutored by every member, including the technical staff, of the Department of Engineering Physics. He gratefully acknowledges a courteous and generous reception on every occasion. He is particularly thankful for the encouragement of his supervisor Professor Shi Dou, and the support and fellowship of staff and students of the Institute for Superconducting and Electronic Materials. Also he acknowledges the helpful guidance provided by the CRYSTAL06 team during workshops at Imperial College, London and The University of Turin (Università di Torino).

Dedicated to the memory of Hans Freeman - teacher, enthusiast, gentleman and an inspiring first degree of separation from Linus Pauling for generations of students.

Contents

List of Figures

Chapter 1

Introduction and outline of work

Note: *Throughout this thesis the words atom or atomic will usually mean ion or ionic and vice-versa. As the thesis shifts to the "topological atoms in crystals" point of view, and also because of the crystal wide nature of some of the crystalline orbitals (to be described later), the distinction blurs - The Bader type atomic basins that exist in perovskite crystals are occupied by ionised species with a degree of co-valency.*

This thesis reports on a theoretical study of the oxide members of the family of crystalline compounds known as perovskites. These are binary or ternary compounds with a distinctive structure.

Most perovskites are oxides with the formula $\mathrm{ABO_3}$ and with certain constraints on ionic "size". Characteristically and uniquely the A site accommodates a large cation capable of 12-coordination and the B site accommodates a small cation capable of 6-coordination within an octahedral cage of the O ions. Thus it happens that typically A is an alkaline earth metal and B is a transition metal. There are also fluorides with the perovskite structure, but these are not considered in this thesis. The perovskite structure maximises coordination of its cations, in contrast to the $\mathrm{ABO_4}$ zircon and scheelite structures, for example, both of which have 4-coordinated B and 8-coordinated A cations. The A sites in perovskites can be unoccupied, as in two binary perovskites $\mathrm{WO_3}$ and $\mathrm{ReO_3}$ included in this study. The essential feature of perovskites is the skeleton structure of 6-coordinated $\mathrm{BO_6}$ octahedra that share all corners but no edges - octahedral "cages".

The perovskite oxygen octahedra are uniform in the cubic phases, but are distorted or re-oriented or both in other phases but still retaining the corner connected characteristic. The distortions lead to many of the important properties described in following sections.

The following diagrams illustrate the cubic perovskite structure.

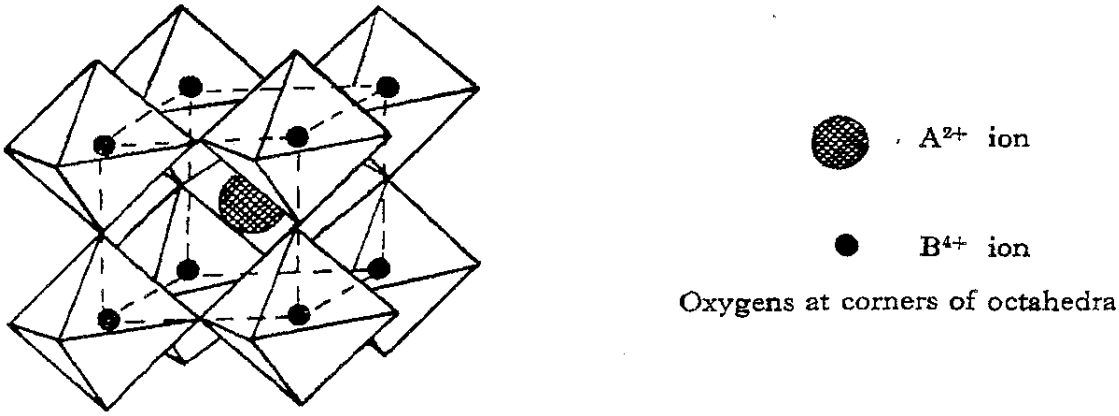

Figure 1.1: The Perovskite Structure after Megaw, 1946 [2] taken from Nara-Szabo, 1943

The second figure 1.2 is a more informative coloured model of the high temperature cubic phase of Perovskite - $CaTiO_3$. It also shows the alternative AO_{12} cub-octahedra surrounding the Ca ions.

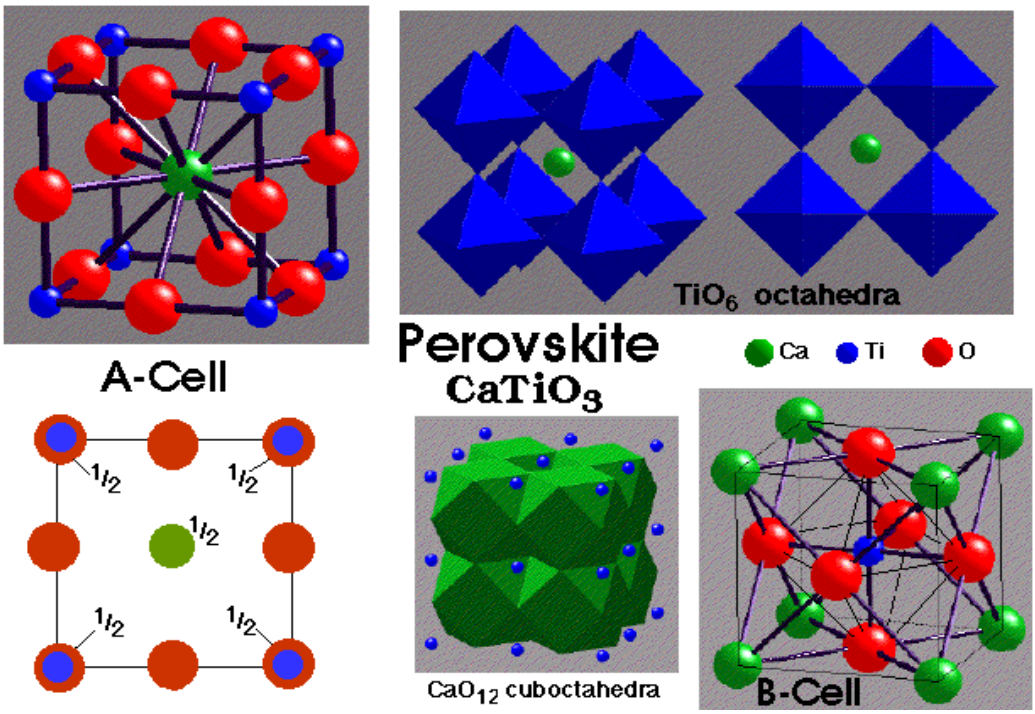

Figure 1.2: The Perovskite Structure cubic $CaTiO_3$.

This picture better illustrates the unique feature quoted above - accommodation of both small

and large cations.

The purpose of this study is to understand the special perovskite structure and its phase changes at the quantum mechanical level.

1.1 Overview of Perovskites

The following succinct background and introduction is quoted from part of the preface, by Alexandra Navrotsky and Donald J. Weidner, to the American Geophysical Union's Geophysical Monograph 45 - "Perovskite: A Structure of Great Interest to GeoPhysics and Materials Science" published in 1989. It is copied here because the author feels that it captures both the history and importance of this mineral group in an intriguing way and because it was an early introduction for himself:

> *"Perovskite, $\mathrm{CaTiO_3}$, was discovered and named in 1839 by Gustav Rose, German chemist and mineralogist (1798-l873), the year he was appointed professor at Berlin University. To Rose we owe sanidine (1808), anorthite (1823), and cancrinite (I859) as well. Alexander von Humboldt whom the Tsar of Russia had asked to explore the far reaches of his empire chose Rose as a fellow traveller. Rose's report "Reise nach dem Ural, Altai und dem Kaspischen Mee", was published in Berlin between 1837 and 1842. It is presumably there that Rose first mentioned perovskite.*
>
> *Lev Alexeievitch Perovsky was born in 1792 at Kharkov, the son of a Ukrainian nobleman of Tartar stock. He pursued a military career and fought in the Napoleonic wars, until he was wounded in the campaign of 8I4. He was promoted to colonel in I8I8. He left the army in 1823. In I84I, he was appointed Secretary of the Interior and in 1852, Director of the Imperial Cabinet he also was chairman of the committee set up to supervise the building of St. Isaac cathedral in St. Petersburg. In 1855, he devoted much effort to promoting the exploitation of the mines of the Altai district. During the Crimean war he mustered a regiment of riflemen and he was promoted to general and adjutant general to the Emperor. He died in 1856 in St.Petersburg.*
>
> *This minor accessory mineral, named after a minor dignitary, has lent its name to all materials possessing similar structures. Because the perovskite structure uniquely accommodates both large and small cations, because distortions of the ideal cubic structure provide further flexibility for incorporating cations of different sizes, and because the structure is remarkably tolerant of vacancy formation and atomic-scale intergrowths with other structural motifs, perovskite related compounds can be syn-*

thesized for an extremely wide variety of combinations of chemical elements. The resulting materials can be insulators, semiconductors, metals, and, as the past two years have shown, superconductors. They find technical application today in ceramics, refractories, and electronics, as possible hosts for nuclear waste. When the high Tc superconductors are commercialized, perovskite-related materials will presumably pioneer a host of new technologies.

Nature has put the perovskite structure to use in the dense hot ceramic interior of our planet. From the 670 km seismic discontinuity to the core-mantle boundary, an $\mathrm{MgSiO_3}$*-rich perovskite phase probably accounts for 50-90% of the volume of that region. Thus this material, accessible to us on the surface in microgram amounts in diamond-cell experiments and in milligram amounts by laborious "large volume" synthesis, may in fact be the most abundant single mineral in the Earth.*

Even before the excitement of high-$\mathrm{T_c}$ *made front-page news in late 1986, a group of mineral physicists had started planning a small interdisciplinary conference on the perovskite structure. Its purpose was to bring together the geophysics and materials science community to discuss fundamental questions of structure, stability, and properties in perovskite-related materials. We felt that the geophysicists, trying to model the lower mantle based on scanty data for the properties of* $\mathrm{MgSiO_3}$ *perovskite had much to learn from the systematic study of perovskite structures done in the materials community. At the same time, the materials scientists could broaden their pressure and temperature horizons by considering* $\mathrm{MgSiO_3}$ *perovskite. The variety of papers and of fields represented, the interest with which these were received, and the spirited discussions which ensued, indeed confirmed this impression and contributed to the success of the Chapman Conference on "Perovskite-A Structure of Great Interest to Geophysics and Materials Science" held in Bisbee, Arizona, Oct. 29-Nov. 2, 1987."*

So it can be seen that the special features of this structural family attracted interest from a diverse group of disciplines. The above quotation is now more than 30 years old, but the interest continues to increase today, because the perovskite structure is connected to many of the the most recent discoveries in materials science and geophysics.

1.2 Perovskites and modern Science and Technology

Perovskites present wide range of useful unusual electronic, magnetic and transport properties that are associated with this distinctive crystal structure. Important effects associated with the per-

ovskite structure include high temperature superconductivity, colossal magnetoresistance, photoconductivity, ferroelectricity and relaxor ferroelectricity. These properties can be varied or "tuned" because the perovskite structure admits a very wide range of doping, mixing cation species, and manipulating oxygen excess/deficiency by exploiting different cation valencies. Examples include:

$CaTiO_3$ - dielectric;

$BaTiO_3$ - ferroelectric;

$Pb(Mg_{1/3}Nb_{2/3})O_3$ - relaxor ferroelectric;

$Pb(Zr_{1-x}Ti_x)O_3$ - piezoelectric;

$(Ba_{1-x}La_x)TiO_3$ - semiconductor;

Na_xWO_3 - mixed conductor, electrochromic;

$SrCeO_3$ - protonic conductor;

$RECoO_{3-\delta}$ (RE = mixed Rare Earth Anions, δ = oxygen deficiency) - mixed electronic/O^{2-} conductor, thermoelectric properties;

$(Li_{0.5-3x}La_{0.5+x})TiO_3$ - lithium ion conductor;

$La_{1-x}K_xMnO_{3-\delta}$ - Giant magneto- resistance;

$YBa_2Cu_3O_{7-\delta}$ - superconductor.

Examples of the topicality of continuing research into perovskites are the recent announcements - in very different applications:

(a) of a breakthrough in the development of a layered ferroelectric dynamic random access memory technology [3]. Compared to a conventional DRAM cell, the new technology obviates the need for a capacitor, has 10^3 longer charge retention, lower power consumption and the ability to store several bits per cell - a very significant advance in the progress to smaller, faster computers that use less power;

(b) of the promise of considerably lower-cost diesel exhaust treatment systems based on strontium doped perovskite oxides [4].

The largest group, Transition Metal perovskites, by their nature, are the geometrically simple examples of periodic d-block systems with an additional cation. There exists a large array of behaviours and properties related to lowering symmetry to break degeneracy amongst the occupied d orbitals. As a group these perovskites fall within the category of strongly correlated electron systems and are one of the main hosts of many of the phenomena that have become foremost in modern technological research, including high critical temperature superconductivity, colossal magnetoresistivity, ultra high and tunable dielectric coefficient, high temperature solid state protonic and ionic conduction, et cetera. Though not a Transition Metal, Aluminium has a suitably

small cation, and the Aluminate perovskites have now attracted interest since fabricated interfaces with Transition Metal perovskites act as two dimensional superconducting layers. Also very currently, the binary perovskite, tungsten trioxide, WO_3, attracts a lot of research interest as a photo-electric and photo-catalytic material for solar energy and hydrogen production. In this case there are no d-electrons on the W^{6+} ion, but a powerful symmetry reduction produces two styles of bond with O^{--} and strongly distorts the octahedral frame.

Less typical, and unknown until 1976 are the Silicate perovskites, which are thought to be the most abundant mineral species of the lower mantle, and therefore the entire planet. The formation of these at the lower mantle boundary and their reaction with molten iron at the outer core boundary are fundamental driving forces of Earth's tectonic and magnetic behaviour. Because they are so difficult to observe in the laboratory, much of the knowledge of their behaviour depends on the above mentioned quantum mechanical ab initio calculation.

Figure 1.3 is copied from [5], an illustrated modern summary of oxide perovskites, to show the range of phenomena relevant to modern technologies that these materials display.

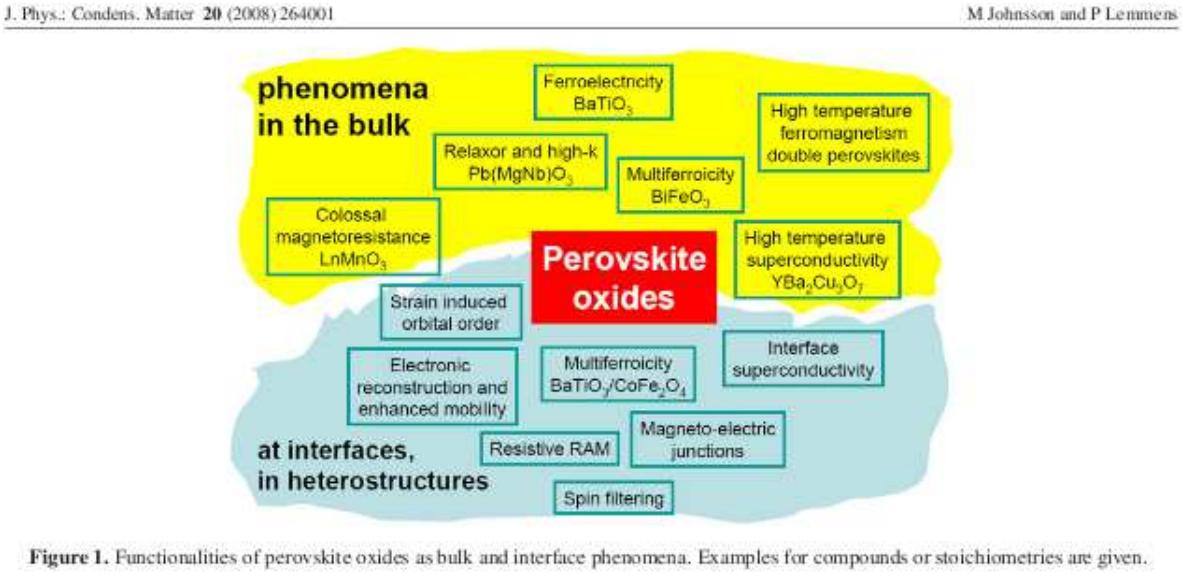

Figure 1.3: Copied from Johnsson and Lemmens, 2008 [5]

From the array of topical research areas provided by perovskites, the author has chosen to research the nature of the octahedral "cages" and the "bonds" that sustain them. This has meant examining the electronic charge densities and electrostatic potential fields at the microscopic level and to consideration of the nature of "bonding" in crystalline materials. To this end the author has undertaken ab initio calculations on selected well characterised perovskites. The way in which the shape, orientation, extent and energies of the atomic orbitals of the participating atoms contributes to the nature of the crystalline orbitals that develop when those atoms interact is examined. This is

a progression from, and calls upon insights gained in, his earlier studies of large anions in oxides with the fluorite structure. Much use is made of the CRYSTAL06 suite of programmes [6] for calculating charge densities and other properties, and the XCrysDen programme [7] for illustrating structures and extracting structural measurements from the CRYSTAL06 calculations. As well as the calculations on perovskites, these programmes were also applied to ab initio calculations of diamond, metallic Cu and Os, highly ionic NaCl and MgO and a range of covalent binary oxides in order to illustrate, compare and contrast the characteristics of the bonds that create crystal structure.

The particular attention to the concept of chemical bonding led to the adoption of the Bader atom paradigm [8]. Bader did not believe in "bonds" as the term is widely used in chemistry [9]:

> the notion of a chemical bond is too restrictive to account for the physics underlying the broad spectrum of interactions between atoms and molecules that determine the properties of matter. A bond path on the other hand, as well as being accessible to experimental verification and subject to the theorems of quantum mechanics, is applicable to any and all of the interactions that account for the properties of matter.

- he makes the point that:

> Interacting Atoms Are Bonded to One Another. The presence of a bond path linking a pair of atoms fulfills the sufficient and necessary conditions that the atoms are bonded to one another. This definition transcends all bonding schemes and categories and provides a unified physical understanding of atomic interactions.

He is talking about Bader topological atoms (see below, especially chapter 3). The present study relates qualitative and quantitative features of the bond path to the conventional notion of the chemical bond between two adjoining atoms in a crystalline material, and the resilience of the perovskite octahedral cages.

1.3 Rationale

Although the discussion above reveals the great interest the perovskite structure holds for earth scientists, and the author has been a practising geologist for over forty years, that was not the motivation for this study. Rather his interest in perovskites was kindled when studying oxides with the fluorite structure [10]. In this work the author became aware of the unique place that the O^{--} ion holds in nature. It can only exist in the environment of a crystal potential, but once so located it can form very stable compounds - particularly the many ceramic oxides. Although very

stable, those oxides with the fluorite and perovskite structures exhibit good O^{--} ion mobility at high temperature and are used as the solid electrolyte for high temperature fuel cells The author used the seminal approach of Watson [11] to study the behaviour of this ion at high temperature in the two element fluorites. The present study is towards examining the behaviour and relevance, from the viewpoint of ground state electronic structure, of the O^{--} ion in the binary (WO_3 and ReO_3) and ternary perovskites. In the case of perovskites the necessary "Watson" potential is less regular. The powerful ability of the CRYSTAL06 programme to map electron density distribution from ab initio quantum mechanical calculations provided a means to carry out this aim. Also in [10] the author was able to demonstrate the that the electrostatic potential in regions where valence electron atomic orbitals of different ions would overlap NOT the electrostatic potential the ionic nuclear sites had most effect in modifying the transition energies between orbitals of different ions. For that purpose he developed a simple method of modelling the electrostatic potential for successively larger crystals. This method depended on the crystal being ionic with closed shells. The saturated or closed shell ions under consideration could be considered as point sources – based on Unsöld's theorem that the sum of the squares of the magnitudes of the wave functions for any given l is independent of orientation, so to the other ions they look spherically symmetrical i. e. point sources [12], [13] . This crude approach served its purpose in that work, but the work of the some of the authors of the CRYSTAL06 programme illustrates that the point source model is not accurate even with closed shell ionic crystals [14] [15]. The power of the CRYSTAL06 programme to map the electrostatic field from accurate quantum mechanical calculations allowed the author to advance his ideas in the more complicated case of perovskites where a more realistic distribution of the electrostatic potential is important.

The Bader concept of " Atoms in Molecules" [16, 8] is adapted for the solid state. Although his book does not mention it, it is well known that the Bader atom concept applies to crystals, e.g. [17],[18], [19] and references (7)-(9) in [20]. This approach revealed a rather different picture of atomic structure in the cases studied to that of the main body of literature on perovskites.

The investigation for this thesis is carried out by way of quantum mechanical ab initio calculation of electron distributions and band structure, and using the concept of "topological atoms" in crystals [8], [21] . By adopting the Bader approach, the study rests on the continuum concept of electronic charge density. There is attraction in this because the electronic charge density is a well known much measured attribute of crystalline materials and it exists as a periodic scalar field in real space amenable to relatively straightforward mathematical analysis. The relatively strong bond that characterises the $B - O_6$ corner connected octahedron within the perovskite structure (see below) can be seen to include a degree of covalency that increases the cohesive energy be-

tween pairs of Bader atoms. In relating the degree of covalency to bond strength a definition of a *Bridge Index* for adjoining atoms or ions in periodic condensed matter is proposed and detailed in chapter 5.

In keeping with the large body of existing literature, the introductory discussion of structure etc. is in terms of spherical atoms or ions that have a radius and are involved in ionic, covalent or metallic bonding. However these (very useful and illustrative) concepts will then be dropped in favour of Bader's as this thesis develops.

1.4 The Perovskite Structure - historical viewpoint

1.4.1 The Structure

For context the features described in the introduction to this chapter are repeated:

Most perovskites are oxides with the formula $\mathrm{ABO_3}$ and with certain constraints on ionic "size". The essential feature of perovskites is the skeleton structure of $\mathrm{BO_6}$ octahedra that share all corners but no edges. Topologically the perovskite structure is the simplest of the three kinds of 3D periodic nets that allow this - perovskite structure, hexagonal tungsten bronze structure and pyrochlore structure - with the net containing 4-rings only. The maximum symmetry of the arrangement is $Pm\bar{3}m$ with one octahedron per unit cell [22] [23].

The octahedral frames of $\mathrm{O^{--}}$ ions are notably stable throughout all of the phase changes that can happen to perovskites. Ideally, A, interstitial between the frames, is a relatively large cation capable of 12-coordination with the $\mathrm{O^{--}}$ ions and B, internal within the frame, is a smaller cation capable of 6-coordination. Thus it happens that typically A is an alkaline earth metal and B is a transition metal. There are also fluorides with the perovskite structure, but these are not considered in this thesis. The diagrams below illustrate the cubic perovskite structure.

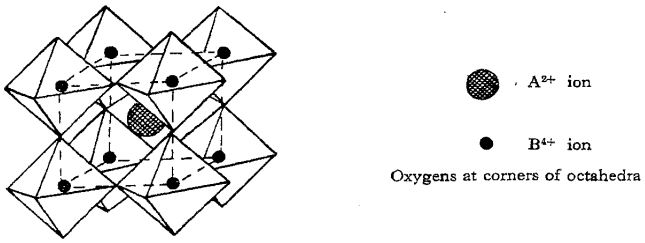

Figure 1.4: The Perovskite Structure after Megaw, 1946 taken from Nara-Szabo, 1943

The second figure, on the next page, is a more informative coloured model of the high temperature cubic phase of Perovskite - $\mathrm{CaTiO_3}$.

The unique feature quoted in the section above - accommodation of both small and large

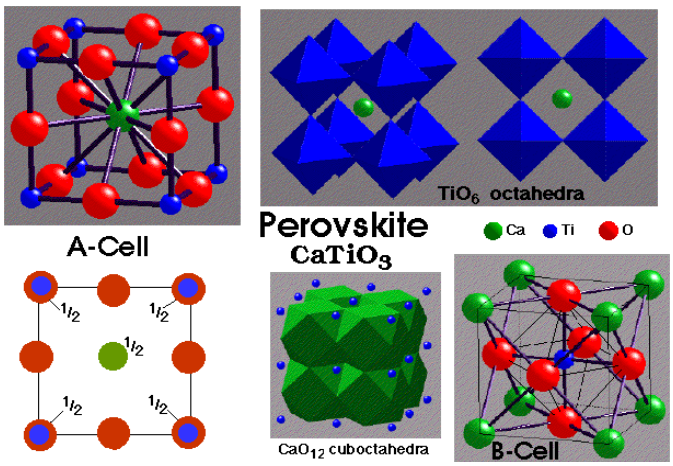

Figure 1.5: The Perovskite Structure. The ions are illustrated smaller than actual ”size”.).

cations - depends on the arrangement of the corner-connected octahedral ”cages” of O^{--} ions that characterise the perovskite structure. These contain the small cations in 6-coordination, while the large interstitial cuboctahedra contain the large cation, usually in 12-coordination, large cation plus vacancies or even no cation.

1.4.2 Goldschmidt's formula and tolerance factor.

Most of the earlier literature about perovskites was in terms of rotation or tilting of the relatively stable oxygen octahedra. It will be seen that the corner-connected octahedral frames of O^{--} ions determine the unit cell dimensions, but that these must vary somewhat if close packing of O^{--} ions and A ions is to be achieved, and that B ions will not always be close packed - they can move within the frame. There is a simple geometric relationship dictated by the cubic strucure with unit cell length a:

A - O distance $= \sqrt{2} \times \frac{a}{2}$ and B - O distance $= \frac{a}{2}$.

If the ions are close packed these distances will be replaced by the sum of the relevant ionic radii. However since there are various versions of such radii, which also vary with coordination number, this relationship is not very precise. Goldschmidt amongst others was an important contributor to what became a more or less standard tables of ionic radii and their variation with coordination number. The Shannon and Prewitt tables [24] are the most often used today - see Appendix A in [10]. Goldschmidt used a formula, based on his ionic radii to account for non close-packing. He introduced the *tolerance factor*, t such that:

$t = \frac{Radius_A + Radius_O}{\sqrt{2} \times (Radius_B + Radius_O)}$

with this scheme, the ideal cubic perovskite SrTiO3 had t = 1.00, $Radius_A$ = 1.44 , $Radius_B$

= 0.605 , and $Radius_O$ = 1.40 , but these radii differ somewhat from the Shannon and Prewitt values, so the formula is best looked upon as a good rule of thumb from which the following generalisations hold:

when $t < 1$ down to 0.75, due to a decreased $Radius_A$, the BO^6 octahedra tilt to optimise the $A - O$ bonding, thus creating tetragonal, orthorhombic or trigonal symmetries. Below this t value, the ilmenite strucure results.

when $t > 1$ due to increased $Radius_A$ or decreased $Radius_B$, the stable structure has hexagonal symmetry, with face sharing octahedra, so it is no longer strictly the perovskite structure.

If the ions are not close-packed, decreased $Radius_B$ can lead to displacement of the B ion from a central point between the O ions, which may be accompanied by displacement also of the A ions relative to the octahedral frame. In the tetragonal Titanates, these asymmetries, due to increased covalency between one oxygen and titanium at the expense of the opposite oxygen where the "bond" becomes ionic, are the principle reason for the pronounced ferroelectricity.

The variations due different packing and ionic radii are nicely illustrated in [5] from which the following two diagrams are copied:

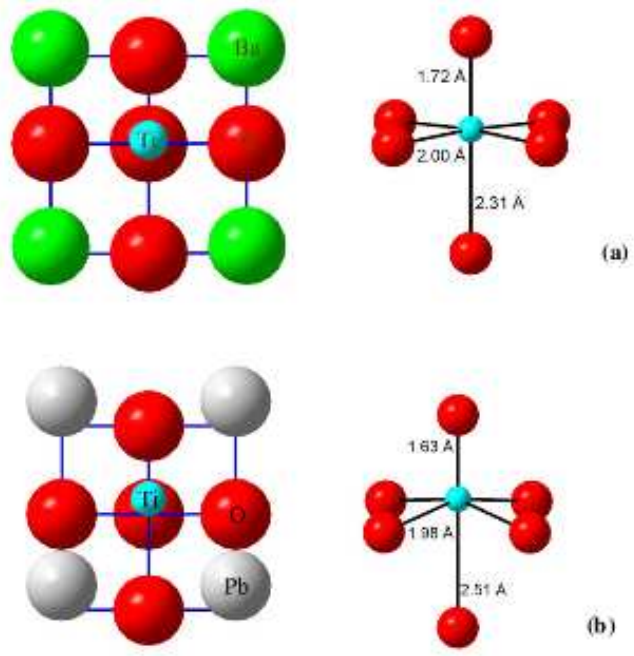

Figure 5. (a) Tetragonal $BaTiO_3$. The shifts of Ti and Ba relative to the O_6 octahedra around the original Ti position: Ti and Ba both shift by 0.30 Å in the same direction. (b) In tetragonal $PbTiO_3$ Ti and Pb are shifted by 0.44 Å.

Figure 1.6: This figure, copied from [5], illustrates the displacement off-centre of the B ion within the octahedral frame when it is too small for close packing. This results in a tetragonal structure.

Goldschmidt's simple scheme based on ionic "size" has worked out remarkably well, and is still used for interpretation of experimental results, e.g. [25] . It describes the geometry and phase changes quite consistently, but there are exceptions, such as $SrTiO3$ which should be the ideal stable cubic perovskite but has subtle phase variations for which the ionic packing model has no explanation. In the density functional picture adopted in this thesis atomic size is an electronic charge density property, not a chemical one, and the combination of electronic charge density at atomic boundaries and the knowledge of predictable orbital energies allows an explanation at a fundamental level of the structure and phase behaviour of all the perovskies studied. This will be discussed in detail in chapter 5.

1.4.3 More on the corner-connected octahedral "cages" of O^{--} ions.

The idea of "cages" [1] arises when $Radius_B$ is smaller than the space allowed by its six coordinated O neighbours, or when at least one dimension of the O structure is stretched by large $Radius_A$ ions, but where the limiting hexagonal structure has not developed. The phrase "the idea that the ferroelectric distortion is due to the B cation 'rattling' in the oxygen cage" was ascribed by Cohen [26] to J. C. Slater [27], but although Slater describes independent oscillations of Ti ions, he mentions neither rattling nor cage. Never the less the imagery seems apt, and this author began his research with the (incorrect) Slater picture in mind. As the work below indicates, and as Cohen showed convincingly, the B ions are far from independent - they become "more attached" to one of the oxygens by a bond that is strengthened by a degree of covalency. But the description of the oxygen octahedron as a cage now pervades the literature, and is adopted here. Also it should be noted that the "rattling" mode (anharmonic, and not within but between the oxygen "cages") is well documented by very recent experimental and theoretical work on the superconducting alkali metal - transition metal pyrochlores e.g. KOs_2O_6[28],[29]. In this case the transition metal and oxygen are strongly bonded as in the perovskites discussed in this thesis, but the alkali metal ions lie in a flat anharmonic potential in the interstices between the transition metal oxide octahedra (which are corner connected as in the perovskites, but not so orderly, and there are actually three different shapes of large interstices). This freedom of the alkali ion to "rattle" is viewed as contributing to the formation of Cooper pairs (*op. cit*).

The corner-connected octahedral "cages" of O^{--} ion are the fundamental skeleton of the perovskite structure. The O^{--} ions, especially their 2p orbitals, participate in the (orbital) hybridisation, super exchange and transport mechanisms that produce the large array of properties amongst

[1] meant as an illustrative descriptive word, not to be confused with the cages in the topology of Bader atoms, to be discussed later

perovskites, but the octahedra formed by them are generally thought to remain intact and rigid [30] or relatively undeformed in lattice dynamic and phase change events [31]. For example, early experimental and theoretical work on $SrTiO_3$ [32] and Na_xWO_3 bronzes [33], in connection with the lattice dynamics of ferroelectric materials, revealed that important modes are vibrations of Ti ions relative to the intact cages, and the in-phase and opposite-phase rotations of the entire cage. Phase changes which affect dielectric properties and may produce ferroelectric states were shown to be the result of softening and eventual condensation or "freezing" of these modes, leaving the octahedra intact but rotated and/or the contained B ion displaced from a central position within its octahedron. The early work found that the so called polarisable shell ionic model well represented the experimental data, but the later models that incorporated quantum mechanical molecular orbital theory and bond length and coordination data yielded more insight into the actual mechanism. In particular the latter explained the role of octahedral tilt angles in lowering the covalent bond strength within the oxygen octahedron [31].

There is an entrenched standard notation introduced by Glazer [34] which describes and classifies 23 tilt systems describing octahedral tilting in perovskites assuming more or less undistorted octahedra. The bulk of the literature describes phases and phase changes in terms of this scheme, and even describes dynamic spectra by this scheme. There are good group theoretical reasons for this approach [35] [36], but it does not actually explain anything in a fundamental or predictive way.

1.4.4 Depicting the octahedral "cages" of O^{--} ions.

Figure 1.5 overleaf, based on calculations of monoclinic WO_3, illustrates the standard scheme that will be used throughout this thesis to describe the geometry of the "cages" and the chemical bonds that are involved. Clearly a robust structural unit such as these "cages" will in some way depend on the nature of the "bonds" between its constituent ions, and this aspect is covered in more detail in chapters 2 and 5.

Two things make it clear that the $B-O$ bonds that create the oxygen octahedra are stronger than the interstitial $A-O$ bonds:

(i) phase changes that involve tilting of the oxygen octahedra leave the B atom 6-coordinated, but reduce the coordination of the A atom from its ideal 12;

(ii) rotational modes of the essentially rigid octahedra involve larger amplitude $A-O$ displacements than $B-O$ displacements.

This thesis sets out to understand these facts in terms of electronic charge density (ECD) distribution, and makes no recourse the models referred to above. The measurements reported in

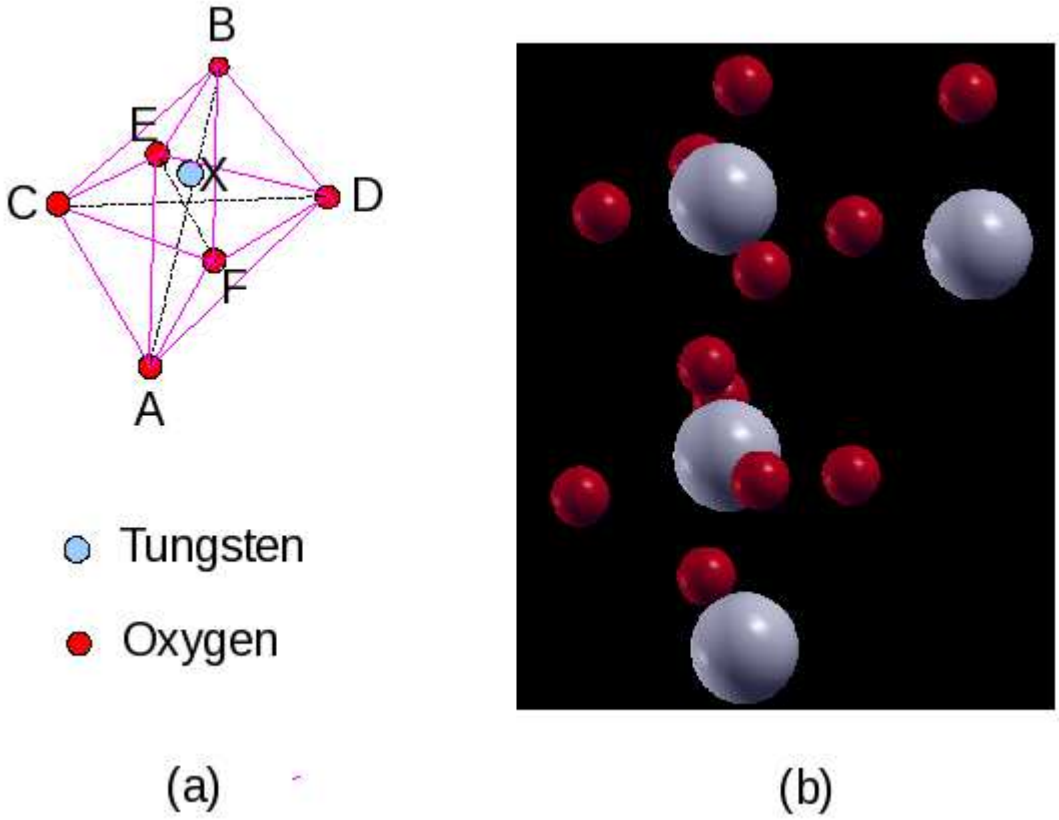

Figure 1.7: **Standardised description of the Octahedral Cage.**The diagram (a) is based on calculated monoclinic WO_3 (b) which was the least symmetrical perovskite studied. The oxygen atoms A and B will be called (south and north) polar atoms. C, E, D and F will be called equatorial atoms, and in this case are NOT co-planar. The atom at X (tungsten in this case) will be called the central cation. “Bond lengths” can then be described as distances such as XB or XD, and ”bond angles” will be the angles such as CXA. Notice that in this rather deformed cage, the tungsten atom X is neither co-linear with any pair of oxygen atoms nor co-planar with any three equatorial atoms.

appendix A are not towards classifying into Glazer’s scheme, rather they are towards matching physical and phenomenological attributes (e.g. polarisability) to features of the ECD distribution. The relationship between atomic bonds and the ECD distribution is examined and simple Bond Path Index is introduced.

1.5 Outline of this Thesis

The chapters that follow are arranged to develop the theme in five sections:

Chapter 2, the physical context and principles including the importance of quantum mechanical calculation of the electrostatic field within a crystal, the nature of partial covalency and an outline of methods;

Chapter 3, introducing Topological Atoms;‘

Chapter 4, the main tool - CRYSTAL06;

Chapter 5, “chemical bonds” in crystals and their effects on structure. Introduction of the *Crystalline Bridge Index*.

Chapter 6, A discussion of the results and their interpretation.

Appendix A systematic study of related types of perovskite, comparing and contrasting metallic/insulator, change of A ion, change of B ion and comparison between a perovskite and the simpler B oxide.

Chapter 2

Background, Physical Principles and Methods

2.1 Introduction

2.1.1 Moving from a Classical to a Quantum Mechanical framework

Much of the discussion of perovskites in the previous chapter was in terms of classical physics - necessarily so in the case of historical references, but also much of the later work was done by geologists and mineralogists who used quasi-classical concepts of ionic radius and coordination. Two exceptions that the author has drawn upon are [37] and [38], chapter 19. Quantum mechanics requires consideration of exchange and correlation energies and so called degeneracy pressure - Pauli repulsion - that add to the classical electrostatic energies in dictating electronic, thence crystalline, structure. The ramifications of this are discussed in the following sections.

2.1.2 Modelling the essential nature of crystalline materials - outer electron interaction

All of the the non-nuclear physical and chemical behaviour of solid materials involves the interactions occurring in non-core regions between atoms or ions. These regions are characterised by a sparse average population of outer (valence and conduction) electrons. Goodenough divided this population into *collective electrons* and *localised electrons* [37]. *Collective electrons* are outer *s*, *p* electrons. *Localised electrons* are outer 4*f* or 5*f* electrons and are tightly bound to their atomic nuclei and are screened from the neighboring atoms by 5*s*, 5*p* or by 6*s*, 6*p* core electrons. Outer *d* electrons are intermediate in character. This is because outer *d* electrons are not screened from their neighbouring atoms by outer core electrons. This intermediate character of the *d* electrons is

manifest by the fact that in some crystals they exhibit the properties of localised electrons, in others they exhibit the properties of collective electrons, and in a few both types of *d* electrons appear to coexist. Note that, depending on the state of the *d* electrons, the collective electrons comprise some or all of the valence and conduction electrons of the participating atoms. The following diagram from [39] based on the Hartree-Fock radial orbital density probabilities in Tungsten gives some context to Goodenough's division. The core orbitals (limited down to 4f) are represented with dashed lines and the valence orbitals with solid lines.

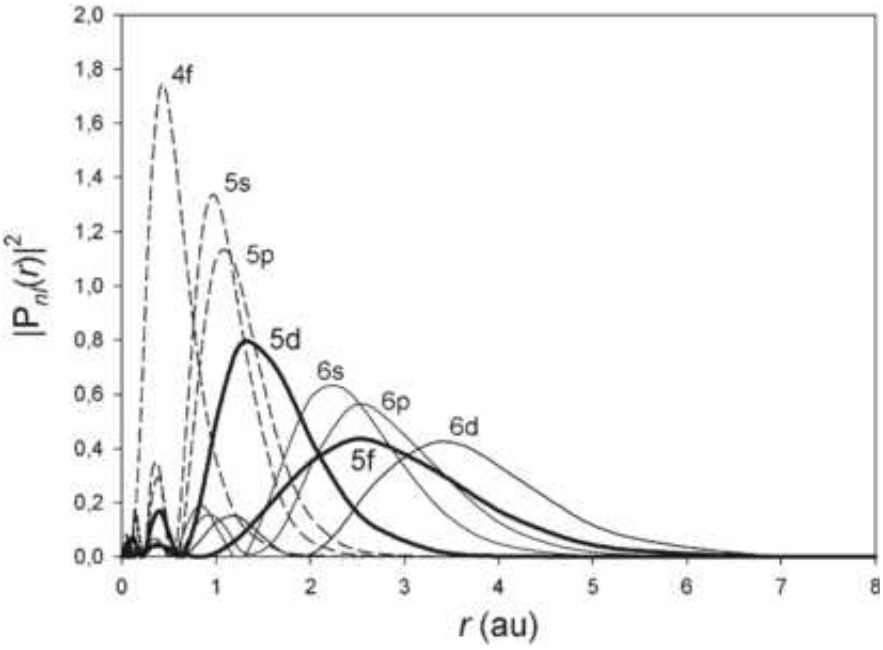

Figure 2.1: HFR orbital density probabilities in Tungsten. The core orbitals (limited down to 4f) are represented with dashed lines and the valence orbitals with continuous lines (the 5d and 5f orbitals are in bold). The importance of the penetration of the valence orbitals into the ionic core can be seen. Copied from [39]

The essential nature of crystalline materials, including symmetry, lattice parameters, bond strength and character etc., are primarily determined by the distribution of these sparse outer electrons. The localised electrons play a part in developing symmetries amongst the participating atoms due to the inherently polar character of their localisation. The calculations, interpretations, and conclusions drawn in this thesis concentrate on the periodic electronic charge density distribution in the outer regions using the methods described in section 2.5 below.

The *collective electrons* are slightly "bunched" along the bond path (to be described later) between atoms. There is a minimum value along such a bond path which has a wide range of values depending on the type of "bonding" in the valence region. In the materials studied in this thesis the highest value was 0.361 electrons per cubic bohr for the highly covalent diamond, and the lowest was 0.010430 electrons per cubic bohr for the highly ionic NaCl. These can only be

studied by quantum mechanical techniques using suitable approximate (so-called one electron) Hamiltonions which yield observables such as total energy, electronic charge distribution and the corresponding electrostatic potential distribution. Actual electron partitioning amongst atomic species is not an observable that can be calculated by these techniques, but arbitrary schemes such as Mulliken analysis (discussed later) are routinely employed. The Hellmann-Feynman theorem informs that the classical "force" on a particular nucleus can be calculated from the quantum mechanical charge distribution. It should be noted that even in strong Ferromagnetic materials, the "forces" that dictate electron configuration are overwhelmingly Coulombic, many orders greater than the magnetic interactions arising from orbital and spin angular momentum.

2.1.3 From the simple quantum mechanical picture of bonds to Bader's picture using Crystal06

The traditional picture is that in ionic crystalline solid materials, charged closed-shell ions are created by the transfer of electrons from one species to another. Net attractive forces between ions (overwhelmingly Coulombic but also inductive and magnetic) are balanced by quantum mechanical repulsive potentials between outer electrons (so-called "degeneracy pressure", a consequence the Pauli exclusion principle) to effect an equilibrium binding condition.

Likewise, in covalent or metallic crystals the binding is due to "sharing of electrons" by neighbouring atoms or by all of the atoms respectively. However, because there is some overlap of outermost *orbitals* of even highly ionic materials, some electrons must always be be shared to a small extent. This will be demonstrated later for the case of MgO and NaCl, traditionally regarded as ionic crystals.

In all of these cases the forces on an atom arising from potential energy include *pairwise* contributions from each neighbour and longer range contributions from more distant atoms.

In Quantum Chemistry an *orbital* is "a wave description of the size, shape, and orientation of the region in space available to an electron; each orbital has a specific energy." [40] - the description being a mathematical wave function. In Mulliken's words (he invented the term) "orbital means, roughly, something like an orbit; or, more precisely, something as much like an orbit as is possible in quantum mechanics. Still more precisely, the term "orbital" is simply an abbreviation for one-electron orbital wave function or, preferably, for one-electron orbital eigen-function. The last-mentioned expression refers to any one of the so-called characteristic solutions or eigenfunctions of Schrödingers quantum-mechanical wave equation for a single electron in an atom or molecule."[41] In this thesis the orbital is regarded as a state that an electron can occupy.

Quantum mechanical pictures of bonding (Valence Bond Theory VBT, Molecular Orbital -

Linear Combination of Atomic Orbitals MO-LCAO) in molecules envisage combinations of participating atomic orbitals (localised in regions of overlap for VBT or molecule-wide for MO) or *hybridisations* that are new orbitals or states of different energies whose total is less than that of the separate atomic orbital energies so that a new stable or bound configuration forms the molecule. The square of the resultant wave function is an expression of the probability density of the presence of an electron: binding orbitals represent constructive interference of the wave functions with increased probability of electrons in the overlap regions between nuclei. This results in stronger nuclear attraction and lower resultant energy. Non binding orbitals result from destructive interference - the probability density of the presence of an electron is decreased i.e. electrons are dispersed from the internuclear zone decreasing nuclear attraction and increasing the total energy (relative to that of the separated atoms). A molecule will exist provided the number of electrons in binding states exceeds the number of electrons in non binding states.

These concepts can be carried across to the crystalline state - the ionic transfer of electrons or the hybridisation to create covalency being processes amongst the *collective electrons*. In this case the participating wave functions are periodic in the crystal's unit cell dimensions in both positional and reciprocal spaces. Allowing this proviso, the octahedral O cage, in the case of the very many $\mathrm{ABO_3}$ perovskites with a *d*-block transition element B, can be understood by analogy with the sp^3d^2 octahedral 6-coordinated *d*-block ligands in molecules.

Some early work on perovskites did not recognise this possibility, due to a wrong perception of the role of the crystal field in hybridisation. For example in [42] it is stated

"Due to the large energy separation ($\approx 4\mathrm{eV}$) of the O 2*p* and Ti *3d* states, one expects, averaged over the whole Brillouin zone, only a very small *pd* hybridization."

In fact it is well known that the increasing crystalline electrostatic field reduces this gap, as is discussed in section 2.3.

But it seems that the geometry of orbital hybridisation cannot be the full story. Many $\mathrm{ABO_3}$ perovskites with $\mathrm{A = La\ and\ B = Ti, V, Cr, Mn, Fe, and Co}$ have been studied and all can be interpreted in terms of the *d* orbital geometry with the O ions acing as ligands. However there are many oxide perovskites, e.g. $\mathrm{NaMgO_3}$ or $\mathrm{LaAlO_3}$ (the latter was studied for this work) which feature the octahedral cage structure, but the B atom has no *d* electrons. Moreover, the appeals to *d* block bonding models may describe the oxygen octahedra but they do not explain the phase distortions and readily polarisable characteristics of perovskites. In the words of Walter A Harrison, "Use of *sd* hybrids as bonding units may have been a case of forcing a concept onto a system it did not fit." [38], page 439.

In looking for a more comprehensive explanation of the perovskite octahedral cages, this thesis

follows the more recent approach pioneered by Richard Bader [16], as mentioned in section 1.2, that concepts of atoms and bonds may be given definite expression in terms of the topology of the electronic charge density distribution. In the case of crystals, Bader's approach requires minor modification because the boundaries of his atomic basins that extend to infinity for a molecule, must be closed surfaces within a crystal. The usefulness of this adaptation has been demonstrated by Aray and Bader [19] and Tsirelson et al.[43] and was employed for the perovskite $SrTiO_3$ by Zhurova et al.[44]. Since then, "the Quantum Theory of Atoms in Molecules has nowadays been elected by the X-ray density community as the primary standard theory to discuss bonding in crystals." [45].

The CRYSTAL06 programme can calculate and map a ground state minimum energy electron charge density distribution and its gradient. It can also map a realistic crystalline electrostatic potential field. Thus one is able to examine the essential nature of the subject materials - at least for the ground state - and view these from the Bader atom perspective. This thesis work has been carried out in the spirit that one is dealing with high quality experimental density data.

2.1.4 The Perovskite Structure in terms of the electronic charge density distribution - London's bridge.

Ab initio quantum mechanical calculations as a means of obtaining a more fundamental understanding of the perovskite structure have been carried out since the early 1960s, and have been adopted for this thesis. The calculations yield the distribution of electronic charge density and electrostatic potential which result from the various structural phases. As a general rule, where there are other phases, the ideal cubic phase is the high temperature form, and lower temperature phases are progressively less symmetrical and lower in energy.

Perovskites are strongly ionic materials, but covalent or hybridisation effects also contribute to the formation and behaviour of the octahedral cages . In addition to the electrostatic attraction between the constituent ions, "bunching up" of the electronic charge density occurs in the region between between the nuclei of adjoining atoms/ions. This was first observed by London, in the early days of valence bond theory, using Schrödinger's definition of the charge density. Richard Bader much later formalised the Quantum Theory of Atoms in Molecules [8] basing his work on the topological analysis of the charge distribution. Although an experimental chemist he derived his work from the physics developed by Schrödinger, Feynman and Schwinger. In a late defense of his ideas [9] Bader summarised Fritz London's approach. Here is a quoted extract that includes quotes of the English translation of London's paper, and London's figures:

> London, in describing the antisymmetric and symmetric density distributions that are

reproduced here in Figure 1, states: "We see that the densities (in his Figure 2 for the antisymmetric solution) are clearly pushed outward, as if they would separate if possible. If we would bring the nuclei ... closer together, the strangling of the density between the atoms would increase"; "In opposition to Fig. 2, (his) Fig. 3 which gives the density for the symmetric solution, shows the two atoms which are in a state of homo-polar binding. Here the two densities seem to draw closer and become one. With the help of these figures, one can imagine how in complicated molecules the atoms which form a Valence are connected by such a bridge of $\Psi * \Psi$-density, while all remaining atoms stay separate." His Figure 3 clearly illustrates the buildup of density between the nuclei, a situation commented on by Feynman: "In a H2 molecule for example ... the (H-L) symmetrical solution can easily permit charge concentration between the nuclei and hence it is the only solution which is symmetrical that leads to strong attraction, and the formation of a molecule, as is well known."[48] London was the first to define a bond path as a "bridge of density" and to postulate its physical significance in the understanding of bonding.

See figure 2.2 on the next page.

London's bridge of density refers to a local increase in the electronic charge density *in the plane normal to, and lying roughly midway along, the path between the two atoms*. This provides increased attraction to each of the nuclei - Coulombic attraction, but also provides increased degeneracy pressure arising from Pauli exclusion - Steric repulsion. These balancing effects are increased if the charge density is increased; i.e. the"bond" becomes stronger. The "bunching" can be regarded as a degree of covalency that also imparts extra directionality to the bond. Materials, including Perovskites, with a covalent component in their bonds tend to be higher shear strength materials than more completely ionic materials, because a shearing between nuclei force operates with a shorter moment arm about the centroid of the attractive electronic charge distribution.

Such a bridge was observed in each of the bonds between the central B and the six O ions that make up the perovskite cage in all of the materials studied. These are the same in the cubic phase. However there is a fixed number of collective electrons that can be arranged to create the charge density distribution, so that if one bridge acquires an increased density so creating a stronger bond, one or more other bridges will be depleted with weaker bonds and the cage will distort to a phase of lower symmetry.

The figures on the following pages illustrate the London "bridge" idea and the role of electronic charge density in forming the Octahedral Cages of O^{--} ions in Perovskites. They are based on the calculations carried out by the author, including data from appendix A. Figure 2.3 shows

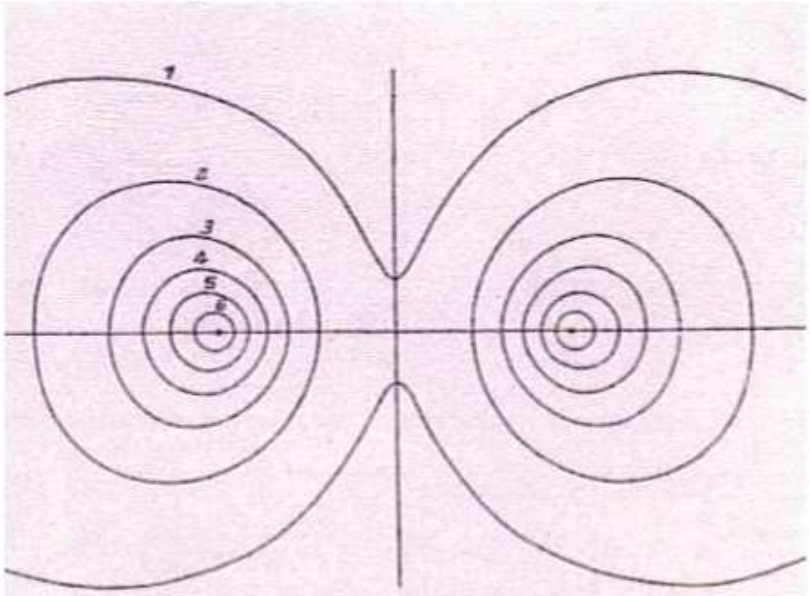

Density distribution for elastic reflection.

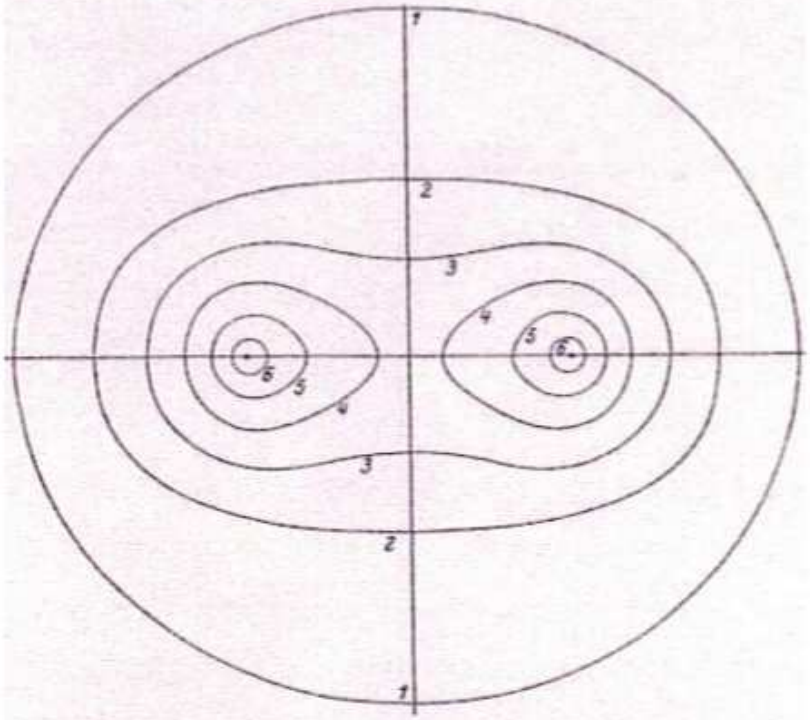

Density distribution for homo-polar reflection.

Figure 1. Electron density distributions for the hydrogen molecule given by London in 1928[57] calculated from the Heitler−London wave functions. His Figure 2 is for the antisymmetric function, the lowest excited (triplet) state, and his Figure 3 is for the symmetric ground state density. Reprinted with kind permission of Springer Science+ Business Media. Copyright 1928.

Figure 2.2: Bader's Figure 1 copying London's illustration of bonding and antibonding charge density distributions.

contour and surface plot displays for CRYSTAL06 calculation of the electronic charge density in the (1 1 0) plane of cubic $CaTiO_3$. Notice that the "bridge" between Ti and O is rather subtle and that between Ca and O is very subtle - the respective electronic charge densities at the turning points of the topological saddles being 0.10 and 0.013 electrons per cubic Bohr respectively.

It will be seen in chapter 3 that such topological features of the electronic charge density distribution within a crystal or molecule are the basis for the Bader formulation. Two principal attributes are the *bond path*, the path between adjoining nuclei, and the *bond critical point (BCP)*, a turning point in the electronic charge density density distribution along the bond path. At the BCP the charge density is minimal along the bond path and maximal for any line through the BCP lying in the plane normal to the bond path at the BCP - forming a saddle point.

Figure 2.4 illustrate the octahedral cage and Figure 2.5 shows profiles to illustrate the topological characteristics of the BCP and the higher electronic charge density between the B ion (Ti) and the O ions of the surrounding cage compared with that between the A ion (Ca) and O ions. This higher charge density serves to preserve the cage strucure during phase changes as will be discussed. Figure 2.5 also displays longitudinal- and cross-sectional profiles of the charge density distribution that form the "London bridge" connecting the Titanium and an Oxygen ion.

In the course of this work the author studied these features in covalent materials, metallic materials and highly ionic materials. *In every case a"London's bridge" exists along a bond path with a topological saddle point determining a BCP.* This is discussed further in Chapter 5. Examples of diamond (the most covalent material studied), metallic copper and two highly ionic materials, MgO and NaCl are illustrated in Figures 2.6 through 2.9. These figures also display longitudinal- and cross-sectional profiles of the charge density distribution that form the "London bridge". They show that London's bridge is always present, but with electronic charge density at the saddle point ranging through 2 orders of magnitude.

Note in Figure 2.5 that within a perovskite the short bonds have higher electronic charge density at the turning point, later to be seen as lying on the boundary between Bader atoms. As was pointed out in the previous section, the short bonds between the B atoms and the O atoms of the surrounding cage are stronger than the bonds between A atoms and O atoms. Based on the Hellmann-Feynman theorem it can be expected that there is a fundamental connection between bond length, bond strength and electronic charge density between the atoms. This connection is analysed in chapter 5.

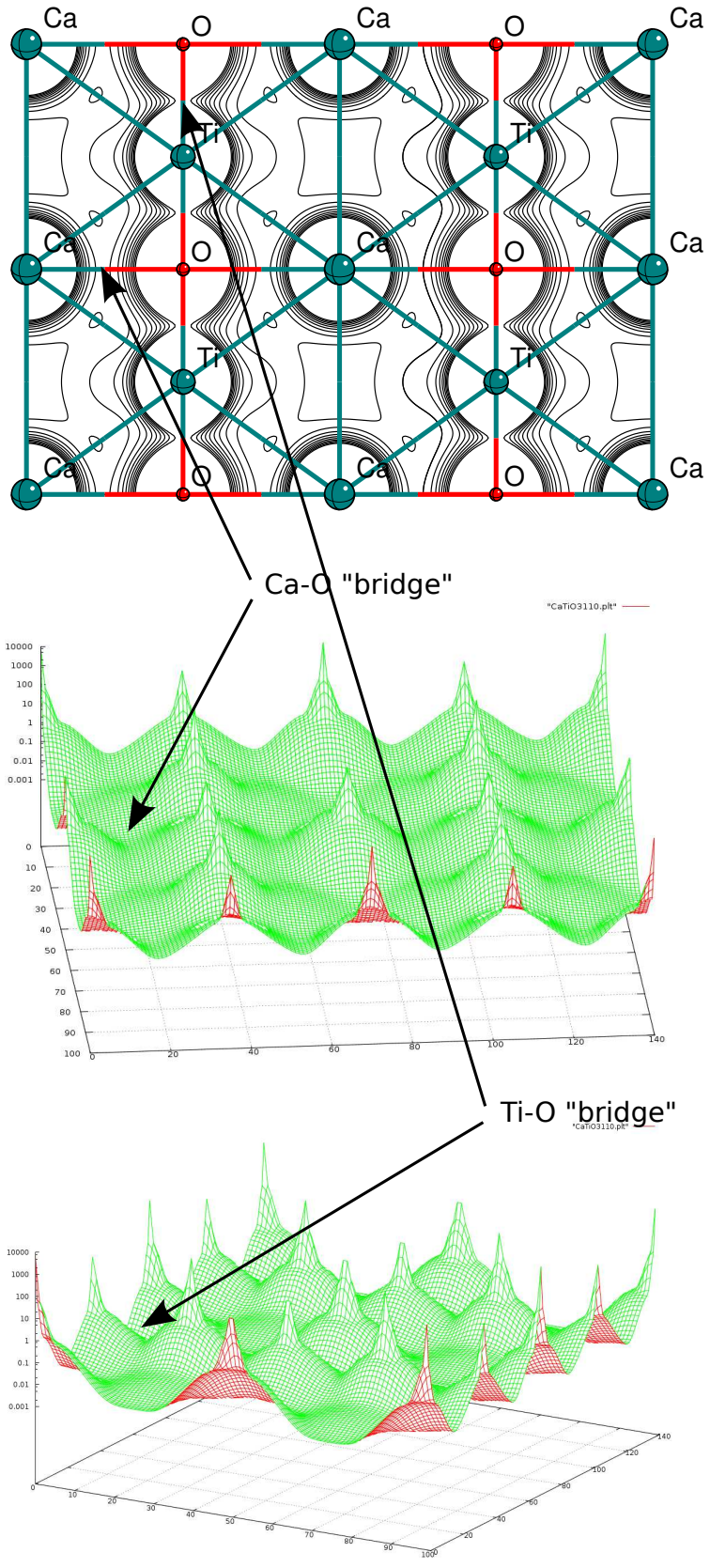

Figure 2.3: Plots of the Electronic Charge Density in the (110) plane cubic $CaTiO_3$.

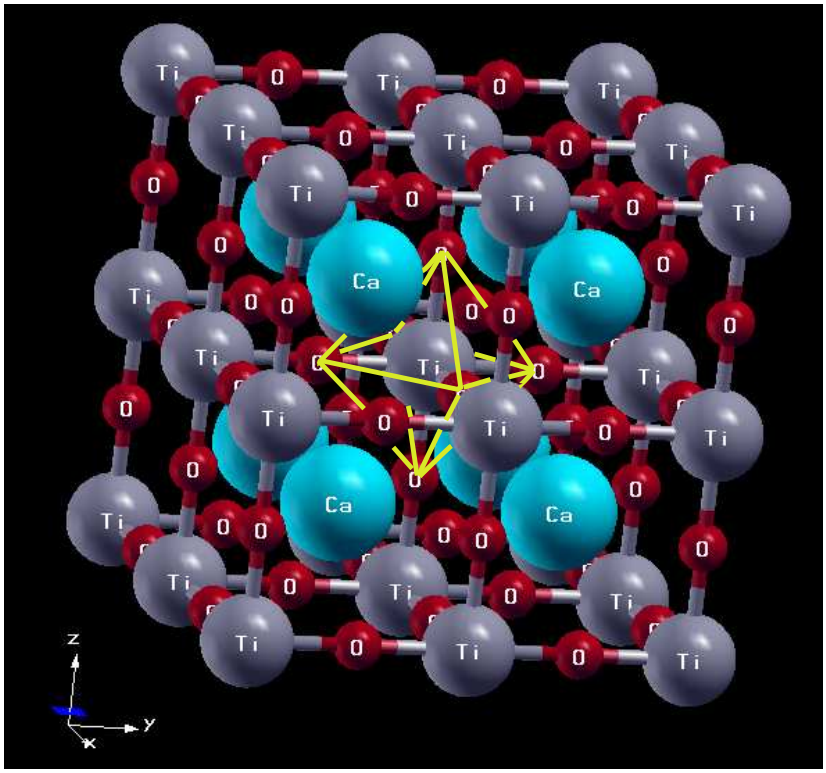

a

Figure 2.4: The Octahedral Cage in cubic $CaTiO_3$, highlighted in yellow. **Note that although this is a highly ionic material, the ions are displayed with Xcrysden's Covalent radii setting.** If Van der Waals radii or the usual Shannon and Prewitt effective ionic radii were used, ionic locations would be obscured and the octahedral cage could not be so clearly outlined.

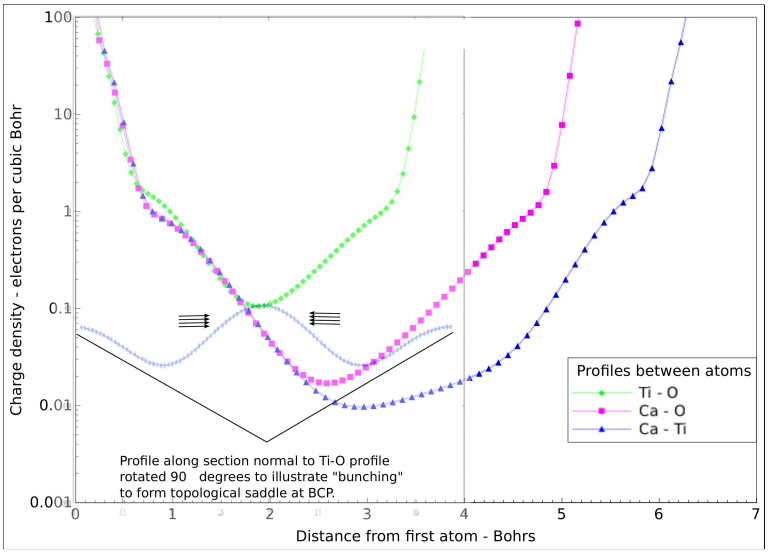

Figure 2.5: A plot of the Electronic Charge Density profiles along the paths (bond paths, see Section 3.1.1) between the ions that make up cubic $CaTiO_3$. Also shown is the charge density profile along a line normal to the $Ti - O$ bond path at the Bond Critical Point (BCP, see Section 3.1.1) to illustrate the London "bunching" effect that creates a topological saddle at the BCP. This profile would be through the page, but has been rotated 90 degrees.

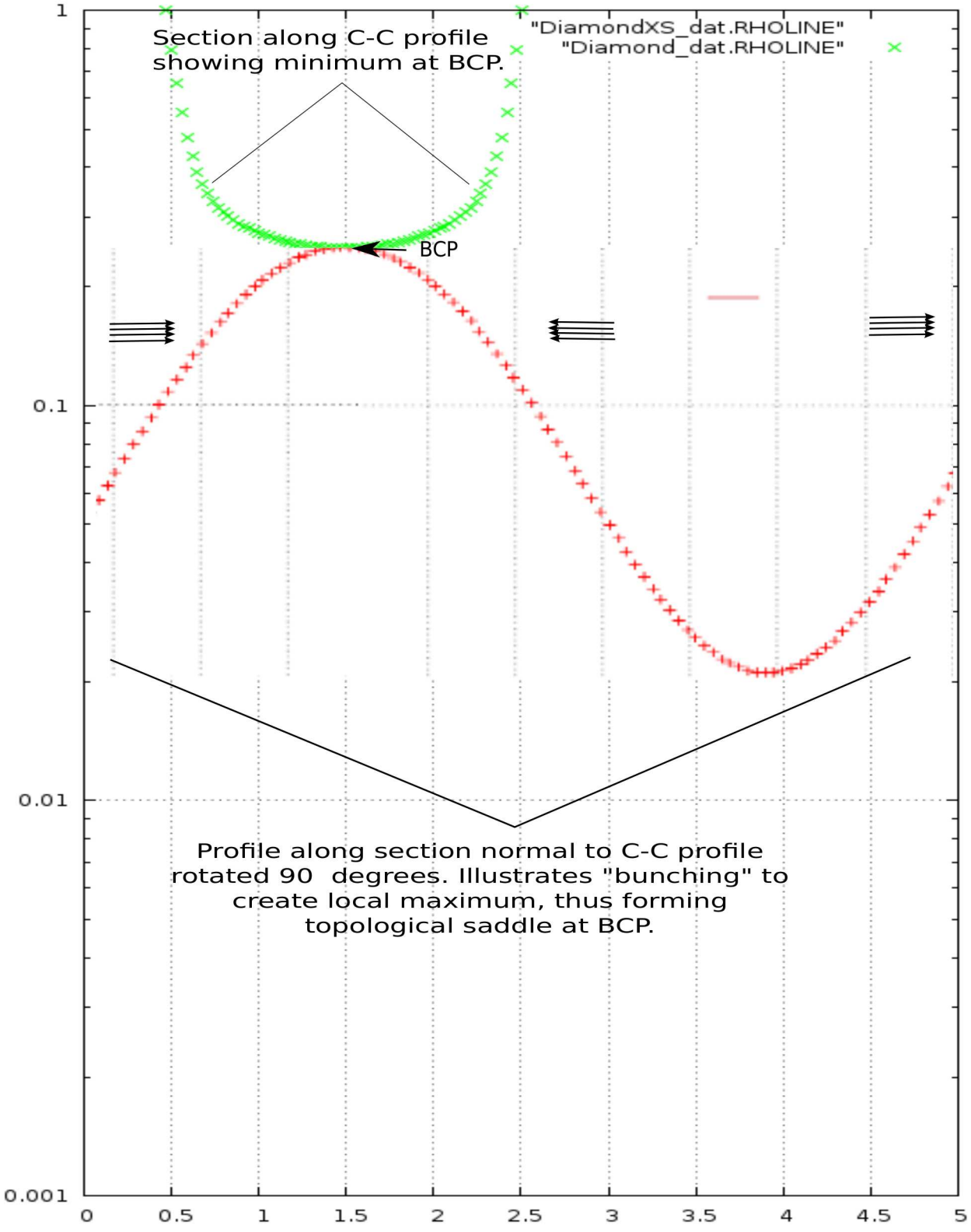

Figure 2.6: Electronic Charge Density profiles along and normal to the bond path at the BCP in the most covalent material studied, diamond, showing that London's bridge is always present.

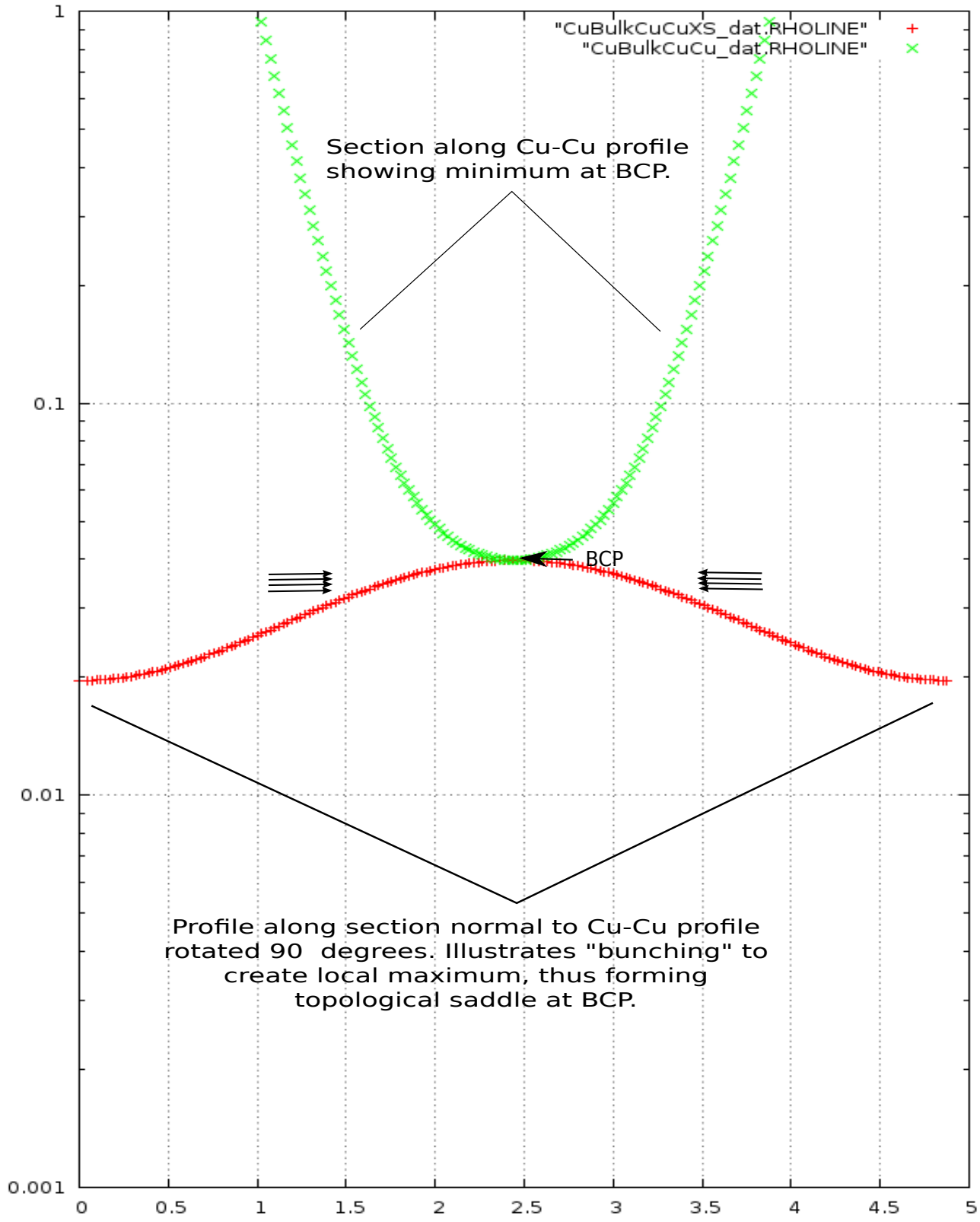

Figure 2.7: Electronic Charge Density profiles along and normal to the bond path at the BCP in metallic copper, showing that London's bridge is always present.

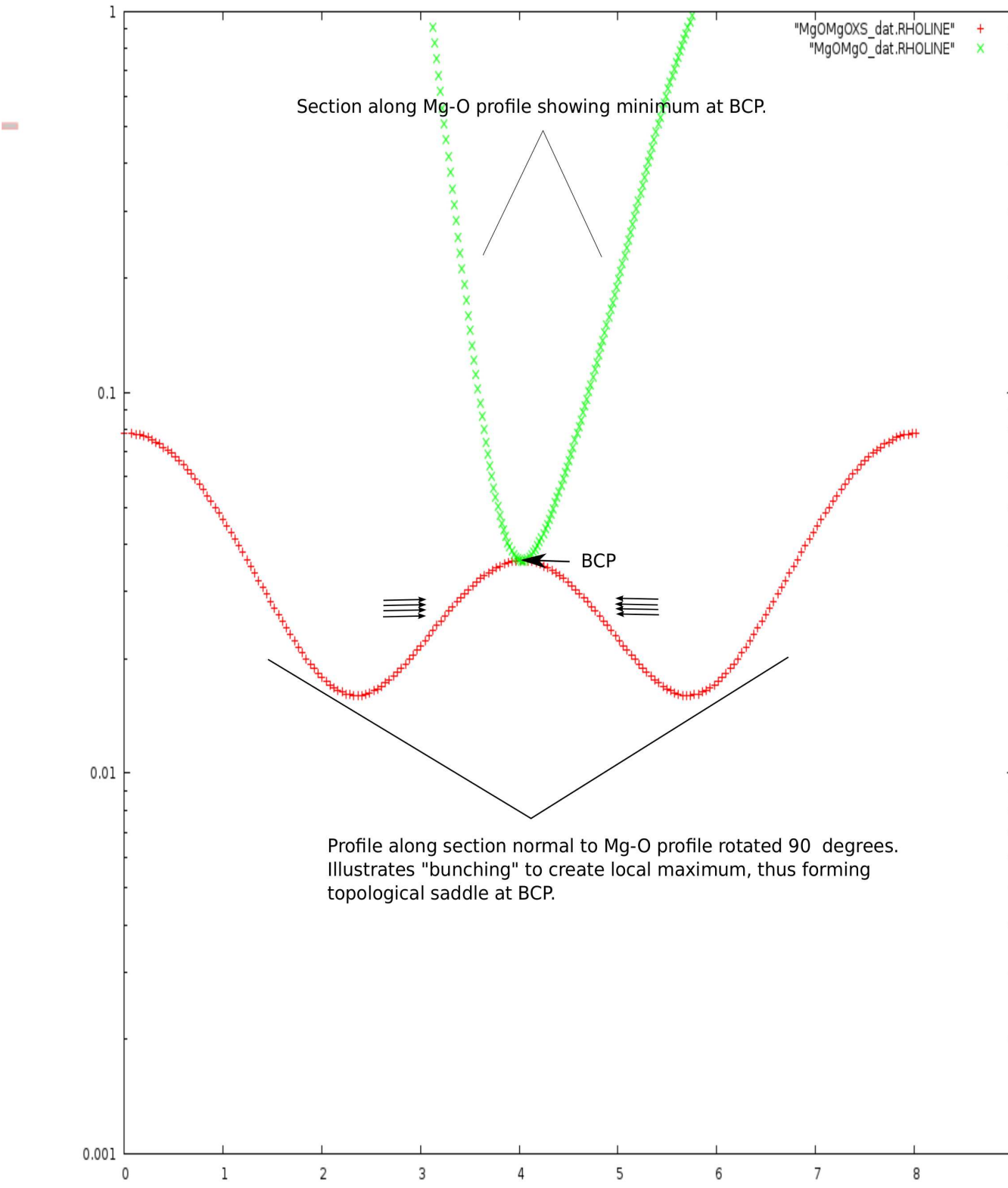

Figure 2.8: Electronic Charge Density profiles along and normal to the bond path at the BCP in the ionic material, MgO showing that London's bridge is always present, but with electronic charge density at the saddle point almost an order of magnitude lower than diamond.

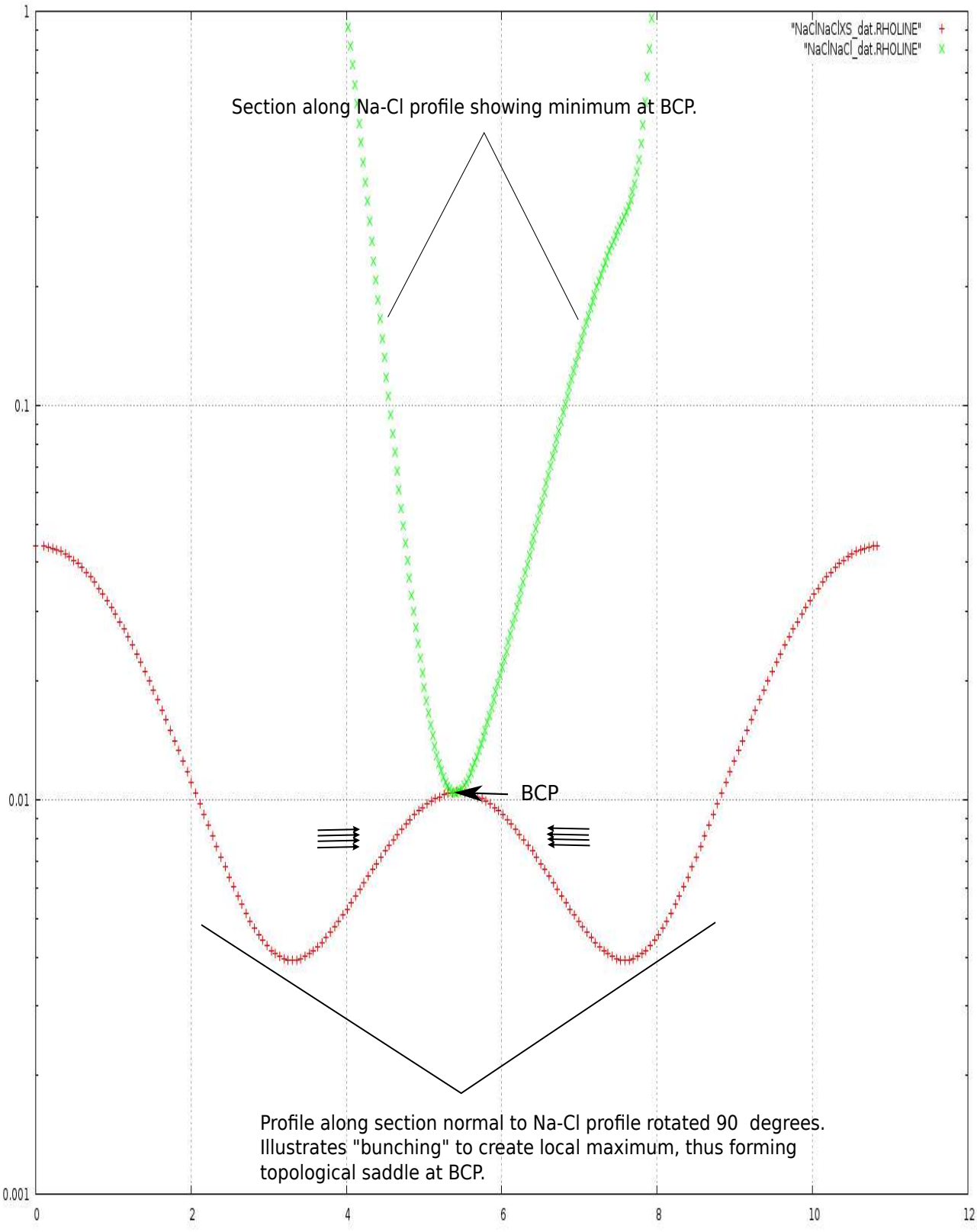

Figure 2.9: Electronic Charge Density profiles along and normal to the bond path at the BCP in the most ionic material, NaCl showing that London's bridge is always present, but with electronic charge density at the saddle point a further order of magnitude lower than diamond.

In Valence Bond Theory the London's Bridge follows because the energy contribution of the exchange integral is negative [46] pp 238 - 240. This integral applies in the overlap region making it attractive to the positively charged nuclei, so it represents increased electronic charge within the overlap region.

In Molecular Orbital Theory the London's Bridge can be interpreted as a σ bond. It will be seen below that *s* orbital contribution to σ bonding is one key to the perovskite cage structure and a reason why there can be perovskites without the A atom.

2.1.5 From Quantum Mechanics to Ab-initio Calculation Calculations with Crystalline Materials

The famous comment by Dirac [47] that "The general theory of quantum mechanics is now complete... The underlying physical laws necessary for the mathematical theory of a large part of physics and the whole of chemistry are thus completely known." may have been true in principle, but it has taken seventy years of further genius and hard slog by "chemists" [1] to rein those underlying laws of chemistry into useful computational paradigms that apply to very large molecules and solids. Notable early (ab initio) calculations of atomic and ionic orbitals by the Hartrees (father and son) and Slater in the late 1930s and through the 1940s continued with Clementi and his co-workers through the 1960s. One of Clementi's coauthors was Carla Roetti who was a principle contributor to the CRYSTAL06 programme. The next development was diatomic molecules - firstly with a basis set of Slater type orbitals. Polyatomic molecules were handled with Gaussian basis sets. An important review was published by Roothan [48] in 1951, following his formal theoretical justification of the linear combination of atomic orbitals -molecular orbital - self consistent field (LCAO-MO-SCF) method. In the 1960s Boys, followed by Pople and others replaced Slater type orbitals with linear combinations of Gaussian functions. Also at this time and predating the Hohenberg-Kohn theorems and the Kohn-Sham theorems that established density functional theory, Bader had started his work on what is now called the Quantum Theory of Atoms in Molecules. In the sixties and early seventies physicists were calculating band structure and optical properties, but stayed wary of Gaussians. The first publication using Gaussians for Hartree-Fock seems to be [49] in 1973. In the late seventies the Torino group led by Cesare Pisani, acknowledging and following the lead of [49], adapted the Pople methods to periodic solids in a widely applicable suite of programmes that would be suitable for public use . In the eighties the team was joined by British contributors, including V. Saunders and N. Harrison of the CCLRC, Daresbury Laboratory,

[1] read physicists, chemists, mathematicians, crystallographers, geophysicists etc.. The 1998 Nobel Prize in Chemistry was shared by physicist Walter Kohn and mathematician John Pople for their contribution.

and the CRYSTALxx series of programmes was released to the public. There are now quite a few ab initio computational programmes for periodic systems, all yielding similar results.

2.2 The energy regimes

The condensed matter or crystalline state that this thesis deals with can come about by crystallisation from a solution or melt or by solid state diffusion during sintering, and quite generally the process occurs at elevated temperatures often in excess of 1,000 K. However the theories and calculations employed relate to electronic ground states so it is worth noting that these remain valid even at the elevated temperatures of molten oxides. Following [50] one can regard a crystalline substance or its melt as a ”particle soup” of protons, electrons, phonons (linear), solitons (nonlinear) and photons. The solitons are a large amplitude development from certain phonons and for this discussion can be lumped with them. In general these particles interact - electrons can thermalise by collision with phonons; phonons are annihilated to produce photons in radiative cooling etc.

The energy distribution of these particles in momentum space is illustrated in the following diagram copied from [50] .The diagram is a rough sketch only to illustrate relative orders of magnitude for a free electron gas and Debye phonons. It could approximate a metal but for other real crystals the values could be 100% - 200% in error and the dispersion curves will flatten at the Brillouin zone boundary, but *the relativities will be similar*.

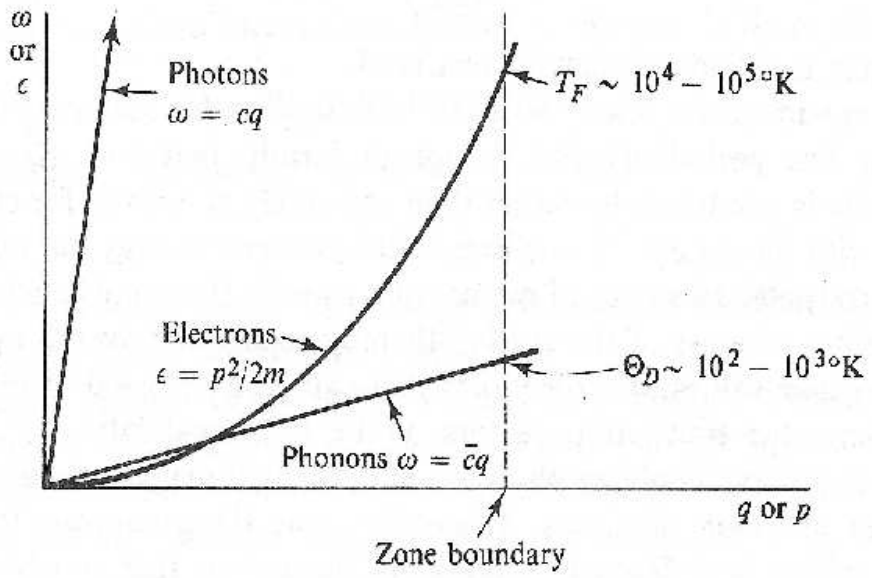

Figure 2.10: Copied from [50], illustrating relative magnitudes and energy distribution in momentum space.

The relationships for bound states are expressed more distinctly in the following diagram from [51]:

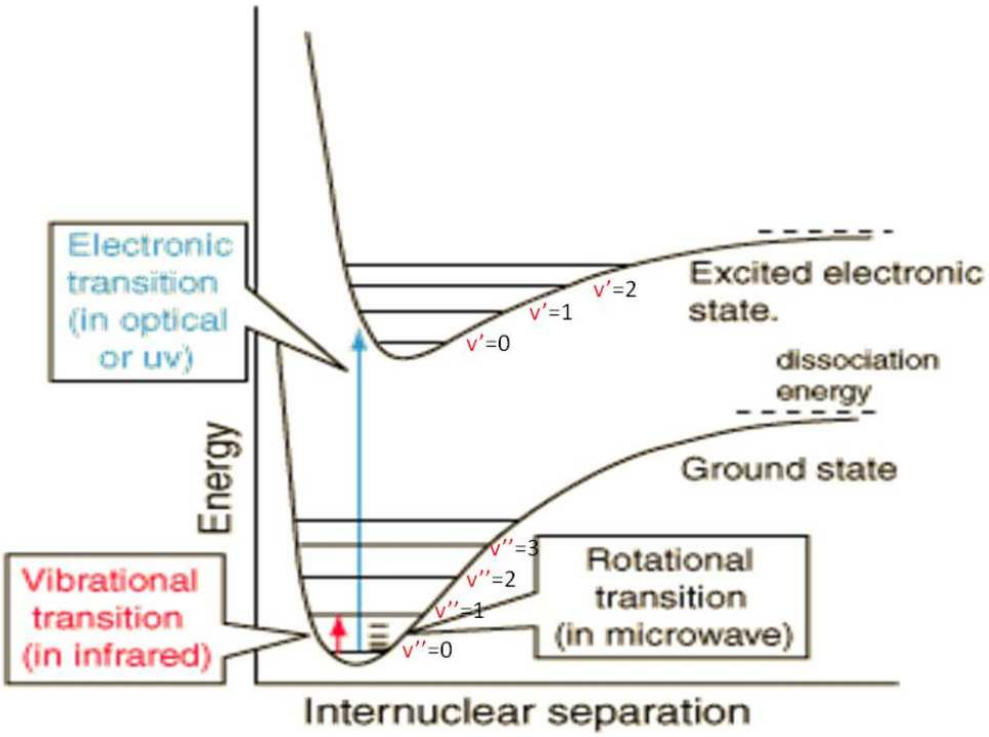

Figure 2.11: Copied from [51], showing that the spacing of electronic levels is much larger than the spacing of vibrational levels in the bound state.

Having established that one is dealing with electronic ground states even at elevated temperatures the following sections examine the interaction between ground state orbital energies of separate atoms or ions that form a bond in a crystal. Importantly, it means that it is appropriate to use the CRYSTAL06 programmes, which are methods for the ground state.

2.3 The Crystalline Electrostatic Field

In the absence of external influences, the scalar electrostatic potential field and the magnetic vector potential field within a crystal are created by the nuclei and electrons. But together these fields constitute the environment that will determine the behaviour of those nuclei and electrons. Study of the magnetic vector potential is beyond the scope of the present work, but the scalar electrostatic potential field is important for the ideas being developed here. It has long been appreciated that the *average* electrostatic potential within a crystal is a few volts positive [126].

The electrostatic potential (ESP) close to atomic sites is dominated by the nucleus and the inner

tightly bound electrons. The important zones controlling the physical and chemical properties of the crystal lie at and around the zones midway between atoms, where the electronic charge density is low and which contain the zero flux boundaries that delineate the atomic basins. The CRYSTAL06 programme can spatially map the ESP calculated from the electronic charge density, using the methods first presented by Saunders et al.[15].

Earlier work on the ESP within a crystal was based on calculations for specific points, usually at ionic sites to give the Madelung Potential for those ions. Also, most calculations were on the basis of fixed +ve and -ve ionic point charge sources located at atomic sites. The difference between that calculation and calculation based on the charge density distribution is demonstrated in the following diagram from [15]:

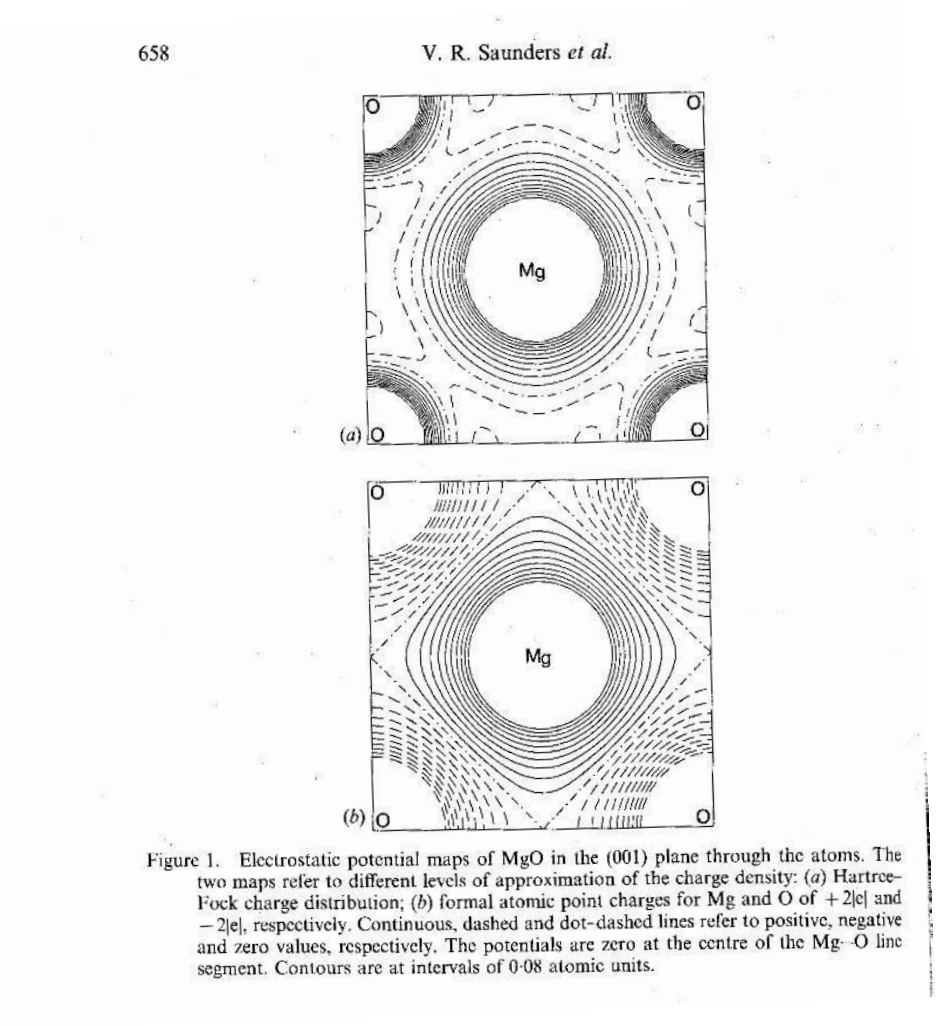

Figure 1. Electrostatic potential maps of MgO in the (001) plane through the atoms. The two maps refer to different levels of approximation of the charge density: (*a*) Hartree–Fock charge distribution; (*b*) formal atomic point charges for Mg and O of $+2|e|$ and $-2|e|$, respectively. Continuous, dashed and dot-dashed lines refer to positive, negative and zero values, respectively. The potentials are zero at the centre of the Mg···O line segment. Contours are at intervals of 0·08 atomic units.

Figure 2.12: The Electrostatic Potential Field inMgO - from Saunders et al.

Quoting from [15]:

"The Hartree-Fock wave function was obtained with a split valence basis set [127]. The net atomic charges resulting from a Miliken analysis are $\stackrel{+}{-}$ $1.998|e|$;

the fully ionic character of MgO is further suggested by the very low $Mg - O$ bond population of $-0.01e$. In many simplified models bulk MgO is represented in terms of $\stackrel{+}{-}\ 2|e|$ atomic point charges. In figure 1 the potential in the (001) plane through the atoms resulting from the Hartree-Fock charge distribution (labelled *a*) is compared with that due to the $\stackrel{+}{-}\ 2|e|$ point charge model (labelled *b*). The Hartree -Fock potential has been shifted so that it is zero at the centre of the $Mg - O$ bond; the two potentials therefore coincide at this point. The two maps are quite different, in particular in the oxygen region, where the point charge model must yield a negative potential, while the Hartree-Fock model becomes positive after the anion valence shell is penetrated. In the $Mg - O$ and $O - O$ regions there are also large differences; the Hartree-Fock model exhibits a slightly negative large plateau in the potential; this plateau is much smaller in the formal charge case."

the following diagram, calculated by the author, demonstrates the slightly negative large plateau in the case of $ReO3$, which is metallic. Here the plateaux no longer extend to bond regions, but occupy the vacant sites where the A cation would be in a ternary ABO_3 perovskite.

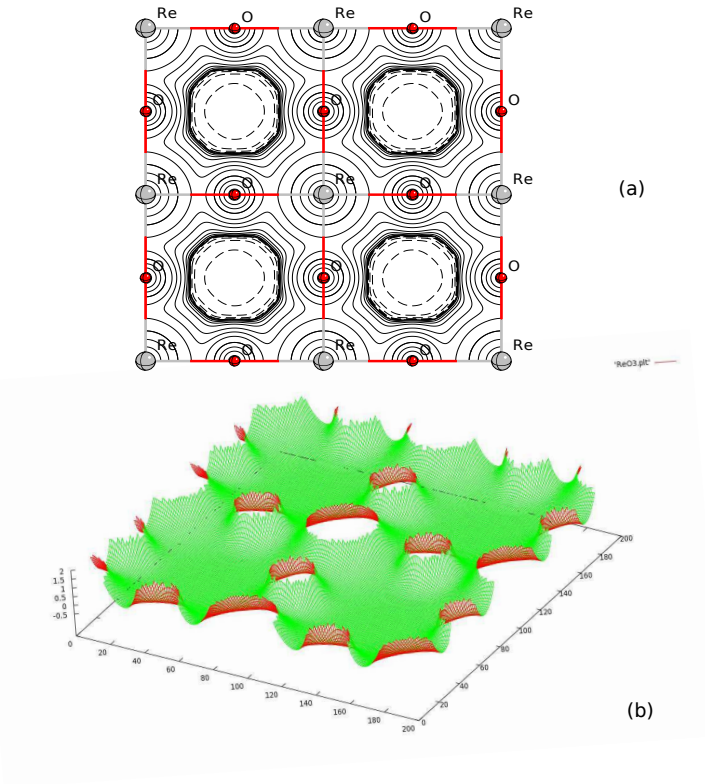

Figure 2.13: The Electrostatic Potential Field in ReO_3 as calculated for this work. (a) is the map as output from CRYSTAL06 and (b) is a perspective of the surface plot of the same data.

2.3.1 The Effects of the Crystalline Electrostatic Field on Orbital Energies

It has been proposed in sections 2.1.3 and 2.1.4 that the unique perovskite octahedral "cages" involve the collective electrons from the participating atoms hybridising to create the bridges between the B ion and the six surrounding O ions. This seems surprising in view of their disparate energies in the free atom state. However it has long been recognised that the crystalline electrostatic field will modify the orbital energies from that of a free ion. Some early authors (e.g. Seitz [52], Slater and Shockley [53], Hodby [54]) simply considered the electron energies to be those of the free ionic states shifted by the Madelung potential energies at the ionic sites. Kahn and Leyendecker [55] proposed an improvement on this by recalculating the Madelung potentials taking into account the incomplete occupancy of the O^{2-} 2p orbitals - i.e. various degrees of covalency or incomplete ionicity. They found that their results were not sensitive to the Sr charge, but were very sensitive to the O charge. The plot below is extracted from their paper.

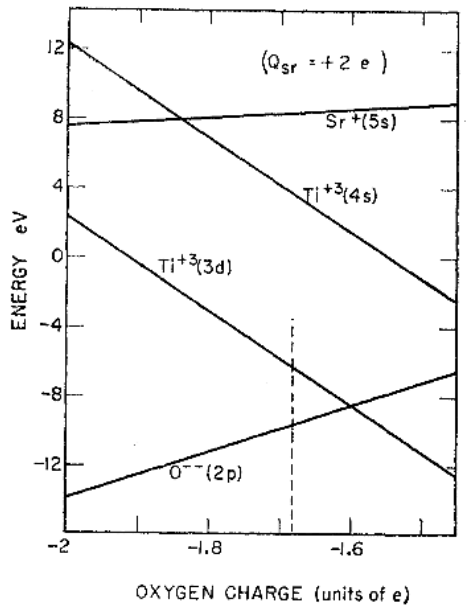

FIG. 2. Plot of energies on the ionic model as a function of oxygen charge. The energy to excite an electron from an oxygen (*2p*) state to various states on cations is represented by the vertical distances from the O^{--} (*2p*) line.

Figure 2.14: Madelung potential in $SrTiO_3$. The diagram in Kahn and Leyendecker illustrating the effect of the crystal electrostatic potential field on orbital energies

It is important to note that the Oxygen (anion) orbital energies are adjusted downwards, and the A ***and*** B ***cation orbital energies are adjusted upwards as the electrostatic field becomes more positive.***

This approach would partially explain how the oxygen *2p* electronic orbitals can overlap transition metal *3d* or *4d* or heavier metal *4s ,5s or 6s* orbitals whose energies are separated by up to

one half a Hartree in the free ions. However it is not accurate (i) because the Madelung potential calculations were based on point charges (albeit adjusted for lower oxygen occupation) rather than on charge distribution; and (ii) the potential term in the one electron Hamiltonian would not be that at the ion nuclear site, rather it will be a function of position and the electrostatic field in the region of orbital overlap.

The following diagram, figure 2.14, copied from the classic chemistry text "University Chemistry" by Bruce M. Mahan and Rollie J. Myers illustrates that the *4d* orbital energy of a heavier element such as Zr is similar to that of the *3d* orbital in Ti, so the behaviour in the crystalline environment will be similar. So also for the *5s* or *6s* orbitals of even heavier elements, so that stannates and cerates also adopt the perovskite structure. This diagram is illustrative only - the text book did not indicate that the energy scale omits the negative sign and is logarithmic.

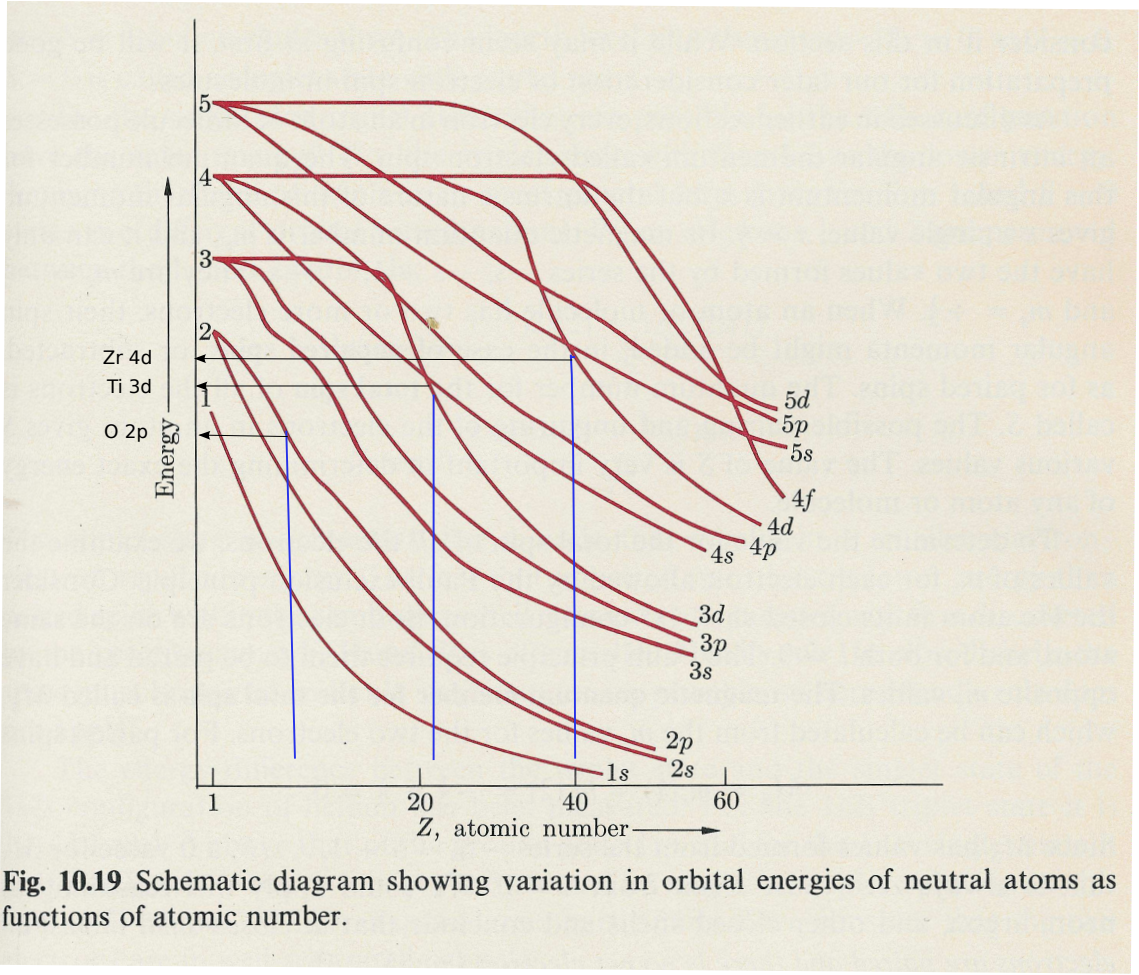

Fig. 10.19 Schematic diagram showing variation in orbital energies of neutral atoms as functions of atomic number.

Figure 2.15: Copied from "University Chemistry" by Bruce M. Mahan and Rollie J. Myers, showing the approach in energy of *O 2p* orbitals with that *d* orbitals of heavier atoms.

2.3.2 Atomic Orbital Energies - a factor in bond formation

Throughout this thesis the *chemical bond* is taken to be that concept about which, in Roald Hoffman's words, "Chemists have built up a great deal of understanding, in the intuitive language of simple covalent or ionic bonding, of the structure of solids .... " [1]. No better illustration of the use of this intuitive language can be given than a recorded lecture by Linus Pauling [56].

An important factor in the bond between two atoms in a molecule or crystal is the orbital energy of the outer shells of those atoms.

The author has compiled an accurate set of curves from the Hartree-Fock calculations for free atoms of Visscher and Dyall [57] - figure 2.16 on page 45. These values are those for the electrostatic field of the isolated atom, and will be different when the atoms occupy a crystal or molecular site. However, when the electrons in the latter cases move from one nucleus towards a neighbouring nucleus, in the case of ionic materials, or between nuclei to be "shared", in the case of covalency, they undergo energy transactions that are easier if the atomic orbitals in the separate isolated atoms have suitable energies. The relevant energies can be "picked out" of this compilation, figure 2.16 . This figure is on a linear scale and is confined to those values less than 1 Hartree to better see the detail of the atom pairs under discussion.

Based on Koopmans' theorem [46], p. 62, and amongst those atoms with incomplete outer shells, vertical separation from one atom's s orbital energy and another atom's p orbital energy is a good indicator of relative electronegativity, and therefore suggestive of whether that pair of atoms will form an ionic bond or one with a degree of covalency. The larger the separation, the stronger the ionic contribution. When the separation is small, orbital overlap is favoured and covalency develops.

An important case is when the donated s electron is not directly attracted to a single more electronegative atom to form an ionic bond with the donor cation. This occurs in binary or ternary compounds where the electronegativity is similarly low in the constituent atoms. Instead of forming a single closed shell anion the electron provides increased electron population for covalency between two or more non donor atoms. This occurs most obviously in Zintl Phase materials where the covalently bonded acceptors form a *polyanion*.

This graphical compilation also has a role in the understanding of the perovskite structure - it reveals:

i. an immediate reason for the $\mathrm{Pb-O}$ bond being stronger in $\mathrm{PbTiO_3}$ than the $\mathrm{A-O}$ bond in $\mathrm{ABO_3}$ perovskites where A is Ca, Sr or Ba as discussed by Cohen [26] - the Pb 6*s* orbital energy is much closer to that of the O 2*p* orbital.

ii. that the A contribution to the $\mathrm{ABO_3}$ perovskite is from its outer *s* electrons. Indeed W.A.

Harrison, in his extensive study of the transition metal perovskites, notes that it is striking that that the role of the A ion (at least in the case of K and Sr) "has no other function than that of providing electrons to the system" [38],page 450. This was not quite the case in the author's work - there was always a slight to significant degree of covalency between the A ions and the O indicated by the density of states plots, strongest in $\mathrm{PbTiO_3}$ - see figure 2.17, plotted from the author's results for $\mathrm{PbTiO_3}$ which accords with Cohen's results . Cohen highlighted the importance of this stating that "the Pb 6*s* and O 2*p* are strongly hybridized in $\mathrm{PbTiO_3}$" [26].

iii. that since the perovskite structure requires increased electronic charge density for its octahedral cage and this will be partly provided by outer *s* orbital electrons, both Tungsten (Atomic Number 74) and Rhenium (Atomic Number 75) can provide these as well as *d* orbital electrons *without the need for* an A atom. Hence binary perovskites.

iv. as an extension to point ii. it can be seen that there is high relative electronegativity between O and $\mathrm{Ca,\ Sr\ and\ Ba}$ respectively. This means that a strong ionic $\mathrm{A-O}$ bond is likely. This occurs in the case of Ca and Sr, but is moderated by the rather diffuse Ba *6s* orbital. It will be seen later that this explains the strong rotation rather than stretching deformation of the non-cubic phases of Ca and Sr perovskites.

Also in connection with point ii. this study found noticeable covalency between La and O in $\mathrm{LaAlO_3}$ (see Appendix A) so Harrison's observation cannot be entirely generalised, but it has guided the author. In any case the A elements in perovskites are all monovalent or bivalent atoms whose outermost electrons are *s* electrons with no orbital angular momentum. Rather than consider the hybridisation or molecular orbitals they might be involved in, one can simply say that they are a necessary constituent of the perovskite structure because they add to the electron density sufficiently to sustain the corner connected octahedral cage of that perovskite structure. This is a principle conclusion drawn in this thesis.

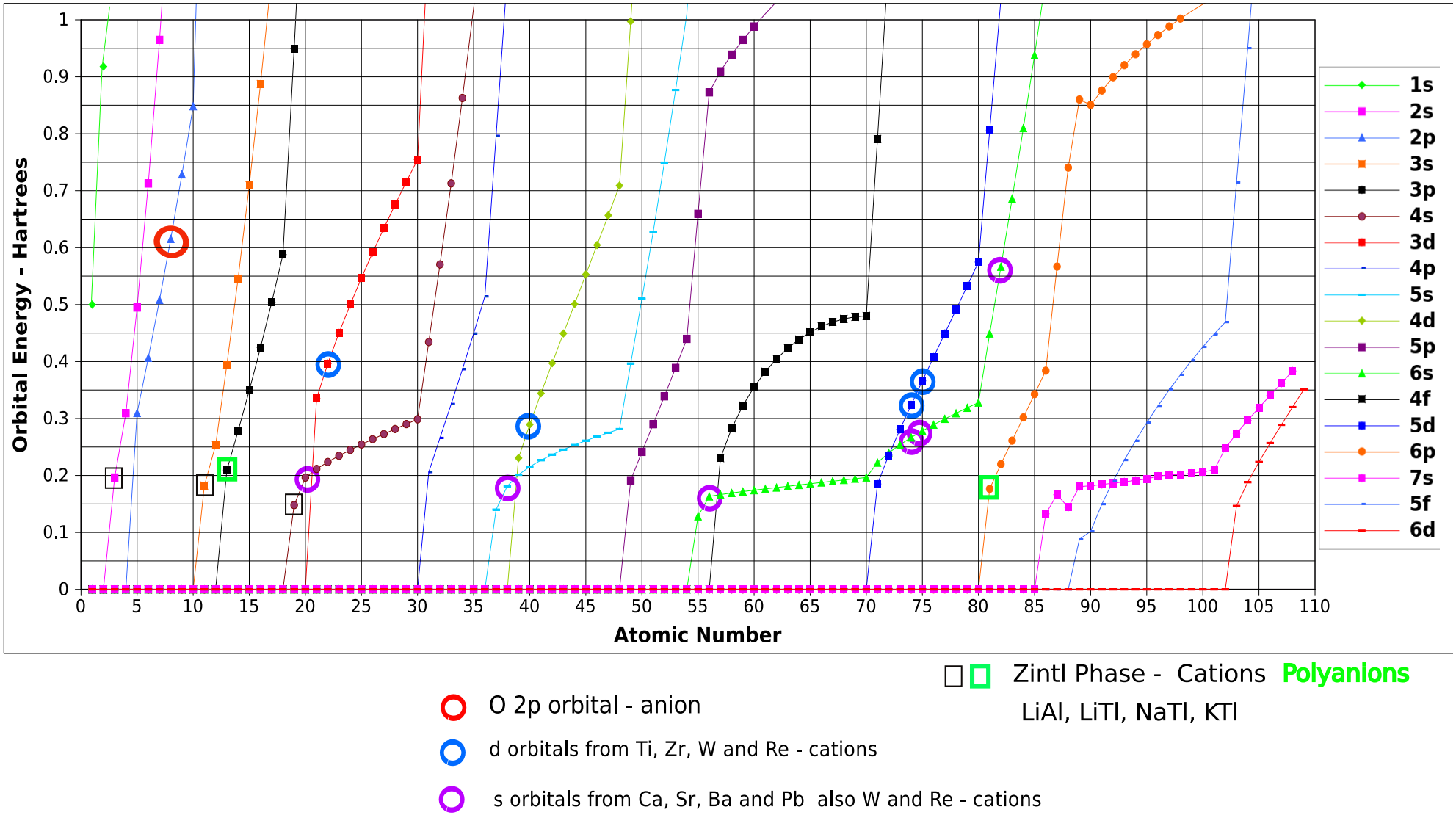

Figure 2.16: Orbital Energies of Free Atoms calculated by Visscher and Dyall [57] . Note that the negative sign of the actual calculated results is omitted. In a crystal, the energy shown for the anion atom will reduce, while the energies of the cation atoms will be elevated, thus approaching equality and maximum overlap for covalency. Several much documented Zintl phase materials are highlighted

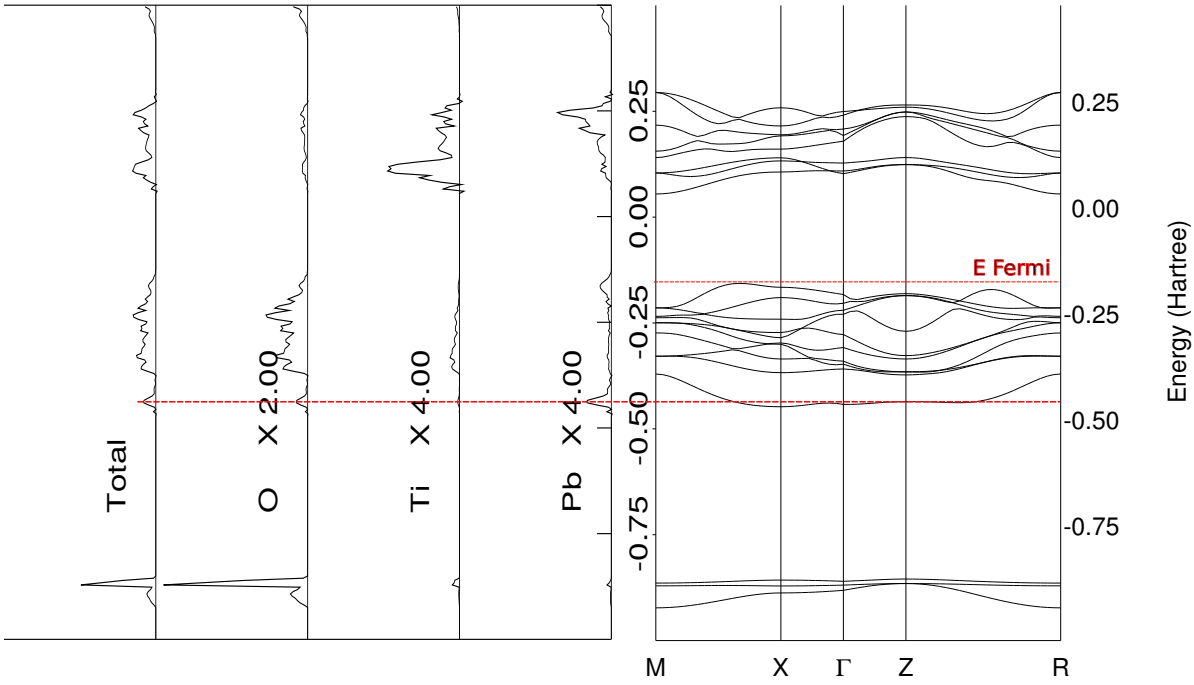

Figure 2.17: Band structure and density of states for tetragonal $PbTiO_3$. Note the covalency in the *sp* band about -0.45 Hartrees.

2.3.3 The special nature of the O^{--} ion

The work of Kahn and Leyendecker. mentioned in the introduction to this section, and their diagram, Figure 2.3, suggests that there is something distinctive about the behaviour of the O^{2-} ion. It is one of a small number of ions that does not exist freely in nature; yet oxygen in the form of this ion is the most abundant element in the Earth's crust, due to its strong tendency to form compounds with or "oxidise" a majority of the other elements. However the O^{--} ion only occurs in the crystalline environment, and so is not seen in stars or intergalactic gases. Thus in nature it is a feature of rocky planets. On Earth the natural and man made ceramic oxides have an array of properties that are due to this unique ion. The free O^{2-} ion is not susceptible to direct calculations to give a Hartree-Fock approximation, although the other (positive and negative) oxygen ions are. This is because the self consistent field calculation will not converge with all ten electrons bound to an ion in the free state and, as mentioned, no one has observed free O^{2-} ions [11] [59] [60]. This ion is unstable by 7 eV relative to O^{-} and an electron in the gaseous phase [61]. Watson [11] used the Roothaan procedure, but modified to incorporate a stabilising potential well, a sphere of charge of $+1$ at the ionic radius . Not only did this give analytic wave functions for the outer orbitals but it gives a physically plausible accounting for the crystal environment of the ion which always features an average net $+ve$ charge. The successive electronic wave functions of the free oxygen ions that can be calculated display the effects of a progressive decrease in the electrostatic field gradient due to the screening of the nuclear charge by added outer electrons. The plot on the next page of the outermost orbitals is based on the calculations in [59] for O^{++}, O^{+}, O, O^{-} and [11] for O^{--} .

It will be seen that the crystal field with its net positive potential about the O^{2-} ion, although stabilising the ion extends its overlap with any neighbour. This coupled with the effects described in the introduction to this section explains the high propensity for the formation of oxides and the frequently robust and stable nature of those oxides.

Perhaps the most important feature of the O^{2-} ion in regard to the perovskite structure is that it has 6 $2p$ electrons, so that it can "hybridise" to a lesser or greater extent with four A atoms and two B atoms to form the ideal corner connected cubic perovskite structure.

Such "hybridisation" will effect an increased average electronic charge density between the A atoms and the B atoms, thus creating London's "bridge" as described in section 2.1.4.

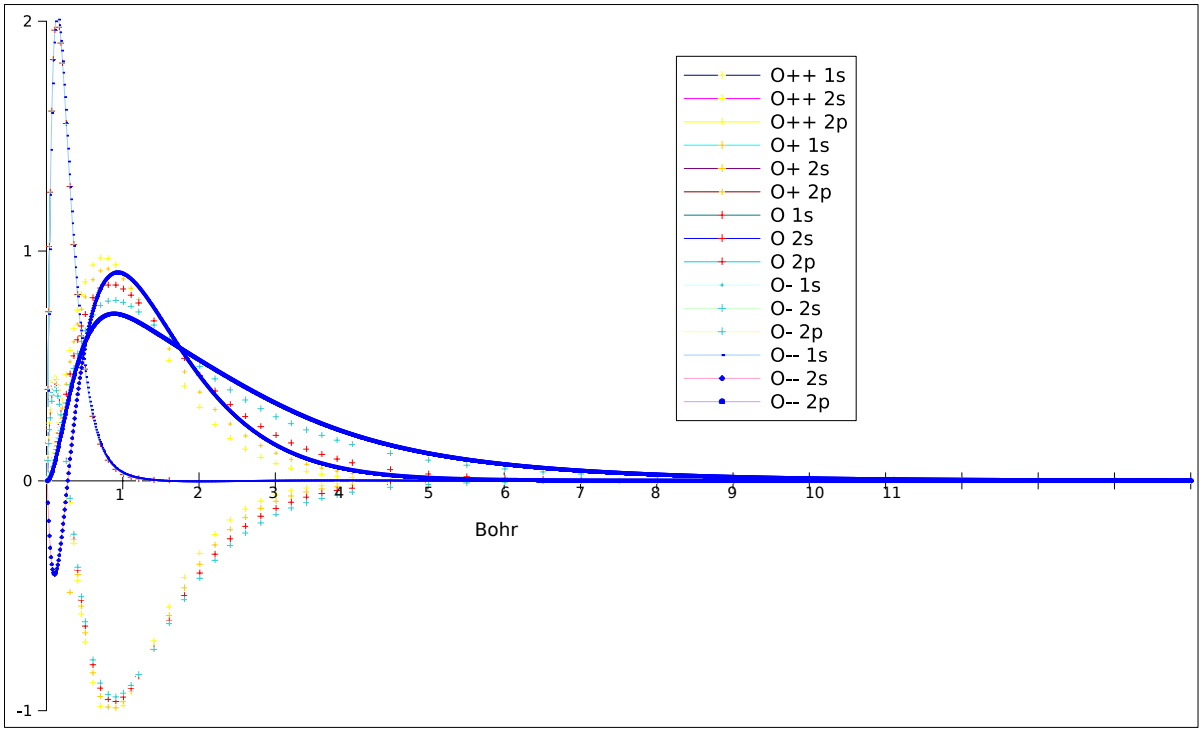

Figure 2.18: **The free Oxygen ions O^{++}, O^{+}, O, O^{-} , based on the calculations in [59] and O^{--}, based on [11], in the crystalline environment. Notice the radial spreading out of the tail as the net nuclear charge decreases due to screening of the added electrons and the crystalline electrostatic potential.**

2.3.4 The influence of the Crystalline Electrostatic Field and Atomic Electronic Structure on Bonding

In terms of valence bond theory the crystalline electrostatic field serves to bring the orbital energies of the valence and conduction electrons of the oxygen anion closer to those of the participating cations - facilitating hybridisation in the overlap region. In Molecular Orbital Theory the contribution to bonding will depend on the number and variety of participating atomic orbitals and the number of collective electrons available to occupy the resulting molecular orbitals. The molecular orbitals are occupied from the lowest energy upwards according to the Aufbau principle and Hund's rules - first the binding orbitals and then, if there enough electrons, some non-binding orbitals. The number of occupied binding orbitals minus that of occupied non-binding orbitals divided by two is known as the bond order, and must be positive for a bond to exist.

The "hybridisation" is a subtle overlay on an essentially ionic and strongly bound structure. However it does not always strengthen the bond to the extent that orbital encroachment might suggest if there are occupied non-binding orbitals. For example in Rhenium trioxide (a binary perovskite) the Mulliken population analysis shows a degree of negative overlap (-0.045), interpreted as anti-bonding. Also for Tungsten trioxide (another binary perovskite) the Mulliken analysis

shows some negative overlap (-0.017). There will only be occupied non-binding orbitals if there are enough collective electrons participating in the bond. The approximate average number of collective electrons available is 12.5 for ReO_3 and 12.0 for WO_3. This compares with values ranging from 6.0 to 8.0 for the ternary perovskites studied.

2.4 Density functional theory and a thought experiment

A succinct summary of density functional theory and its use in the CRYSTAL programmes is provided by N.M. Harrison [58]. In part, introducing hybrid functionals for the exchange component he states

> "There is an exact connection between the non-interacting density functional system and the fully interacting many body system via the integration of the work done in gradually turning on the electron-electron interactions. This adiabatic connection approach allows the exact functional to be formally written...." as an expression from which " the exact energy could be computed if one knew the variation of the density-density correlation function with the coupling constant, λ. The LDA is recovered by replacing the pair correlation function with that for the homogeneous electron gas.
>
> The adiabatic integration approach suggests a different approximation for the exchange-correlation functional. At $\lambda = 0$ the non-interacting system corresponds identically to the Hartree-Fock ansatz, while the LDA and GGA functionals are constructed to be excellent approximations for the fully interacting homogeneous electron gas that is, a system with $\lambda = 1$. It is therefore not unreasonable to approximate the integral over the coupling constant as a weighted sum of the end points...."

and goes on to introduce the hybrid functionals that are used in the CRYSTAL06 calculations for this thesis.

The author has performed CRYSTAL06 DFT calculations on both the ternary perovskites and separately on the binary oxides from which the perovskites can be synthesised (from a either stoichiometric melt or sinter of fine enough powder). The results suggest a thought experiment analogue of the above adiabatic reasoning:

If the elementary atoms of the (highly ionic) compounds in question are at first held far apart by, there will be no quantum mechanical interaction outside of the individual atoms. If the atoms are then brought gradually closer to each other several interrelated effects will commence: (recalling Goodenough's *collective electrons*)

i. a lowering of energy, mainly due to charge transfer and in total amounting to the cohesive energy of the crystalline material.

ii. a degree of charge transfer amongst the collective electrons, towards forming “closed shell” cations and anions, initiating an electrostatic field that decreases the energy gap that existed between the separate atom orbital energies. Where there is high relative electronegativity the predisposition to form strong ionic bonds would give rise to the rotated cages of the non-cubic phases of certain perovskites. This is discussed further in chapter 6.

iii. lobate orbitals in the constituent atoms, intrinsically polar, may cause rotations of the entire atom to adjust to the developing crystal field and eventually to the crystal symmetry.

iv. the orbital angular momentum, if any, of collective electrons, initially sustained with “good quantum numbers” by the separate atomic central electrostatic potentials, will be affected by the increasing crystal field that has the emerging symmetry of the crystal lattice - to the extent that that the angular momentum may be fully or partially quenched;

v. outer electron orbitals will begin to overlap: as well as the classical Coulombic interactions, quantum mechanical effects of electron interaction - Pauli repulsion and its attendant exchange interaction and correlation interaction - will begin to “switch on” and will combine to re-arrange collective electrons;

vi. collective electrons will move to crystalline orbitals and may gain or regain angular momentum relative to new centres.

In this scenario the extent to which regions of orbital overlap happen is related to the difference in orbital energies of the outer electrons of the separate free atoms, and, as was demonstrated in section 2.3, as a crystalline electrostatic field develops, the orbital energies of the O anion will reduce while those of the A and B cations will increase.

In summary, a crystal forms from atoms mainly by interaction and re-arrangement of collective outer electrons. The process involves energy transactions the net result of which is the transfer of energy, amounting to the cohesive energy, from the atoms to phonons. Electron angular momentum transactions must involve (low energy) photon emission/absorption

In terms of Molecular Orbital Theory, the end result is the crystal, comprising primitive cells and crystalline orbitals that are periodic amongst those cells. At any point the square of a crystalline orbital is proportional to the probability of finding an electron belonging to that orbital in unit volume about that point. Crystalline orbitals are analogous to Mulliken’s molecular orbitals except that they are periodic. The electronic charge density is the sum over occupied orbitals of the squared quantities. The crystal can be represented by mapping the electronic charge density. The Bader atoms to be described in the next chapter are enclosed within boundary surfaces that

are defined by the topology of the charge density. The boundary surfaces lie in regions occupied by the re-arranged collective electrons.

In actual practice oxide perovskites are frequently synthesised by sintering stoichiometric mixtures of very fine powders of the constituent oxides. In this case the above processes would occur via solid state diffusion. Much attention is paid to the redistribution of the collective electrons in the oxides in chapters 5 and 6.

2.4.1 Bonds and Crystal phases

Only the *collective electrons* are involved in re-arrangement to form the lower energy state that the crystal represents. This means that there is a limited, fixed number of electrons available per primitive cell to be distributed in such a way that augments the ionic bonding. In chapter 5 it is shown that the electronic charge density profile and the value at the BCP differs in a significant way between that in the binary oxides, AO and BO_2, which contribute to the ABO_3 perovskite and those within the perovskite when the octahedron is deformed. In the (higher temperature) cubic phase the collective electrons are evenly shared by the six O anions surrounding a B cation (in degenerate states). As the temperature lowers to the extent that phonons no longer disrupt a stronger bond, that bond will form with added electronic charge density in the vicinity of the BCP. The lowering of energy in a phase change from cubic is an increase in the negative energy of each formula unit - i.e. an *an increase in the attractive bond strength* of at least one of the bonds within the formula unit - however since the total electronic charge density available is limited, the remaining bonds have a lower electronic charge density, so are weaker and the cage, hence the crystal must distort to a lower symmetry phase.

Ferroelectric perovskites often exhibit a slight to very evident λ anomaly at phase changes, strongest at the change to the cubic system [62]. It is most pronounced in PbTiO_3. Perovskites, and the ferroelectric properties and phase behaviour of some of them have been extensively studied in terms of vibronics and Pseudo-Jahn-Teller (PJT) behaviour [63], [64] and references therein. Vibronics is the analysis of departures from the adiabatic (Born-Oppenheimer) approximation in terms of electronic interaction with nuclear or core vibrations. PJT behaviour is invoked when almost degenerate systems break the near degeneracy by a decrease in symmetry. Instead of trying to analyse the PJT behaviour, the author's picture is paralleling these concepts but simplifying by dealing with the changes in of electronic charge density distribution as a result of weaker phonon interactions. As a crystal cools through the phase change temperature the phonon interaction decreases because the crystal loses heat to the surroundings. It also loses entropy (as the exterior gains both heat and entropy), and the change to the lower symmetry phase, increasing the crystal

entropy, can be viewed as a compensating adjustment. The anomalous Transition Energy, the area under the λ in the graph of specific heat vs. temperature, is $0.04945\ eV$ per "molecule" for $\mathrm{PbTiO_3}$ [62], p. 110, represents about 10% of the energy lowering of $0.426628595\ eV$, calculated by the author from the results for $\mathrm{PbTiO_3}$ in appendix A, and represents the increase in entropy of the less symmemetric phase.

2.5 Methods

Ab-initio calculations were carried out using the CRYSTAL06 suite of programmes [6], which is outlined in some detail with examples in chapter 4. In order to illustrate matters in the text and to cover various bond types many elemental, binary and ternary crystals have been studied. All calculations were carried out by the author. It may be the first time some of these materials have been calculated with the Kohn-Sham Hamiltonian using Gaussian type basis sets. All of the examples used were calculated with the DFT (Kohn-Sham) Hamiltonian, Becke gradient-corrected (GGA) exchange functionals (of the electron density and its gradient) [65] with a 10% linear combination of Hartree-Fock (HF) exchange to counter the DFT tendency to under-estimate the band gap, and Lee - Yang - Parr GGA correlation functional [66]. As far as possible all input parameters and tolerances were kept the same , because results were to compared across bond types, but level shift and mixing techniques, subsequently adjusted, were needed to achieve SCF convergence for the metallic minerals. All structural measurements are after full geometry optimisation.

2.5.1 The Ab Initio approach using CRYSTAL06

Essential reading for a background to ab-initio calculations for the solid state in general, and for the CRYSTALxx programmes in particular are the volume nos. 48 and 67 of the Springer-Verlag "Lecture Notes in Chemistry" series [67], [68]. These are both written mainly by the people who collectively created CRYSTAL06 [6] . An outline of how this programme suite works in practice and the details of the common inputs for this study are provided in chapter 4.

Underlying principles of the Crystal06 approach are:

(i) that crystalline orbitals can be represented by linear combinations of Bloch functions that are in turn derived from localised atomic (or ionic) orbitals. This implies the fundamental assumption of linear quantum mechanics that the wave function of a many body system is a separable product of single body wave functions. In modern computational quantum chemistry the Slater type atomic orbitals are replaced by a good fitting combination of Gaussian-Type functions. The Bloch functions and crystal symmetry are inherent in the nature of periodic systems and make

feasible the extension of computational quantum chemistry from molecules to crystals.

(ii) the variational principle that convergence to a minimum energy by a series of self consistent calculations will yield energy and geometry estimates that are successively closer to the real ground state.

The author has adopted the particular programme, CRYSTAL06, because he believes it to be the most completely developed adaption of the chemical ab-initio paradigms for molecules to the crystalline state. In particular it can handle both Hartree-Fock and Kohn-Sham (density functional theory or DFT) Hamiltonians and has a good library of basis sets modified for the periodic nature of crystals. However, it is one of the many ab initio approaches that inherit the shortcomings of the so-called local density approximation for the exchange/correlation potential. The calculations in this thesis are optimised in this regard by the use of the generalised gradient and an exchange functional that is a linear combination of Hartree-Fock, local and gradient-corrected exchange terms.

As might be expected, the method used is not satisfactory in certain circumstances. The author has steered clear of the well known problem areas: d block compounds with three or more d outer electrons give rise to strong correlation effects that create wrong answers (e.g some manganites and manganates). Today these problems are being successfully challenged by the so called Dynamical Mean-field theory [69] in combination with the density functional theory and the "hybrid density functional theory" methods employed in this thesis [70].

2.5.2 Computation and Visualisation

This thesis utilises CRYSTAL06 output of electronic charge density distribution and electrostatic potential distribution, and does not draw directly on the calculated electronic wave functions. The output is supplied in tabulations corresponding to 2D slices or 3D grids. An associated package, Crgra2006, displays contoured maps of electronic charge density and electrostatic potential; plots of total and projected density of states and plots of band structures along selected paths in the Brillouin zone.

The XCrysDen package [7] was used to display crystal structure and to measure bond lengths and angles, and to select planes within the crystals.

The author wrote several suites of shell script and C++ programmes to extract the grid data and present profiles, cross-sectional slices and surface images, and derivative maps and images from CRYSTAL06 outputs.

For 2-D representation, components of the respective spatial gradients along the crystal X, Y and Z axes for any selected plane were calculated. Vectors were determined from these gradient

components and their normalised projection onto the selected plane was calculated, thus giving a picture of the flux directions, which clearly mark the Bader or Tsirelson atoms (see below).

For 3-D representation a series (between 100 and 300) of CRYSTAL06 2-D runs on closely spaced planes were concatenated to create orthogonal 3D blocks of data in those (most) cases where the CRYSTAL06 3D grid was not orthogonal. This was in order to use simple six-sided voronoi cells for further analysis, including via the Yu and Trinkle algorithm (see below).

These programmes output profiles and surface maps of electronic charge distribution, its gradients, the Laplacian, ELF (electron localisation factor, discussed later), Electrostatic Potential, the Kinetic Energy etc. and tabulated integrated results for Bader or Tsirelson atom volume and charge (zero for Tsirelson atoms). The general scheme of the programming effort is illustrated in figure, 2.19 overleaf.

Two published algorithms were adopted by the author:

1. That of Tsirelson and Stash [71] - utilising the Kirzhnits approximation for kinetic energy density to calculate the ELF;

2. That of Yu and Trinkle [72] to integrate the Bader and Tsirelson atoms by following the "flow" of density through adjoining Voronoi volumes about the grid points from peak values down to the gradient turning points, and weighting the allocation of density at boundaries where voronoi volumes include more than one atom. As just mentioned, in order to keep the Voronoi volumes as simple six sided rectangular prisms, orthogonal 3D grids were created by stacking multiple (usually 101 to 301) 2D grids. There are three complications not mentioned in [72], but confirmed by personal communication.

i. Firstly, it is not sufficient just to order the data in descending magnitude. The location of all the nuclei in the "stack" must be supplied and then a "closeness" criteria used to determine which nucleus a high value " belongs to" until all the nuclei have been located.

ii. Secondly, the allocation of a nucleus (or a boundary) to any electronic charge density data point is only accurate for atoms that are so far inside the stack that all of their adjoining neighbours are also well inside the stack. Thus in a large stack, the integration over the Bader or Tsirelson atoms is only accurate when they are near the centre. The Tsirelson atom charge is a good check on this - if it is not nearly zero, that atom is not used.

iii. Thirdly, in detail the charge density values do not decrease uniformly, but by way of steps between plateaux of equal value, usually containing between four and fifteen data points. Again a closeness criterion is used to attach data points to the correct atoms.

The idea of Yu and Trinkle can be understood from the diagrams on the following pages, based on the calculations for orthorhombic $CaTiO_3$. 37 atoms contribute to the data set of about

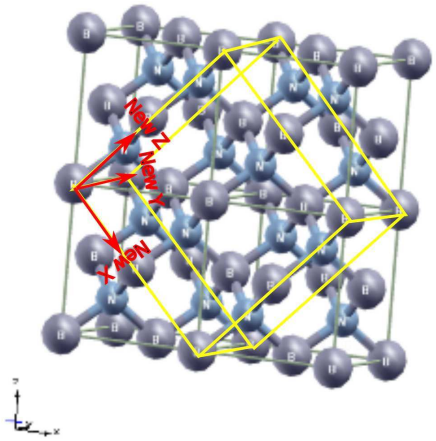

Use XCRYSDEN to select a rectangular prismatic region that contains atoms and bonds that one wishes to study....

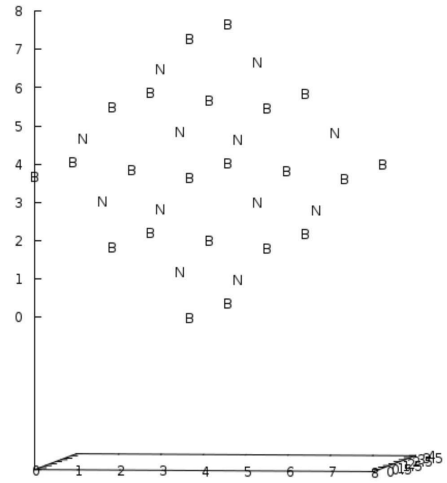

and read off nuclear locations of the atoms within the selected region and record in a *.atms file.

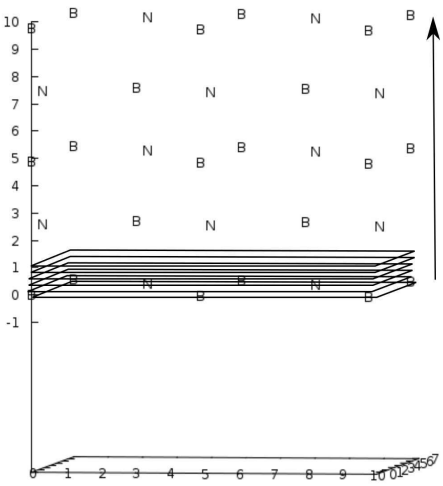

C++ programmes transform the *atms to a new grid, whose origin and axes are read off from the XCRYSDEN image and recorded in a *refs file.
A shell script employs CRYSTAL06 to calculate field data for each 2-D slice in the ascending stack, yielding a 3-D orthogonal grid of data points with rectangular prismatic voronoi cells

C++ programmes then outline and integrate Bader and Tsi atoms and map surfaces and profiles of ECD, ESP, Laplacian Kinetic energy, ELF etc.

Figure 2.19: A rectangular prismatic region enclosing a representative portion of the crystal is covered by stacked 2-D sections to create an orthogonal data set with rectangular voronoi cells.

1,000,000 points (the largest data set used in the thesis was about 70,000,000 points). In the C++ programmes a data point is an object that always knows where it is in space and to which various tags, such as index numbers, chemical name, flux weights etc can be allocated. The first diagram illustrates the distribution by value of the points within the selected rectangular prismatic region.

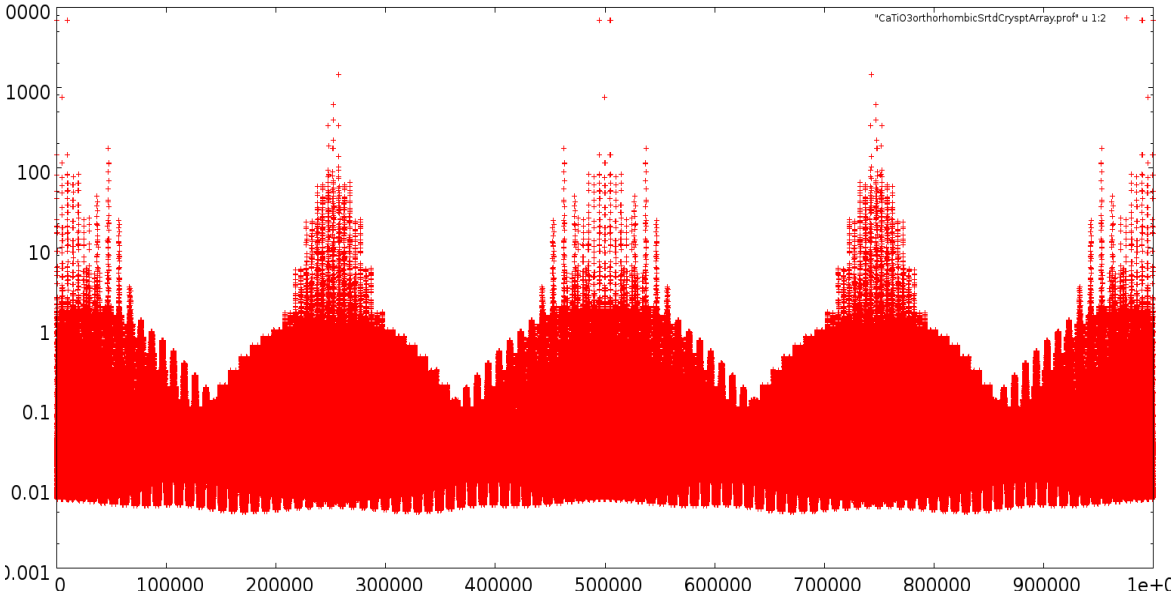

Figure 2.20: Electronic charge density value distribution from 100 concatenated CRYSTAL06 *.f25 files that together include data from 37 Bader atoms.

The next diagram shows the same data sorted by descending value of electronic charge density. Experience with over 40 different oxide compounds suggests that the separate nuclei will occur within the first 800 values. The nuclei are first located from the top values by a spatial closeness test. Then the programme considers, in descending order, each of the points not so located and allocates it to the closest equal or higher value, hence to a nucleus. Very quickly, at least one face of the voronoi cell about a new point will have an allocated, or labelled, adjoining neighbour. When a point has neighbours with different labels, it lies on a boundary.

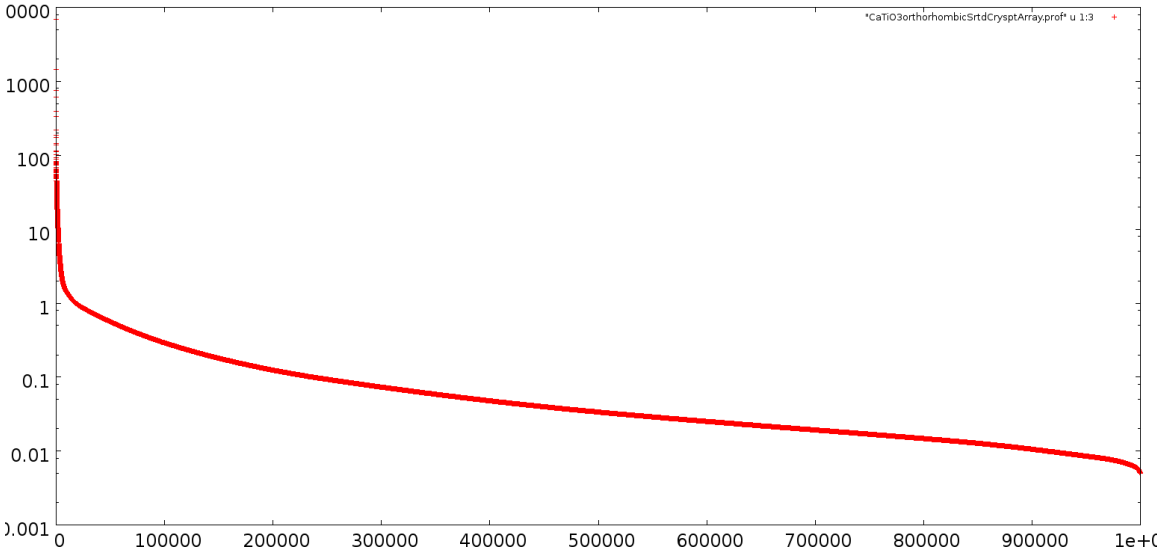

Figure 2.21: Electronic charge density value, sorted in descending order, from 100 concatenated CRYSTAL06 *.f25 files that together include data from 37 Bader atoms.

Figure 2.22 is a more detailed plot of the first two hundred points illustrates the third complication mentioned above:

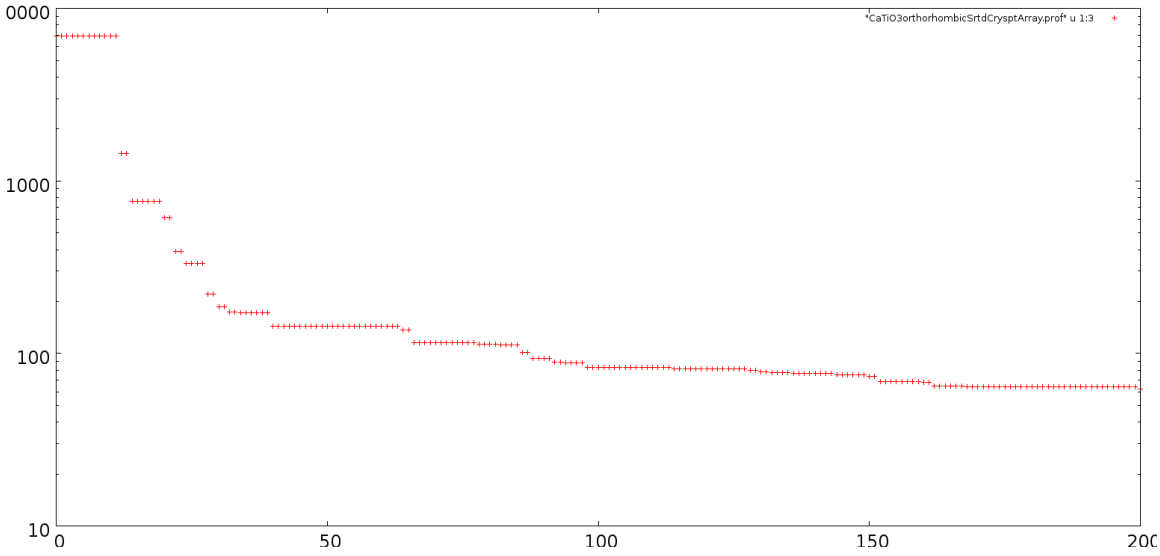

Figure 2.22: The first 200 values of electronic charge density value, sorted in descending order, from 100 concatenated CRYSTAL06 *.f25 files that together include data from 37 Bader atoms.

And figure 2.23 is a plot of the spatial distribution of the first 700 points of the sorted array.

Note: When pseudo-potential representations replace full electronic basis sets for the cores of heavier atoms, even with small core basis sets, the charge density distribution and gradients thereof are distorted in the region of the core. The important regions around the boundaries of the Bader atoms - at the edge of the valence region and well removed from the cores - are not distorted.

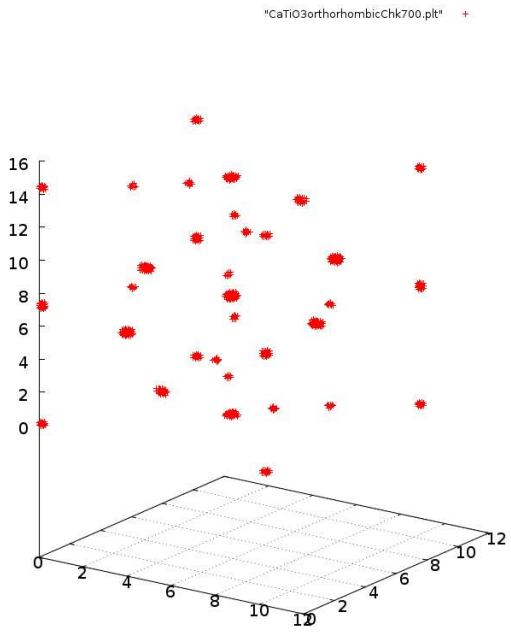

Figure 2.23: Spatial distribution of the first 700 values of electronic charge density value, sorted in descending order, from 100 concatenated CRYSTAL06 *.f25 files that together include data from 37 Bader atoms. This illustrates how atoms “grow” out from the nuclei as one descends the sorted values. Scales are Bohrs.

The following figure 2.24 illustrates the problem displaying various derivative plots (to be explained later) for SrO. The first panel was calculated using the Hay and Wadt HAYWSC-311(1d)G basis set for Sr whilst the second, undistorted result employed an all electron basis set modified from that of Federica Freyria-Fava, available on the Mike Towler Crystal Resources Web site.

The gnuplot package [73] was used to display calculated results, and was invaluable in the preparation of illustrations.

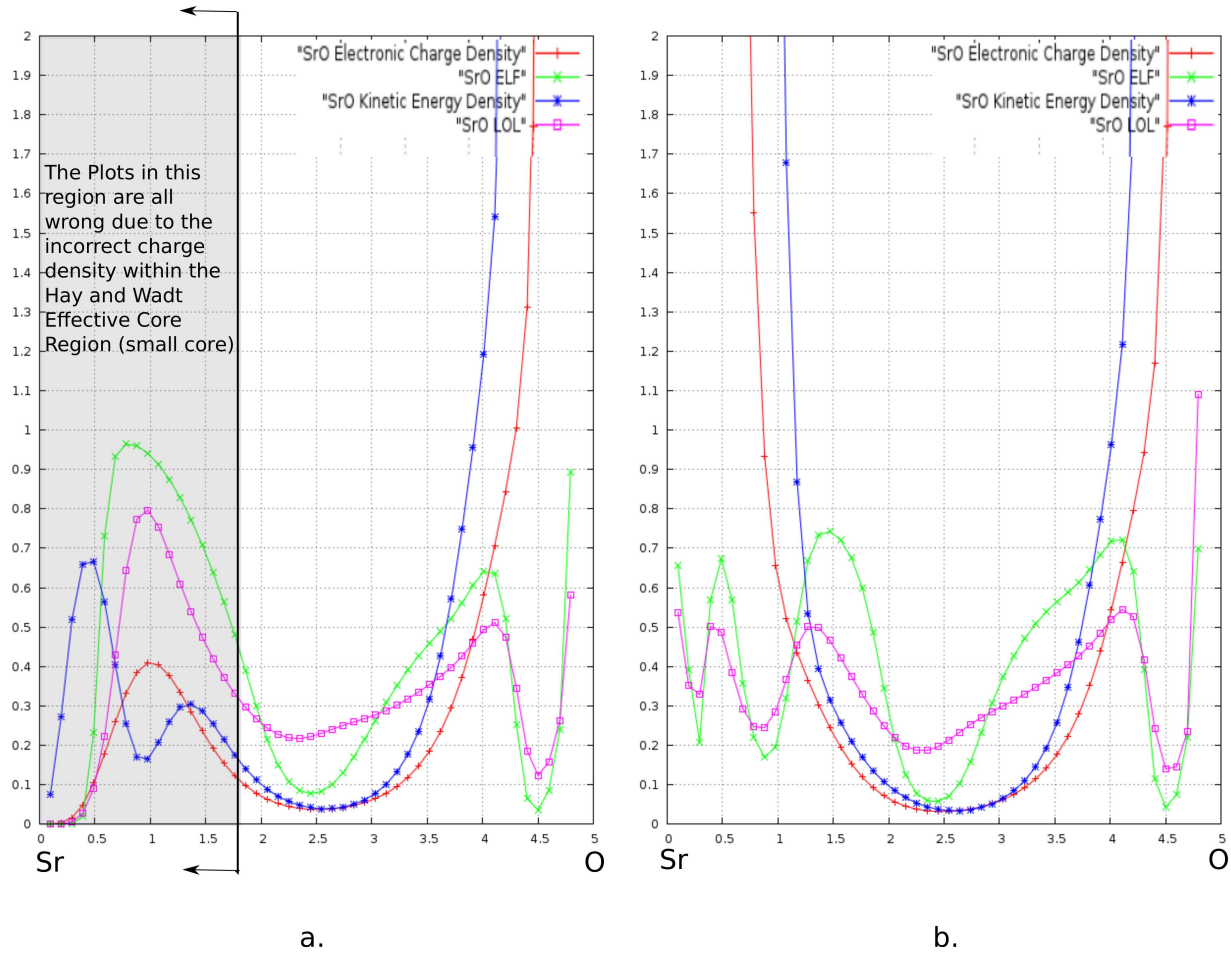

Figure 2.24: Two calculations of derivative profiles for SrO- a. small core pseudo potential; b. all electron basis sets.

Chapter 3

Electronic Charge Density, Electrostatic Potential within a Crystal and the Topological Atom concepts

3.1 Introduction

The two ground state scalar functions of position (vector) $\mathbf{r}$ in real space within an infinite crystal, the electronic charge density distribution $\rho(\mathbf{r})$ and electrostatic potential distribution $\varphi(\mathbf{r})$ are related by the Maxwell equation $\nabla \cdot \mathbf{E} = \frac{\rho(\mathbf{r})}{\epsilon_0}$ leading to Poisson's equation $\nabla^2\varphi(\mathbf{r}) = \frac{\rho(\mathbf{r})}{\epsilon_0}$ and can be calculated one from the other subject to boundary conditions. They can also be mapped quite accurately by experimental measurement - by X-ray diffraction and more recently by high energy electron diffraction [21], [74]. These scalar fields are representations of a quantum mechanical phenomenon, but they are averages and so lose some information compared with the ground state wave function. Never the less in principle the wave function, the energy and other characteristics of the system are functionals of the electronic charge density distribution. In practice no exact functional expression has been developed for the kinetic energy and non-classical part of the electron-electron interaction *Ibid*, pages 5 and 6.

The advantage of the scalar field representation is that it can be discerned from measurement - the wave function of a crystal system cannot and in any case is also an approximation for all but the simplest systems.

In this thesis ab initio methods are used to simulate the scalar functions which then determine the topological atoms for various crystalline materials. Such calculated charge density from modern self-consistent methods are accurate to within 2-5% of the total charge density at any point in

space [8], page 41.

Within the crystal the scalar functions are periodic under translation of the conventional unit cell which is usually chosen with atoms of the constituent species at or near the lattice points of the underlying crystal structure. The Wigner-Seitz cell of such a crystal will enclose some atoms, but dissect others.

Another choice of periodic unit, whose surfaces and vertices only enclose atoms, is a Wigner-Seitz cell made up of the topological atoms that will now be described.

3.1.1 The Topological Atoms

The scalar fields give rise to topological atomic features defined by surfaces of zero flux in their respective vector gradient fields. Mathematically:

if $\rho(\mathbf{r})$ is the scalar electronic charge distribution over general points whose position vector is $\mathbf{r}$,
then there exist surfaces $\mathbf{S}_i$ for any point within which $\nabla\rho(\mathbf{r}) \cdot \mathbf{n} = 0$
where $\mathbf{n}$ is the normal to $\mathbf{S}_i$ at that point.
The $\mathbf{S}_i$ is a closed zero flux surface and encloses the i^{th} nucleus and the electronic charge that can be ascribed to that nucleus under the Bader scheme, but contains point and line ("sharp edge") singularities. The atoms so determined in the case of electronic charge density will be referred to as Bader atoms or ECD atoms.

The same applies to $\varphi(\mathbf{r})$, the scalar electrostatic potential distribution. In this case the atoms so determined will be called Tsirelson atoms or ESP atoms.

The ECD atoms are introduced and described exhaustively in texts by Bader [8], and the ESP atoms are similarly treated by Tsirelson and Ozerov [21]. The atoms in both cases always contain one nucleus and an associated bounding surface that connects points that are, along corresponding rays from the nucleus, of minimal electron density for ECD or minimal electrostatic potential for ESP. They have contiguous boundaries, filling the whole space. The ECD atoms and ESP atoms of a given element in a given crystal usually differ in size and shape, but in both cases, the volume of the atoms in whatever number of formula units comprises a crystallographic unit cell is the same as the volume of that unit cell. In both cases the arrangement of the atoms matches the symmetry of the crystal. According to the Bader scheme, when there is a common ray connecting two nuclei it is called a bond path; the bond path includes a (saddle) point that is minimal along the ray, but maximal along any normal so it is designated a (3,- 1) critical point because the scalar field has 3 principle curvatures at this point, one positive and two negative. Such a point is called a *Bond Critical Point* (BCP).

3.1.1.1 Bader ECD Atoms in Molecules/Crystals

The Bader scheme starts out from the electronic charge density distribution determined by the wave function for the system. This is intellectually satisfying, because it corresponds to what has been measured experimentally by X-ray diffraction methods since 1925 [75], and more recently by high energy ($20\,KeV\ -\ 1\,MeV$) electron diffraction [74], [44] . The charge density $\rho(\mathbf{r};\mathbf{X})$ is the limiting value of the (time-averaged) probability that an electron will be present within the local volume around a given point $\mathbf{r}$, accounting for spin - for a given configuration of the nuclei $\mathbf{X}$:

$\rho(\mathbf{r};\mathbf{X}) = \sum(spins)\,[\int dv_1 \int dv_2 .... \int dv_{i-1} \int dv_{i+1} .... \int dv_N \psi^*(\mathbf{r};\mathbf{X})\psi(\mathbf{r};\mathbf{X})]\,dv_i \times \frac{\mathbf{N}}{dv_i}$

i.e. the probability per unit volume for any i^{th} electron of the total $\mathbf{N}$ electrons to be found in the region at $\mathbf{r}_i$ surrounded by the elemental volume dv_i.

Bader's book [8] presents in considerable detail the ideas discussed here. The approach has been widely accepted and usefully applied, including its use in the case of the Urea crystal by a team that included two of the main authors of the CRYSTAL06 programme [76]. An early criticism of the method by an eminent organic chemist, Charles L. Perrin, of the University of California at San Diego, [77] was refuted [78]. This author believes that Perrin's claim that "the greater Bader population of an electronegative atom arises not only because of electronegativity differences but also because the location of the zero-flux surface depends on atomic sizes, which ought to be irrelevant" is a strangely circular misreading of the Bader technique which relies on molecular (or crystalline) wave functions *after* SCF convergence. Particularly in crystals, atomic "size" must be disregarded because diffuse basis functions will not converge.

The charge density is a scalar continuum concept, represented by a positive real number or zero at any point within the crystal, and varying smoothly between points. In the regions of the crystal where physics and chemistry occurs, it is of the order of a fraction of an electronic charge per cubic bohr. This scalar will have a local maximum close to a nucleus. The three dimensional scalar field has the translational symmetry of the crystal. It determines a three dimensional gradient vector field that describes the magnitude and direction of the change in the scalar values (the "slope" of the scalar field) at each point. Mathematically the gradient field is the first spatial derivative of the charge density. Another important concept in what follows is the scalar second derivative. The Hessian is the matrix of partial second derivatives, and its trace, the Laplacian, is important in the Bader theory.

Bader Atoms are described by shared envelope surfaces that are surfaces of zero flux in the vector gradient field of the electronic charge density. Such a formulation using continuum concepts allows use of tensors ("stress" , "strain" etc.) normally associated with macroscopic treatments.

Thus Bader can talk of the Laplacian of the electronic charge density being "viewed as a measure of the pressure exerted on the electronic charge density" [8], p. 277.

An atom in a crystal is the smallest region about an interior nucleus whose enclosing zero-flux surface includes that nucleus. The atom is made up of smaller regions enclosed by zero flux surfaces, the set of gradient trajectories that start at a given minimum and end at but do not enclose the nucleus - the *Primary Bundles* [79] - rather like the cloves of a garlic bulb. The atom will always contain a single nucleus, because of the local maxima near nuclei and the lows between nuclei. A zero flux surface in the gradient field is one that no gradient vector crosses - at points in this surface, the gradient vectors are tangential. The zero flux surfaces that define the atoms and primary bundles, however lie within the periodic extent of the spatial wave function and so are open to fluxes associated with that wave function [1].

Figure 3.1 below, constructed with the methods described in chapter 2, displays normalised gradient vectors overlaid on maps of electronic charge density, thus revealing the traces of the bounding surfaces of the Bader atoms. Notice the compression of the Bader atoms over the more covalent $\mathrm{Ti}-\mathrm{O}$ bond and corresponding extension over the more ionic $\mathrm{Ti}-\mathrm{O}$ bond in the tetragonal phase.

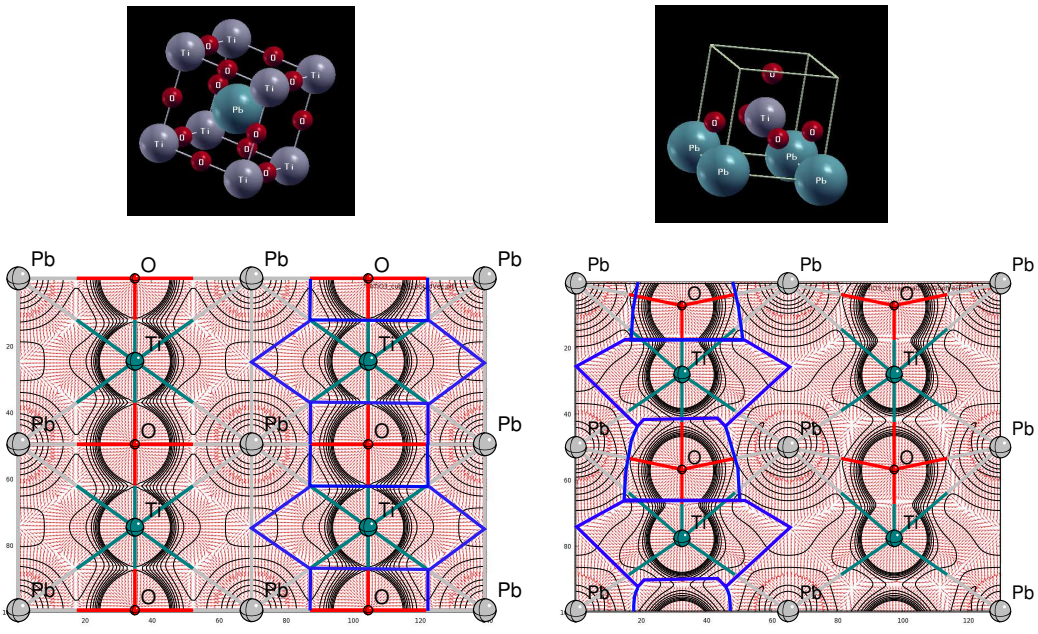

Figure 3.1: (110) sections of cubic and tetragonal phases of $\mathrm{PbTiO_3}$ illustrating the definition of Bader atoms by the gradient field of the electronic charge density. The Bader atom boundaries are traced in blue. Notice the distortion of the atoms in the tetragonal phase.

[1] e.g. A quantum particle such as an electron produces electric current because of its motion. That current is associated with the flow of its probability. The form of the wave function that describes the state of a particle determines these currents. [80]

The important features of ECD or Bader Atoms are:

- They are entities defined in terms of a quantum mechanical observable.
- They are a subsystem for which the virial theorem holds.
- They are a subsystems for which the kinetic energy is well defined.
- Hence they represent “containers” of kinetic energy.
- They are open quantum subsystems in the sense that charge and momentum may pass through freely (as noted above).
- They are statistical objects - in particular the integral of charge density over an atom is not likely to be integral number of electrons and the atomic location, shape and qualities are ground state time averages.
- They adjoin their neighbours without overlap, and without gaps or voids.
- Their shapes may be complex, including partially wrapping around neighbours, but the total volume of the non equivalent atoms that make up a primitive cell is the same as the volume of the primitive cell. A formula unit of Bader atoms has the same volume as a formula unit fraction of the primitive cell when there are multiple formula units in unit cells of low symmetry. Refer to Figure 3.5 on page 67 to see the complexity in 3-D of the simple compound Boron Nitride.

These features suggest that the Bader atoms or minimal assemblages of these may be more fundamental physical concepts than the conventional near-spherical ions and the crystal unit cells or primitive cells that they occupy. Note that the kinetic energy is not well defined over a primitive or conventional cell of the crystal lattice nor any collection of these, nor over any other volume not enclosed by zero flux surfaces [8], pp 147-149.

3.1.1.2 Tsirelson ESP Atoms

Similarly, The Tsirelson scheme starts out from electrostatic potential (ESP) distribution, also determined by the wave function for the system. Again the electrostatic potential distribution is measured experimentally by both X-ray and high energy electron diffraction methods. The electrostatic potential $\varphi(\mathbf{r};\mathbf{X})$ is the value of the (time-averaged) electrostatic potential a given point $\mathbf{r}$, and related to the electronic charge density distribution by Poisson’s equation as stated in the introduction to this section.

Again, the ESP is a scalar function whose gradient field gives rise to atomic basins just as for the case of the ECD atoms. In this case if $\varphi(\mathbf{r})$ is the scalar electrostatic potential distribution over general points whose position vector is $\mathbf{r}$, then there exist surfaces $\mathbf{S}_i$ for any point within which $\nabla\varphi(\mathbf{r}) \cdot \mathbf{n} = 0$ where $\mathbf{n}$ is the normal to $\mathbf{S}_i$ at that point.

As before, the $\mathbf{S}_i$ is a closed zero flux surface and encloses the i^{th} nucleus and the electronic charge that can be ascribed to that nucleus under the Bader scheme, but contains point and line ("sharp edge") singularities. The atoms so determined will be called Tsirelson or ESP atoms.

Now, Gauss's law states that for any closed surface S, $\oint_S \mathbf{E} \cdot d\mathbf{a} = \frac{1}{\epsilon_0} Q_{enc}$ where Q_{enc} is the total charge enclosed within the surface [81] - but $\oint_S E \cdot d\mathbf{a}$ is zero for the enclosing surface of the Tsirelson atom because the vector $\mathbf{E}$ (the$\nabla\varphi(\mathbf{r})$ above) is always a tangent to that surface and $d\mathbf{a}$, the infinitesimal surface element, is expressed as an outward *normal* vector - the dot product thus measuring the flux component in this direction . Hence, the net charge within the atom must be zero - in other words, the electronic charge within the atom screens the nuclear charge.

The important features of ESP or Tsirelson atoms are:

- They are entities defined in terms of a quantum mechanical observable.
- They are open quantum subsystems in the sense that charge and momentum may pass through freely, but charge is conserved.
- They are charge neutral - the net charge integrated over the atom is zero.
- They adjoin their neighbours without overlap, and without gaps or voids.
- Their shapes may be complex, including partially wrapping around neighbours, but the total volume of the non equivalent atoms that make up a primitive cell is the same as the volume of the primitive cell. A formula unit of ESP atoms has the same volume as a formula unit of ECD atoms which has the same volume as a formula unit fraction of the primitive cell when there are multiple formula units in unit cells of low symmetry.

3.2 Some examples

Note that in the diagrams that follow, in the case of Tsirelson atoms the bold contours refer to ($V_{electrostatic} = 0$*).*

3.2.1 Unary Systems

In Unary systems the atoms are identical if there is only one kind of bond:

3.2.1.1 (i) Diamond - strongly covalent

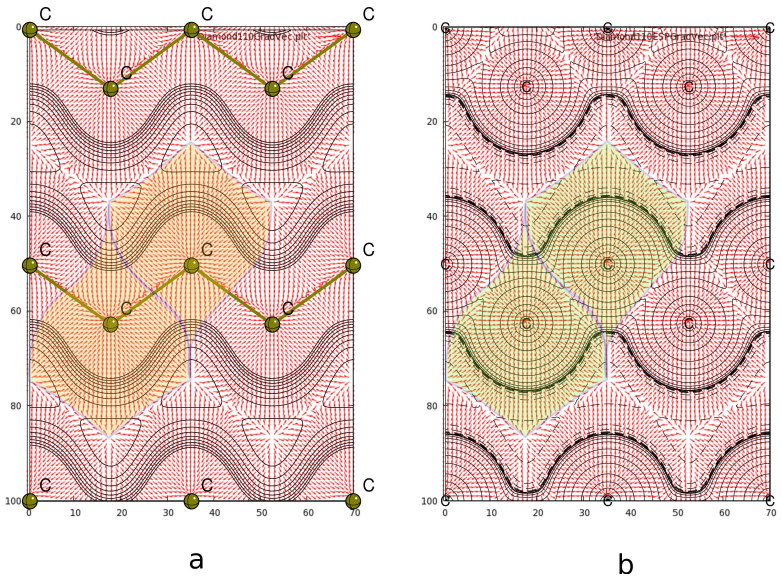

Figure 3.2: Topological atoms in diamond - (110) sections. **a** Electronic Charge Density, and **b** Electrostatic Potential. Normalised gradient vectors point “uphill” for clarity. Two adjoining atoms of differing orientation are shown. In this case the ECD and ESP atoms are identical.

3.2.1.2 (ii) Bulk Copper - metallic bond

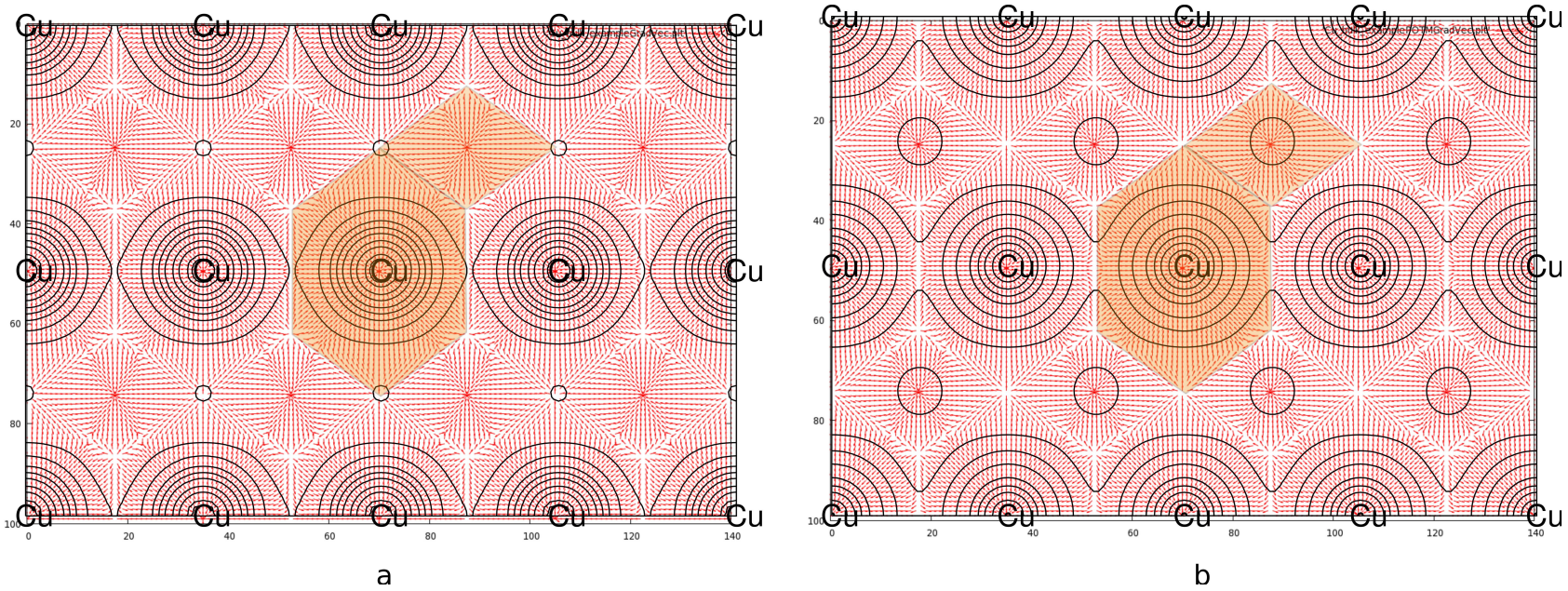

Figure 3.3: Topological atoms in copper - $(1\bar{1}0)$ sections. **a** Electronic Charge Density, and **b** Electrostatic Potential. Normalised gradient vectors point "uphill" for clarity. The cross-section also shows part of an adjoining out of plane atom. Again the ECD and ESP atoms are identical.

3.2.2 Binary Systems

These range from highly ionic crystals, such as NaCl to those with strong covalent bonds that make for very tough materials. However, even these are somewhat ionic. Here is cubic boron nitride BN , next only to diamond in hardness. It exhibits ionic bonding along with its strong covalency, evidenced by the different sizes and shapes of the Bader and Tsirelson atoms:

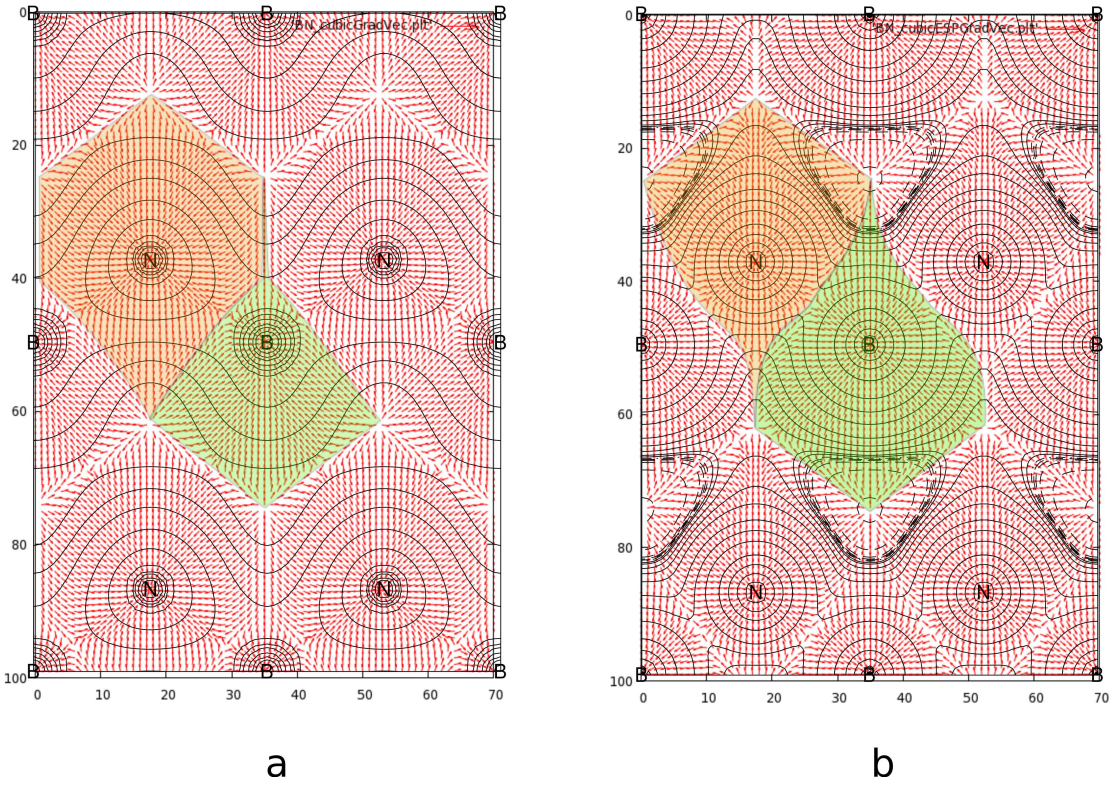

Figure 3.4: Topological atoms in boron nitride - (011) sections. **a** Electronic Charge Density, and **b** Electrostatic Potential. Normalised gradient vectors point "uphill" for clarity. The B ECD atoms are smaller than the B ESP atoms, meaning it is cationic. Similarly the N ECD atoms are larger than the N ESP atoms because it is anionic.

Cubic BN is a good example because it has the diamond structure and the geometry and physical characteristics are suggestive of sp^3 bonding. However in the condensed state the bonds are formed by Crystalline Orbitals ([68], p. 126) and the electrons are influenced by the entire crystal, not just a particular bond. There is a degree of charge transfer because of the different sizes of the Bader Atoms and the Tsirelson Atoms.

Note that the single plane vector diagram masks the complexity in the shape of Bader and Tsirelson atoms. Figure 3.5 overleaf displays sections of the 3-D shapes, revealing that a simple cubic compound like BN develops complex shapes in its Bader atoms.

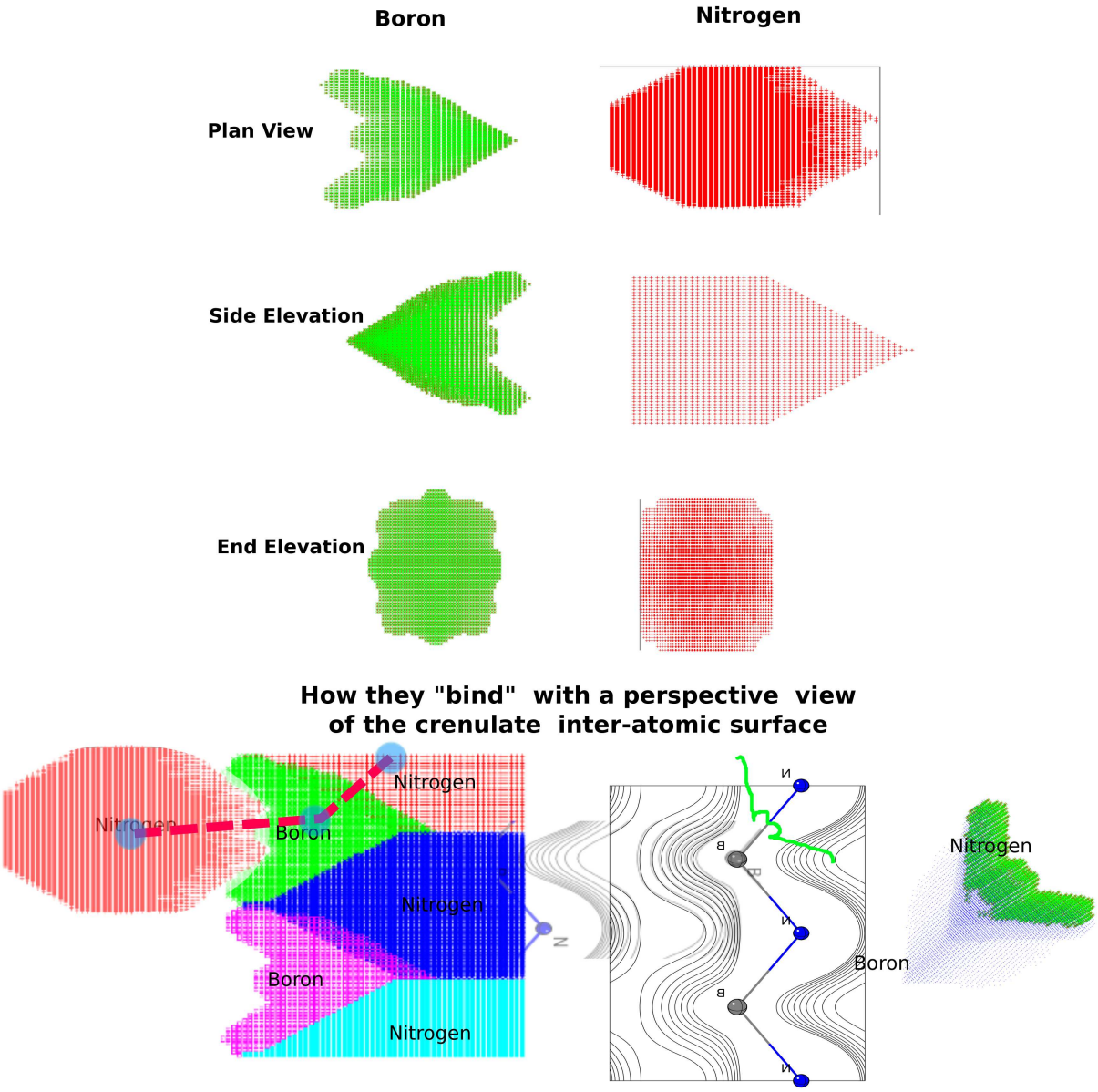

Figure 3.5: Topological atoms in boron nitride - 3-D representation. The short $B-N$ bond is very strong. Although it looks like the nitrogen has "hooked" on to the boron in both cases, the long $B-N$ bond involves much lower electron density and is much weaker.

3.2.3 Ternary Systems

The Tetragonal phases of perovskites such as $SrTiO_3$ $BaTiO_3$ and $PbTiO_3$ are chosen as examples, partly because the latter two were the subjects of Cohen's seminal paper on ferroelectricity

in 1992 [26], but also because they display a range of displacement of the titanium atom from its central position within the oxygen octahedron. This displacement, which creates the ferroelectricity, is a result of different $\mathrm{Ti} - \mathrm{O}$ bonding along the c axis, and this in turn is related to the *electronic charge density at the Bond Critical Point*.

3.2.3.1 (i) Tetragonal strontium titanate

Until 1964 Strontium Titanate $\mathrm{SrTiO_3}$ had been described as an example of the ideal, temperature-invariant, cubic perovskite structure. However in that year Lytle published results of very detailed single crystal X-ray diffractometry augmented by optical birefringence that confirmed earlier evidence of a phase transformation near $110\,K$ [82]. He reported three, possibly four phases, including Tetragonal $I4/mcm$ between $65 - 110\,K$. In the tetragonal phase, the interior Ti atom is not displaced along the c axis.

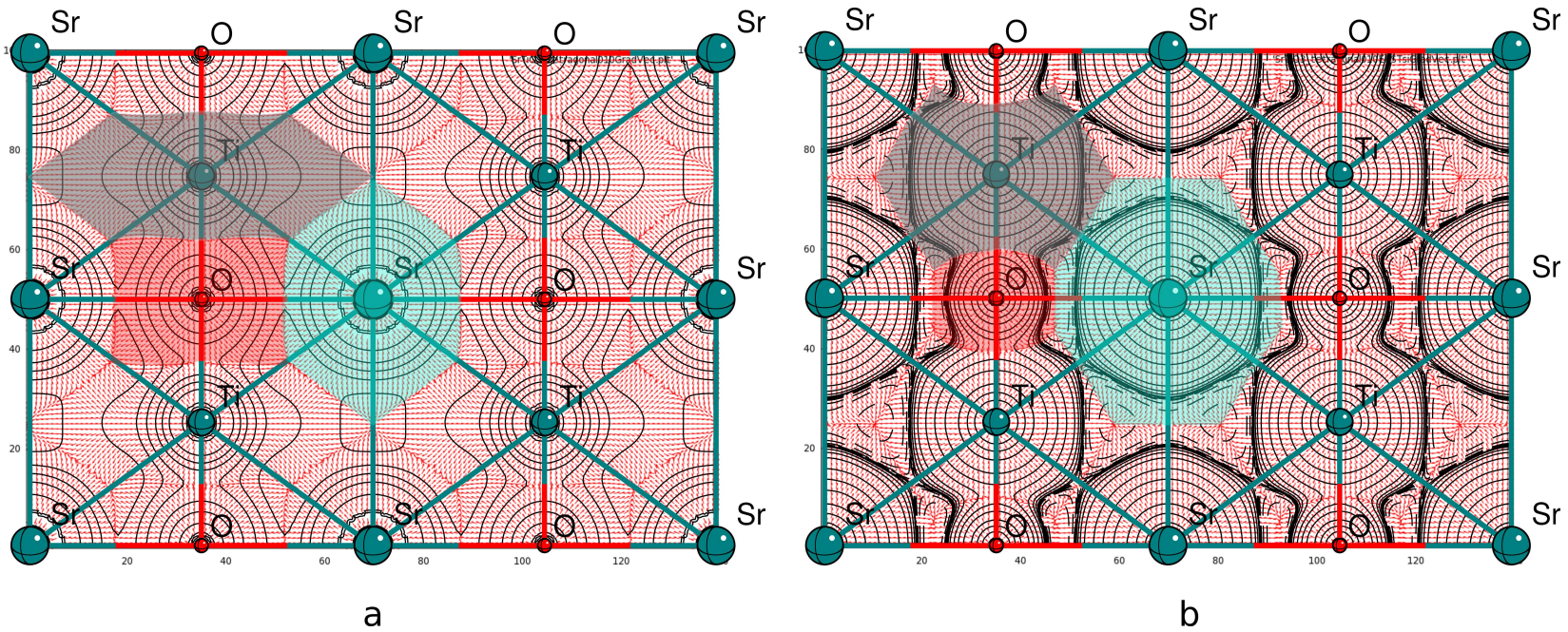

Figure 3.6: Topological atoms in tetragonal strontium titanate - (010) sections. **a** Electronic Charge Density, and **b** Electrostatic Potential.

3.2.3.2 (ii) Tetragonal barium titanate

In contrast $BaTiO_3$ is somewhat deformed.

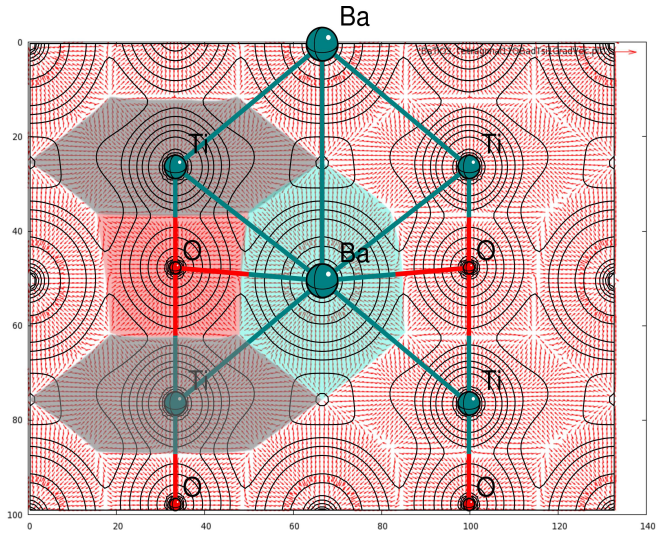

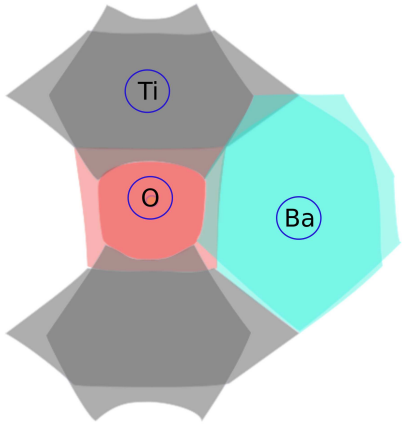

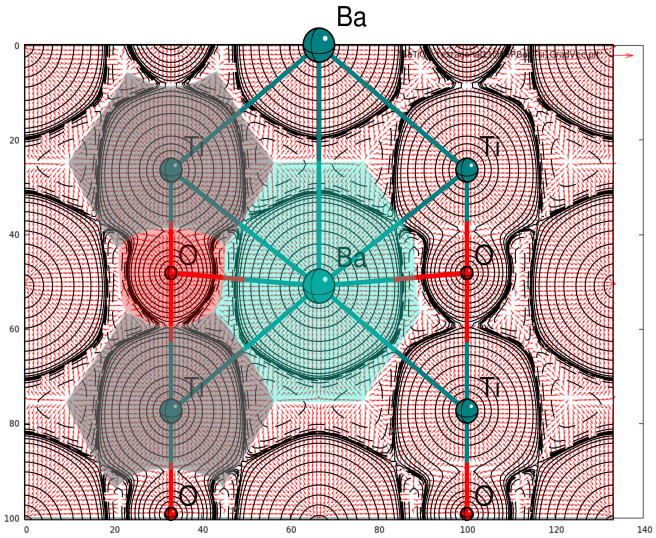

If the Tsirelson Atoms are superimposed over the Bader atoms as shown above, it will be seen that the Tsirelson Oxygen atom (over which the integrated charge is zero) is much smaller than the Bader Oxygen atom - so the latter will have a total negative charge, as expected from the conventional view of ionicity.

The reverse occurs in the case of the Barium atom.

From the DFT approach, the story is that the Bader Titanium nucleus is not totally screened by its own electrons. The Titanium Tsirelson atoms intrude significantly into the Bader Oxygen atom and the "Oxygen electrons" so affected are attracted to the Titanium nucleus.

Figure 3.7: Topological atoms in tetragonal barium titanate - (110) section. **a** Electronic Charge Density, and **b** Electrostatic Potential.

3.2.3.3 (iii) Tetragonal lead titanate

In further contrast $PbTiO_3$ is strongly deformed with an offset of the Ti atom of more than one half of a Bohr from the central position.

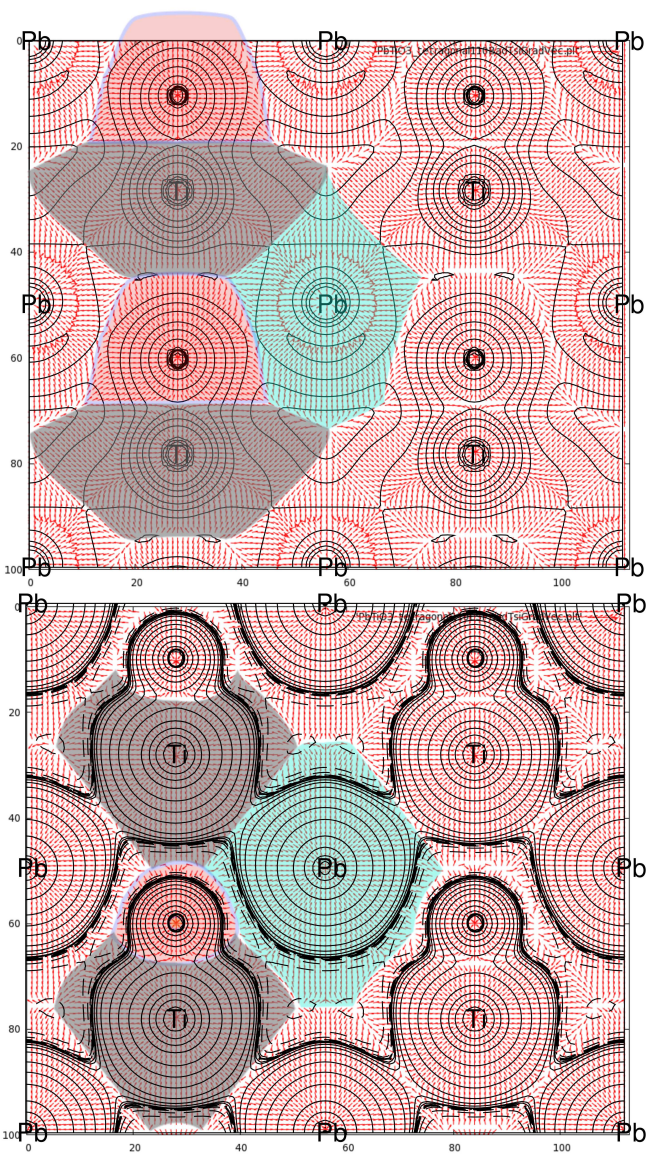

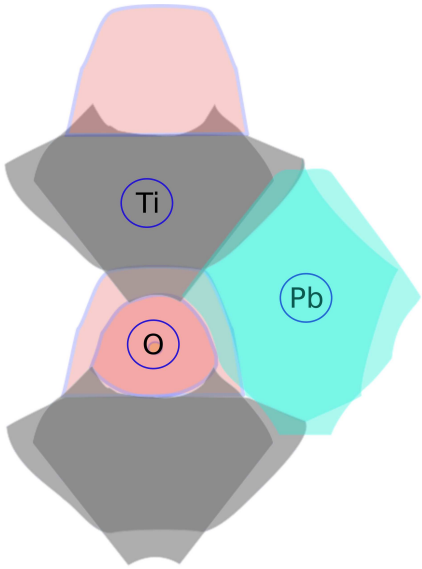

If the Tsirelson Atoms are superimposed over the Bader atoms as shown above, it will be seen that the Tsirelson Oxygen atom (over which the integrated charge is zero) is much smaller than the Bader Oxygen atom - so the latter will have a total negative charge, as expected from the conventional view of ionicity.

The reverse occurs in the case of the Lead atom.

From the DFT approach, the story is that the Bader Titanium nucleus is not totally screened by its own electrons. The Titanium Tsirelson atoms intrude significantly into the Bader Oxygen atom and the "Oxygen electrons" so affected are attracted to the Titanium nucleus.

Figure 3.8: Topological atoms in tetragonal lead titanate - (110) section. **a** Electronic Charge Density, and **b** Electrostatic Potential.

As pointed out in the notes on the diagrams, the extent of ionicity between atoms is indicated by overlap of the Tsirelson atom of one element on the Bader atom of its neighbour. This can be seen when the profiles of electronic charge density and electrostatic potential are taken into account, as illustrated in the following figure.

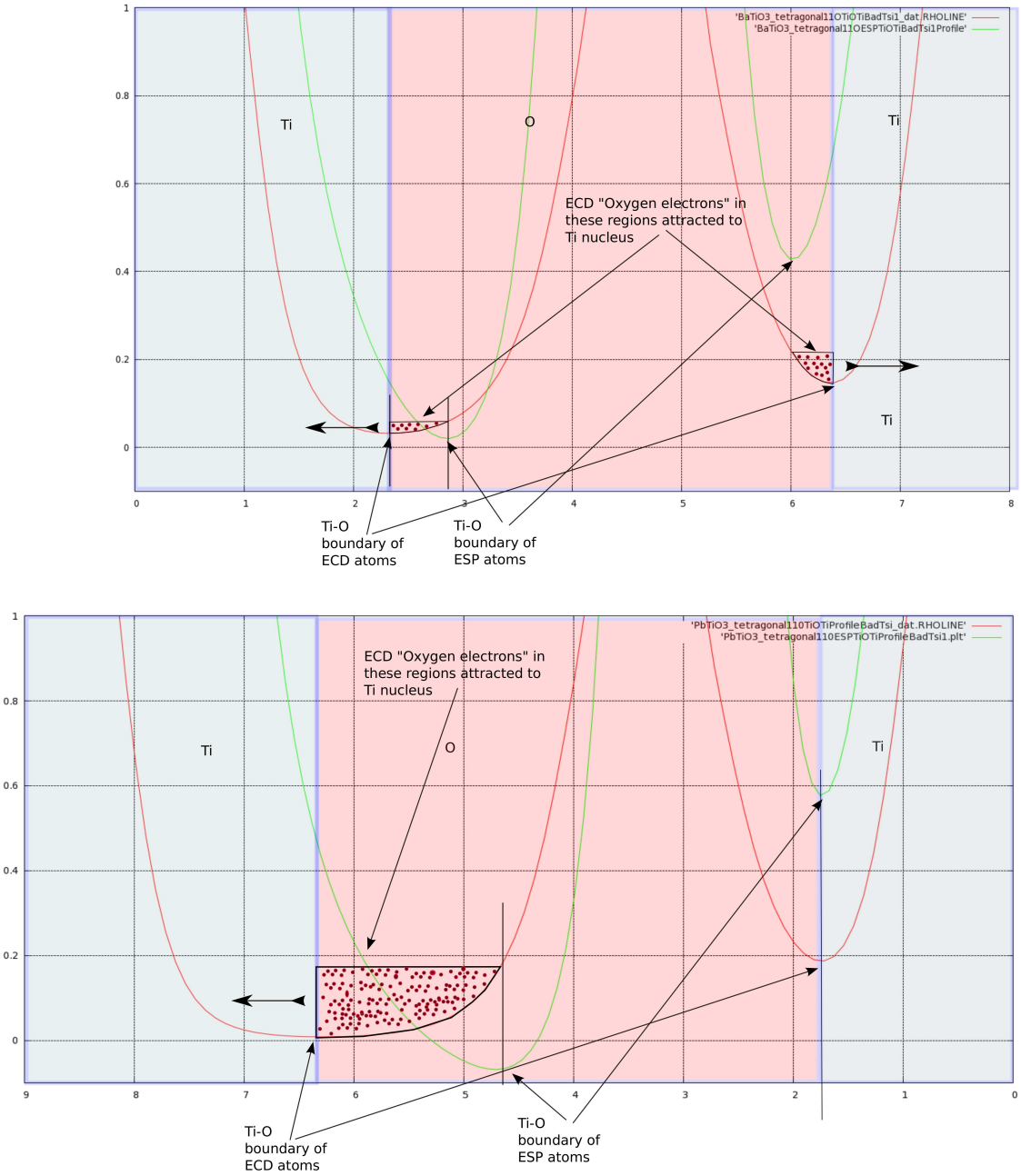

Figure 3.9: Profiles along the c axis across the topological atoms in tetragonal barium titanate and tetragonal lead titanate, showing the differing bond characteristics about the interior oxygen atom. Red - Electronic Charge Density, and Green - Electrostatic Potential.

3.2.4 Bond paths and Bond Critical Point:

The concept of bonding is developed mainly with reference to the ECD or Bader atoms. Again, the terminology is defined and fully explained in [8]. As stated, within the crystal, $\mathbf{S}_i$ encloses the i^{th} nucleus, but is also common with parts of the enclosing surface of each of its nearest neighbours. Because the highest electronic charge density occurs close to nuclei, within the core, a path crossing the valence regions between any two neighbouring nuclei must contain at least one minimal turning point in the electronic charge density. If there is just one such point, and along the path the normal plane exhibits local maximum, $-ve$ curvature in $\rho(\mathbf{r})$,the (saddle) point is a (3, -1) critical point or *Bond Critical Point* (BCP)- detailed below - and the path is a *Bond Path*. Inside the crystals studied for this thesis the bond path is a straight line. Figures 3.9 and 3.10 illustrate Bader atoms and bond paths in the $(10\bar{1}1)$ plane of $\mathrm{ReB_2}$. Notice the effect of the (small core) pseudopotential used in the basis set for Re - within the region covered by the pseudopotential the electronic charge density drops off towards zero. This has no bearing on the structure of the boundaries of the Bader atoms, but is a nuisance in illustrations of electronic charge density profiles.

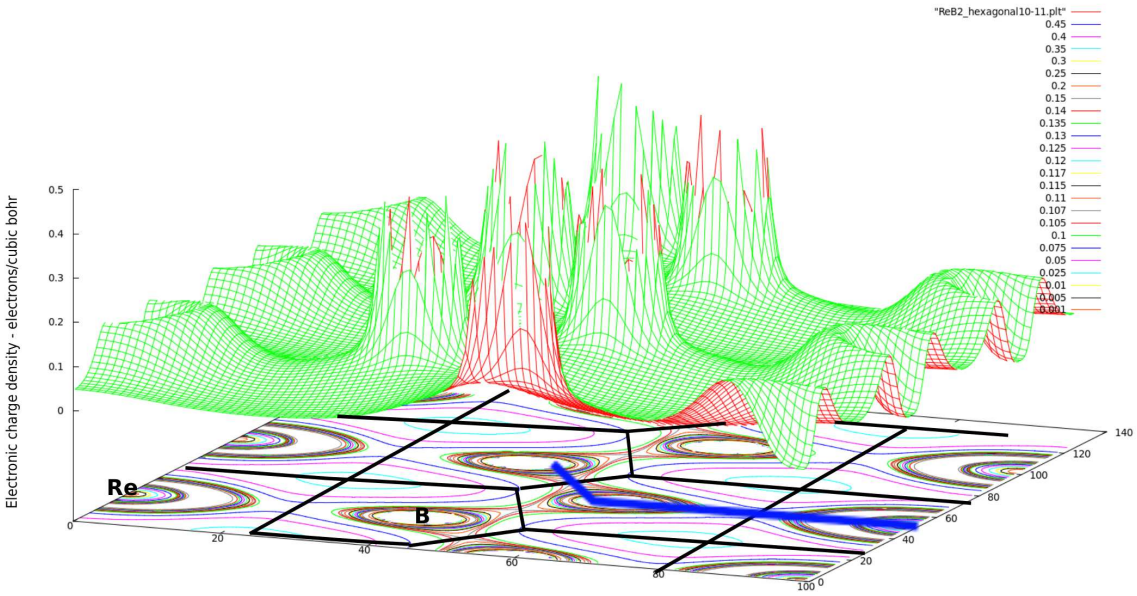

Figure 3.10: Bader atoms and bond paths in the $(10\bar{1}1)$ plane of $\mathrm{ReB_2}$. This diagram is a surface plot of the electronic charge density in that plane.The contours are selected to highlight the subtle "bunching" of charge density along bond paths.

The BCP just described necessarily lies within the shared zero flux surface between the the

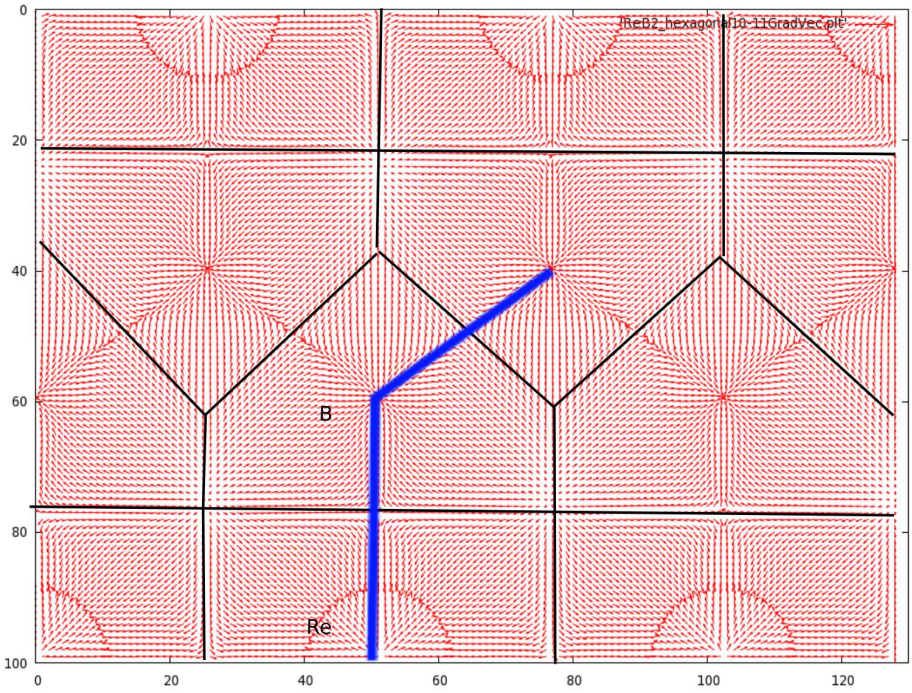

Figure 3.11: Bader atoms and bond paths in the $(10\bar{1}1)$ plane of $\mathrm{ReB_2}$. This diagram shows the bond paths, drawn in blue, over a plot of the direction of the gradient vector at each grid point . The gradient reversals near the cores of the Re atoms are artifices of the pseudopotential basis set - see text.

two atoms. Along the bond path the BCP lies at the local minimum in the electronic charge density - the first derivative being zero and the second derivative, the curvature, in this direction is $+ve$. But along any normal to the line between the nuclei at this point of intersection there is a local maximum and the curvature is $-ve$. So there is a topological saddle in the charge density surface at this point of intersection, the *Bond Critical Point* (BCP) mentioned above. Bader demonstrates that when there is a relatively pronounced concentration of charge density along the bond path, the Laplacian (see next section) will become negative, and the locality is dominated by potential energy. Figure 3.11 illustrates these curvatures.

3.2.4.1 The other Critical Points

The (3,-1) Critical Point (3 curvatures, 1 +ve and 2 -ve) is the most important in respect to a bond between atoms. However it should be pointed out that:

- A (3, -3) Critical Point (3 curvatures, 0 +ve 3 -ve) is very important - with few exceptions [79] that are not encountered in this thesis, it will be an atomic nucleus. In the topological language of Bader, the trajectories of the gradient field terminate at such a point so it is an

attractor. All trajectories which terminate at a given attractor form the basin of that attractor. *An atom (or ion) is defined as the union of an attractor and its associated basin.*

- A (3, +3) Critical Point (3 curvatures, 3 +ve 0 -ve), known as a Cage Critical point in a molecule, is important in crystals because it is a local minimum in the electronic charge density distribution **and** the Laplacian is positive. It will be seen in the next section that it therefore lies in a local region of maximum average electronic kinetic energy. The author believes that electronic transport is most likely to occur via pathways of (3, +3) Critical Points.

3.2.5 The Laplacian of the Electronic Charge Density and the Virial Theorem

The following discussion is based on [83], a short monograph now available on the web, and the derivations in Bader's book [8].

The (scalar) Laplacian of the electronic charge density is the trace of the Hessian matrix, the real symmetric matrix of the nine second derivatives of the electronic charge density.

$\mathbf{L}\rho(\mathbf{r}) \;=\; \nabla^2\rho(\mathbf{r}) \;=\; \nabla\cdot\nabla\rho(\mathbf{r}) \;=\; \frac{\partial^2\rho}{\partial x^2}+\frac{\partial^2\rho}{\partial y^2}+\frac{\partial^2\rho}{\partial z^2}$

The three partial second derivatives are the respective principle curvatures of the scalar field of electronic charge density. At a BCP the curvature along the bond path is positiver (convex down) whilst the the two perpendicular to the bond path are negative (convex up). It is not possible to display the full differential geometry of a three dimensional scalar field on the printed page, but it is hoped that the diagram following on the next page, Figure 3.11, will illustrate this important aspect of the BCP. This diagram shows two of the three principal curvatures at the BCP between Titanium and Oxygen in the case of the somewhat covalent bond of the distorted perovskite $\mathrm{PbTiO_3}$ (there is also a weaker, less covalent, bond and four intermediate bonds in the Oxygen Octahedron).

So it is seen that charge accumulates where curvatures are negative and is depleted where curvatures are positive. Thus a map of the Laplacian will provide a map of where electronic charge density is locally concentrated or depleted. Bader takes this further by use of the virial theorem:

If forces act on the particles of a system, then the system will possess potential energy and if the particles move the system will possess kinetic energy. The term *virial* and the theorem were introduced by Clausius in 1870. In modern language the theorem says that the average kinetic energy of a system is equal to half the average potential energy. The virial is defined as a scalar quantity $\mathcal{V}(\mathbf{r}) \;=\; \frac{1}{2}\langle\sum_i \mathbf{F}_i\cdot\mathbf{r}_i\rangle$, where $\mathbf{F}_i$ is the force on the ith particle at $\mathbf{r}_i$. The theorem implies time averages over long to infinite time, and applies to the entire system. It is implicit in Lagrangian mechanics, 100 years earlier than Clausius' presentation, if the system is

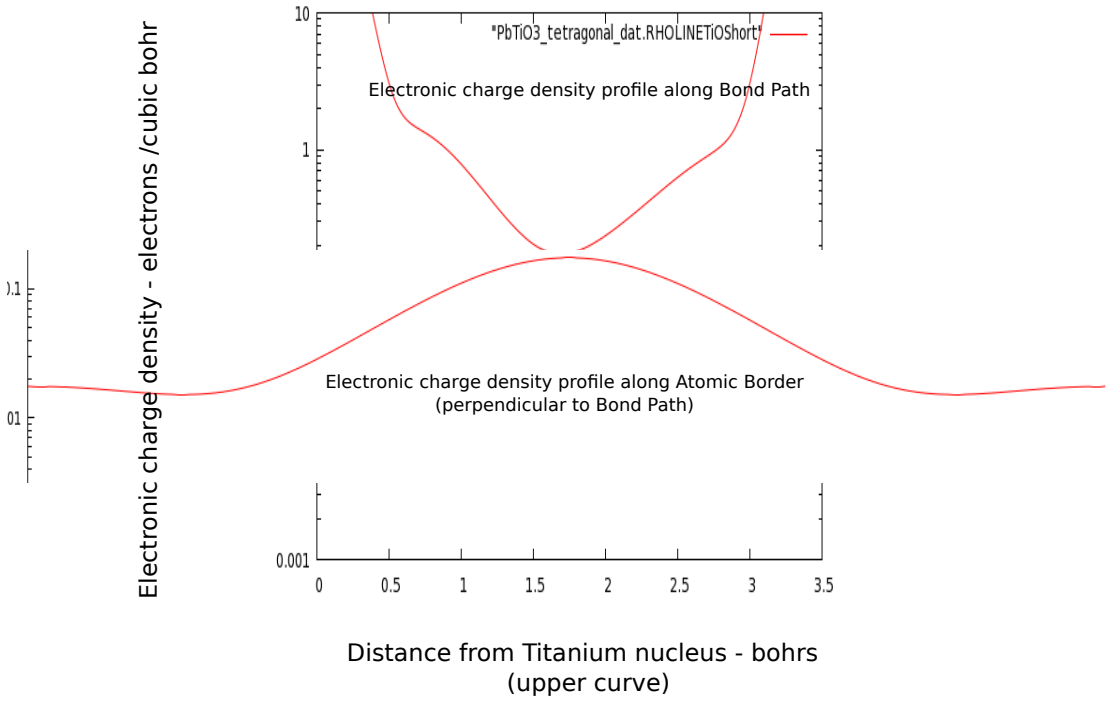

Figure 3.12: Profiles through the bond path and one of the perpendiculars at the BCP of the somewhat covalent $\mathrm{Ti}-\mathrm{O}$ bond in $\mathrm{PbTiO_3}$. There is a "bunching" of charge density from either side along the bond path, but in the section between the nuclei, the charge density drops to a minimum at the BCP from the very high values at the nuclear sites. The vertical scale is logarithmic and density values are electron (probabilities) per cubic bohr.

ergodic. Bader showed that the virial field $\mathcal{V}(\mathbf{r})$ defines the electronic potential energy density of an electron at $\mathbf{r}$ [8], and that the virial theorem applies to certain subsystems of a molecular or crystal system - namely the atoms as defined by the bounding zero flux surfaces. Also Keith, Bader and Aray demonstrated that in all the molecules they studied $\mathcal{V}(\mathbf{r})$ exhibits the same relatively simple topology as does the electron density. Thus, of the fields determined by the one-electron density matrix $\Gamma^{(1)}$, only the (negative) virial field is homeomorphic with the electron density, in addition to paralleling its transferable behavior over bounded regions of space (i.e. its atomic nature).[84]. Hence there is a virial path corresponding to a bond path between nuclei along which the potential energy density is locally minimal i.e. stabilising and intrinsically bonding.

Bader derived the equation to yield the local result [8] p.178 :

$$\frac{\hbar^2}{4m}\nabla^2\rho(\mathbf{r}) = 2T(\mathbf{r}) + \mathcal{V}(\mathbf{r}) \tag{3.1}$$

where $\nabla^2\rho(\mathbf{r})$ is the Laplacian, $\mathbf{L}\rho(\mathbf{r})$, of the electronic charge density at $\mathbf{r}$, m is the electronic mass, $T(\mathbf{r})$ is the kinetic energy density at $\mathbf{r}$ and $\mathcal{V}(\mathbf{r})$is the electronic potential energy at $\mathbf{r}$.

This is the local relationship between the Laplacian and the energy densities and Bader used it extensively in his efforts to characterise bonds and to predict mechanisms of Lewis acid-base

reactions (which are electron pair transactions).

Integrating equation $(\mathbf{1})$ over an entire atom $\mathbf{\Omega}$:

$$\int_{\mathbf{\Omega}} \mathbf{L}(\mathbf{r}) \;=\; 0 \;=\; 2T(\mathbf{\Omega}) + \mathcal{V}(\mathbf{\Omega}) \tag{3.2}$$

the integral of the Laplacian over the whole atom vanishing because of the zero flux enclosing surface (using Gauss' theorem) - thus establishing the virial theorem for the atom.

This means that taking a whole atom $\mathbf{\Omega}$ the atomic energy $\mathbf{E}_{\mathbf{\Omega}}$ satisfies the identity:

$$\mathbf{E}_{\mathbf{\Omega}} \;=\; -T(\mathbf{\Omega}) \;=\; \frac{1}{2}\mathcal{V}(\mathbf{\Omega}). \tag{3.3}$$

Bader demonstrated that the Laplacian of the electronic charge density forms enclosing shells of negative and positive values corresponding to potential and kinetic energy concentrations, relative to their virial average, around each nucleus of atoms whether they are free or in a molecule or crystal. For lighter atoms up to Ca these shells correspond to the orbital shells (above Z=40 relativistic effects and other effects interrupt the alternation of the Laplacian). The shells will be polarisable, but with very high electrostatic potential gradients, and so will be evidenced by "hard" very high frequency phonons. Apart from these polarisation effects, only the valence and conduction electrons are involved in the interaction of Bader atoms. This means that the core regions of an atom reduce the volume over which the valence electron kinetic energy is distributed. Not only chemical attributes, such as oxidation states or the nature of bonding, but also mechanical, electromagnetic and thermal properties are thus determined by very small and sparse electronic populations.

Bader related the Laplacian of the electronic charge density to the valence shell charge concentration (VSCC) thence the valence shell electron pair repulsion (VSEPR) model of Gillespie, describing the latter as a natural extension of the localised electron pair model of Lewis [85]. He demonstrated that such extension of the Lewis model could be recovered in the Laplacian of the electronic charge density. The use of the Laplacian (or minus the Laplacian) is discussed further in chapter 5. Figure 3.12 overleaf is a copy of Bader's illustration with the VSCC shaded in.

However this proposition seems better served by the electron localisation function (ELF - see chapter 5), proposed by Becke and Edgecoombe in 1990 [86] and which, in their words, "easily reveals atomic shell structure and core, binding, and lone electron pairs in simple molecular systems as well". In 1997 Savin et al. applied ELF to crystals for the first time, treating several unary systems with the diamond structure. Since then ELF has become "an acknowledged tool for the description and the understanding of the bonding in molecules and solids" [87].

ELF can be recovered directly from the CRYSTAL06 wave function output, but the author chose to recover it from the electronic charge density, as if this was provided by experiment rather than ab initio calculation. In order to proceed this way it was necessary to calculate the Laplacian from a 3D array of the ECD and apply the Tsirelson and Stash algorithm mentioned in chapter 2, section 2.4.0.2. Chapter 5 also includes additional discussion of ELF.

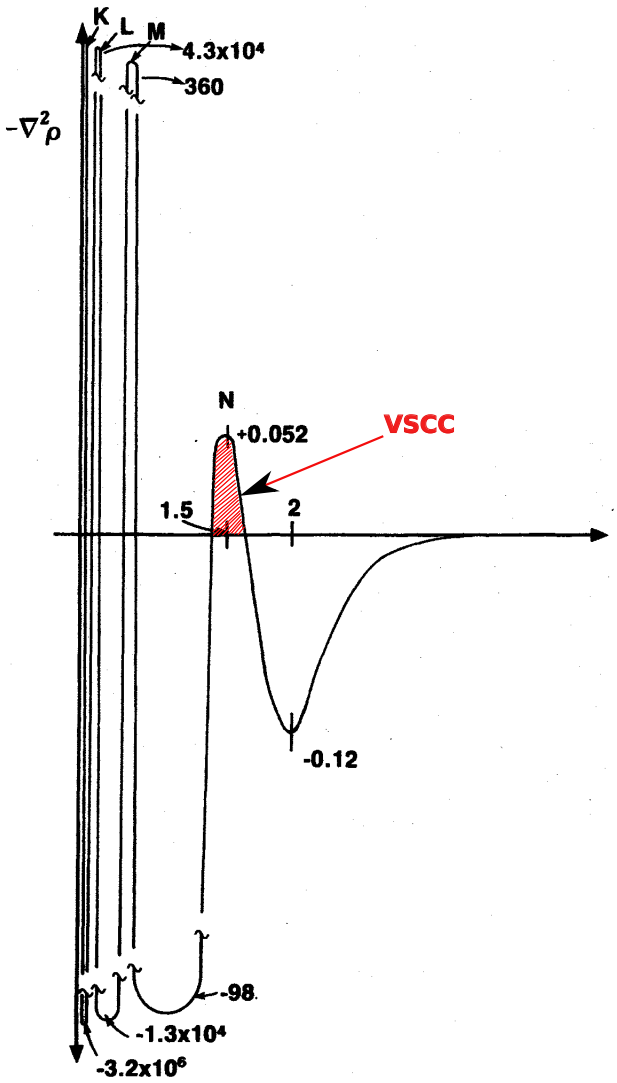

FIG. 7.3. Schematic representation of the profile of $-\nabla^2\rho$ for the krypton atom along a radial line. Unlike a radial distribution plot, which is a one-dimensional function, the Laplacian distribution displays shell structure in three-dimensional space.

Figure 3.13: Copied from [8], showing orbital shells as revealed by a plot of the -ve Laplacian.

Chapter 4

The CRYSTAL06 suite of programmes

The CRYSTAL06 programme, so apparently convenient and widely applicable, is a re-application to physics of decades of hard work by chemists as was sketched out in chapter 2, section 2.1.5.

4.1 The CRYSTAL06 programme and Crystalline Orbitals

The study is in terms of electronic charge density calculated from crystalline orbitals.

The idea of crystalline orbitals is the extension of or adaptation of molecular orbital theory to periodic systems. This is achieved by

(i) the crystalline orbitals will be linear combinations of Bloch functions

(ii) the Bloch functions will in turn be linear combinations of a suitable of normalised atomic functions (orbitals) adjusted from their counterparts in molecular linear combination of atomic orbital theory. The adjustment involves contracting the combinations so that they can be periodic in conformity with the crystal lattice. Diffuse functions that may well help to describe an isolated molecule need to be discarded if they create excessive overlap or do not fit within a a unit cell.

(ii) the crystalline orbitals will inherit the symmetry of the crystal.

The successful calculation of crystalline orbitals (by a self consistent variational scheme) means that any particular phenomenon can be looked at on a crystal-wide basis rather than on a local basis. For example, lowest level excitations can be described by the Wannier (weak binding) model [88] rather than the Frenkel (tight binding) model [89]. These models correspond to the Hund-Mulliken-Bloch scheme of electrons spread throughout the entire crystal and the Heitler-London scheme of localised atomic wave functions respectively [90].

The following theoretical explanation is drawn from the manual [6] - fuller details can be found in chapters 8 and 11 of [68] and in other references cited in [6], especially [14]. It should be noticed that the computational procedures are switching between direct space and reciprocal

space at various stages :

CRYSTAL06 is an ab initio Hartree-Fock LCAO program for the treatment of periodic systems. LCAO, in the present case, means that each Crystalline Orbital, a function of the direct space vector $\mathbf{r}$ and the reciprocal space vector $\mathbf{k}$, $\psi_i(\mathbf{r};\mathbf{k})$, is a linear combination of Bloch functions (BF), $\phi_\mu(\mathbf{r};\mathbf{k})$, defined in terms of local functions, $\varphi_\mu(\mathbf{r})$ (here referred to as Atomic Orbitals, AOs).

$$\psi_i(\mathbf{r};\mathbf{k}) = \sum_\mu a_{\mu,i}(\mathbf{k})\phi_\mu(\mathbf{r};\mathbf{k}) \tag{4.1}$$

$$\phi_\mu(\mathbf{r};\mathbf{k}) = \sum_{\mathbf{g}} \varphi_\mu(\mathbf{r}-\mathbf{A}_\mu-\mathbf{g})e^{i\mathbf{k}.\mathbf{g}} \tag{4.2}$$

$\mathbf{A}_\mu$ denotes the coordinate of the nucleus in the zero reference cell on whichφ_μ is centred, and the$\sum_{\mathbf{g}}$is extended to the set of all lattice vectors $\mathbf{g}$.

The local functions are expressed as linear combinations (so-called *contractions*) of a certain number,n_G , of individually normalized (basis set) Gaussian type functions (GTF) characterized by the same centre, with fixed coefficients,d_j and exponents,α_j , defined in the input:

$$\varphi_\mu(\mathbf{r}-\mathbf{A}_\mu-\mathbf{g}) = \sum_j^{n_G} d_j G(\alpha_j;\mathbf{r}-\mathbf{A}_\mu-\mathbf{g}) \tag{4.3}$$

where the GTF, split into Cartesian components, is of the form
$G(\mathbf{r}) = x^l e^{-\alpha x^2} y^m e^{-\alpha y^2} z^n e^{-\alpha z^2}$.
The exponents $l,\ m,\ and\, m$ are not quantum numbers but are integers that are used by CRYSTAL06 to define "shells" according to the value of $l+m+n:$ 0 for an s-type, 1 for a p-type 2 for a d-type etc. Real spherical harmonics are generated internally by CRYSTAL06 using appropriate linear combinations of the Cartesian components as multipliers of the GTFs to give the number of "shaped" orbitals per shell as follows:
s 1 (1); p 3 (x, y, z); d 5 ($2z^2-x^2-y^2$, xz, yz, x^2-y^2, xy).

To assist computation, CRYSTAL06 allows sp shells s and p shells that have the same exponent but different contraction coefficients.

The expansion coefficients of the Bloch functions, $a_{\mu,i}(\mathbf{k})$ in (2.1), are calculated by solving the matrix equation for each reciprocal lattice vector, $\mathbf{k}$:

$$\mathbf{F}(\mathbf{k})\mathbf{A}(\mathbf{k}) = \mathbf{S}(\mathbf{k})\mathbf{A}(\mathbf{k})\mathbf{E}(\mathbf{k}) \tag{4.4}$$

in which $\mathbf{S}(\mathbf{k})$ is the overlap matrix over the Bloch functions,$\mathbf{E}(\mathbf{k})$ is the diagonal energy matrix and$\mathbf{F}(\mathbf{k})$ is the Fock matrix in reciprocal space:

$$\mathbf{F}(\mathbf{k}) = \sum_{\mathbf{g}} \mathbf{F}^{\mathbf{g}} e^{i\mathbf{k}\cdot\mathbf{g}} \tag{4.5}$$

The matrix elements of F^g, the Fock matrix in direct space, can be written as a sum of one-electron and two-electron contributions in the basis set of the AO:

$$\mathbf{F}^{\mathbf{g}}{}_{12} = \mathbf{H}^{\mathbf{g}}{}_{12} + \mathbf{B}^{\mathbf{g}}{}_{12} \tag{4.6}$$

The one electron contribution is the sum of the kinetic and nuclear attraction terms:

$$\mathbf{H}^{\mathbf{g}}{}_{12} = \mathbf{T}^{\mathbf{g}}{}_{12} + \mathbf{Z}^{\mathbf{g}}{}_{12} = \langle \varphi_1^{\mathbf{0}} | \hat{\mathbf{T}} | \varphi_2^{\mathbf{g}} \rangle + \langle \varphi_1^{\mathbf{0}} | \hat{\mathbf{Z}} | \varphi_2^{\mathbf{g}} \rangle \tag{4.7}$$

In core pseudopotential calculations, $\hat{\mathbf{Z}}$ includes the sum of the atomic pseudopotentials. The two electron term is the sum of the Coulomb and exchange contributions:

$$\mathbf{B}^{\mathbf{g}}{}_{12} = \mathbf{C}^{\mathbf{g}}{}_{12} + \mathbf{X}^{\mathbf{g}}{}_{12} = \sum_{\mathbf{3,4}} \sum_{\mathbf{n}} \mathbf{P}^{\mathbf{n}}_{\mathbf{3,4}} \sum_{\mathbf{h}} [(\varphi_1^{\mathbf{0}} \varphi_2^{\mathbf{g}} | \varphi_3^{\mathbf{h}} \varphi_4^{\mathbf{h+n}}) - \frac{1}{2} (\varphi_1^{\mathbf{0}} \varphi_3^{\mathbf{h}} | \varphi_2^{\mathbf{g}} \varphi_4^{\mathbf{h+n}})] \tag{4.8}$$

Seven indices are involved in equation (2.8); four of them $(1, 2, 3 \text{ and } 4)$ refer to the AOs of the unit cell; in principle, the other three $(\mathbf{g}, \mathbf{n} \text{and} \mathbf{h})$ span the infinite set of translation vectors: for example, $\varphi_2^{\mathbf{g}}(\mathbf{r})$ is **AO** number 2 in cell $\mathbf{g}$. P is the density matrix; the usual notation is used for the bi-electronic integrals[1].

The Coulomb interactions, that is, those of electron-nucleus, electron-electron and nucleus-nucleus, are individually divergent, due to the infinite size of the system. The grouping of corresponding terms is necessary in order to eliminate this divergence.

The$\mathbf{P^n}$ density matrix elements in the **AO**s basis set are computed by integration over the volume of the Brillouin zone (BZ),

$$\mathbf{P^n}_{3,4} = 2 \int_{BZ} d\mathbf{k}\, e^{i\mathbf{k}\cdot\mathbf{n}} \sum_j a^*_{3j}(\mathbf{k}) a_{4j}(\mathbf{k}) \theta(\epsilon_F - \epsilon_j(\mathbf{k})) \tag{4.9}$$

where a_{in} denotes the$i-th$ component of the $n-th$ eigenvector, θ is the step function, ϵ_F , the Fermi energy and ϵ_n , the n-th eigenvalue. The total electronic energy per unit cell is given by:

[1] e.g. $(\varphi_1^{\mathbf{0}} \varphi_2^{\mathbf{g}} | \varphi_3^{\mathbf{h}} \varphi_4^{\mathbf{h+n}}) = \int_{R^3} \int_{R^3} \frac{\varphi_1^{\mathbf{0}}(\mathbf{r}) \varphi_2^{\mathbf{g}}(\mathbf{r}) \varphi_3^{\mathbf{h}}(\mathbf{r}') \varphi_4^{\mathbf{h+n}}(\mathbf{r}')}{|\,\mathbf{r}-\mathbf{r}'\,|}\, d\mathbf{r}\, d\mathbf{r}'$ etc. Obviously the integrations cannot be extended over all of R^3 (i.e. to infinity in each component of $\mathbf{r}$) and equation (2.8) requires meaningful approximations and cut-offs. There is a long history of successful dealing with this, solving a number of complicated problems mainly to do with balancing or weighting compartments of the electronic distribution so that integration can be truncated as soon as convergence is reasonable. The Crystal manual and references therein contain detailed discussions of the methods used, but are quite difficult to follow, partly because the subject matter is difficult, but also because there are references within references that need to be followed up simply to appreciate the notation adopted. A helpful discussion that uses diagrams to illustrate the bi-electronic integrals and the range over which they must be undertaken is [91].

$$E^{elec} = \frac{1}{2}\sum_{1,2}\sum_{\mathbf{g}} P^{\mathbf{g}}_{1,2}(H^{\mathbf{g}}_{12} + B^{\mathbf{g}}_{12}) \tag{4.10}$$

4.2 Crystal06 in action

The author has found that it is easier to understand and apply the above theory if one has a "picture" of the various steps. Using MgO, one of the simplest materials used in the CRYSTAL06 web-based tutorials and applying the input routines used later for the perovskites rather than those used in the tutorials, he hopes to illustrate the operation of this remarkable tool.

4.2.1 Input

Here is the input script - it is saved to a file called MgO.d12 and is called by the command "runcry06 MgO". The line numbers are included only for this discussion - the programme would not run if they appeared in the actual input script.

```
1   MgO bulk from CRYSTAL examples.
2   CRYSTAL
3   0 0 0
4   225
5   4.21
6   2
7   12 0. 0. 0.
8   8 0.5 0.5 0.5
9   END
10   12 3
11   0 0 8 2. 1.
12   68371.875 0.0002226
13   9699.34009 0.0018982
14   2041.176786 0.0110451
15   529.862906 0.0500627
16   159.186000 0.169123
17   54.6848 0.367031
18   21.2357 0.400410
19   8.74604 0.14987
20   0 1 6 8. 1.
```

```
21      156.795 -0.00624 0.00772
22      31.0339 -0.07882 0.06427
23      9.6453 -0.07992 0.2104
24      3.7109 0.29063 0.34314
25      1.61164 0.57164 0.3735
26      0.64294 0.30664 0.23286
27      0 1 1 0. 1.
28      0.4 1. 1.
29      8 3
30      0 0 8 2. 1.
31      4000. 0.00144
32      1355.58 0.00764
33      248.545 0.05370
34      69.5339 0.16818
35      23.8868 0.36039
36      9.27593 0.38612
37      3.82034 0.14712
38      1.23514 0.07105
39      0 1 5 8. 1.
40      52.1878 -0.00873 0.00922
41      10.3293 -0.08979 0.07068
42      3.21034 -0.04079 0.20433
43      1.23514 0.37666 0.34958
44      0.536420 0.42248 0.27774
45      0 1 1 0. 1.
46      0.210000 1. 1.
47      99 0
48      END
49      DFT
50      EXCHANGE
51      BECKE
52      CORRELAT
53      LYP
54      HYBRID
```

```
55      10
56      NUMERICAL
57      XLGRID
58      END
59      TOLINTEG
60      7 7 7 7 14
61      SCFDIR
62      SHRINK
63      3 6
64      FMIXING
65      50
66      MAXCYCLE
67      200
68      LEVSHIFT
69      10 0
70      TOLDEE
71      10
72      END
```

Line 1 is a comment line that allows a brief description of the material and data sources

Line 2: CRYSTAL adopts four keywords: CRYSTAL, SLAB, POLYMER and MOLECULE, for 3D, 2D, 1D and 0D systems, respectively. In this case the keyword to specify is CRYSTAL.

Line 3: three integer numbers: - convention for the space group identification: sequential number (0) or alphanumeric code (1) - type of cell for rhombohedral groups: hexagonal (0) or rhombohedral (1). - setting of the origin (see CRYSTAL User's Manual for further details).

Line 4: Crystal Space Group

Line 5: Lattice parameters.The minimal set of crystallographic cell parameters is indicated (in Angstrom and degrees). For MgO, cubic system, the length of the edge of the cell fully defines shape and size of the conventional unit cell (note, however, that CRYSTAL works on the primitive cell).

Lines 6, 7 & 8: The first line gives the number of atoms in the asymmetric unit. One line per atom in the asymmetric unit follows, to specify the conventional atomic number and the coordinates in fractional units of the crystallographic lattice vectors. These atoms are usually indicated as non-equivalent atoms, i.e. atoms not symmetry related. The whole structure of MgO is defined by 2 atoms.

Line 9: the keyword END denotes the end of the geometrical input data. These data (lines 3 through 8) are obtained from published measurements, usually through the ICSD - http://icsd.fiz-karlsruhe.de/icsd/ .

Now follows Basis set input:

For each atom (i.e. as many blocks as different types of atoms in the crystal structure including atoms of the same species but with different oxidation states) the following must be specified on separate lines:

a. the conventional atomic number and the number of shells making up the atomic basis set;

b. for each shell, type of basis set (0-1-2), type of shell (0-1-2-3-4; s, sp, p, d,f), number of primitives GTF, shell electronic charge, scale factor;

c. for each primitive: exponent, contraction coefficient, [contraction coefficient] (the second contraction coefficient in the case of sp shells).

Line 10: (a.) This begins the input for Magnesium. The conventional atomic number is 12 and 3 "shells" will be used to describe it. Each shell can contain either all AOs with the same quantum numbers, n and l (for instance 3s, 2p, 3d shells), or all the AOs with the same principal quantum number n and different l (sp shells; exponent of s and p gaussians are the same).
Line 11: (b.) The five numbers here refer to the first shell and are:

- a code to identify basis set type - in CRYSTAL three basis set types are available: 0 general basis set where exponent and contraction coefficients defined in input; 1 Pople STO-nG type basis set; 2 Pople 3(6)-21G type basis set. In this case 0 is used.

- a code to indicate the shell type according to the following table:

Code	Shell type	Atomic orbitals	AO order	Max. shell charge
0	s	1	s	2
1	sp	4	s, x, y, z	8
2	p	3	x, y, z	6
3	d	5	$2z^2 - x^2 - y^2$, xz, yz, $x^2 - y^2$, xy	10
4	f	7	$(2z^2 - 3x^2 - 3y^2)z$, $(4z^2 - x^2 - y^2)x$, $(4z^2 - x^2 - y^2)y$, $(x^2 - y^2)z$, xyz, $(x^2 - 3y^2)x$, $(3x^2 - y^2)y$	0 (polarisation only)

in this case 0 is used for an s shell

- an integer, being the number of Gaussian type functions employed for this shell - in this case 8.

- a real number, representing the electronic charge, therefore the number of electrons in the shell, in this case 2. The ionicity of atoms can be adjusted by varying this for outer shells, provided the net charge of the total of atoms is zero.

- a real number, called the scale factor. In this case it is 1.0, as it is in all the published sets that the author has seen.

Lines 12 - 19 incusive: (c.) These define the 8 primitive Gaussian type functions for this shell. In each line the first number is the exponent, α_j and the second is the contraction coefficient, d_j.
Line 20: as for Line 11, but this is the second shell, this time an sp shell with 6 primitive functions and 8 electrons, scale factor 1.0.
Lines 21 -26 inclusive: the 6 primitives for this shell, each with the additional contraction coefficient for the p shell.
Lines 27 & 28: the third shell for Mg, another sp shell but with just one primitive and no electrons.
Lines 29 - 46: These repeat the input procedure for 3 shells of O.
Line 47: the numbers 99 0 are CRYSTAL06 code for “end of basis set input”.
Line 48: end of the input block

Here is what these Gaussian type functions look like, plotted about the respective atomic locations:

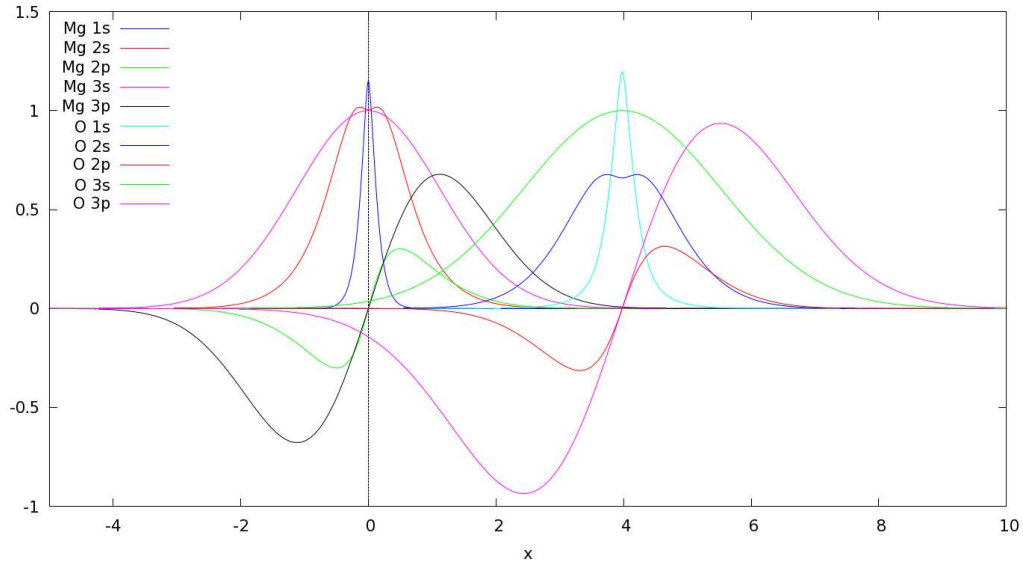

Figure 4.1: DFT calculation for MgO. Atomic Orbitals, centred at 0 bohr for Mg and 3.9779 bohr for O, are made up of these Gaussian-type basis functions.

The ensuing lines instruct the programme on the type of calculation and the parameters to be used. All of the examples used in this thesis were calculated with the DFT (Kohn-Sham) Hamiltonian, Becke gradient-corrected (GGA) exchange functionals (of the electron density and its gradient) [65] with a 10% linear combination of Hartree-Fock (HF) exchange to counter the DFT tendency to under-estimate the band gap, and Lee - Yang - Parr GGA correlation functional [66]. As far as possible all input parameters and tolerances were kept the same , because results were to compared across bond types, but level shift and mixing techniques, subsequently adjusted, were needed to achieve SCF convergence for the metallic minerals. All structural measurements are after full geometry optimisation.

Line 49: the DFT (Kohn-Sham) Hamiltonian will be employed instead of Hartree-Fock Theory (HF) methods. The keyword DFT selects a DFT Hamiltonian. Exchange-correlation functionals are separated in an exchange component (keyword EXCHANGE) and a correlation component (keyword CORRELAT).

Lines 50 & 51: the Becke gradient-corrected (GGA) exchange functionals (of the electron density and its gradient) [65] is specified.

Lines 52 & 53: the Lee - Yang - Parr GGA correlation functional [66] is specified.

Lines 54 & 55: the Hartree-Fock exchange functional is incorporated in 10% linear combination.

Lines 56 & 57: these prescribe numerical integration on an “extra large” predefined grid (i.e. high resolution).

Line 58: this ends the DFT input block

Lines 59 & 60: specifies truncation criteria for the bielectronic integrals in the Coulomb and HF exchange series. The five parameters $ITOL$ are used at the five successive relevant stages in the calculation so that when the overlap/penetration between the two atoms is less than 10^{-ITOL} the corresponding integral is discarded.

Line 61: SCFDIR is a keyword that saves on disc access if the computer CPU is fast enough. In the SCF step monoelectronic and bielectronic integrals are evaluated at each cycle. Very compact crystalline systems, and/or very diffuse basis functions and/or very tight tolerances can produce billions of integrals to be stored. The storage of bielectronic integrals can be avoided by running the direct SCF code SCFDIR rather than the standard SCF, at the expenses of a certain amount of CPU time.

Lines 62 & 63: SHRINK is an essential keyword whose two parameters determine the density of calculated points. The first number (or shrinking factor) generates a commensurate grid of k points in reciprocal space, according to Pack-Monkhorst method. The Hamiltonian matrix computed in direct space, Hg (g, direct lattice vector), is Fourier transformed for each k value (k,

reciprocal lattice vector) and diagonalized, to obtain eigenvectors and eigenvalues. The second number (shrinking factor defines the sampling of k points, in the ”Gilat net”, used for the calculation of the density matrix and the determination of Fermi energy in the case of conductors, when bands are not fully occupied. It is needed for non-conductors in case the initial calculations result in a (temporary) possible conducting state.

Lines 64 & 65: FMIXING adds the number specified as a %ge of the previous cycle results to smooth out the convergence in the calculation. In this case 50% of the previous values is averaged with the current values in the Fock or Kohn-Sham matrix.

Lines 66 & 67: number of cycles to calculate before giving up.

Lines 68 & 69: level shifting downwards of diagonal matrix elements in occupied orbitals, thus reducing coupling with the ”unoccupied” set, and hastening convergence. The shift is the specified number times 0.1 Hartree.

Lines 70 & 71: specifies the threshold, $10^{-specified\,number}\ Hartrees$ for convergence on total energy.

Line 72: end of input script.

4.2.2 Computation

The CRYSTAL06 programme **runcry06** uses this script to converge to an energy minimal solution of equation (4.4) as outlined in section 4.1. At successful completion it will have computed the energy, analytical gradient and wave function for the given geometry. It is not possible to illustrate a resulting Crystalline Orbital, which are generally complex functions, but here is what the squared modulus of one looks like profiled along a line the X-Z plane:

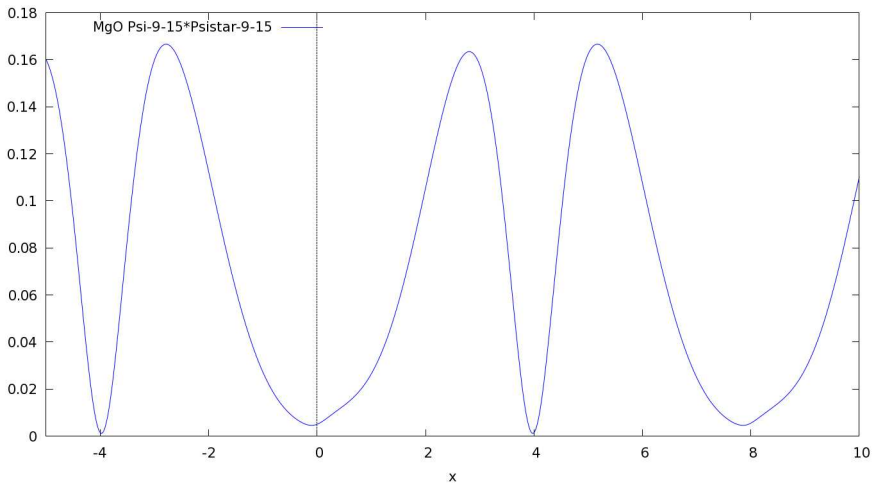

Figure 4.2: Output of **runcry06**. The squared modulus of the resulting CO for the 9th band (an occupied valence band) at the 15th **k** point is plotted along a line in the XZ plane. Notice that $\psi_9(x;15)\,\psi_9^*(x;15)$ is **not** zero at the crystal cell boundaries, at 0 bohr and 7.9558 bohr.

4.2.3 Calculating properties

The computation achieved by **runcry06** on a valid input script produces a wave function which is a best approximation to the true multi-electron wave function by a variational procedure using a Hartree-Fock or Kohn-Sham Hamiltonian. They are actually intrinsically antisymmetric products of one-electron wave functions obtained by calculating the Slater determinant of those one-electron wave functions. The density matrices obtained by squaring these functions are naturally the one-density matrices required to to calculate the properties of the system (see [8], page 11). The properties that CRYSTAL06 can calculate are known as one-electron properties and are many, including Mulliken population analysis, electronic charge density distribution and gradients of this, electrostatic potential and gradients, band structure and density of states.

This is achieved by running the programme **runprop06** on the output of **runcry06**. Again a script file is required - here is a typical script file for MGO:

```
PPAN
ECHG
0
200
COORDINA
-4. -4. 0.0
4. -4. 0.0
4. 4. 0.0
END
NEWK
6 12
1 0
BAND
MgO
4 8 60 1 18 1 0
0 0 0 4 0 4
4 0 4 4 2 6
4 2 6 4 4 4
4 4 4 0 0 0
NEWK
6 12
1 0
```

```
DOSS
2 200 7 14 1 12 0
-1 1
-1 2
NEWK
6 12
1 0
ANBD
0 0 .00004
END
```

This script produced the output in the following figure (overleaf) , together with the eigenvalues, including those used to calculate the graph in Figure 4.2.

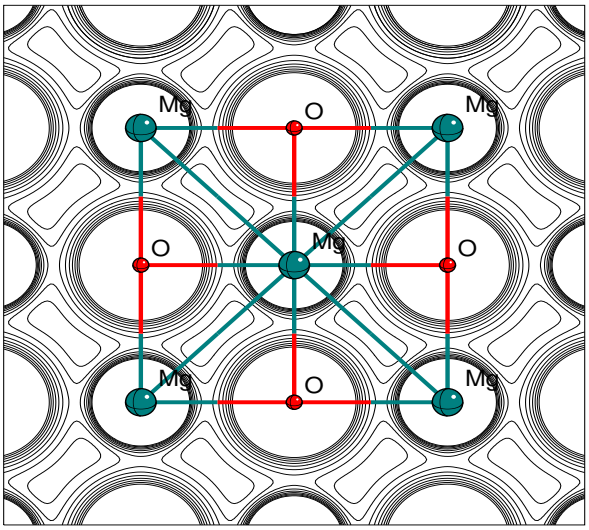

a

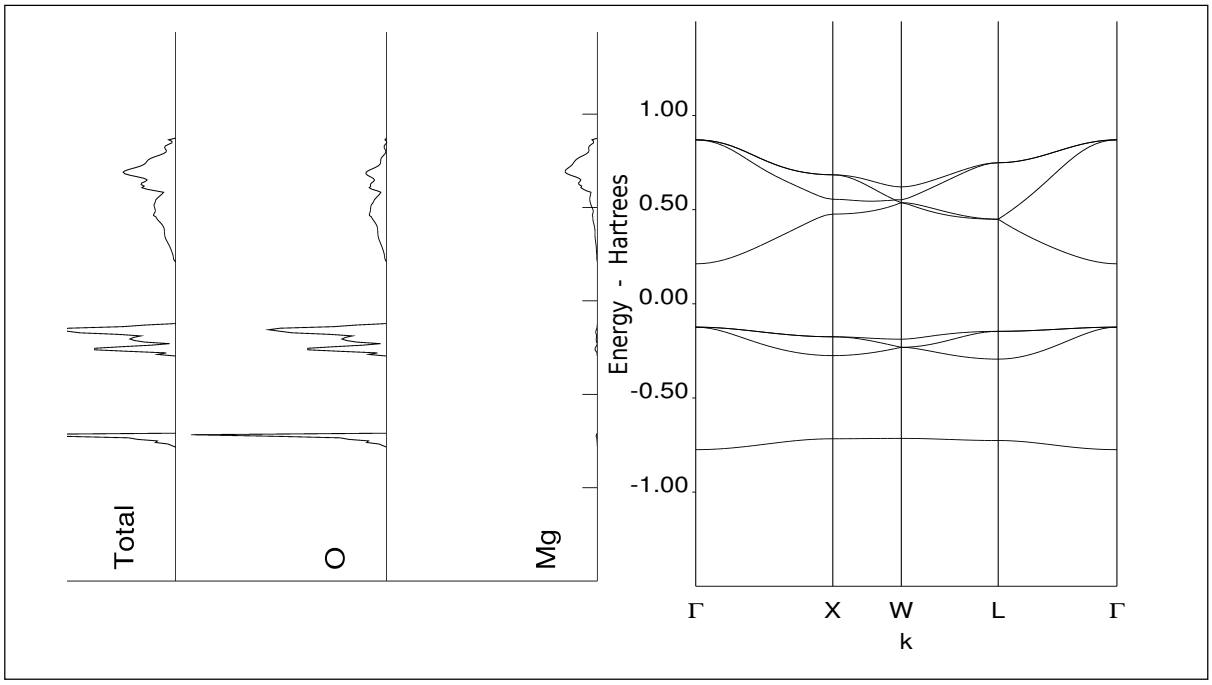

b c

Figure 4.3: Output of **runprop06** for MgO showing a) electronic charge density distribution in a (0 0 1) section, b) density of states, projected separately onto the O and Mg atoms and total, corresponding to c) the band structure.

Chapter 5

Chemical Bonds in perovskites

5.1 Introduction

Having reviewed the background theory and described the main computational tool, the principal ideas used in this study can now be developed.

The concept of a chemical bond is something of a work in progress. As recently as 2007 there was a special issue of The Journal of Computational Chemistry devoted to chemical bonding [92] in which no clear single definition can be found. Quoting Frenking and Crapp from a lead article: "A unicorn is a mystical animal whose appearance is known to everybody although nobody has ever seen one. .....There are many unicorns in the world of chemical bonding models carrying quite different names: resonance, conjugation, hyper-conjugation, frontier orbitals, covalent bonding, donor-acceptor bond, agnostic interactions, π bonding, to name just a few."

Bader points out that bonds as such don't exist except that within a molecule (or crystal) atoms are bonded because they are clustered together in an energy minimal configuration. He describes Bond Paths that are loci of *local* electron density maxima (London's bridges). Atoms are described by interfacing envelope surfaces that are surfaces of zero flux in the vector gradient field of the electron density. This formulation using continuum concepts is very suitable for working with tensor macroscopic qualities ("stress" , "strain" etc.) which sit oddly in the Schrödinger or Heisenberg pictures. The ideas of a chemical bond were formed before quantum mechanics or knowledge of the electron, and so were naturally in terms of macroscopic forces binding elemental atoms into compounds.

The 1916 paper by Lewis [85], introducing the idea of chemical bonding through atoms sharing electron pairs, was insightful, coming only six years after Rutherford had demonstrated the point-like localisation of the nucleus. Very broadly it is still the way to look at a compound, although it is not successful for metals. The theory has been successively updated with Valence

Bond and Molecular Orbital concepts both based on quantum mechanics. But in a review of the bond valence model in 1992 [93] Brown described limitations to the use of quantum mechanical calculations. “In particular they cannot shed light on the strains introduced by translational symmetry”. However by 2007, in the special issue of The Journal of Computational Chemistry referred to above, electronic density calculations from wave functions that were molecular orbitals derived from linear combinations of atomic orbitals were a routine tool in the analysis of chemical bonds in both molecules and crystals. Most recently, advances continue with Bader’s Atoms in Molecules concepts - now called the Quantum Theory of Atoms in Molecules and Crystals(QTAIMAC) [94].

The steric or geometric picture that atoms are spherical objects bound into molecules and stacked into crystals deserves to be deeply rooted in both chemistry and crystallography, particularly when such chemically researched atomic radii as those of Shannon and Prewitt [95] [24] are used, because such relevant features as bond lengths, bond angles, coordination number and crystal symmetry can be constructed and accord with experiment. Chemical properties such as oxidation state or Lewis acid strength are more or less overlaid on and constrained by the steric framework, via the mechanism of paired electron sharing. This picture suits a vast amount of inorganic chemistry and can be translated into the band theory of solid state physics [96].

A comprehensive review of current and emerging trends in conceptualising chemical bonding in crystals was provided by Gatti in 2005 [45]. Particular attention was paid to the application of QAIM to schemes of bond classification by way of topological characteristics of the electronic charge density distribution and bond visualisation by way of the Electron Localisation Function (ELF). The schemes of classification identify bonds as having open-shell or shared interactions (covalent, polar and metallic) or closed-shell interactions (ionic, hydrogen, and molecular) and relate functions (of varying complexity) of the local and integral values of the Laplacian of the electronic charge density distribution. ELF is an expression that relates the spherically averaged same spin conditional pair density at a location in the crystal to that of a uniform electron gas of the same density.

The Bader view, incorporated in QTAIMAC and adopted in this thesis, - that a bond path is an observable criterion for the bonding between the atoms it links, as opposed to the hazier view that there is an object or entity that can be called a chemical bond which will affect the observable properties of the molecule (or crystal) - has been controversial.

This is particularly the case for closed shell pair-wise interactions such as those between the Hydrogens in Lithium Hydride crystals or at the “ends of” molecules such as Phenanthrene. Key contributions are to be found in Bader, 1998 [97], Gatti, 2005 [45] pp. 405 - 407, Grimme et al., 2009 [98] and Bader, 2009 [9] and references within [9]. According to [45], use of the bond

path as a universal indicator of bonding in crystals often causes bewilderment, if not discomfort, amongst structural chemists.

Grimme et al. was the most recent attack on the bond path concept. It reported a neat experiment that partly substituted Deuterium for Hydrogen in Phenanthrene (**1**). Quoting them: ‘

> Opening paragraph:
>
> “The concept of chemical bonding is fundamental to natural science.[1] Despite its importance, a precise and unambiguous definition of when a chemical bond exists between (usually two) atoms is difficult. For diatomic and small molecules energetic (thermochemical) criteria are sufficient, but for polyatomic systems, the problem prevails although exper- imental data, for example from vibrational spectroscopy (bond force constants), can be related to bonding. The other approach is based entirely on theory in the context of ab initio schemes derived from wave function and electron density calculations. Although these methods have advanced extra- ordinarily in recent years,[2] the theoretical definition of bonding is still problematic. The simple reason is that no quantum mechanical bond operator exists that would provide the desired answer, for example, as a conventional expectation value. In any case one basic assumption of the present work (that is likely shared by many chemists and physicists) is that the existence of a chemical bond must be related to some observable; in other words, chemical bonding must have an effect on measurable properties of the system. Any definition of bonding that has no real consequences is meaningless in our opinion and must be abandoned. .....
>
> As a solution to the problem we propose selective isotopic substitution of the hydrogen atoms H-C4 and H-C5 by deuterium. The C-D and the C-H vibrations are completely separated simply by a change in the vibrating masses, but the electron density and electronic structure remain unchanged (within the usual BornOppenheimer approximation).”

concluding paragraphs:

> “We therefore conducted a detailed study of the various contributions (H-H electrostatic interactions, H-H van der Waals bonding, C-C through-bond coupling) to the coupling force constant k at the force field level. This provides a convenient way for separating the potential into chemically meaningful parts. Based on the MM3 force

field (for details see the Supporting Information) we conclude that the major contribution to the coupling comes from a typical van der Waals interaction between the hydrogen atoms. Other terms like through-bond coupling due to C-C-C stretching/bending deformations account only for about $3cm^{-1}$ of the splitting. And very importantly: as expected, an artificial change of the H-H potential in the direction of attraction in the equilibrium structure of **1** leads to a calculated inverted ASS splitting, which is in disagreement with experimental observation. .....

In conclusion, the presented results indicate that there is no need to rewrite chemical textbooks. The existence of a BCP is neither a necessary nor a sufficient condition for a sensible definition of a chemical bond. BCPs might arise just for topological reasons by addition of atomic electron densities as already pointed out by Cioslowski and Mixon.[12] The resulting energy changes are well-defined in AIM but represent only local quantities that must need not be interpreted in a conventional sense as bond energies. Our results are in complete agreement with the traditional view of this HH interaction as steric (Pauli) repulsion. .....

As long as no conclusive experimental evidence for their reality is presented, we suggest to abandon the use of the term hydrogenhydrogen bonding in cases where molecules or their fragments approach closely and are subjected to conventional van der Waals interactions. Intramolecular closed-shell interactions in organic and many main-group-element molecules should be interpreted in a more conventional way, and all theoretical energy partitioning schemes should be applied with great care."

It seems that, although they avoid defining a bond, they identify a bond with the "bond spring" that can be determined from oscillatory modes. They mistakenly assume that the kinetic energy that is associated with the electronic charge density within region of the bond path would represent the bond energy (whose spatial derivative would be the "bond spring") thereby ignoring all the non-local contributions.

In [9] Bader refutes the above conclusions. In the earlier review paper Gatti [45] had reconciled the Bader concepts with the problems perceived by structural chemists and it is difficult to see what motivated Grimme et al. to see the Bader paradigm as rewriting chemical textbooks, when Bader all the time made it clear (and Gatti further clarified) that he was adding to, not altering, the Lewis concept.

This issue is important to the concepts and modelling presented in Section 5.4, where the author develops a model of just that pairwise component that the localised kinetic energy represents.

For the purposes of background to Section 5.4 two more points:

1. Gatti's Paragraph **A** on page 406 of [45] (in agreement with Bader) points out that the crystal is at electrostatic equilibrium and the Hellmann-Feynman forces acting on each nucleus must necessarily be zero and that an attractive restoring force is created from the electronic charge density when the nuclei are displaced from equilibrium. To complete this picture it should be noted that crystals in equilibrium possess a net positive charge, evidenced by the work function; and that if the nuclear displacement from equilibrium is compressive, the restoring force is repulsive, created partly from kinetic energy increase - so-called degeneracy pressure - amongst the intervening electrons.

2. Bader, in [97], notes that: "In a sense, the inter-atomic surface replaces the bond in the theory of atoms in molecules, since it is through the exchange of electrons and the fluxes in properties across this surface described by the physics of a proper open system that atoms adjust to the presence of their bonded neighbors."

5.1.1 Degree of Covalency

From the earliest studies of perovskites it has been stated that covalency or "covalent forces" related to overlap were involved, e.g. [62], pp 175-176. Chemical bonding in terms of electron sharing is a simple concept for the end-point cases - the equal sharing as in a hydrogen bond or total appropriation as in an ionic bond. In most bonds which have some ionic and some covalent character a fractional amount of electronic charge is "shared". This is interpreted as a the time average and so fits in with the statistical nature of quantum mechanics. In the systematic studies reported in Appendix A, the density of states (DOS) diagrams will reveal a small degree of contribution from one or both cations at the same energy as the oxygen anion in several parts of the valence band. Dovesi, in [68], p44, points out that "this "mixing" is a clear indication of a covalent interaction". This effect is an expression of the overlap or "hybridisation" or resonance of separate electronic wave functions contributing to the various crystalline orbitals, but its quantification from DOS considerations is compromised by the inexact character of the Mulliken scheme used to derive the DOS. The author believes that the electron charge density picture - the Bader picture - suggests a more satisfactory approach to understanding and quantifying partial covalency.

5.2 Qualitative and Quantitative expression of bonding in crystals

Many graphical devices and numerical schemes are employed to illustrate and characterise bonds in molecules and crystals. The following summary touches only on those used in this thesis. These

tend to be more graphical than numerical and display bonding regions but do not provide a simple quantitative expression of pairwise bond strengths. Such an expression would help explain the distortions that occur in the cooler perovskite phases which never the less retain the corner connected octahedral cages. The author proposes a *Bridge Index* as a simple single number that represents the pairwise bond strength and is an ordinal indicator of the decree of covalency between Bader atoms in a crystal.

5.2.1 Mulliken Analysis

According to Patricia Hunt “The Mulliken analysis is the most common population analysis method, it is also one of the worst and is used only because it is one of the oldest and simplest” [99]. Never the less it comes with the CRYSTAL06 package at no extra charge, and is used internally in that package to derive the DOS projections (see below). The author has found the Mulliken population analysis to be of help as a guide to interpreting results.

The following two outputs for Diamond and Sodium Chloride show that degrees of ionicity (difference in atomic number and charge) and covalency (overlap population between neighbours) are at least qualitatively representative.

Diamond

```
    ALPHA+BETA ELECTRONS
MULLIKEN POPULATION ANALYSIS - NO. OF ELECTRONS   12.000000

 ATOM    Z CHARGE  A.O. POPULATION

  1 C    6  6.000  1.996  0.345  0.550  0.550  0.550  1.001  0.318  0.318
                   0.318  0.006  0.014  0.014  0.006  0.014
  2 C    6  6.000  1.996  0.345  0.550  0.550  0.550  1.001  0.318  0.318
                   0.318  0.006  0.014  0.014  0.006  0.014

 ATOM    Z CHARGE  SHELL POPULATION

  1 C    6  6.000  1.996  1.994  1.956  0.053
  2 C    6  6.000  1.996  1.994  1.956  0.053

OVERLAP POPULATION CONDENSED TO ATOMS FOR FIRST   6 NEIGHBORS

ATOM A   1 C    ATOM B     CELL      R(AB)/AU R(AB)/ANG    OVPOP(AB)
                 2 C    (  0  0  0)     2.919     1.545     0.338
                 1 C    ( -1  0  0)     4.766     2.522    -0.059
                 2 C    (  1  0 -1)     5.589     2.958    -0.007
                 1 C    ( -1 -1  1)     6.741     3.567     0.001
                 2 C    ( -1  0  0)     7.345     3.887     0.003
                 1 C    ( -2  0  1)     8.256     4.369     0.000
```

NaCl

```
    ALPHA+BETA ELECTRONS
MULLIKEN POPULATION ANALYSIS - NO. OF ELECTRONS   28.000000

 ATOM    Z CHARGE  A.O. POPULATION

  1 NA  11 10.035  1.999  1.382  1.590  1.590  1.590  0.547  0.325  0.325
                   0.325  0.088  0.090  0.090  0.090
  2 CL  17 17.965  1.999  1.946  2.030  2.030  2.030  0.388  0.509  0.509
                   0.509  1.189  0.787  0.787  0.787  0.484  0.660  0.660
                   0.660

 ATOM    Z CHARGE  SHELL POPULATION

  1 NA  11 10.035  1.999  6.154  1.523  0.359
  2 CL  17 17.965  1.999  8.036  1.914  3.550  2.465

OVERLAP POPULATION CONDENSED TO ATOMS FOR FIRST   6 NEIGHBORS

ATOM A   1 NA   ATOM B     CELL      R(AB)/AU R(AB)/ANG    OVPOP(AB)
                 2 CL   ( -1  0  0)     5.390     2.852     0.000
                 1 NA   ( -1  0  0)     7.623     4.034     0.000
                 2 CL   (  0  0  0)     9.337     4.941     0.000
                 1 NA   ( -1 -1  1)    10.781     5.705     0.000
                 2 CL   (  1  0 -1)    12.053     6.378     0.000
                 1 NA   ( -2  0  1)    13.204     6.987     0.000

ATOM A   2 CL   ATOM B     CELL      R(AB)/AU R(AB)/ANG    OVPOP(AB)
                 1 NA   (  1  0  0)     5.390     2.852     0.000
                 2 CL   ( -1  0  0)     7.623     4.034    -0.002
                 1 NA   (  0  0  0)     9.337     4.941     0.000
                 2 CL   ( -1 -1  1)    10.781     5.705     0.000
                 1 NA   ( -1  0  1)    12.053     6.378     0.000
                 2 CL   ( -2  0  1)    13.204     6.987     0.000
```

5.2.2 Projected Density of States

This is a graphical expression in k-space of states per hartree per volume of k-space and is usually plotted to accompany the plot of band structure. It suffers the shortcomings of Mulliken analysis, on which it is based in CRYSTAL06, and in that application the Crgraph-2006 package outputs an arbitrary, though scalable, energy scale. Despite these, the author has found this process invaluable in gleaning even small indications of covalency. The DFT calculations are valid for the ground state only, and no notice should be taken of the output for bands above the top of the valence bands which is taken as the Fermi level in insulators.

The following diagrams illustrate its use, in the highly covalent Boron Nitride, to be compared with the highly ionic Sodium Chloride.

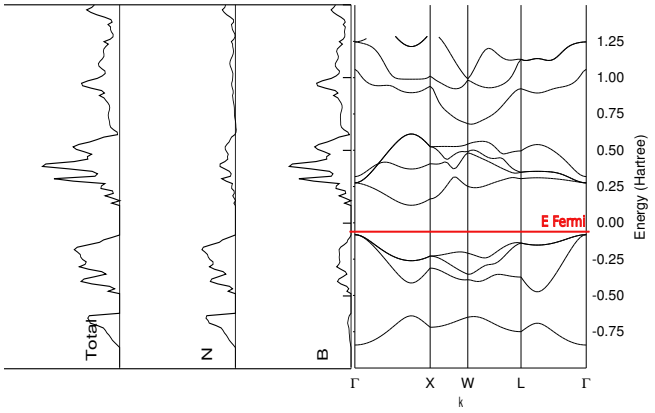

Figure 5.1: Projected density of states and band strucure of cubic Boron Nitride. Note that the atomic projections coincide, particularly in the upper three occupied bands, indicative of the strong covalency. No heed should be paid to the virtual bands above the Fermi level.

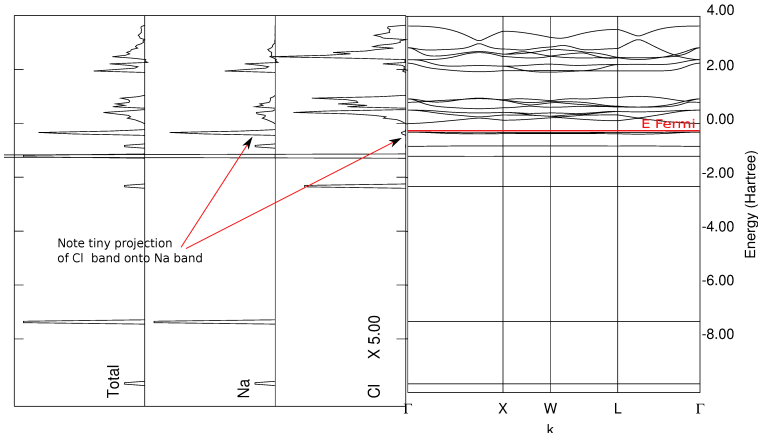

Figure 5.2: Projected density of states and band strucure of cubic Sodium Chloride. The occupied bands are flat, expected for closed shell ions, and the atomic projections are quite separate, so there is almost no covalency - except for the very small chloride presence in the uppermost band. The Cl projections required 5x magnification to reveal this, but it is responsible for the London's bridge effect seen in figure 2.9. No heed should be paid to the virtual bands above the Fermi level.

5.2.3 The Lapalacian of the Electronic Charge Density $L(r)$

The negative of the Laplacian, $\mathbf{L}(\mathbf{r}) = -\nabla^2\rho(\mathbf{r}) = -\nabla\cdot\nabla\rho(\mathbf{r}) = -\left[\frac{\partial^2\rho}{\partial x^2} + \frac{\partial^2\rho}{\partial y^2} + \frac{\partial^2\rho}{\partial z^2}\right]$, is in effect a scalar second derivative and has its own topology and critical points. It has a great virtue when the original scalar field is monotonically, though not uniformly, decreasing from a central maximum: $\mathbf{L}(\mathbf{r})$ highlights subtle local concentrations - nicely illustrated on page 254 of [8], chapter 7. In this chapter Bader discusses this topology and its relationship to the valence shell electron repulsion (VSEPR) model of Gillespie and Nyholm [100] [101] [1].

Referring back to Figure 3.12 on page 73, the shaded area is a cross-section of an annular region within the outer shell that has local (i.e. within the annulus) maximal and minimal values in electronic charge density. It turns out that the maxima provide a one-to-one mapping of the electron mapping of the electron pairs (both bonded and non-bonded) of the Lewis model.

Popelier [102] and Malcom and Popelier [103] have advanced Bader's work, presenting full graphs for the charge concentration and depletion in $\mathbf{L}(\mathbf{r})$ whereas previous studies of the Laplacian had concentrated on the location of the critical points.

This thesis has not pursued this "topology of a topology" approach because it is seeking answers more directly connected to the original scalar data - the electronic charge density distribution.

The following pages illustrate successively more complicated examples of the Laplacian of this distribution in crystalline materials, as calculated by the author from the CRYSTAL06 output. Note that the positive Laplacian, *not* $\mathbf{L}(\mathbf{r})$ has been mapped. Maps of the electronic charge density distribution have been superimposed over the contours to identify the atoms. Only the negative contours have been plotted in order show what Bader identified as the Bond regions of increased charge density. The case of the diamond $\mathrm{C}\dot{-}\mathrm{C}$ bond region is clear cut, but the successively complex $\mathrm{Ti} - \mathrm{O}$ bonds in orthorhombic $\mathrm{CaTiO_3}$ and tetragonal $\mathrm{PbTiO_3}$ seem less localised.

[1] Bader and Gillespie were colleagues at McMaster University for many years

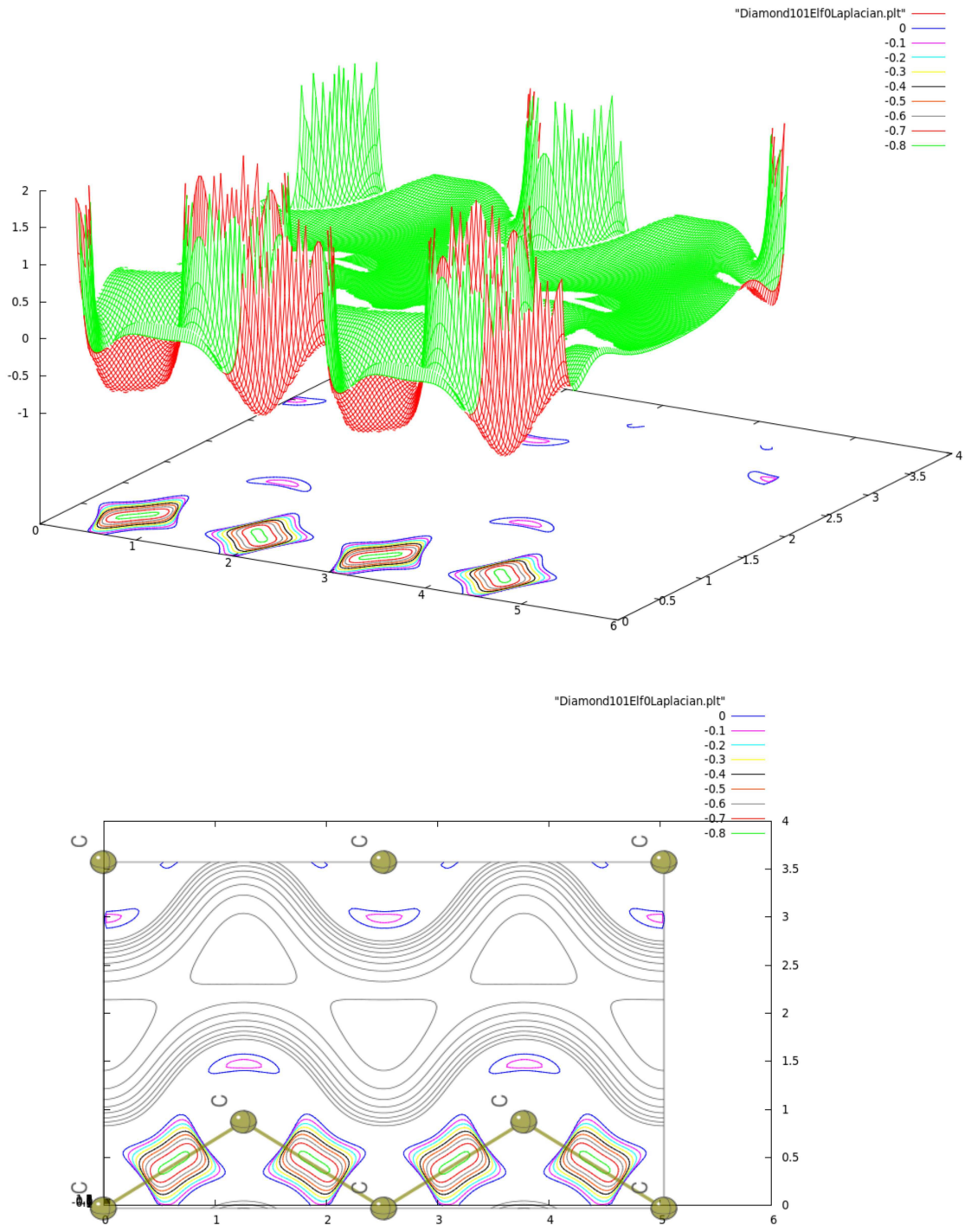

Figure 5.3: Laplacian Diamond (1 0 1) plots

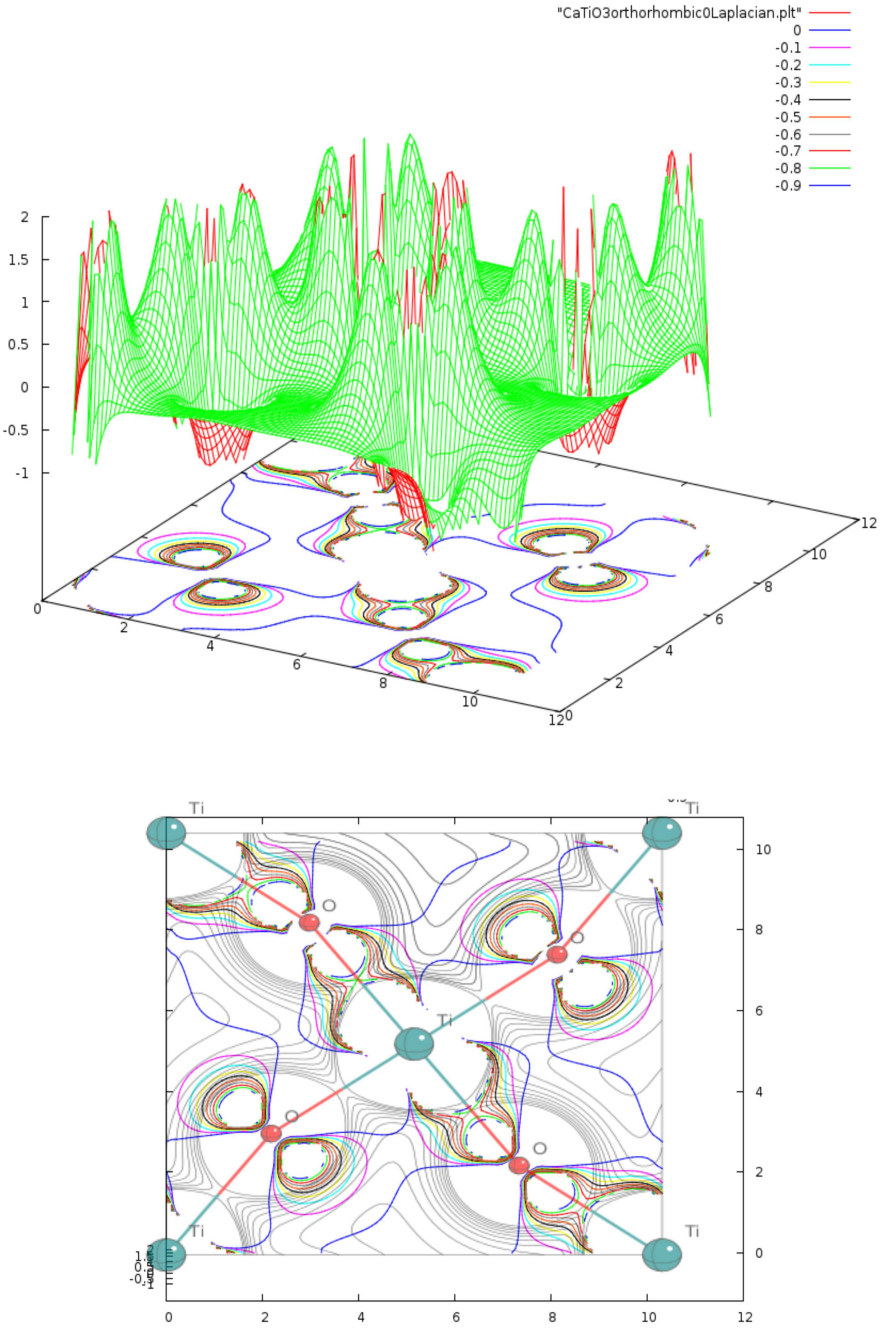

Figure 5.4: Laplacian $CaTiO_3$ orthorhombic plots

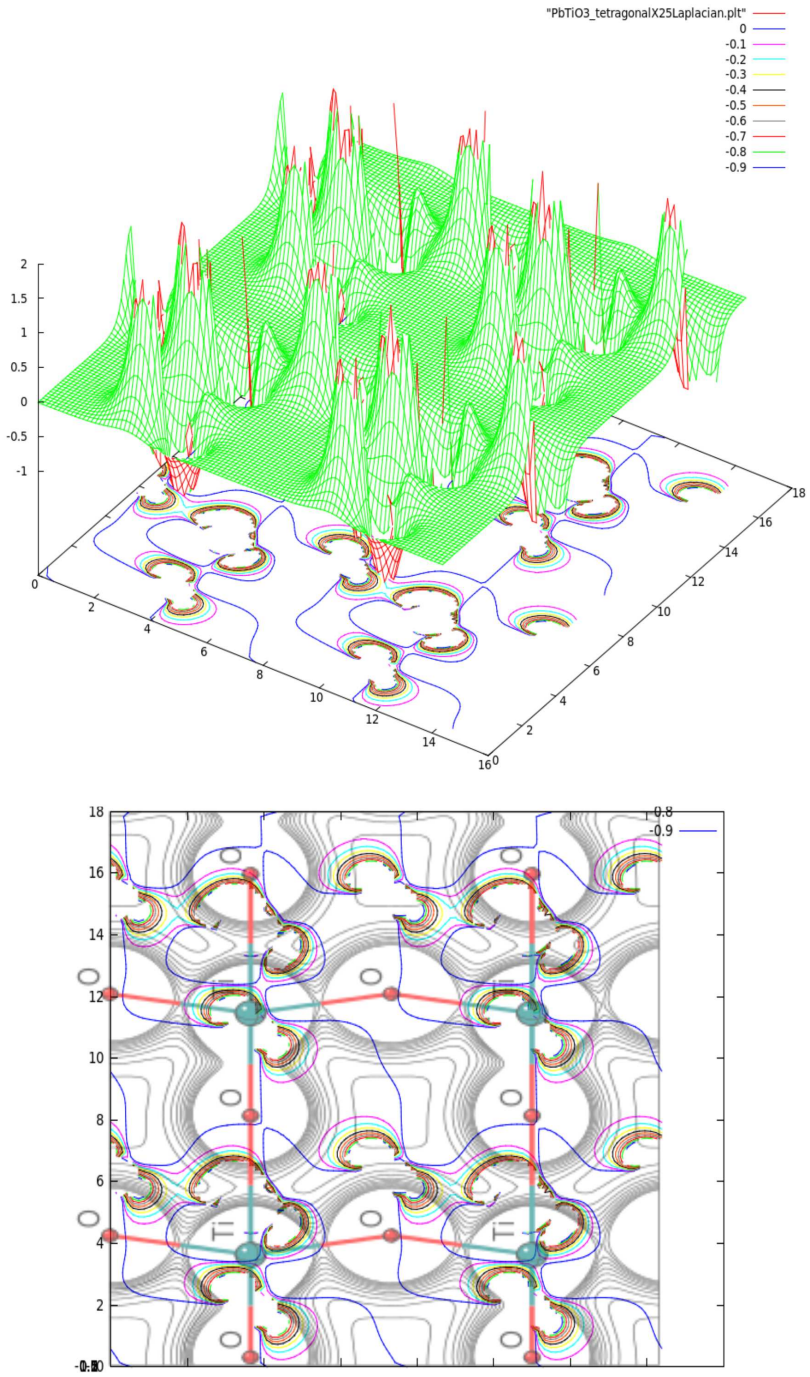

Figure 5.5: Laplacian $PbTiO_3$ tetragonal plots

5.2.4 The Electron Localisation Function ELF

As explained by Savin et al. [104], the electron localization function (ELF) was introduced by Becke and Edgecombe as a measure of the probability of finding an electron in the neighborhood of another electron with the same spin. ELF is thus a measure of the Pauli repulsion. The explicit formulation was initially given in terms of the spherically averaged electron pair density from the Hartree-Fock formulation in comparison with that in a homogeneous electron gas. Savin et al. adopted ELF to a local density functional (Kohn and Sham) formulation and applied it to solids for the first time.

The ELF values lie by definition between zero and one. Values are close to 1 when, in the vicinity of one electron, no other with the same spin may be found, for instance as occurs in bonding pairs or lone pairs. Small values are typical for the region between two electron shells (Pauli principle). In a homogeneous electron gas, ELF = 0.5.

It was mentioned in chapter 3, ELF gained favour over the Laplacian as a representation of the (VSEPR) model, and also it maps more than four core orbitals faithfully, which the Laplacian does not. Like the Laplacian it is a scalar function of position within the crystal or molecule hence possesses a topology. As with the Laplacian, the topology of the ELF has become much studied, yielding considerable additional structural information [105] [106] [87] [107].

ELF calculations for crystals are usually displayed as colour-coded or contoured maps. The following pages illustrate successively more complicated examples of the ELF in crystalline materials, as calculated by the author from the CRYSTAL06 output. Maps of the electronic charge density distribution have been superimposed over the contours to identify the atoms. The case of the diamond $\mathrm{C}\dot{-}\mathrm{C}$ bond region is clear cut, but the successively complex $\mathrm{Ti}-\mathrm{O}$ bonds in orthorhombic $\mathrm{CaTiO_3}$ and tetragonal $\mathrm{PbTiO_3}$ have become complex and seem difficult to interpret.

However when viewed carefully in conjunction with a profile the complexity is revealed to be a demonstration of how informative the ELF can be. Figure 5.9 is a profile plot from tetragonal $\mathrm{PbTiO_3}$ running $part\,\mathrm{O}{-}short-bond-\mathrm{Ti}{-}long-bond-\mathrm{O}{-}short-bond-part\,\mathrm{Ti}$. It displays the electronic charge density profile in red and the ELF values in green. It will be seen how narrow the high ELF value zone is in the bond region. As can be seen on the surface plot this is zone is like a crescent shaped ridge that wraps partly around the Ti atom. Also it is revealed that the outer shells of the Titanium atom are re-localised out of the plane of section. These warpings of the shell strucure are interpreted to be due to collective electrons from the Pb atom contributing to the bonding effects. These profiles are rather coarse grained due to computer constraints, and one should keep in mind Tsirelson's note that "Kirzhnits approximation provides a compromise solution giving an acceptable local behaviour of the approximate ELF over all the position space

excluding small areas surrounding the nuclei.”

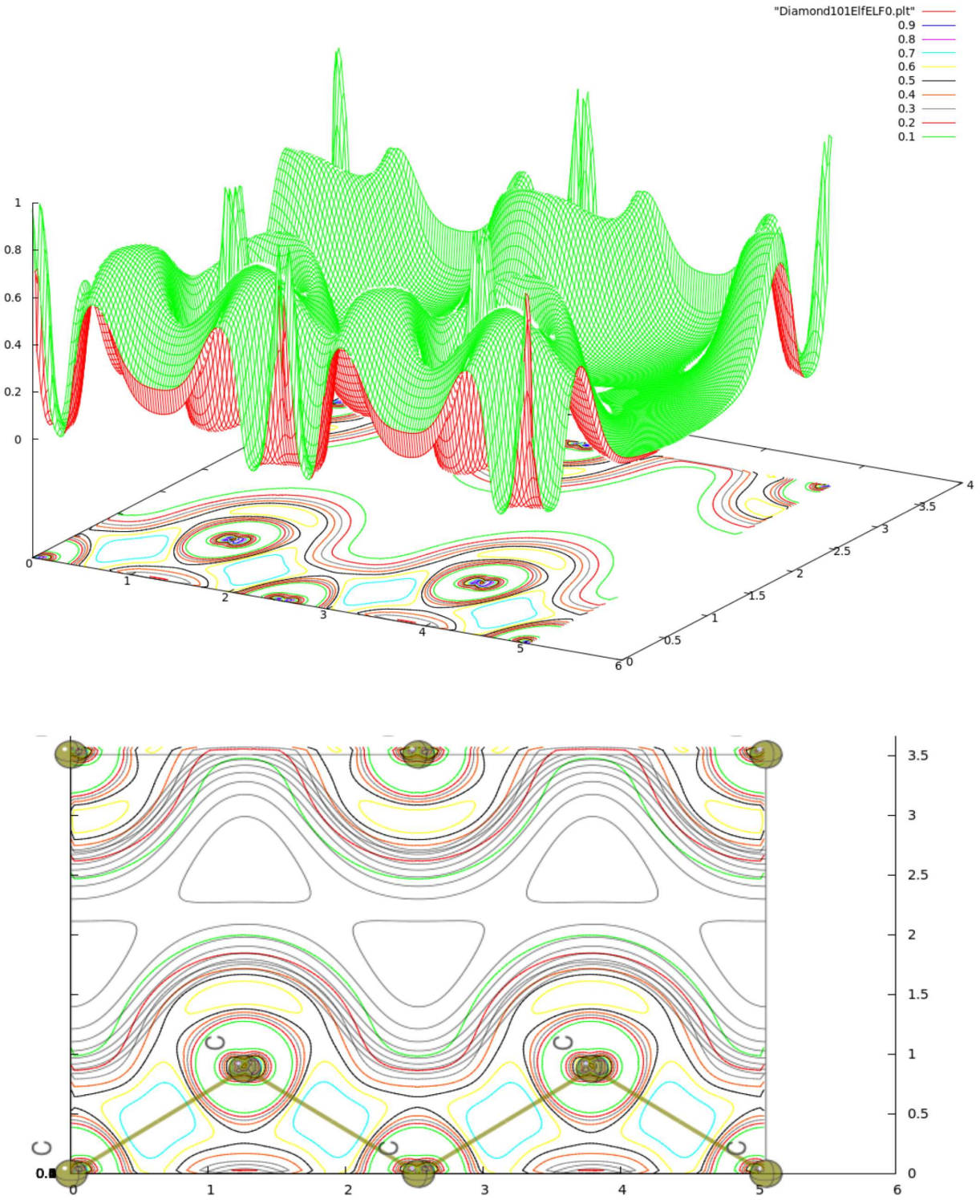

Figure 5.6: ELF Diamond (1 0 1) plots

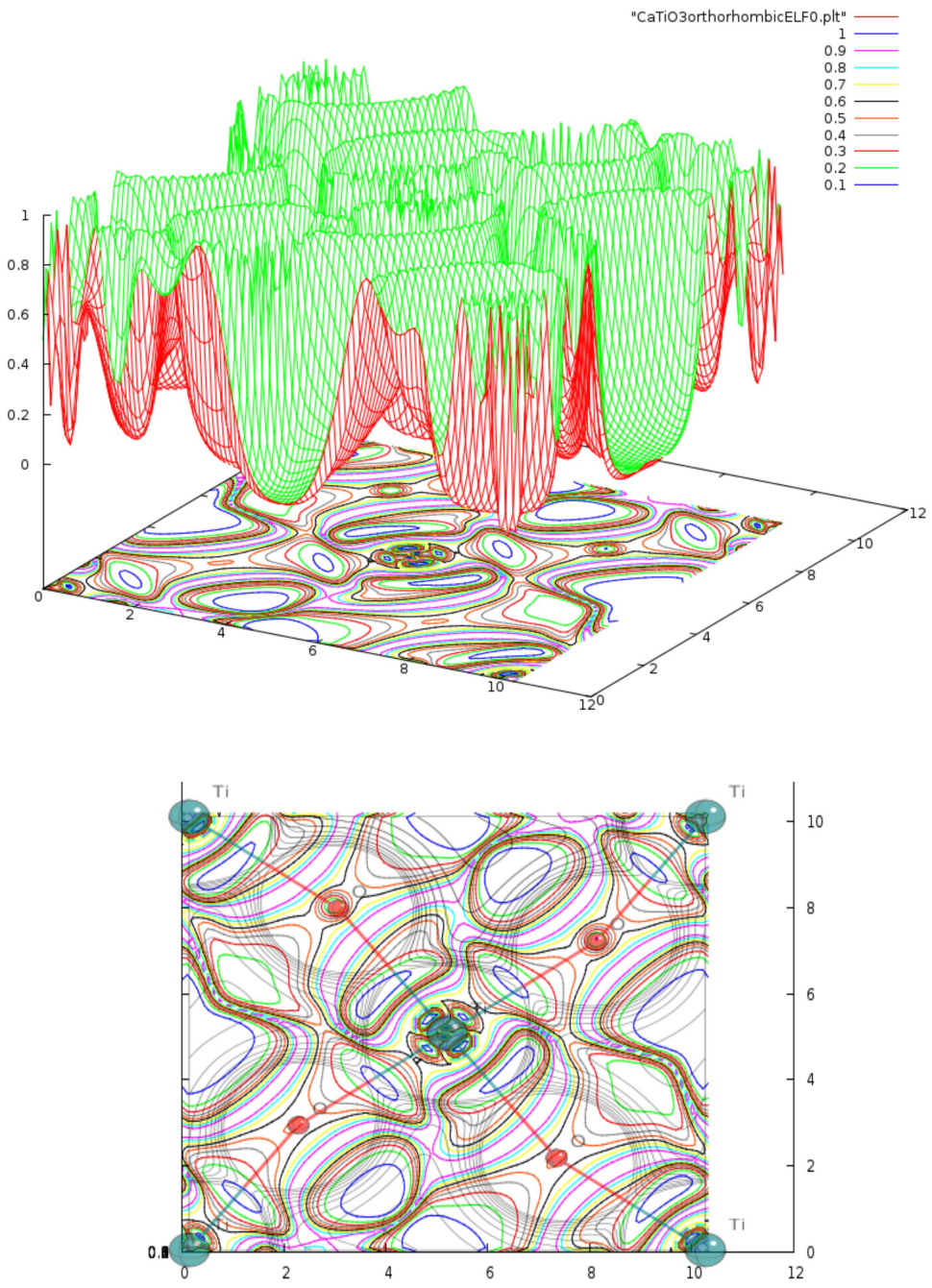

Figure 5.7: ELF $CaTiO_3$ orthorhombic plots

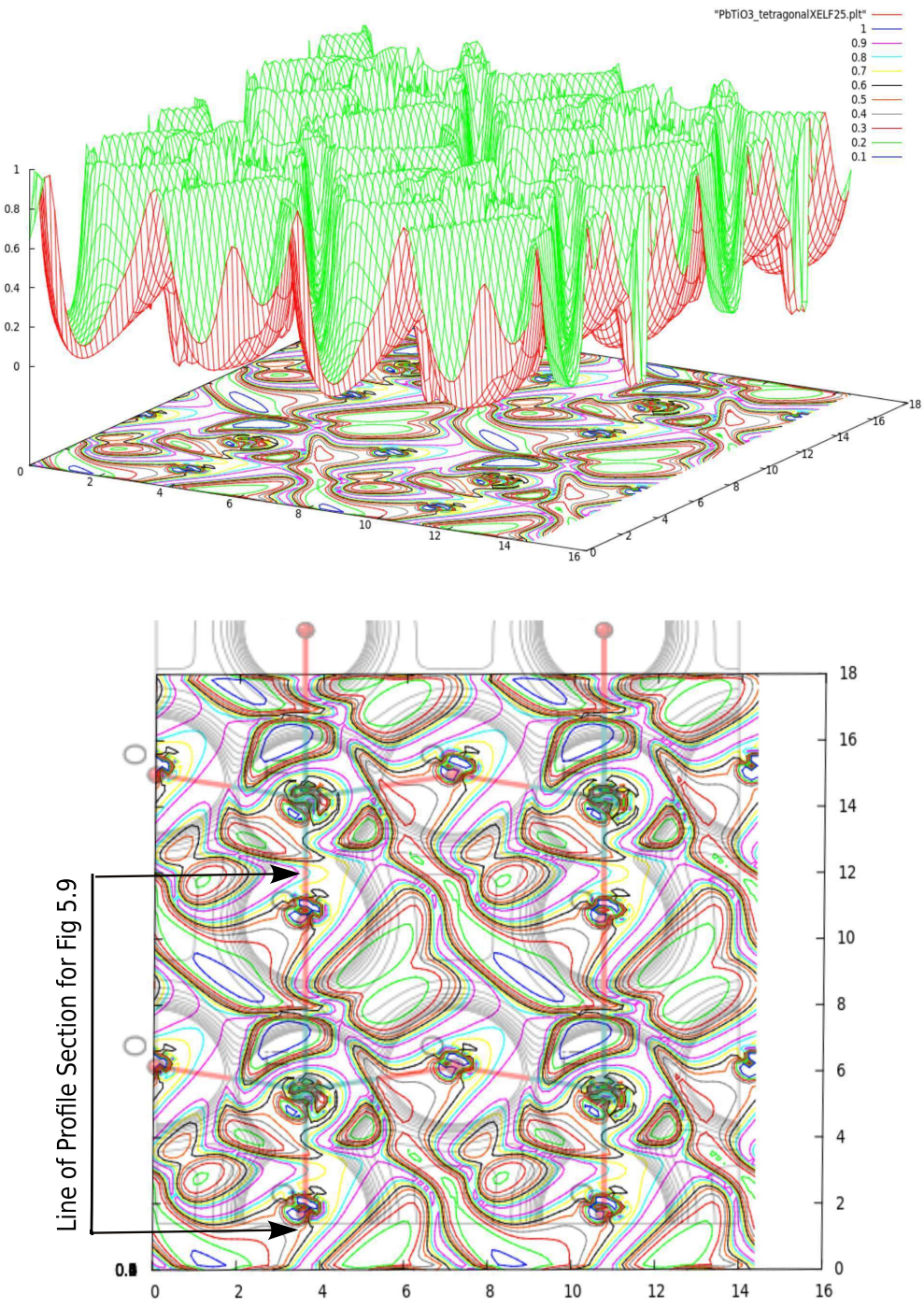

Figure 5.8: ELF $PbTiO_3$ tetragonal plots

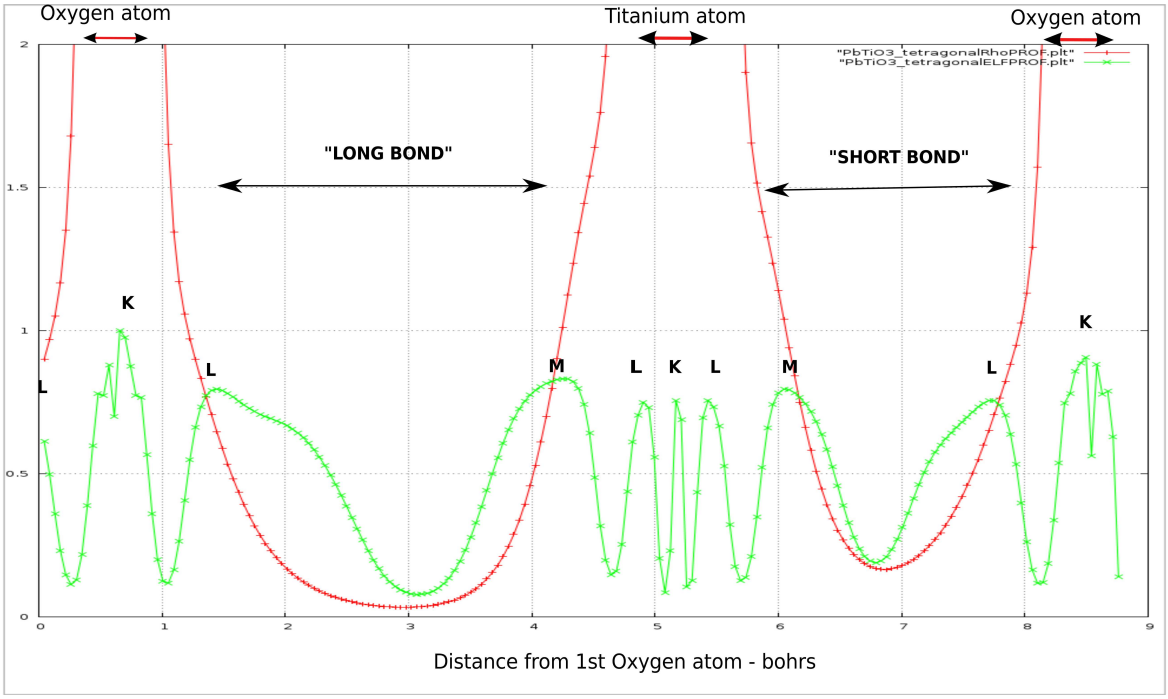

Figure 5.9: Electronic charge density (red) and ELF profiles (green) $PbTiO_3$ tetragonal

Figure 5.9 is a reminder that even the most deformed oxide perovskite is a highly ionic material.

5.2.5 The localized-orbital locator LOL

Introduced by Schmider and Becke [108] in 2000, - selectively quoting them:

> "the localized orbital locator (LOL) is based on the dimensionless variable $t_\sigma = \tau_\sigma^{LSDA}/\tau_\sigma^{exact}$ dependent on local kinetic energy densities τ.
>
> The numerator is the local spin density approximation:
>
> $\tau_\sigma^{LSDA} = \frac{3}{5}(6\pi^2)^{\frac{2}{3}}\rho_\sigma^{\frac{5}{3}}$
>
> and the denominator is the positive definite, non-inter- acting Kohn-Sham kinetic energy density:
>
> $\tau_\sigma^{exact} = \sum_i |\nabla\psi_{i\sigma}|^2$.
>
> The range of τ_σ is semi-infinite: $0 \leq \tau_\sigma \leq \infty$ For plotting purposes, it is preferable to transform to the infinite variable ν_σ
>
> $\nu_\sigma = \tau_\sigma/(1+\tau_\sigma)$
>
> with range
>
> $0 \leq \nu_\sigma \leq 1$.
>
> clearly displays the locations of the classic VSEPR electronic groups. Atomic shells are clearly delineated, as are bonding electron pairs with their expected s and

p shapes, and lone pairs as well. The chemical content in ts and vs is similar to that of the electron localization function (ELF) of Becke and Edgecombe [3]. ELF is also dependent on the kinetic energy density, but its mode of operation is founded on consideration of electron pair density. LOL, on the other hand, simply recognizes that gradients of localized orbitals are maximized when localized orbitals overlap. Moreover, LOL is a simpler function than ELF and generates somewhat cleaner plots (i.e. ELF does not always vanish asymptotically, depending on the degeneracy of the HOMO energy, whereas LOL always does)."

The following profiles of diamond and NaCl compare ELF and LOL. For this thesis only ELF has been employed.

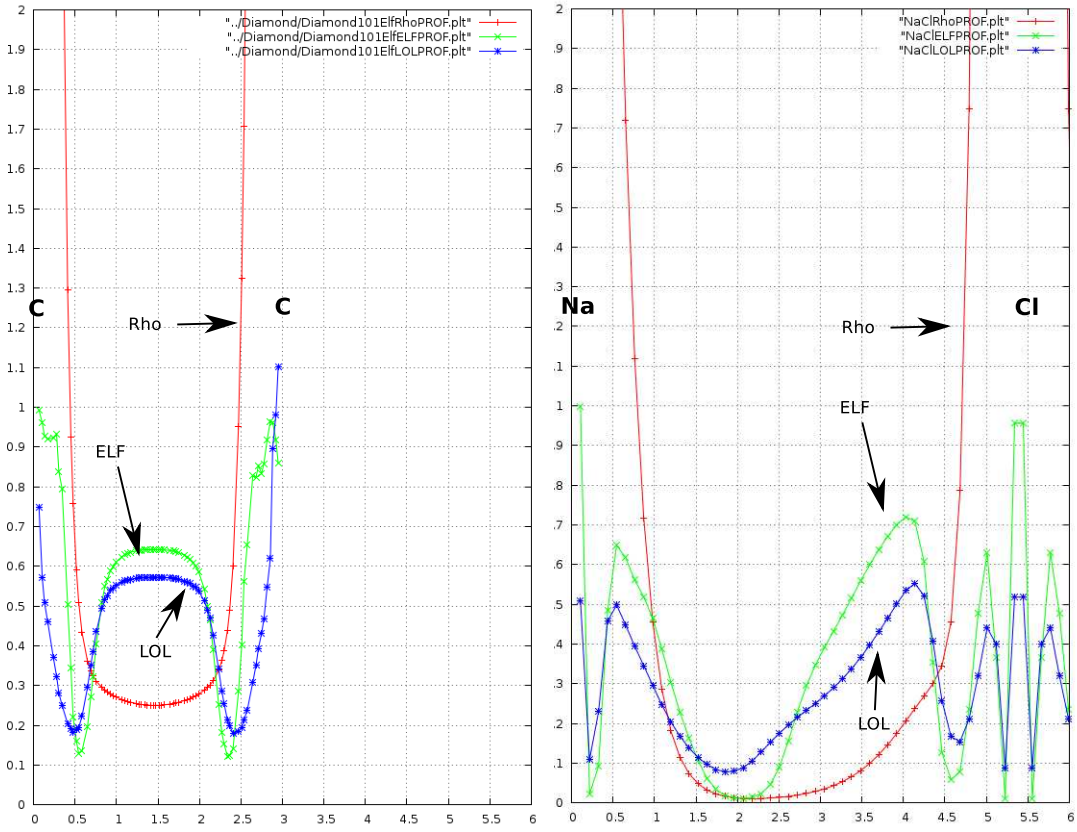

Figure 5.10: Electronic charge density (red), ELF (green) and LOL profiles (blue) for Diamond and NaCl. The author believes that ELF characterises ionic and covalent "shapes" better than LOL.

5.3 Towards a simple numerical index - the Bridge Index

The expressions of bonding in crystals reviewed above, especially studies of the topology of the ELF in molecules and crystals, have become important in the understanding of chemical structure but the author looked for a simpler expression of the effects that he was trying to understand. Some hours of computer time requiring tedious manual preparation and interaction can be involved in preparing a 3D grid such as those from which the above illustrative diagrams were extracted. The author believes that a quantitative expression of the *pair-wise interaction between each pair of Bader Atoms that were bonded in the sense that Bader proposed. [9]* can be derived in minutes or, in some cases, seconds.

Quoting Bader

> **"Interacting Atoms Are Bonded to One Another.** The presence of a bond path linking a pair of atoms fulfills the sufficient and necessary conditions that the atoms are bonded to one another. This definition transcends all bonding schemes and categories and provides a unified physical understanding of atomic interactions. It is based upon the theorems of quantum mechanics that govern the interactions between atoms. There are only two forces operative in chemistry, the Feynman force exerted on the nuclei and the Ehrenfest force exerted on the electrons. The virial theorem relates the virial of the Ehrenfest force to the kinetic energy of the electrons, the virial including a contribution from the virial of the Feynman forces acting on the nuclei. Thus, through the Ehrenfest and Feynman theorems, one has the tools that are needed to describe the forces acting in any system and, through the virial theorem, to relate these forces to the systems energy and its potential and kinetic contributions. This is the physics underlying all bonded interactions, and when combined with the properties of the electron and energy densities at a bond critical point, it provides one with a classification scheme that establishes trends and the distinguishing features of atomic interactions over the entire spectrum of bonding."

This is not so simple from a DFT approach, because the Ehrenfest force exerted on the electrons includes exchange and correlation components that are not directly recoverable from the electronic charge density distribution - so the energy densities at a bond critical point are not available from the local electron density. Also the author believes that it is the *strength*, the spatial derivative of the pairwise force, that is important in comparing bonds. The strength attributable just to the pair-wise interaction of two adjoining Bader atoms can be represented, at least ordinally, by a numerical index, now defined as the Bridge Index (BI), formed by dividing the Electronic

Charge Density at the Bond Critical Point by the length of the inter-nuclear bond path. This could be normalised by multiplying by 80.6 so that the BI of diamond is 10; but in the computations for this thesis the author has left it in atomic units. The justification for this index is:

i. along the bond paths outside the core orbitals (i.e. in the valence region around the BCP - within London's Bridge) electronic charge density is higher than it is at nearby points not on the bond path. Therefore the region of the BCP must be the source of the local *pairwise* "covalent" augmentation of the ionic and long range net-attractive forces between nuclei. Moreover, the balancing Pauli repulsive forces, being a function of charge density, will also be most significant in the region of the BCP. The electronic charge density at the BCP is thus a significant parameter.

ii. the other significant pairwise parameter is the separation between the nuclei - the bond length. The balancing attractive and repulsive forces are both inversely related to this: one because of the inverse square relationship, the other because the density of the electronic population giving rise to Pauli exclusion is increased if this parameter decreases. It is proposed that combining these parameters by dividing the electronic charge density at the BCP by the nuclear separation will provide a numerical index that is an enhanced discriminant for highlighting differences between bonds and which bears some relationship to the bond strength.

iii. the BI as defined here is proposed to be both an index of the degree of covalency and an index of bond strength, as will be seen when some calculations are carried out. It has as its nearest counterpart in the literature Miedema's n_{ws} - the parameter representing the electronic charge density at the boundary of the Wigner-Seitz cell [109] - but the incorporation of the bond length amplifies the discrimination and makes the index dimensionally equivalent to the properties that it is intended to proxy - see following section.

In the materials studied the Bond Paths were straight lines between nuclei.

5.3.1 Dimensional considerations

To explain item iii. above:

Bader demonstrated that the charge density integrated over the interface surface divided by the squared nuclear separation was proportional to the pairwise bonding energy for various weakly ionic bonds [8], section 6.5.2 . To do this he employed the operator r^2, $\mathbf{r}$ being the displacement of a point (which possesses local charge density) from the nucleus. He inserted the commutator of $\hat{\mathbf{H}}$ and r^2 :

$[\hat{\mathbf{H}}, r^2] \; = \; -(\frac{\hbar^2}{m})(3 \, + \, 2\,\mathbf{r}\cdot\nabla)$

into the equations he had rigourously derived in chapters 5 and 6 of [8] to arrive at the surface integral associated with the bond between two atoms A and B :

$\mathbf{R}_{ab} \cdot \oint dS(A|B, \mathbf{r})\rho(\mathbf{r})\mathbf{n}_a(\mathbf{r})$

where $\mathbf{R}_{ab}$ is the vector linking nucleus A to nucleus B.

Bader ascribes two important features to this integral. Firstly it "counts the electrons" in the interface between the two atoms that create the distortion in the gradient vector field of the electronic charge density (as compared to that of the free atoms) i.e. it represents a quantity of charge. Secondly, reinstating the units of $\frac{\hbar^2}{m}$, the integral, and so also a quantity of charge, has the dimensions of $energy \times (length)^2$

Now, the Bridge Index has the dimensions of $\rho \times (length)^{-1}$ and ρ is quantity of charge per volume - so the BI dimensions are $energy \times (length)^2 \times (length)^{-3} \times (length)^{-1}$ which are the dimensions of strength.

5.3.2 Illustrative profiles

The bonding of two Bader atoms can be thought of as the result of the electronic charge density distribution, i.e. of a quantum mechanical observable, not of any particular theoretical mechanism such as electron pairing or bonding orbitals or net Coulombic attraction - it involves all of these. An atom in a crystal will be subject to as many bonds as there are bond paths to its neighbours. The traditional classification of bond types in crystals (molecular, ionic, covalent and metallic [110], e.g.) is to some extent revealed by plots of the electronic charge density (ECD) profile between nuclei, as seen in the following diagram which it is hoped is as suggestive to the reader of the above reasoning as it was to the author.

In this diagram the BCPs are at the minimal turning points of each graph. The ECDs range from 0.01 to 0.3 electrons per cubic bohr between the least dense, highly ionic $\mathrm{Na-Cl}$ bond and the most dense, highly covalent $\mathrm{C-C}$ bond in diamond. The stronger covalent bonds also have a shorter Bond Length, as exemplified by the two types of $\mathrm{Ti-O}$ bond in the highly distorted tetragonal perovskite, $\mathrm{PbTiO_3}$. The covalent bond is short and at 0.2 $e/bohr^3$ has ten times the ECD at the BCP than the much longer ionic bond which at 0.02 $e/bohr^3$ compares with MgO - the latter, though slightly covalent, is often quoted as a typically ionic substance [110]. The metallic bond in metallic copper has a similar low ECD to the ionic bonds, but the low region is broader with lower curvature at the BCP. Perhaps the most interesting bonds are those (of differing lengths) in metallic Osmium which are both metallic and rather strongly covalent, leading to its extreme toughness, hardness and incompressibility. Finally, notice the asymmetry of the highly covalent $\mathrm{B-N}$ bond in BN.

To provide more detail, the following table and suite of electronic charge density profiles along the Bond Path or "London's Bridge" between atoms is presented (figures 5.12 - 5.15 inclusive). It

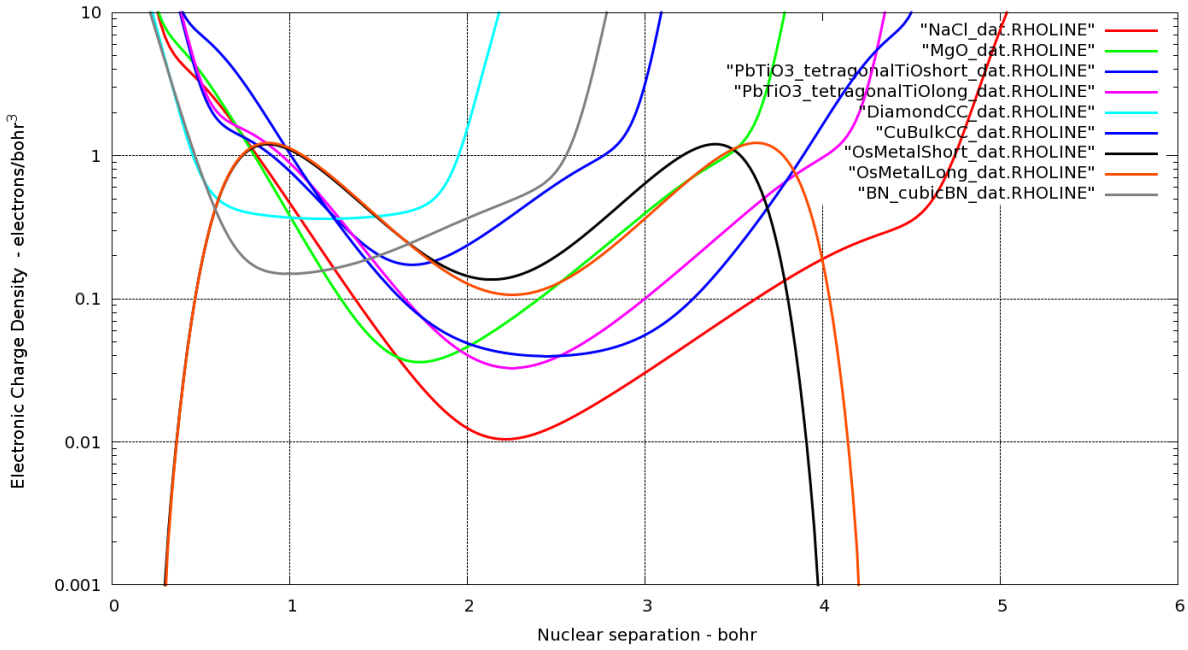

Figure 5.11: Profiles through the bond paths between atoms of various crystalline materials - see discussion in text. The vertical scale is logarithmic and density values are electron (probabilities) per cubic bohr. The reversals in electronic charge density at either end of the metallic Osmium bonds are artifacts of the pseudopotentials used in the basis sets. They occur at the boundaries of the core electron zone and do not affect the valence/conduction electrons

is a representative selection of the perovskites studied for this thesis and the oxides they comprise and displays the electronic charge density at the BCP and the nuclear separation for each profile. It serves to illustrate the redistribution of the collective electrons when a perovskite forms from a stoichiometric mixture of oxides. As mentioned, the Bond Paths were straight lines between nuclei in all cases.

In this selection the annotated width dimension refers to the the distance between nuclei in Bohrs, and the density at the BCP is in electrons per cubic Bohr. Notice that for Sr, Ba, and Pb the small core pseudo-potential basis sets have created a false profile towards the cation site (except for $\mathrm{BaZrO3}$ where the Towler all electron basis set [111] was used for Ba). As mentioned earlier this nuisance effect does not affect the conclusions drawn about events at the BCP.

The selection displays $\mathrm{ABO_3}$ oxide perovskites, and the AO and $\mathrm{BO_2}$ oxides where A is Ca, Sr, Ba, and Pb and B is Ti , and Zr .

Profile	Rho	Separation	Bridge Index
TiO2 :TiO	0.11337	3.59208	2.54527
CaTiO3:TiO	0.10011	3.69724	2.18365
CaO:CaO	0.03780	4.55838	0.66868
CaTiO3:CaO	0.03851	4.45218	0.69759
TiO2 :TiO	0.11337	3.59208	2.54527
SrTiO3:TiO	0.09944	3.6987	2.16814
SrO:SrO	0.03659	4.84318	0.60925
SrTiO3:SrO	0.02086	5.23075	0.3216
TiO2 :TiO	0.11337	3.59208	2.54527
BaTiO3:TiO	0.14935	3.69724	3.25762
BaO:BaO	0.03374	5.18442	0.52482
BaTiO3:BaO	0.02609	5.30759	0.39637
TiO2 :TiO	0.11337	3.59208	2.54527
PbTiO3:TiO	0.16623	3.33042	4.02531
PbO:PbO	0.05771	4.48313	1.03809
PbTiO3:PbO	0.04296	4.74236	0.73050
ZrO2:ZrO2	0.07179	4.16502	1.39013
CaZrTiO3:ZrO2	0.08883	3.98783	1.79648
Ca:CaO	0.03780	4.55838	0.66868
CaZrO3:CaO	0.03998	4.42798	0.72822
ZrO2:ZrO2	0.07179	4.16502	1.39013
SrZrO3:ZrO2	0.08755	3.99618	1.76684
SrO:SrO	0.03659	4.55838	0.64732
SrZrO3:SrO	0.03350	4.82287	0.56015
ZrO2:ZrO2	0.07179	4.16502	1.39013
BaZrO2:ZrO2	0.08975	3.96038	1.82766
BaO:BaO	0.03374	5.18442	0.52482
BaZrO3:BaO	0.01975	5.60278	0.2843

Table 5.1

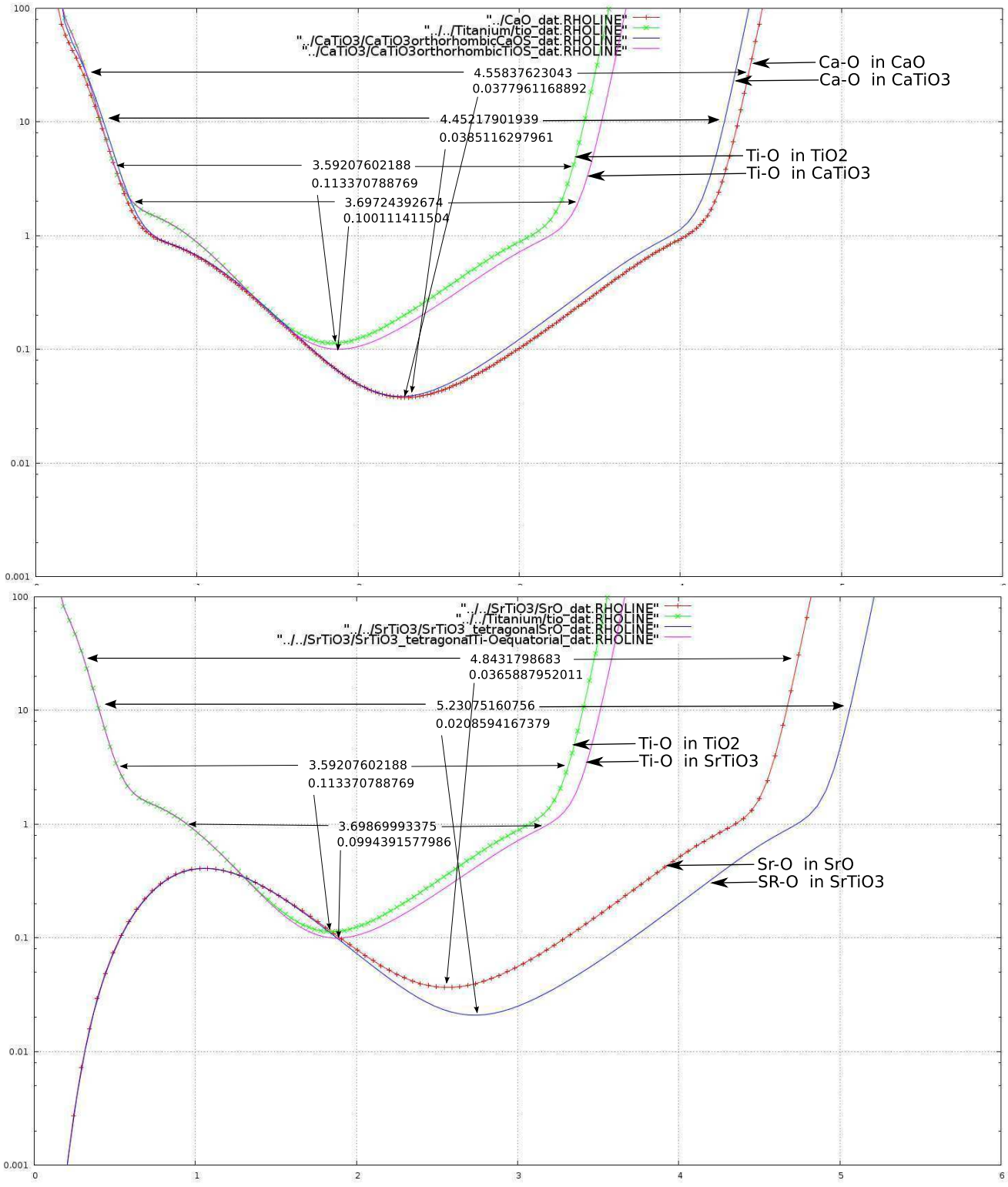

Figure 5.12: Electronic charge density profiles of CaO, TiO_2 and $CaTiO_3$; and SrO, TiO_2 and $SrTiO_3$ illustrating the shift in charge density and bond length between oxides and the perovskites that they form

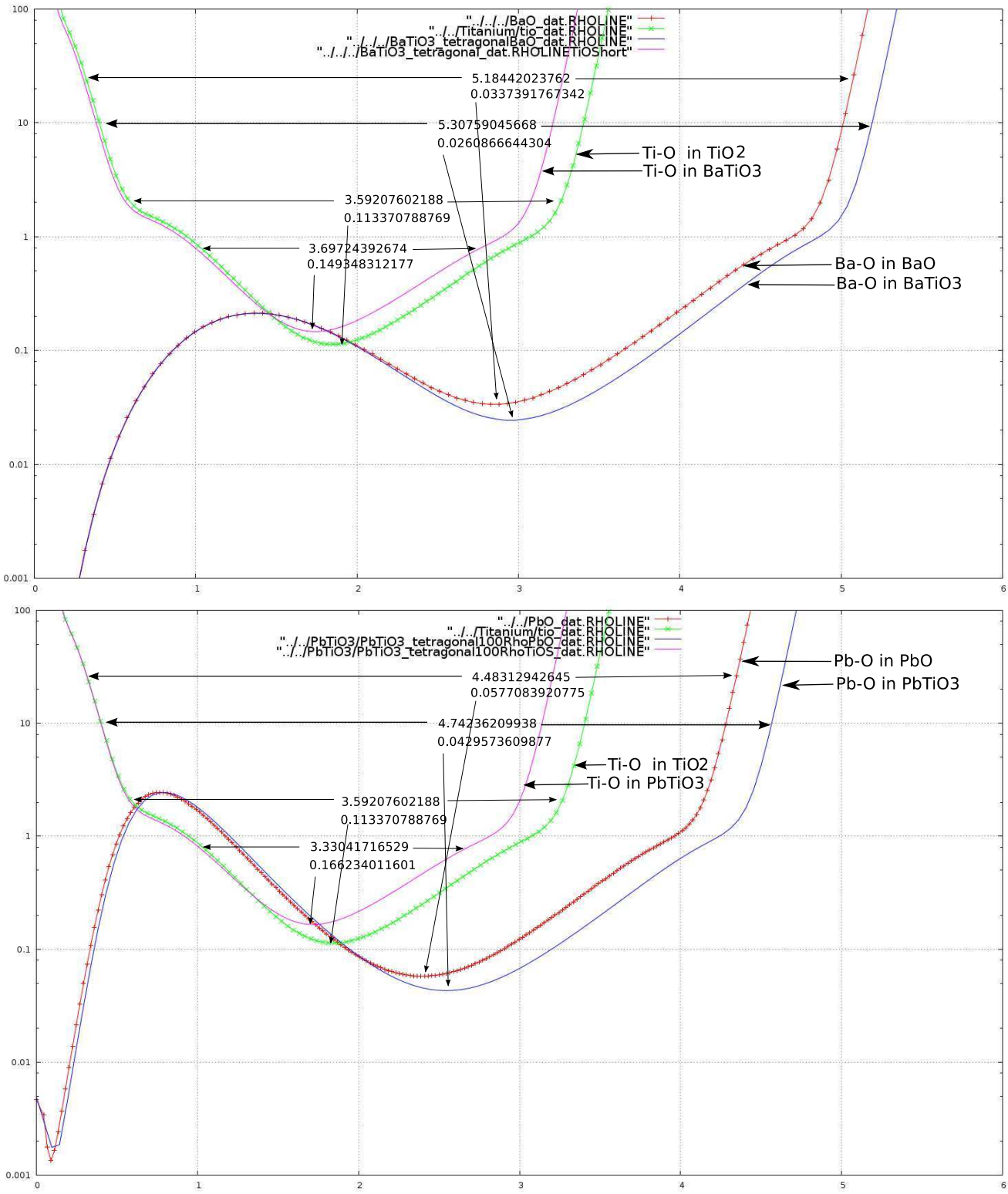

Figure 5.13: Electronic charge density profiles of BaO, TiO_2 and $BaTiO_3$; and PbO, TiO_2 and $PbTiO_3$ illustrating the shift in charge density and bond length between oxides and the perovskites that they form. Both of these perovskites show strong offset of the O atom along the c axis

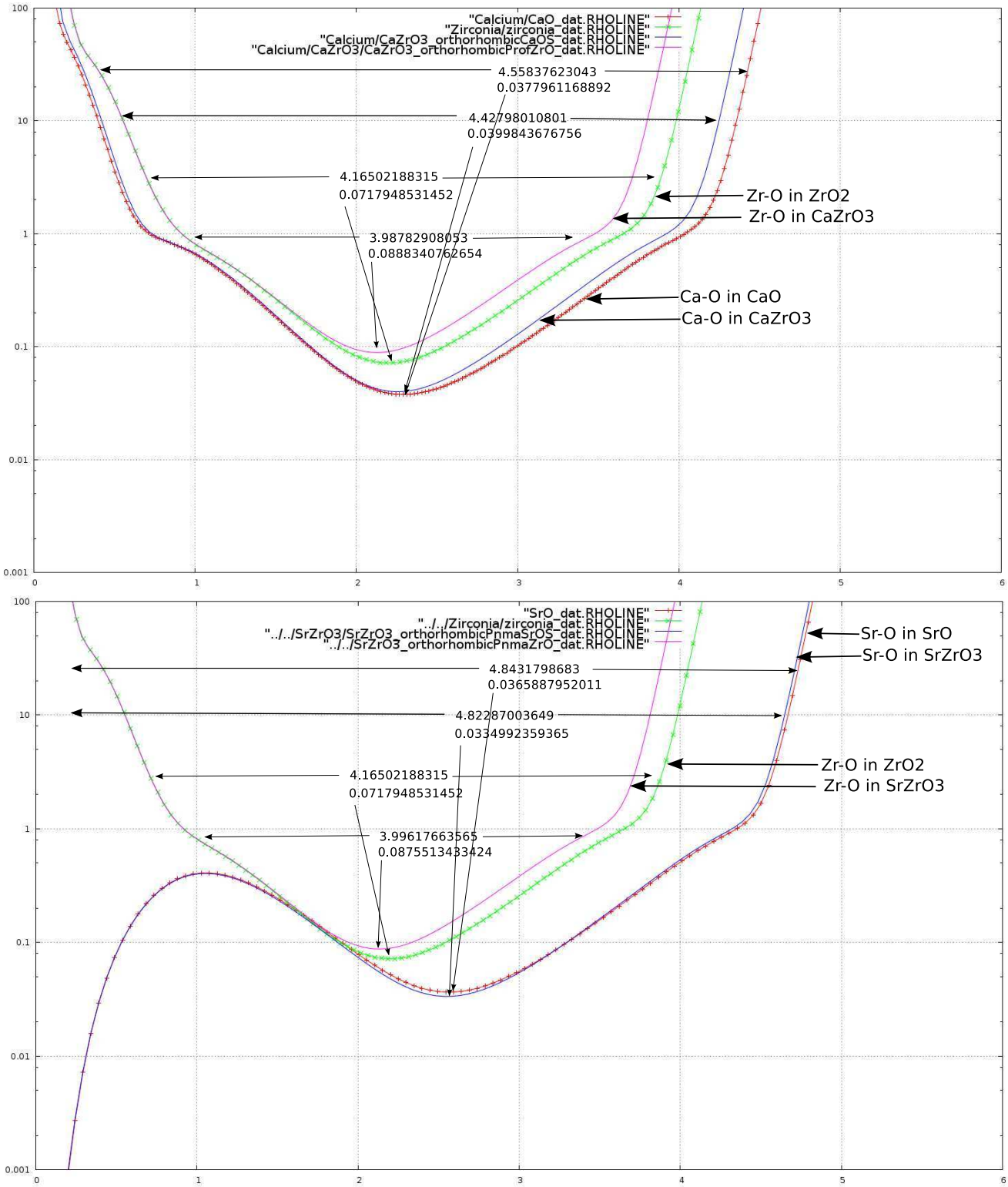

Figure 5.14: Electronic charge density profiles of CaO, ZrO_2 and $CaZrO_3$; and SrO, ZrO_2 and $SrZrO_3$ illustrating the shift in charge density and bond length between oxides and the perovskites that they form

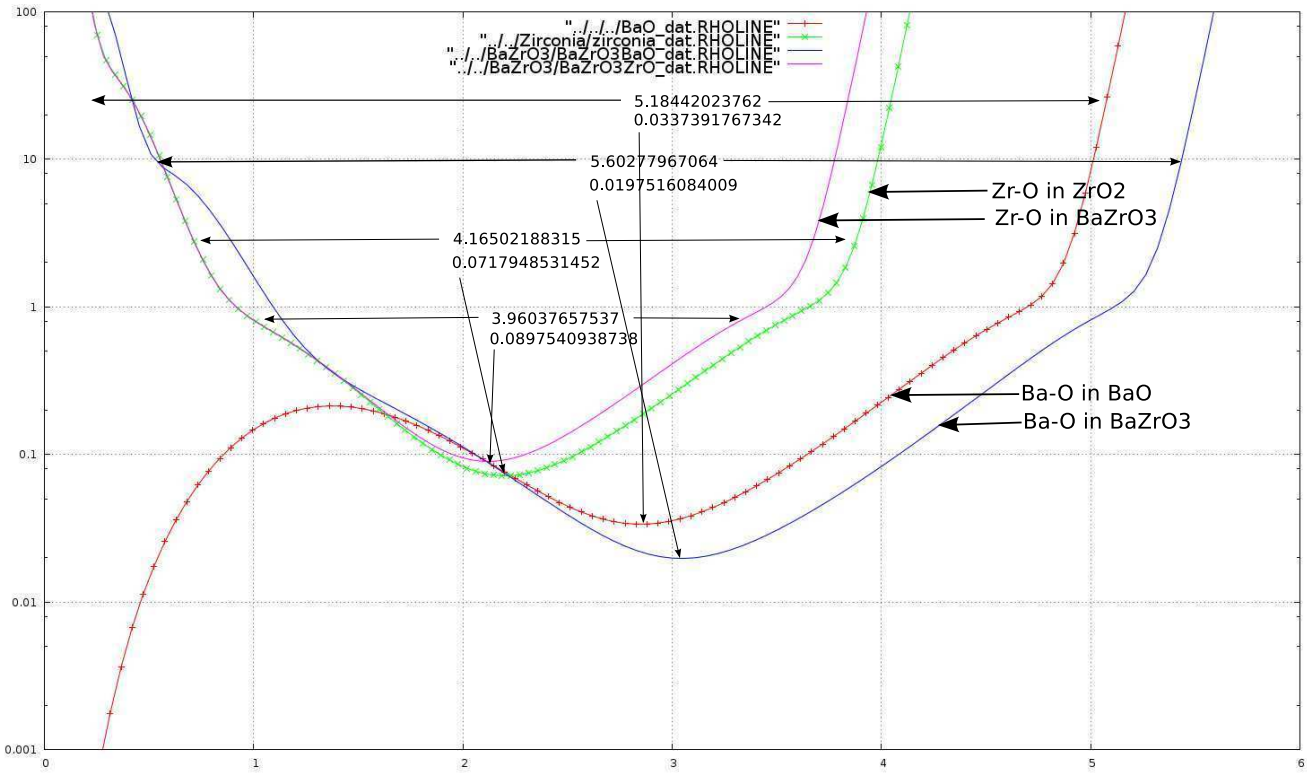

Figure 5.15: Electronic charge density profiles of BaO, ZrO_2 and $BaZrO_3$ illustrating the shift in charge density and bond length between oxides and the perovskites that they form

5.4 The Bridge Index, Cohesive Energy and Forces in a Crystal

It would be desirable to see how the Bridge Index introduced above relates to measurable bond strengths or bond forces - derivatives of the pair-wise cohesive energy. The following graphical summary (Fig 5.16 overleaf) illustrates that there is a quasi logarithmic relationship between the Bridge Index and published experimental bulk modulus data and also between the Bridge Index and pair-wise bond strength as calculated by the author for some binary compounds and several perovskites in the work detailed in following sections.

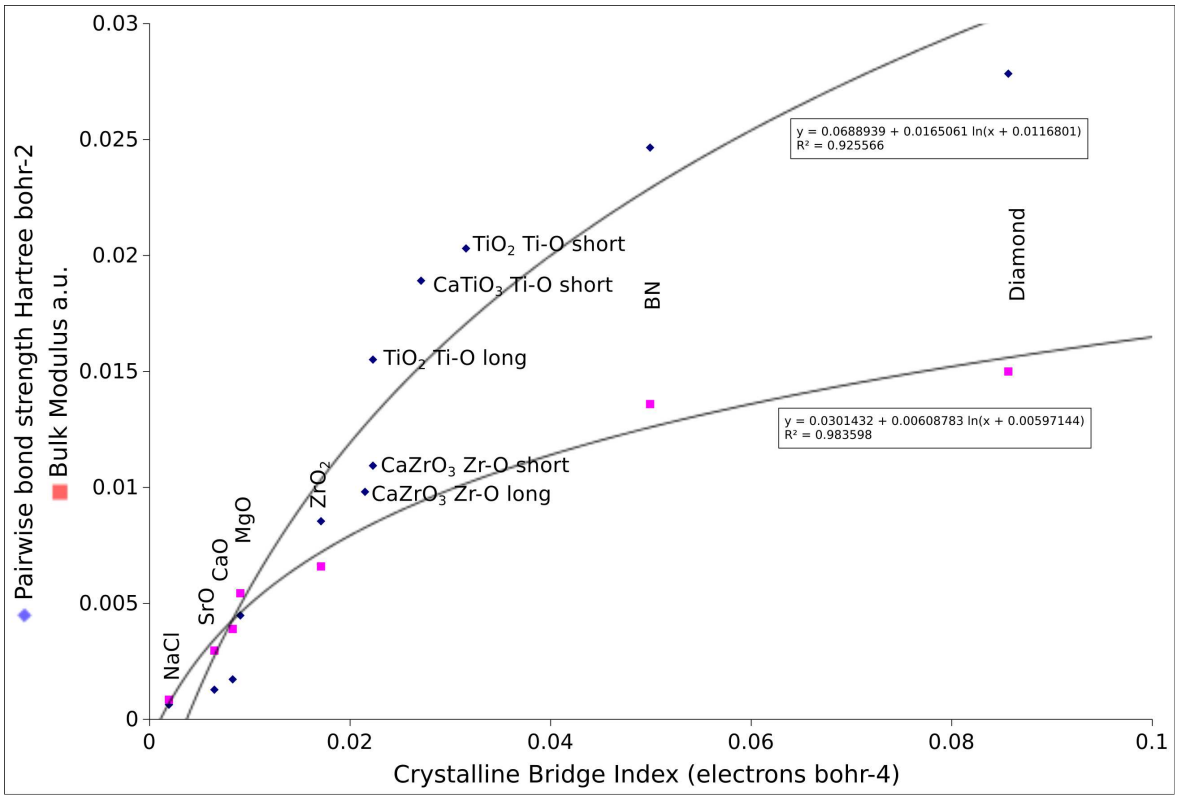

Figure 5.16: Published experimental bulk modulus and calculated *pairwise* bond strength plotted against the Crystalline Bridge Index for various binary compounds and two orthorhombic perovskites, $CaTiO_3$ and $CaZrO_3$. Details of the calculations are described in the text.

Force is a derived quantity in computational quantum chemistry, where the inputs are usually basis sets, coordinates and system Hamiltonians and the outputs are expectation values or energy eigenvalues. It is usually calculated either by spatially differentiating energy or integrating stress and sometimes the concept of force is the best way to formulate the mechanisms involved in crystal strain. The net forces in an unstrained crystal are zero.

Bader shows that one can derive an expression for the average force on the entity that is the Bader Atom, but this is not helpful in the consideration of any specific bond between two atoms.

It has been seen in chapter 3 that Bader atoms may be deformed by the bonds in which they participate - for example the oxygens in a cubic perovskite are symmetrical, but in a tetragonal perovskite along the c axis the atoms are compressed by the more covalent bond and extended by the less covalent bond and the forces (whose resultant is zero) are different at the respective bounding surfaces.

The cohesive energy of a crystalline system can be found using *ab initio* methods by subtracting the separate atomic ground state energies from the crystalline ground state that has been calculated. The resultant energy should then represent the work required per primitive cell to separate the atoms to a large distance, thus disintegrating the crystal structure. This work would be done against the forces that hold the atoms at their equilibrium sites. Experimentally cohesive energy is found by the Born Haber method of summing the measurable heats of formation of the various chemical steps involved in the formation of the crystalline substance. However, for ionic substances there exists two sets of calculated and experimental data according to whether the substance is "assembled" from the constituent ions or from neutral atoms. The commonly used experimental values (per primitive cell) for MgO are 0.375 au for separation into atoms [112] and 1.1553 au for separation into ions [113] a 300% difference. From the point of view of mechanical toughness and hardness the ionic version of cohesive energy is more relevant than the atomic version when the material is ionic, because when a material specimen yields or breaks, it retains its ionicity rather than splitting into a collections of neutral atoms.

There is a conceptual problem with the ionic cohesive energy of ionic oxides (such as MgO) since they cannot be disassembled into Mg^{++} and O^{--} because the latter ion does not exist in the free state. Earlier calculations were incomplete because they did not account for the $\mathrm{O}^{2-} \Longrightarrow \mathrm{O}^{-} + \mathrm{e}^{-}$ step [113] [114]. The latter reference is a good review of the problems and complexity of calculating the ionic cohesive energy with a detailed examination of the crystal potential, the correlation energy and dispersion terms. Further work used the coupled cluster approach to set up an incremental expansion for the correlation energy and also revealed a nearly 15% contribution by dispersion (van der Waals-like) effects [115] [116]. The *pair-wise* cohesive energy across a face between two atoms cannot be deduced from the cohesive energy of a unit cell except for the cubic binary materials. In any case such an approach suffers from the difficulty of accurately deriving a small quantity by the subtraction of two very much larger quantities. Various empirical connections between cohesive energy and Bulk Modulus have been proposed [117] [118], and in the case of cubic binary compounds, the bond energy can be derived from the Bulk Modulus together with crystal structure and electronic density data.

However in the model that follows, the author has calculated the *pair-wise* cohesive energy

across a face between two atoms, hence the *pair-wise* bond strength. Firstly, that proportion of the volume of the participating atoms that contains that bond's share of the collective (valence and conduction) electrons, accounting for the coordination numbers of the participating atoms is determined. Then the energies are calculated using the approximations of of a heteronuclear atom pair as treated by Gordon and Kim [119] and discussed in [122], chapter 10. Only with the collective electrons are included and no attention is paid to the individual atom or ion energies, or to the core energies. This is because the balancing forces (spatial energy derivatives) include a kinetic component that is contained like a spring within the volume occupied by those collective electrons shared across the common boundary.

For a given pair of atoms, the pair interaction energies are summarised as Coulombic, including Hartree-Fock/DFT exchange and correlation, and non-Coulombic including the zero-point kinetic energy arising from Pauli exclusion, the Bloch-Dirac exchange component, and the Gordon and Kim extrapolation for correlation energy [119]. The binding forces in a molecule or crystal are overwhelmingly electrostatic forces [110] p. 397, note 4, the spatial derivative of the electrostatic energy. The text book model is that in the ground state the net attractive electrostatic force between nuclei, created by the bonding electronic orbitals between them (i.e. the population of the collective - valence and conduction - electrons in the London's bridge), is balanced by the so called degeneracy pressure of electronic kinetic energy [120], [110]. At equilibrium there is no net force between nuclei, but a decrease in nuclear separation (compression) is resisted mainly by the increase in kinetic energy, whilst an increase (extension) is resisted by an electrostatic potential which decreases more slowly than the decrease in kinetic energy. In other words, considering the bond between two atoms, there is a kinetic energy spring which always produces a repulsion and an electrostatic spring which is net and always attractive. Density functional theory has been used to evaluate this simple but realistic picture; e.g. Lopez and Alonso [121] used it to calculate the bulk modulus of the alkali metals and obtained good agreement with experimental values. The calculation below is based on consideration of the collective electrons only, since the atomic cores provide a net Coulombic component to bonding, but do not participate in the "degeneracy pressure". This is justified by Bader's demonstration that an atom contains zones where the kinetic energy predominates, and zones where potential energy predominates. These zones are marked out by the Laplacian of the electronic charge density. The fact that the repulsive component of a bond resides within the zone of sparse collective electrons about the region of the BCP explains the behaviour of materials that are super-hard and highly incompressible, but are not correspondingly brittle. The incompressibility arises from higher kinetic energy of the collective electrons which balance strong Coulombic attractions.

The energies within the non-core region are small compared to those within the cores. Remembering that the balancing pairwise repulsive energy is kinetic, the following diagram, figure 5.17 illustrates the very large difference between bonding energy and the core energies. Also note the overlapping or merging of the L shell in the covalent diamond bond, whereas closed shells abut in apposition in the highly ionic bonds.

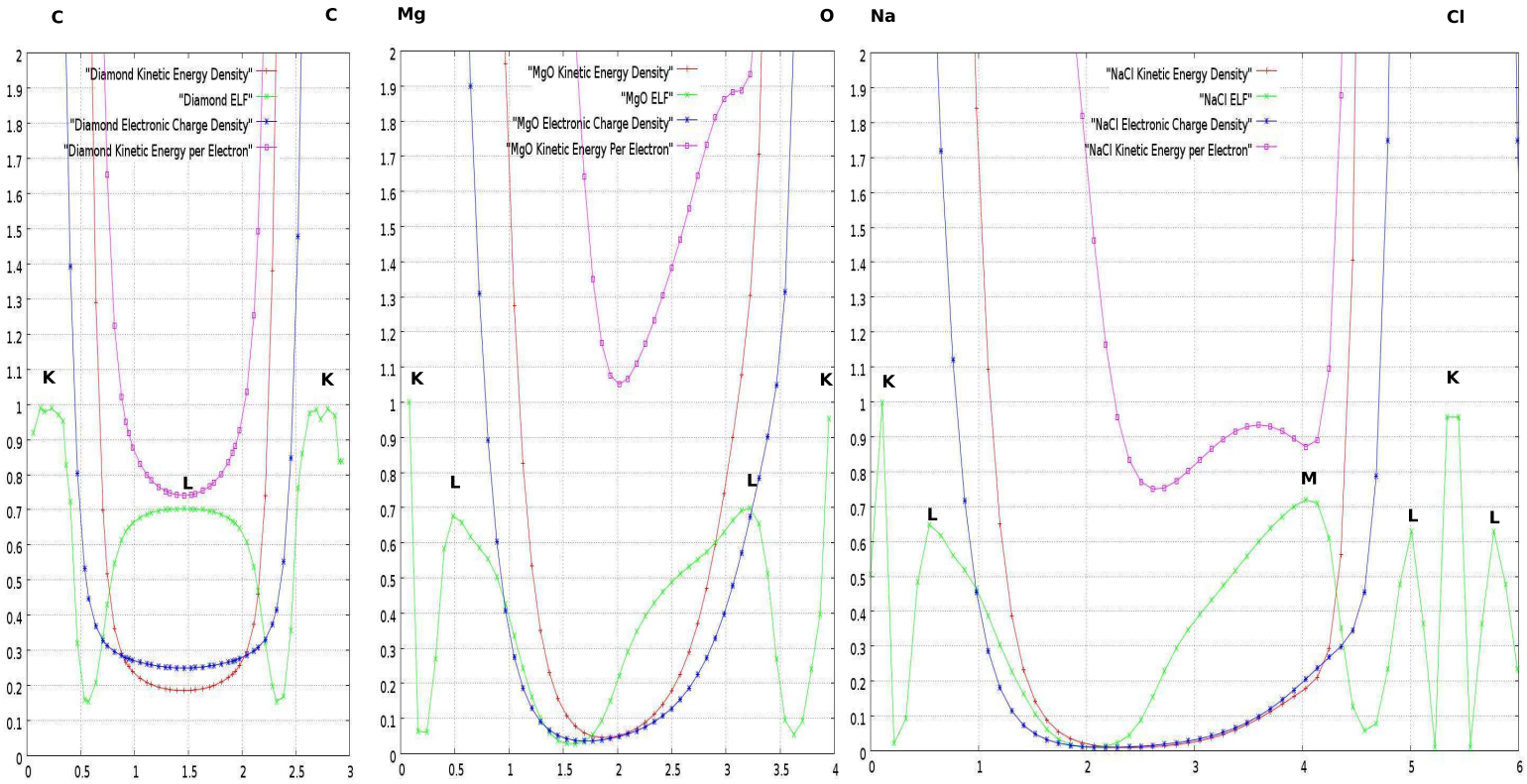

Figure 5.17: Electronic charge density, ELF and Kinetic Energy profiles for strongly covalent diamond, slightly covalent MgO and strongly ionic $NaCl$. The kinetic energy and ELF were calculated from the electronic charge density using the Kirzhnits approximation.

5.4.1 “Springs” in London’s bridge - details of the simple model

For a pair of adjoining Bader atoms within a crystal, one can calculate the pairwise bonding energy and bond strength, designate it κ, using crystal structural data and electronic charge density data from the CRYSTAL06 outputs. The simple model will treat the collective (valence plus conduction band) electrons within the pair of atoms as a uniform electron gas. This gas of collective electrons is in turn contained within a smaller fraction of the combined volume that does not include the core volumes. detailed below.

The average potential energy and kinetic energy of any given bonded (in the Bader sense - i.e. there is a BCP) pair of atoms are reproduced identically periodically throughout the crystal and the combined pair represents a subsystem for which the virial theorem holds. Therefore for any given bond only the two Bader atoms need to be considered, and their contribution to the bond Energy is sought. The volume of each atom is obtained from the CRYSTAL06 output using the Yu and Trinkle integration described in Chapter 2.

Then it must be taken into account that each member atom also has pair-wise connection to other atoms. Therefore both the volume and the number of collective electrons for each Bader atom are subdivided into portions that correspond to the coordination number of that atom.

Also the volume of the volume of the core regions, assumed to be rigid, should be subtracted from the atomic volumes as a first step. Two assumptions are made: firstly that only changes in the non-core volume affect the Kinetic energy of the collective electrons; and secondly that this volume is altered only by change in nuclear separation s, the interface area A remaining constant for small changes in s. For uniformity across all materials the non-core region was taken to be that within which the kinetic energy was less than 2 Hartrees. Reference to any of the bond path profiles graphed in this thesis will show that the kinetic energy curve is so steep between core and non-core regions that not too large an error is created by such an arbitrary choice.

The following diagrams illustrate the calculation procedure:

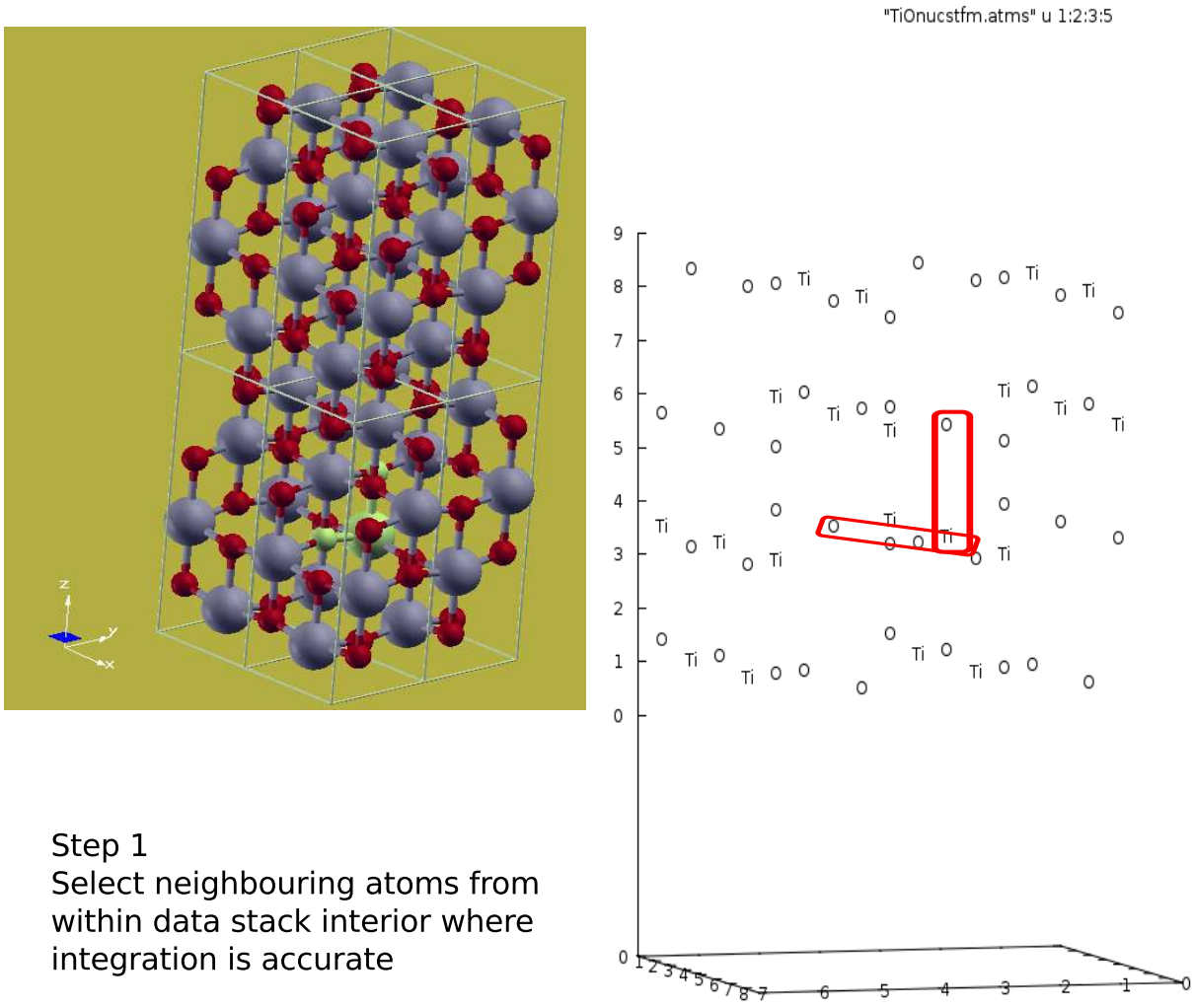

Figure 5.18: Sixty atoms are located from the XCrysden image of six conventional cells of anatase TiO_2 (tetragonal). Ti atoms are grey, O atoms are red and the selected long (c axis) and short bonds are green.

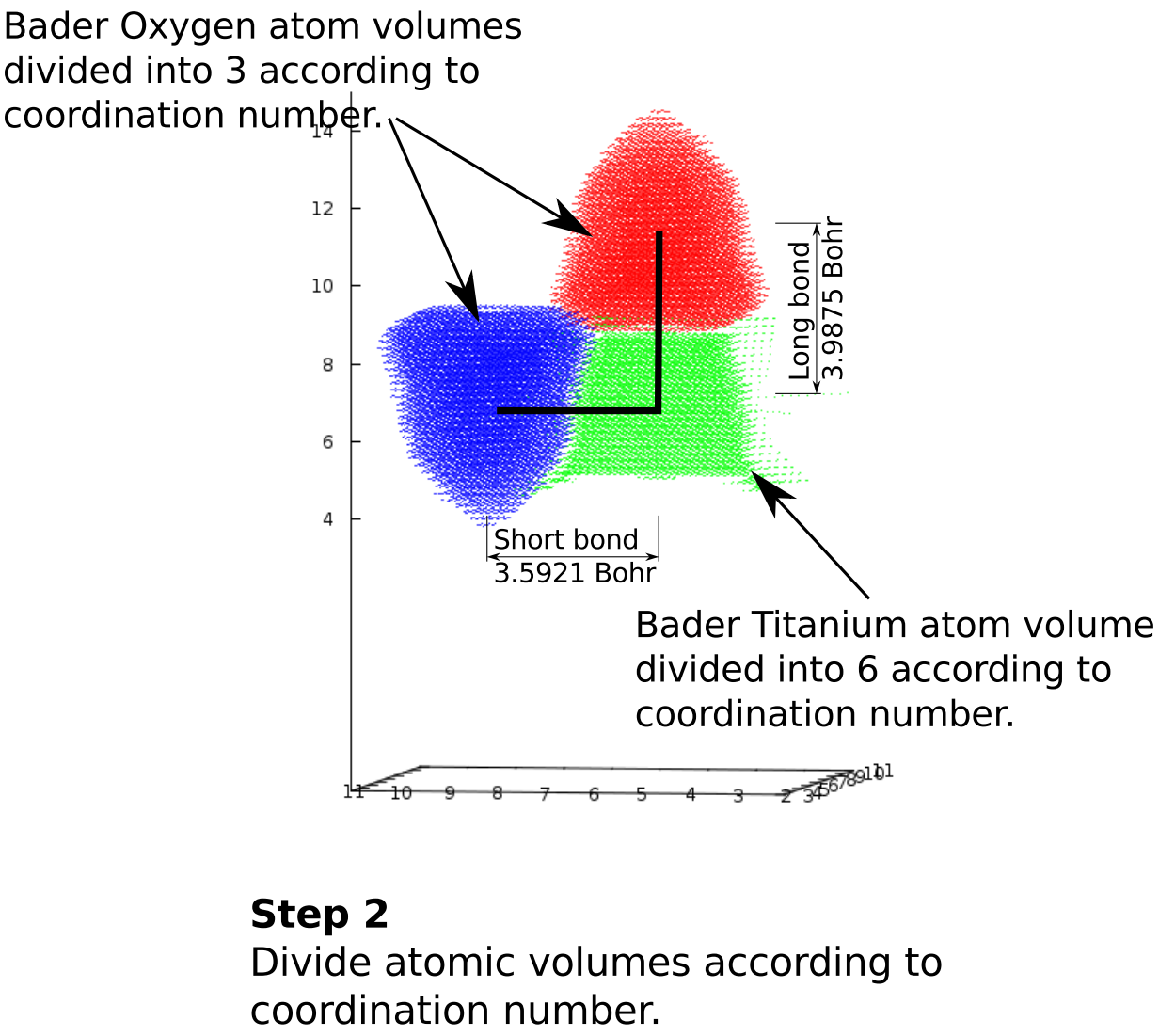

Figure 5.19: The selected atoms are integrated using the Yu and Trinkle procedure and the volumes and collective electron populations subdivided according to coordination.

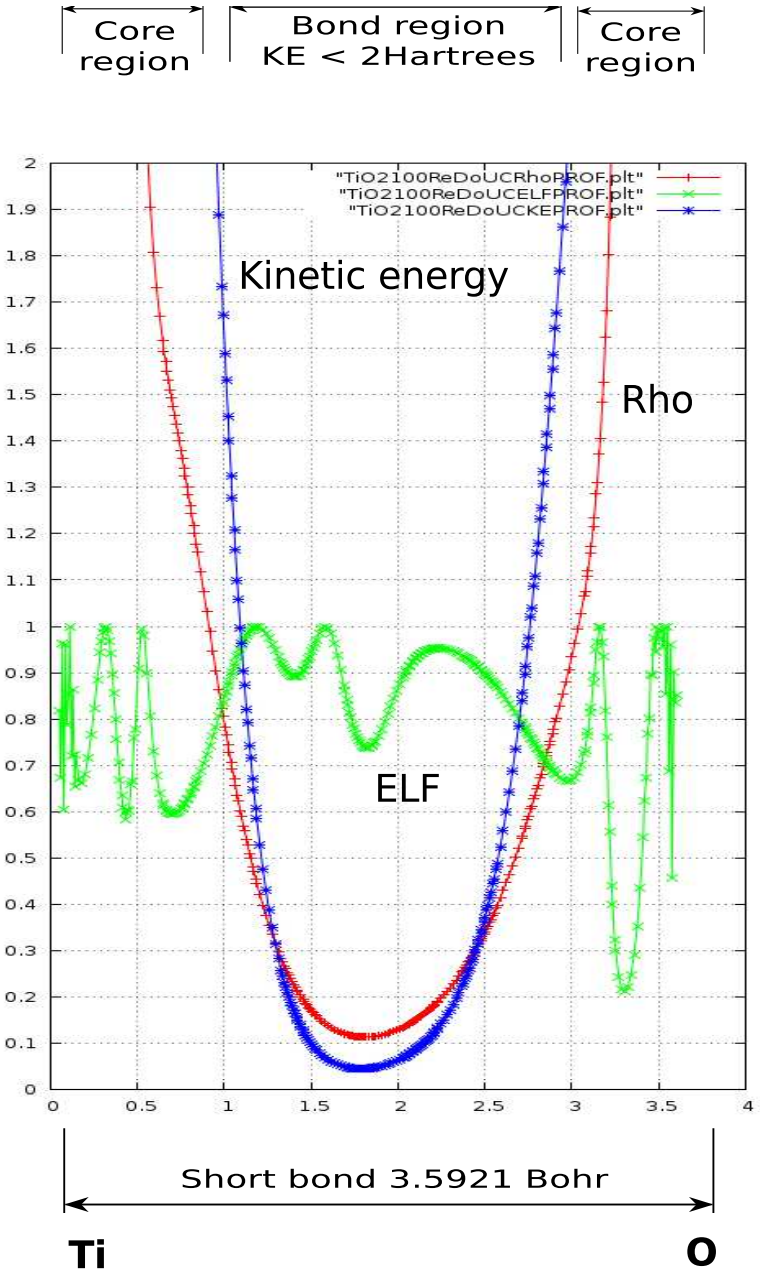

Step 3
Use kinetic energy profile to measure ratio of bond region to bond length. Apply this ratio to the gross bond volume of step 2. to give participating bond volume.

Figure 5.20: The pairwise subdivided volumes must then be reduced to the non-core value. This was arbitrarily taken to be the region within which the kinetic energy was less than 2 hartrees.

Now:

$$Pairwise\,Bond\,Energy\;=\;Potential\,Energy\;+\;Kinetic\,Energy \tag{5.1}$$

where these energies are contained within the two atoms and can be derived from purely local considerations.

5.4.1.1 The Potential Energy contribution

This is attractive and mainly Coulombic. The relatively much smaller spin and dispersion (van der Waals) effects are not considered here.

As has been established theoretically [15] and experimentally [123], the electrostatic potential (EP), even in a highly ionic crystal, cannot be modelled by a simple point charges at the ground state ionic sites. The calculated EP maps for two ionic crystals, NaCl and MgO in Figure 5.16 illustrate this. Notice how similar these maps, DFT with hybrid exchange and Lee-Yang-Parr GGA correlation, are to the HF maps of [15]. Importantly the symmetries are the same, because the model depends on the symmetrical disposition of electrostatic potential about the bond path.

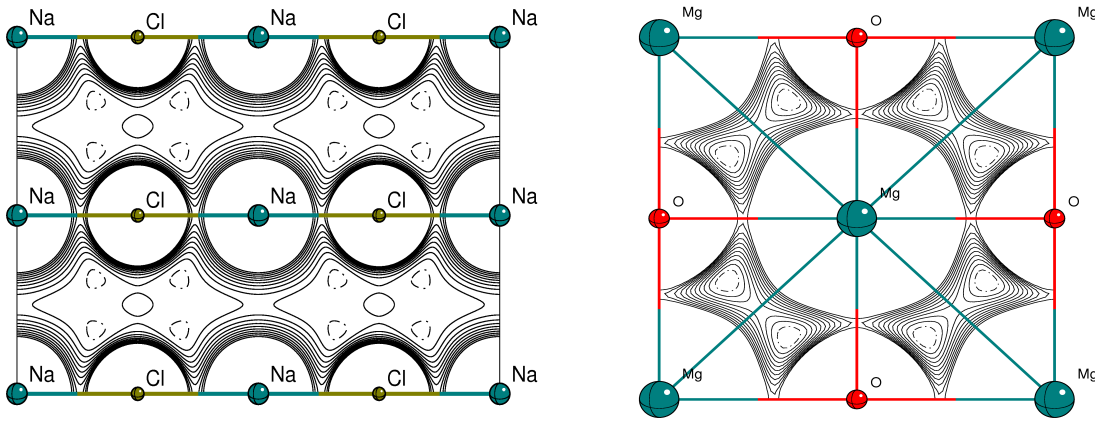

Figure 5.21: Maps of calculated Electrostatic Potential in the (101) plane of NaCl (left) and the (010) plane of MgO (right). Notice that the potential is highly positive at all of the ion sites. The small regions of negative potential are contoured with dashed lines.

The negative EP regions are symmetrically disposed about the bond paths, so any resultant attractive (-ve) force between ions,net of the nuclear repulsion, will still be along those bond path. The potential energy contribution to the bond energy would be approximated by $K\,\alpha\,e^2\,s^{-1} + Pec$ where K is a bond specific constant, α is the Madelung constant, e is the charge transfer between the atoms, s is the nuclear separation along the bond path and Pec is the exchange-correlation component. In the calculated examples to follow neither α nor e is used because enough information is supplied by the ground state equilibrium crystal structure, the electronic charge density

distribution and the reduced integrated volumes, taken as a function of s to calculate the potential energy and the kinetic energy contributions. α and e^2 are incorporated in a bond specific parameter K_P, so giving the potential energy $E_P(s) = K_P\, s^{-1} + Pec$. However, since Pec is included in the net negative regions mapped by the DFT calculation, it can be included in the $E_P(s) = K_P\, s^{-1}$, modifying K_P but retaining the s^{-1} dependence.

i.e.

$$E_P(s) = -\, K_P\, s^{-1} \tag{5.2}$$

5.4.1.2 The Kinetic Energy contribution

This is net repulsive.

Figure 5.17 reveals that the electronic charge density is low in value, low in gradient and rather flat in the non-core region between adjoining atoms. Therefore instead of functionals of the form $\int_V F(\rho)\, dv$ this simple model will assume an average value over the non-core region and apply this to the three components of kinetic energy. These are:

i. the ground state kinetic energy [124], p 197, in atomic units:
$\frac{(3\pi^2 N)^{\frac{5}{3}}}{10\pi^2} V^{\frac{-2}{3}}$

where N and V are the number of electrons in, and the volume of the non core region.

ii. the non-Coulombic part of the exchange energy, using the Bloch-Dirac calculation [125]:
$-V\, \frac{3}{4}\, (\frac{3}{\pi}\, \frac{N}{V})^{\frac{4}{3}}$ and

iii. the non-Coulombic part of the correlation energy, using the Gordon and Kim logarithmic interpolation formula [119]:
$-V\, \left(0.06156 - 0.01898\, ln\left((\frac{3V}{4\,\pi\, N})^{\frac{1}{3}}\right)\right)$.

Thus,

$$E_k(V) = \frac{(3\pi^2 N)^{\frac{5}{3}}}{10\pi^2} V^{\frac{-2}{3}} - V\, \frac{3}{4}\, (\frac{3}{\pi}\, \frac{N}{V})^{\frac{4}{3}} - V\, \left(0.06156 - 0.01898\, ln\left((\frac{3V}{4\,\pi\, N})^{\frac{1}{3}}\right)\right) \quad \text{.... (5.3)}$$

5.4.1.3 The Crystalline Bond Energy and Crystalline Bond Strength Strength

For this model, the reduced volume is a function of nuclear separation s .

$V(s) := ratio * Area * s$.

where $ratio$ is read off the kinetic energy profile plot for each material (step 3 above) and $Area$ is the reduced volume from step 2 divided by the equilibrium nuclear separation.

Using this, the net binding energy of the crystalline bond is, rewriting equations (5.2) and (5.3) into equation (5.1) and remembering that N is the subdivided number from step 2 :

$$E_b(s) =$$
$$-K_P\, s^{-1} + \frac{(3\pi^2 N)^{\frac{5}{3}}}{10\pi^2} V(s)^{\frac{-2}{3}} - V(s)\,\frac{3}{4}\,(\frac{3}{\pi}\,\frac{N}{V(s)})^{\frac{4}{3}} - V(s)\,\left(0.06156 - 0.01898\, ln\left((\frac{3V(s)}{4\,\pi\,N})^{\frac{1}{3}}\right)\right)$$

... (5.4)

Differentiating w.r.t. s one obtains $BF(s)$, the pairwise component of the force between the nuclei:

$$BF(s) = \frac{d\,E_b(s)}{d\,s} \quad \text{... (5.5)}$$

The bond force is zero at s_0, the equilibrium nuclear separation, and K_P is obtained by solving $BF(s) = 0$ at s_0.

The pairwise Crystalline Bond Strength κ can then be defined as the derivative of the bond force with respect to nuclear separation evaluated at the equilibrium separation s_0:

$$\kappa = \left|\frac{d^2\,Eb(s)}{d\,s^2}\right|_{s=s_0} \quad \text{... (5.6)}$$

5.4.2 Results and Discussion

The Gnumeric spreadsheet presenting input data and calculated results is imaged in the accompanying figure 5.22. Entries are in atomic units and are truncated, not rounded. CRYSTAL06 outputs range from 10E-6 to 10E-10 in precision whilst experimental bulk moduli are rather imprecise with published results varying by up to 10 GPa or more in the case of Diamond. The conversion factor used for Bulk Modulus is $1\,au = 29421.033\,GPa$. It will be noticed that the actual κ is negative, representing a restorative "bond spring" and therefore stable equilibrium, but a positive figure, being the magnitude of the "spring constant" was used in the graph.

These results surprise this author, as he had assumed that the increasing kinetic energy coupled with the restriction of the kinetic energy volume would outweigh the net binding potential energy increase associated with decrease in the nuclear separation - thus indicating less compressible but brittle materials. The results above show that the rate of increase in Crystalline Bond Strength, κ (and Crystalline Bond Energy, Eb_0) with decreasing separation moderates, as is revealed by the flattening in the plots in Figure 5.16.

This is good news, for instance in the search for new tough materials. A CBI above 0.06, i.e. half that of diamond, with evenly matched bonds should result in a tough and hard to super-hard material. The flat curve beyond this figure allows room for many candidates, which can be tested by ab-initio analysis in the first instance.

	A	B	C	D	E	F	G	H	I	J	K	L	M	N	O	P	Q	R	S	T	U	V
1		BadVol	TsiVol	BaChg	Collectiv	Coord	EffVol	Bond	Xsection	Graph	Graph	Eff Non	EffColEl	Eff Rho	BCP Rho	BI		Kappa	Kp		Bulk	
2					electrons			length	Area	Bond Lgt	Val Lgth	Core vol									Modulus	
3																						
4	NaCl																					
5	Na	58.2256	208.502	1.08635	1	6	9.7042666667															
6	Cl	240.693	89.759	−0.286545	7	6	40.1155															
7					8		49.819766667	5.3904	9.2423134956	108	72	33.213177778	1.3333333333	0.0401447083	0.01043029	0.0019349753	0.0006341	−0.0006341	0.9729	0.000846	24.9	
8	SrO																					
9	Sr	100.817	197.894	2.3429	2	6	16.8029															
10	O	120.998	24.3915	−1.79429	6	6	20.166333333															
11							36.969233333	4.8757	7.5823437318	134	93	25.657751493	1.3333333333	0.0519661021	0.0315189	0.0064644874	0.00127883	−0.0012788	1.1046	0.002967	87.3	
12	MgO																					
13	Mg	27.8085	97.7267	1.793	2	6	4.6347416667															
14	O	94.6478	23.9993	−1.71755	6	6	15.774633333															
15					8		20.409375	3.9903	5.1147470115	140	96	13.995	1.3333333333	0.095272121	0.03612036	0.0090520413	0.00448	−0.00448	1.501	0.005438	160	
16	CaO																					
17	Ca	75.5469	154.71	1.5655	2	6	12.591141667															
18	O	105.871	26.7735	−1.48688	6	6	17.645166667															
19							30.236308333	4.5584	6.6330967737	142	109	23.209560622	1.3333333333	0.0574475905	0.03779612	0.0082915314	0.00172485	−0.0017248	1.1259	0.003899	114.7	
20	TiO2																					
21	Ti	47.6784	158.278	3.79084	4	6	7.9464															
22	O	78.1913		−1.05514	6	3	26.063766667															
23	long						34.010166667	3.9875	8.5291954023	88	45	17.3915625	2.6666666667	0.1533310573	0.08883408	0.0222781382	0.015512	−0.015512	4.402			
24	Ti	47.6784	158.278	3.79084	4	6	7.9464															
25	O	78.2232		−1.05268	6	3	26.0744															
26	short						34.0208	3.5921	9.4710058183	79	38	16.364435443	2.6666666667	0.1629550054	0.11337079	0.0315611449	0.0203053	−0.0203053	4.159			
27																						
28	ZrO2																					
29	Zr	61.9336	162.713	−1.40388	4	8	7.741696875															
30	O	75.2947	24.9277	−1.2842125	6	4	18.8236625															
31							26.565359375	4.1988	6.3268932493	237	141	15.804707476	2	0.1265445756	0.07179485	0.0170988981	0.00854436	−0.0085444	2.987	0.006594	194	
32	BN																					
33	B	15.4321	45.9572	2.0732225	3	4	3.8580125															
34	N	57.2223	30.2469	1.64855	5	4	14.305575															
35							18.1635875	2.9925	6.0697034252	143	85	10.796538024	2	0.1852445659	0.14937592	0.0499167639	0.0246543	−0.0246543	2.864	0.013596	400	
36	Diamond																					
37	C	34.4436	35.3114	0.247047	4	4	8.6109															
38	C	36.5731	34.7818	0.102887	4	4	9.143275															
39							17.754175	2.9188	6.0826966562	121	69	10.124281612	2	0.1975448804	0.24996755	0.0856405185	0.0278406	−0.0278406	2.917	0.015	442	
40																						
41	CaZrO3	orthorhombic Ignoring Ca-Zr coordination.																				
42	Zr	66.5495	164.615	4.66689	4	6	11.091583333															
43	O	90.7528	23.2515	−1.38653	6	3	30.250933333															
44	long						41.342516667	4.0118	10.305228742	146	94	26.617784703	2.6666666667	0.100183644	0.08620178	0.0214870572	0.009811	−0.009811	3.1675			
45	Zr	66.5495	164.615	4.66689	4	6	11.091583333															
46	O	90.7528	23.2515	−1.38653	6	3	30.250933333															
47	int						41.342516667	3.9986	10.339247903	158	90	23.54953481	2.6666666667	0.1132364902	0.08977566	0.0224517724						
48	Zr	66.5495	164.615	4.66689	4	6	11.091583333															
49	O	90.7528	23.2515	−1.38653	6	3	30.250933333															
50	short						41.342516667	3.9878	10.367249277	158	94	24.596180802	2.6666666667	0.1084179161	0.08883408	0.0222764623	0.010939	−0.010939	3.355			
51																						
52	CaTiO3	orthorhombic Ignoring Ca-Ti coordination.																				
53	Ti	45.8416	114.809	2.08669	4	6	7.6402666667															
54	O	75.1516	22.6186	−1.293255	6	3	25.050533333															
55	short						32.6908	3.6972	8.8420426269	187	95	16.607625668	2.6666666667	0.1605688086	0.10011141	0.0270776294	0.0189141	−0.0189141	4.2325			
56	Ti																					
57	O																					
58	long							3.71279731							0.09812862							

Figure 5.22: A copy image of the spreadsheet of input data and calculated results. The graphs in figure 5.16 were created from this spreadsheet.

5.5 Summary

It has been proposed that the Bader “quantum atoms in molecules and crystals” concept allows a definition of a Crystalline Bridge Index based only on quantum mechanical observables, namely the Bond Path and the electronic charge density at the Bond Critical Point. These can be determined from currently available experimental techniques. A simple model was used to demonstrate the concept. The mechanical model suggests a useful ordinal relationship between the Crystalline Bridge Index, and the strength of the pairwise bond between the atoms. The Crystalline Bridge Index will be used as an ordinal indicator of pairwise bond strength in interpreting the work that is recorded in the appendix A.

Chapter 6

Results and Conclusions

6.1 Summary

The measurements carried out in the appendix are summarised in the following table 6.1.

Mineral and Phase	Band Gap (Hartrees)	Unit Cell Volume (cubic Bohrs)	Outer Electrons per Unit Cell	Average Outer Electron Density (e/cubic Bohr)	Bond Length $B-O$ (Bohrs)	Volume of Oxygen Octahedron in cubic phase (cubic Bohrs)	Crystalline Bridge Index of $B-O$ bond in ABO_3	Electronic Charge Density at BCP (electrons per cubic Bohr)
WO3-Monoclinic	0.2308103	1477.2886	96	0.0649839172	3.0944		0.054937952	0.170 (approx)
WO3-Tetragonal	0.0966177	805.79506	48	0.0595684962	3.0404		0.056591212	0.170 (approx)
ReO3-cubic	0	337.65894	25	0.0740392065	3.4817	56.275393037	0.032541474	0.113299648946
CaTiO3-orthorhombic	0.227472	1521.1925	96	0.0631083837	3.6972		0.027077629	0.100111411502
CaTiO3-tetragonal	0.2233189	764.38247	48	0.0627957886	3.6798		0.02762726	0.101662791995
CaTiO3-cubic	0.20984052	388.84298	24	0.0617215720	3.6495	64.80770716	0.028909472	0.105505118730
SrTiO3-tetragonal	0.21791275	809.77146	64	0.0790346452	3.6987		0.026884894	0.099439157799
SrTiO3-cubic	0.1398971	404.86249	32	0.0790391819	3.6989	67.476224002	0.026861819	0.099359181682
BaTiO3-orthorhombic	0.23644628	434.1688	28	0.0644910459	3.5063		0.036895414	0.129366390037
BaTiO3-tetragonal	0.21059762	446.53386	32	0.0716630985	3.4083		0.04381844	0.1493485765
BaTiO3-cubic	0.1407499	434.9676	32	0.0735686980	3.7884	72.494513671	0.023506531	0.089052140761
CaZrO3-orthorhombic	0.2973993	1778.911	96	0.0539656003	3.9878		0.022276462	0.088834076263
CaZrO3-cubic	0.2810266	478.15606	24	0.0501928178	3.9098	79.692839196	0.024741653	0.096734916008
SrZrO3-orthorhombic Pnma	0.3019678	1907.09681	128	0.0671177254	3.9962		0.021908649	0.087551343342
SrZrO3-orthorhombic Cmcm	0.2989548	1912.30914	128	0.0669347844	3.9798		0.022410305	0.089188530548
SrZrO3-tetragonal	0.3022386	956.13762	62	0.0648442219	3.9656		0.022827432	0.090524464916
SrZrO3-cubic	0.2944933	488.64896	24	0.0617215720	3.9382	81.440217594	0.023750264	0.093533289266
BaZrO3-cubic	0.3275056	512.09561	24	0.0468662483	4.0003	85.350165689	0.021408156	0.085639046667
PbTiO3-tetragonal	0.134082	464.61691	26	0.0559600812	3.3001		0.052327282	0.172685263353
PbTiO3-cubic	0.17467749	410.99291	26	0.0632614319	3.7175	68.49915882	0.026111896	0.097070971877
LaAlO3-trigonal	0.41763716	724.15289	48	0.0662843450	3.5646		0.0183313	0.065343752735
LaAlO3-cubic	0.43863784	361.67888	24	0.0663572061	3.5624	60.279237404	0.018363842	0.065419351817

For non-cubic phases, bond length and electronic charge density refer to the shortest bond, which is also the strongest bond.

Table 6.1

6.2 Discussion

Using the Bridge index as a guide to bond strength, the answer to the main question "why is the BO_6 cage so resilient?" can be seen in the table.

It is because the $B-O$ bonds that hold it together are very strong!

At the risk of producing too "noisy" a picture, Figure 5.16 is reproduced with some of the the above data plotted against the best fit curve:

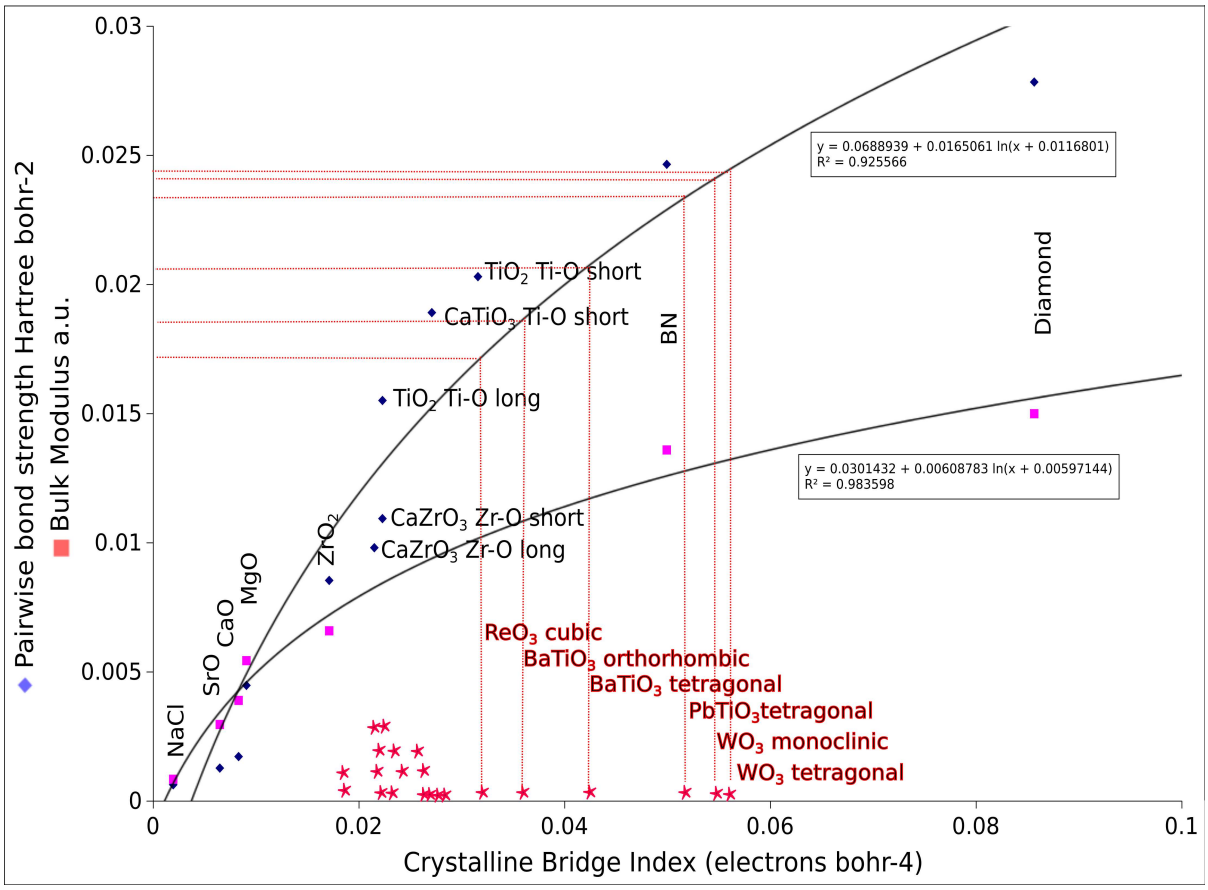

Figure 6.1: Bridge Indeces from Table 6.1 plotted with red "stars" and annotated in red. Notice how strong the bonds are. These materials will all be as tough or tougher than cubic zirconia.

The crystalline Bridge Index (CBI) can furthermore help to understand the deformation of the ABO_3 perovskite's BO_6 octahedral cage, and the way in which the redistribution of collective electrons plays a role.

This deformation can involve changing the $B-O$ bond length along one or more axes, rotation of these axes relative to each other at a common corner, or twisting of the normal plane about an axis (usually alternating left - right along the axis) or combinations of these.

The following table 6.2 should be read together with table 5.1 and figures 5.12 to 5.15 inclusive, and recalling the ideas of electron re-arrangement in section 2.4.

Mineral and Phase	Bond Length $A-O$ (Bohrs)	Charge Density at BCP $e.bohr^{-3}$	CBI of $A-O$ bond in ABO_3
$CaTiO_3$ orthorhombic $Ca-O$	4.45217901939	0.0385116297961	0.00865006317769
$CaTiO3$ tetragonal $Ca-O$	4.63746536874	0.0310650323856	0.00669870929819
$CaTiO_3$ cubic $Ca-O$	5.16110969239	0.0169447987771	0.00328316966448
$SrTiO_3$ tetragonal $Sr-O$	5.23075160756	0.0208594167379	0.00398784310609
$SrTiO_3$ cubic $Sr-O$	5.23103368858	0.020848313382	0.00398550547046
$CaZrO_3$ orthorhombic $Ca-O$	4.47977784268	0.0375233259335	0.00837615775854
$CaZrO_3$ cubic $Ca-O$	5.52936030355	0.011859989213	0.00214491162845
$SrZrO_3$ orthorhombic $Sr-O$	4.82287003649	0.0334992359365	0.0069459130524
$SrZrO_3$ tetragonal $Sr-O$	4.96639062686	0.028703935454	0.00577963708669
$SrZrO_3$ cubic $Sr-O$	5.56951436326	0.0148602761312	0.00266814575957
$BaTiO_3$ tetragonal $Ba-O$	5.3075904566	0.02608666443	0.00491497312072
$BaTiO_3$ cubic $Ba-O$	5.35760433217	0.02501332876	0.00466875252616
$PbTiO_3$ tetragonal $Pb-O$	4.74236209938	0.0429573609877	0.00905822037362
$PbTiO_3$ cubic $Pb-O$	5.25730426718	0.0211984584379	0.00403219166337
CaO $Ca-O$	4.5584	0.037796116889	0.00829153143406
SrO $Sr-O$	4.8757	0.031518901201	0.00646448739689
BaO $Ba-O$	5.18442023762	0.0337391767342	0.00650780129461
PbO $Pb-O$	4.48312942645	0.0577083920775	0.01287234576299
$BaTiO_3$ $Ti-O$ long	4.49346627879	0.0341144835492	0.00759201948621
$BaTiO_3$ $Ti-O$ short	3.40834387935	0.149348312177	0.04381844011746
$PbTiO_3$ $Ti-O$ long	4.52177286638	0.0340994375981	0.00754116551312
$PbTiO_3$ $Ti-O$ short	3.33041716529	0.165617290762	0.04972869239568

Table 6.2

The first thing to notice is that the $A-O$ bond in the ABO_3 cubic perovskites is reduced in strength from that in the oxides, and often significantly so in all the less symmetrical phases except for orthorhombic $SrZrO_3$. This is one indication that the A ion has supplied electronic charge density to other bonds - W.A. Harrison's idea discussed earlier in section 2.3.2 page 43. This seems clearly to be the case in the strongly polarised materials where the $B-O$ bond lengths along an axis are different, producing polarisation and ferroelectric effects. There is a clear difference in bond strengths and charge density at the BCP on either side of the B atom. $BaTiO_3$ and $PbTiO_3$ are the best examples of this.

On the other hand, where significant rotation of the octahedral cage exists in a deformed phase, some of the A atoms have retained or even gained on their binary oxide bond strengths. Contrary to W.A. Harrison's idea, they act as electron acceptors. And this is confirmed by the fact that phases with strong rotational deformation have little or no length deformation - there are not enough electrons for both to occur.

The rotations are caused by large electronegativity difference between the A ion and the O ion in its vicinity creating a strong ionic bond. This bond will not break the even stronger somewhat covalent bonds of the octahedral cage but it will attract the O ion at the vertex of the cage, thus rotating it.

6.3 Conclusions

The distinctive structure of the oxide perovskites is created by the quantum mechanical constraints on the small number of outer valence and conduction (collective) electrons as they are re-arranged from their precursor atom or oxide states. In general the oxide perovskites are tougher with stronger bonds than the precursor oxides.

A useful ordinal index of pairwise bond strength has been proposed and justified with a simple local density approximation model.

It has been demonstrated that knowledge of atomic outer orbital energies enables prediction of suitable elements to form oxide perovskites, and of the type and strength of the bonds in the resultant perovskite.

High electronegativity differences will favour rotationally distorted phases. Low electronegativity differences will favour polarisation along one or more axes.

These considerations should help in the prediction of or search for certain mechanical or electrical properties

Appendix A

A systematic Study of Selected Perovskites

This appendix reports the results of “identical” calculations on various groups of perovskites in order to compare and contrast the effects of different A and B cations with regard to electronic structure, bond characteristics and physical properties. By “identical” is meant that all of the examples studied were calculated with the DFT (Kohn-Sham) Hamiltonian, Becke gradient-corrected (GGA) exchange functionals (of the electron density and its gradient) [65] and the Lee - Yang - Parr GGA correlation functional [66] . A linear combination of Hartree-Fock (HF) exchange to counter the DFT tendency to under-estimate the band gap was employed. This varied between 10% and 40% between mineral species, but was maintained at the same level for all phases of each mineral studied . As far as possible all input parameters and tolerances were kept the same , because results were to be compared across bond types, but level shift and mixing techniques, subsequently adjusted, were needed to achieve SCF convergence for metallic minerals. All structural measurements are after full geometry optimisation. All measurements and calculations are in atomic units.

The following species and phases were studied:

The binary perovskite oxides

- WO3-Monoclinic
- WO3-Tetragonal
- ReO3-cubic

The Alkaline Earth Titanates

- CaTiO3-orthorhombic
- CaTiO3-tetragonal

- CaTiO3-cubic
- SrTiO3-tetragonal
- SrTiO3-cubic
- BaTiO3-orthorhombic
- BaTiO3-tetragonal
- BaTiO3-cubic

The Alkaline Earth Zirconates

- CaZrO3-orthorhombic
- CaZrO3-cubic
- SrZrO3-orthorhombic Pnma
- SrZrO3-orthorhombic Cmcm
- SrZrO3-tetragonal
- SrZrO3-cubic
- BaZrO3-cubic

Other perovskites

- PbTiO3-tetragonal
- PbTiO3-cubic
- LaAlO3-trigonal
- LaAlO3-cubic

A.1 The binary perovskite oxides - Tungsten trioxide and Rhenium trioxide

These binary oxide perovskites would seem to be simpler than the ternary compounds, because their Shannon and Prewitt radii of W and Re are conveniently small and their valences allow complete coordination with the oxygen. In fact they are both complex and interesting.

A.1.1 Tungsten trioxide WO_3

WO_3 might be expected to possess a simple set of properties and crystal phases of high symmetry because the $4f$ shell of the W atom is full and the 4 $5d$ and 2 $6s$ valence electrons would lend themselves to a simple relationship with the six surrounding O atoms. This is not the case. There are eight phases [128], [129], [130], [131] :

1. $0 - 243\,K$ - monoclinic Pc
2. $243 - 290\,K$ - triclinic $P\bar{1}$
3. $290 - 623\,K$ - monoclinic $P2_1/n$
4. $623 - 993\,K$ - orthorhombic $Pbcn$
5. $993 - 1073\,K$ - monoclinic $P2_1/c$
6. $1073 - 1173\,K$ - tetragonal $P4/ncc$
7. $1173\,K - upwards$ - tetragonal $P4/nmm$
8. $973\,K and\, 0.66 GPa$ - cubic $Pm\bar{3}m$

Phase 1. is a ferroelectric insulator while the other phases are indirect band gap semi-conductors. Phase 2 can be continued up to at least $298\,K$ with careful preparation, and room temperature specimens are usually mixtures of phase 2 and phase 3. Phase 5 was first observed in 2002 [130]. Phase 8 was also announced in 2002, [131]. It was prepared by the pressurised heating of a nano-particle powder and was stable enough for ex-situ testing and probing which showed that the sample was slightly non-stoichiometric, being $W_{0.90(3)}O_3$. It should be noted that WO_3 readily forms bronzes such as Na_xWO_3 $(0.4 < x < 1.0)$ which are stable cubic metals.
The figures on the next pages illustrates various properties of the end phases, 1 and 7 of the above series at normal pressure. The crystal structure, electronic charge density maps, band structure and density of states were calculated by the author for this study. The band gaps are both in the region $-0.25\ -\ 0.00\ Hartree$. The unoccupied bands are not very well represented by CRYSTAL06, which is a ground state calculation. Notice that the monoclinic form is an insulator, band gap of $0.231\ Hartree$ and the tetragonal form is a slightly indirect-gap semi-conductor.

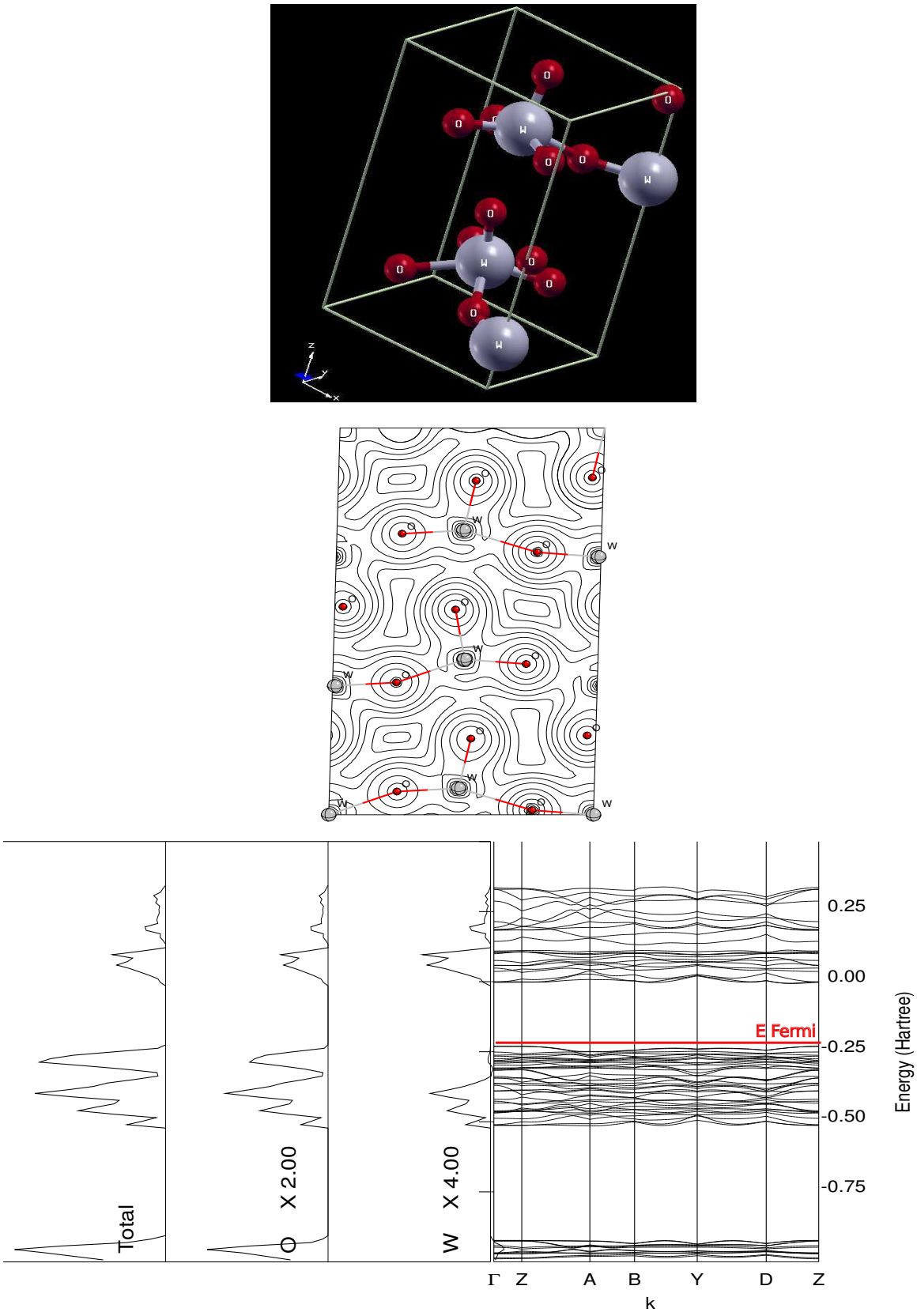

Figure A.1: Monoclinic phase of WO_3 : conventional unit cell, electronic charge density in the $(1\,\bar{1}\,0)$ plane Band Structure and Density of States of phase1 - monoclinic $P1C1$.

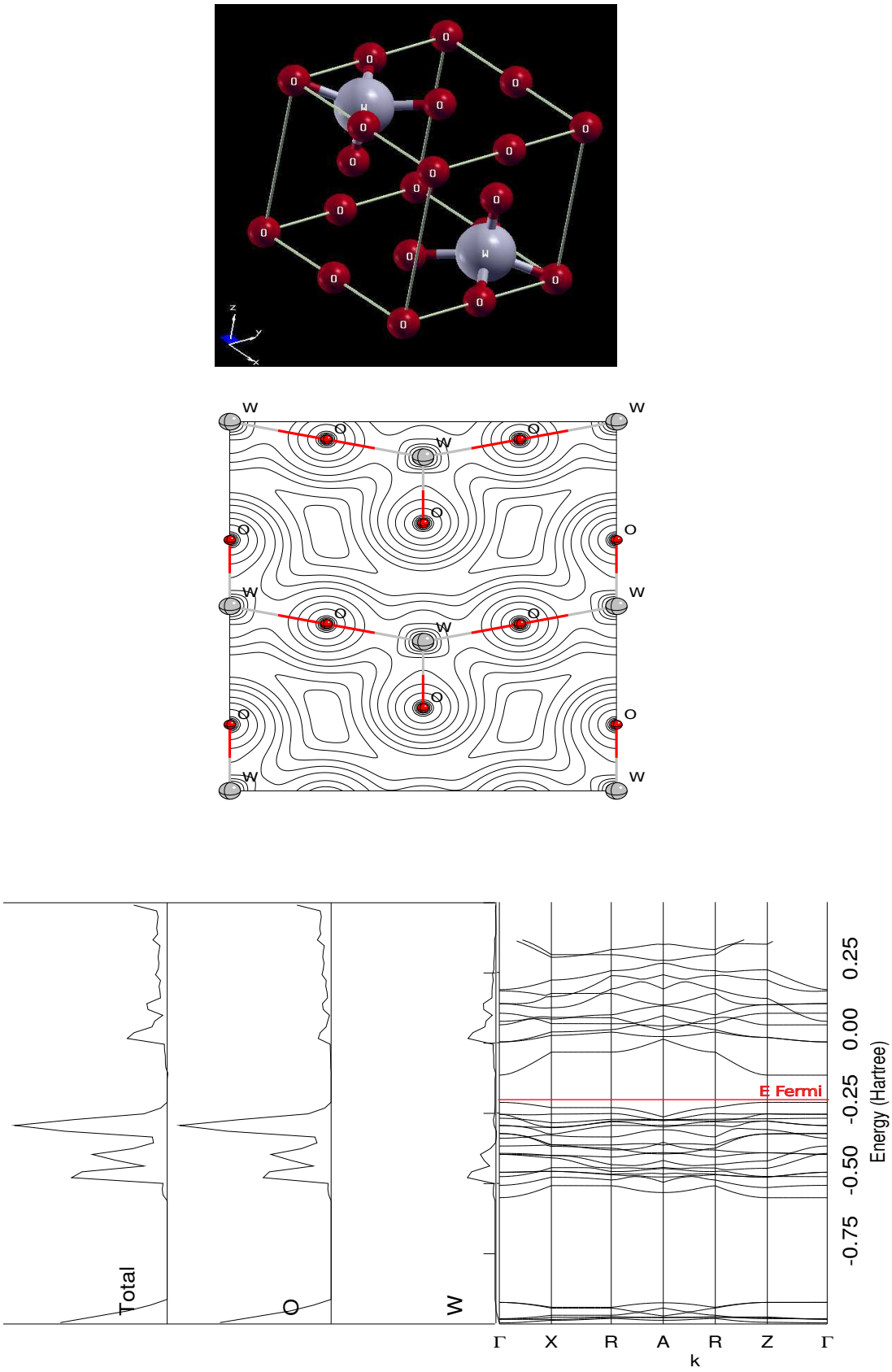

Figure A.2: Tetragonal phase of WO_3 : conventional unit cell, electronic charge density in the $(1\,\bar{1}\,0)$ plane Band Structure and Density of States of phase7 - tetragonal $P4/nmm$.

Unfortunately the Bader atom forms cannot be accurately represented for this phase because the pseudo-potential used for the W atom obscures the Bond Critical Point and the Bader atom boundary for the shorter of the axial Crystalline Bonds and the equatorial Crystalline Bonds. This does not happen in the case of $\mathrm{ReO_3}$, where a BCP can be discerned on the Bond Path electronic charge density profile. There will be a degree of estimation in the electronic charge density and the Crystalline bridge index measurements that are recorded below because of this. The following diagram illustrates the problem:

Never the less it is clear that the ECD at the BCP will be higher in the short $\mathrm{W-O}$ bond in $\mathrm{WO_3}$ than for the equal bonds in $\mathrm{ReO_3}$, and the bond length is shorter so the bridge index, therefore the Crystalline Bond Strength, will be greater.

The same problem occurs with the tetragonal phase, as seen in the following diagram:

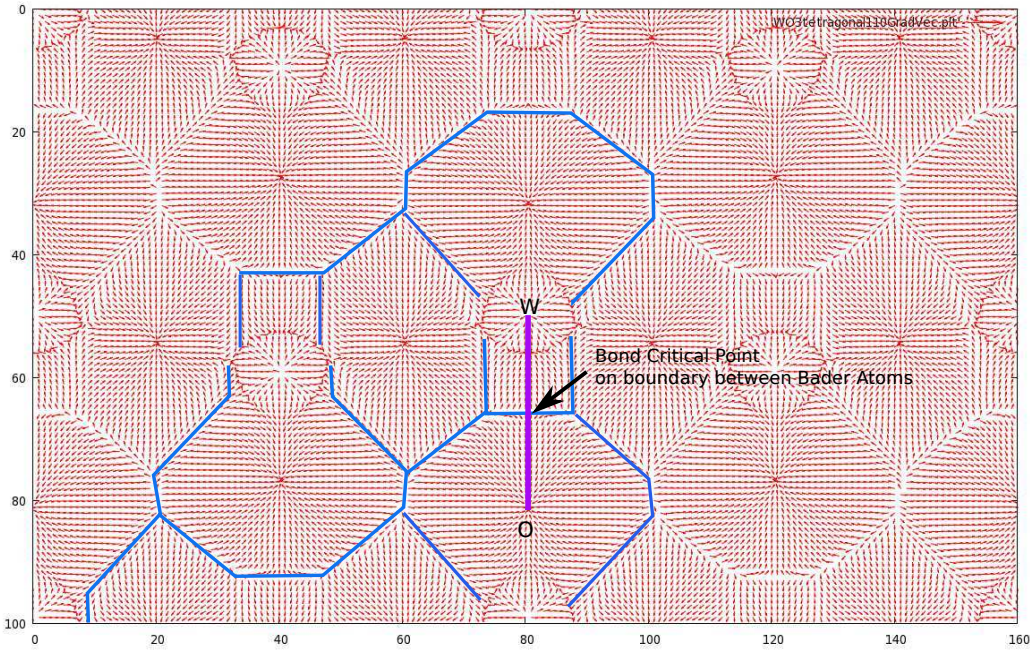

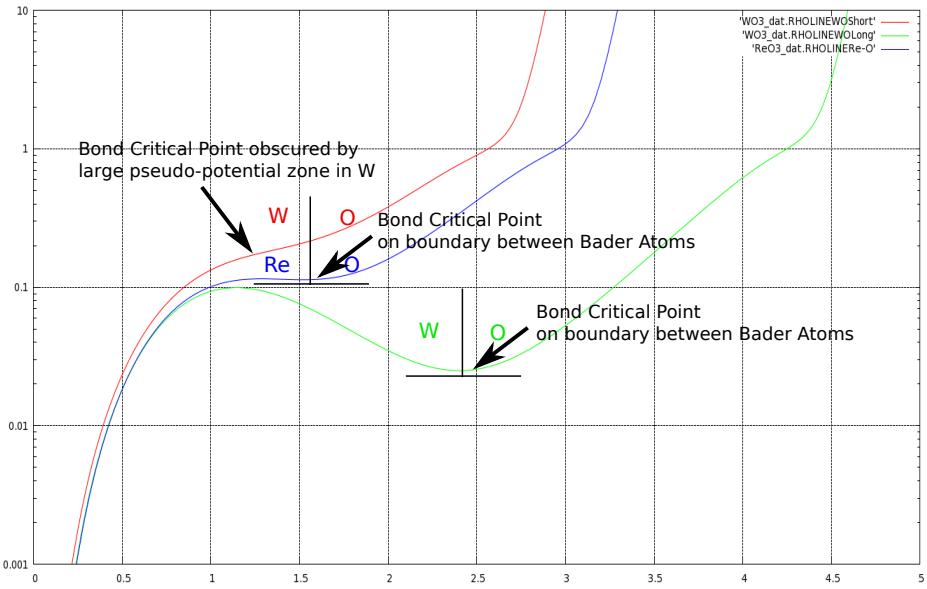

Figure A.3: The Pseudo-Potential used in the CRYSTAL06 calculation extends far enough spatially to obscure the boundaries of the W Bader atom. Comparison of the Bond Path electronic charge density profiles illustrate the problem, which does not occur in the case of ReO_3

A.1.1.1 Measurements

Phase 1 - monoclinic:

Band Gap = 0.2308103 Hartrees

Electrostatic Potential at short $W - O$ BCP 9.08561E-01 a.u

LATTICE PARAMETERS (BOHR AND DEGREES) - PRIMITIVE CELL

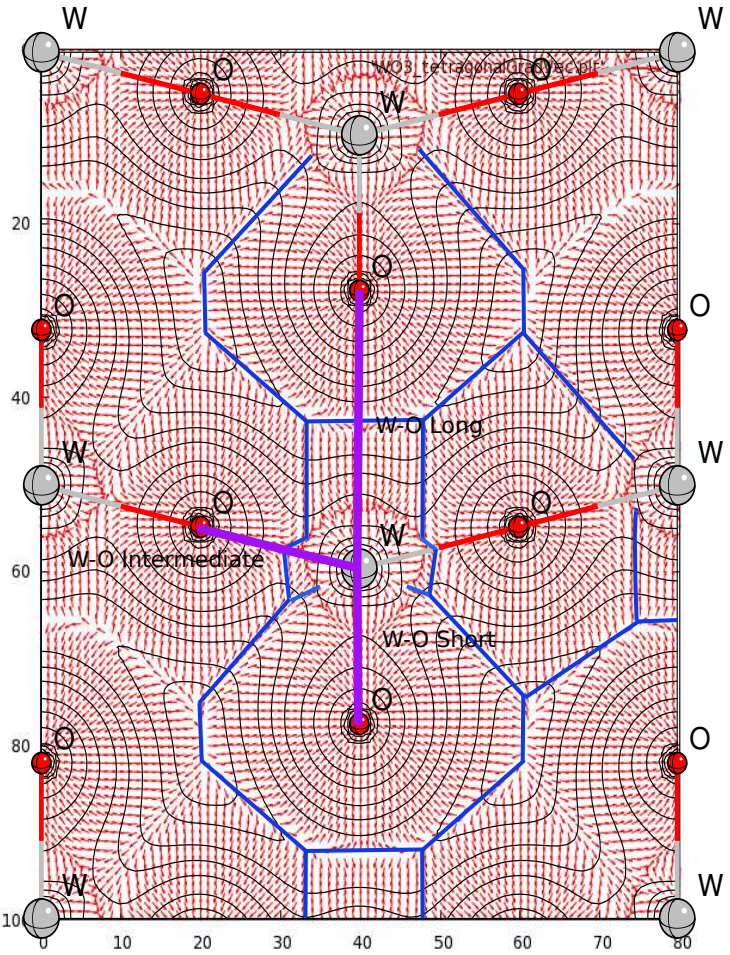

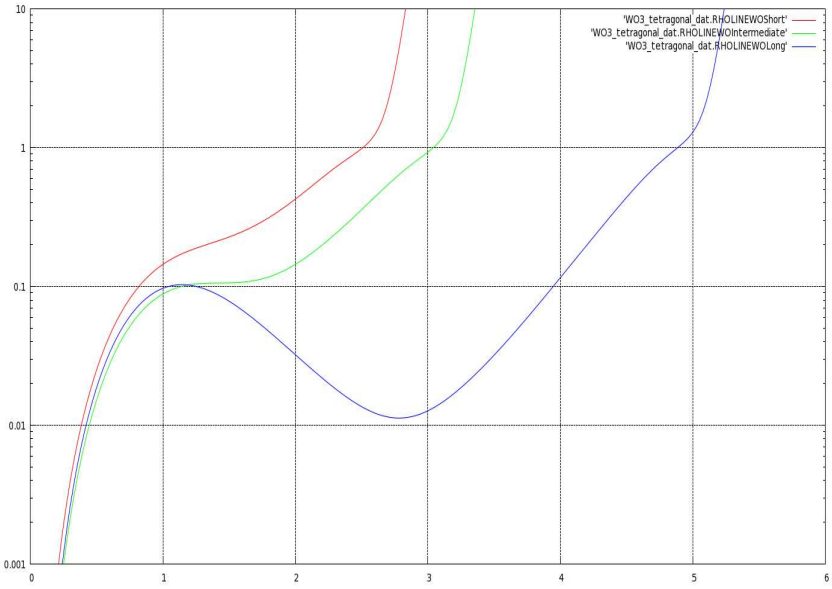

Figure A.4: The same problem that Pseudo-Potential used in the CRYSTAL06 calculation extends far enough spatially to obscure the boundaries of the W Bader atom also occurs in the tetragonal phase. Again the Bond Path electronic charge density profiles illustrate the problem which occurs for the short and intermediate $W-O$ bonds, but not for the long bond

A	B	C	α	β	γ	Volume $Bohr^3$
9.86823	9.66115	15.49995	90.0000	91.4158	90.0000	1477.28860

N. OF ATOMS PER CELL	16	NUMBER OF SHELLS	76
NUMBER OF AO	288	N. OF ELECTRONS PER CELL	120
CORE ELECTRONS PER CELL	24		
N. OF SYMMETRY OPERATORS	2	CORE PSEUDO POTENTIAL	
TOTAL ENERGY	-9.3412039200723E+02		
ENERGY per FORMULA UNIT		-233.530098002 Hartrees	

Axial short bond $\mathrm{W}-\mathrm{O}$: Bond Length $3.0944\,Bohrs$

Electronic charge density at BCP: $0.054937952\ electrons\,Bohr^{-3}$

Crystalline bridge index 0.017753992

This monoclinic phase is really very irregular. It consists of alternating planes parallel to $(0\,1\,0)$ within which all the W atoms are displaced down, towards $(-Z)$ or up, towards $(+Z)$. The following diagram illustrates this, and the measurements show that the corresponding O_6 octahedra are inverted, similar but not at all congruent, and quiet deformed.

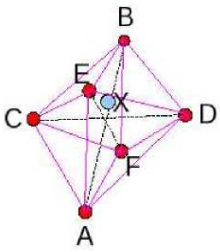

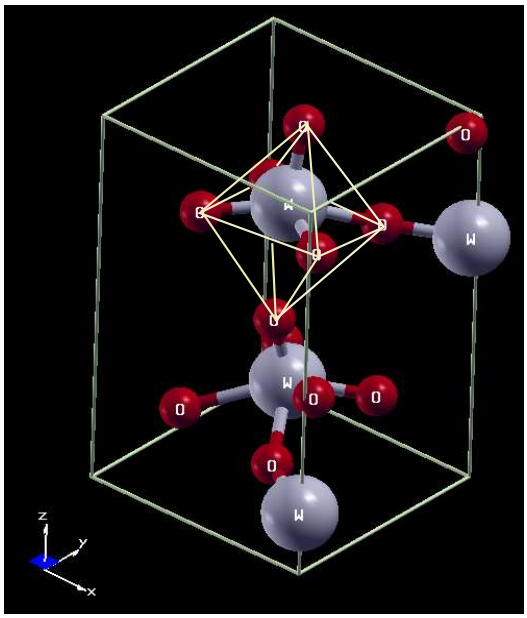

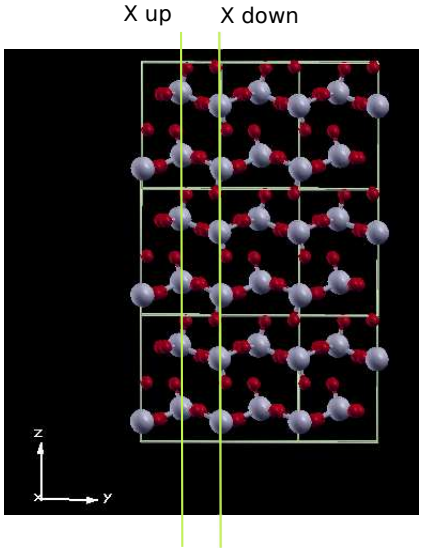

X up:

AX = 4.719 Bohrs	AXB = 171.360 deg
BX = 3.0944 Bohrs	AXC = 80.988 deg
CX = 3.2218 Bohrs	AXD = 74.082 deg
DX = 3.9158 Bohrs	AXE = 75.957 deg
EX = 4.0557 Bohrs	AXF = 82.496 deg
FX = 3.3010 Bohrs	CXE = 85.811 deg
	EXD = 75.925 deg
	DXF = 88.339 deg
	FXC = 101.137 deg

X down:

AX = 3.0960 Bohrs	BXA = 171.476 deg
BX = 4.7887 Bohrs	BXC = 82.647 deg
CX = 3.9082 Bohrs	BXD = 75.937 deg
DX = 3.2299 Bohrs	BXE = 74..206 deg
EX = 4.2961 Bohrs	BXF = 80.955 deg
FX = 4.0610 Bohrs	CXE = 88.677 deg
	EXD = 75.924 deg
	DXF = 85.656 deg
	FXC = 109.039 deg

Figure A.5: Geometry of phase 1 monoclinic WO_3 with measurements according to the scheme outlined in 1.4.3.

WO3-monoclinic ALPHA+BETA ELECTRONS
MULLIKEN POPULATION ANALYSIS - NO. OF ELECTRONS 120.000000

ATOM	Z	CHARGE	A.O. POPULATION
1 W	274	2.002	-0.034 0.000 0.000 -0.001 -0.210 -0.229 -0.198 -0.163 0.817 0.624 0.630 0.600 0.755 -0.218 -0.057 -0.080 -0.058 -0.175
2 W	274	2.002	-0.034 0.000 0.000 -0.001 -0.210 -0.229 -0.198 -0.163 0.817 0.624 0.630 0.600 0.755 -0.218 -0.057 -0.080 -0.058 -0.175
3 W	274	1.994	-0.034 0.000 0.000 -0.001 -0.214 -0.229 -0.201 -0.163 0.817 0.623 0.631 0.597 0.755 -0.218 -0.057 -0.081 -0.058 -0.174
4 W	274	1.994	-0.034 0.000 0.000 -0.001 -0.214 -0.229 -0.201 -0.163 0.817 0.623 0.631 0.597 0.755 -0.218 -0.057 -0.081 -0.058 -0.174
5 O	8	9.337	1.997 0.535 0.735 0.702 0.730 1.101 0.622 0.603 0.652 0.520 0.350 0.358 0.390 0.009 0.015 0.015 0.002 0.003
6 O	8	9.337	1.997 0.535 0.735 0.702 0.730 1.101 0.622 0.603 0.652 0.520 0.350 0.358 0.390 0.009 0.015 0.015 0.002 0.003
7 O	8	9.324	1.998 0.521 0.727 0.711 0.758 1.075 0.651 0.628 0.647 0.499 0.363 0.340 0.375 0.003 0.004 0.005 0.013 0.005
8 O	8	9.324	1.998 0.521 0.727 0.711 0.758 1.075 0.651 0.628 0.647 0.499 0.363 0.340 0.375 0.003 0.004 0.005 0.013 0.005
9 O	8	9.329	1.998 0.522 0.727 0.710 0.757 1.076 0.652 0.629 0.647 0.501 0.364 0.341 0.374 0.003 0.004 0.005 0.013 0.005
10 O	8	9.329	1.998 0.522 0.727 0.710 0.757 1.076 0.652 0.629 0.647 0.501 0.364 0.341 0.374 0.003 0.004 0.005 0.013 0.005
11 O	8	9.342	1.998 0.518 0.731 0.717 0.752 1.070 0.655 0.643 0.643 0.484 0.368 0.351 0.384 0.004 0.007 0.003 0.008 0.007
12 O	8	9.342	1.998 0.518 0.731 0.717 0.752 1.070 0.655 0.643 0.643 0.484 0.368 0.351 0.384 0.004 0.007 0.003 0.008 0.007
13 O	8	9.342	1.998 0.518 0.730 0.717 0.751 1.070 0.656 0.644 0.645 0.484 0.366 0.352 0.384 0.004 0.007 0.002 0.008 0.007
14 O	8	9.342	1.998 0.518 0.730 0.717 0.751 1.070 0.656 0.644 0.645 0.484 0.366 0.352 0.384 0.004 0.007 0.002 0.008 0.007
15 O	8	9.332	1.997 0.535 0.735 0.702 0.730 1.101 0.621 0.603 0.652 0.518 0.350 0.359 0.387 0.009 0.015 0.015 0.002 0.003
16 O	8	9.332	1.997 0.535 0.735 0.702 0.730 1.101 0.621 0.603 0.652 0.518 0.350 0.359 0.387 0.009 0.015 0.015 0.002 0.003

ATOM	Z	CHARGE	SHELL POPULATION
1 W	274	2.002	-0.036 -0.801 3.427 -0.589
2 W	274	2.002	-0.036 -0.801 3.427 -0.589
3 W	274	1.994	-0.036 -0.807 3.424 -0.588
4 W	274	1.994	-0.036 -0.807 3.424 -0.588
5 O	8	9.337	1.997 2.702 2.977 1.617 0.043
6 O	8	9.337	1.997 2.702 2.977 1.617 0.043
7 O	8	9.324	1.998 2.717 3.002 1.577 0.030
8 O	8	9.324	1.998 2.717 3.002 1.577 0.030
9 O	8	9.329	1.998 2.717 3.004 1.580 0.031
10 O	8	9.329	1.998 2.717 3.004 1.580 0.031
11 O	8	9.342	1.998 2.718 3.011 1.587 0.028
12 O	8	9.342	1.998 2.718 3.011 1.587 0.028
13 O	8	9.342	1.998 2.717 3.014 1.585 0.028

14 O	8	9.342	1.998	2.717	3.014	1.585	0.028
15 O	8	9.332	1.997	2.702	2.976	1.614	0.043
16 O	8	9.332	1.997	2.702	2.976	1.614	0.043

OVERLAP POPULATION CONDENSED TO ATOMS FOR FIRST 6 NEIGHBORS

ATOM A	ATOM B	CELL	R(AB)/AU	R(AB)/ANG	OVPOP(AB)
1 W	15 O	(0 0 -1)	3.096	1.638	-0.360
	8 O	(0 0 0)	3.230	1.709	-0.165
	12 O	(0 0 0)	3.296	1.744	-0.114
	14 O	(0 0 0)	3.908	2.068	0.055
	10 O	(0 0 0)	4.061	2.149	0.065
	16 O	(0 0 0)	4.789	2.534	0.025
3 W	5 O	(0 1 0)	3.094	1.637	-0.365
	10 O	(0 0 0)	3.222	1.705	-0.178
	14 O	(1 0 0)	3.301	1.747	-0.110
	12 O	(1 1 0)	3.916	2.072	0.054
	8 O	(0 1 0)	4.056	2.146	0.067
	6 O	(0 0 -1)	4.792	2.536	0.025
5 O	3 W	(0 -1 0)	3.094	1.637	-0.365
	4 W	(0 0 0)	4.792	2.536	0.025
	10 O	(0 -1 0)	4.978	2.634	0.003
	14 O	(1 -1 0)	5.012	2.652	-0.018
	11 O	(1 -1 0)	5.292	2.800	-0.014
	9 O	(0 0 0)	5.339	2.825	-0.010
7 O	2 W	(0 0 0)	3.230	1.709	-0.165
	4 W	(0 1 0)	4.056	2.146	0.067
	11 O	(1 0 0)	4.905	2.596	-0.047
	16 O	(0 0 0)	4.984	2.637	0.003
	9 O	(0 1 0)	4.992	2.642	-0.035
	9 O	(0 0 0)	4.994	2.643	-0.035
9 O	4 W	(0 0 0)	3.222	1.705	-0.178
	2 W	(0 0 0)	4.061	2.149	0.065
	13 O	(0 0 0)	4.904	2.595	-0.046
	6 O	(0 -1 0)	4.978	2.634	0.003
	7 O	(0 -1 0)	4.992	2.642	-0.035
	7 O	(0 0 0)	4.994	2.643	-0.035
11 O	2 W	(0 0 0)	3.296	1.744	-0.114
	4 W	(-1 1 0)	3.916	2.072	0.054
	7 O	(-1 0 0)	4.905	2.596	-0.047
	16 O	(0 0 0)	5.003	2.647	-0.016
	7 O	(0 0 0)	5.037	2.666	-0.028
	13 O	(0 1 0)	5.048	2.671	-0.030
13 O	4 W	(-1 0 0)	3.301	1.747	-0.110
	2 W	(0 0 0)	3.908	2.068	0.055
	9 O	(0 0 0)	4.904	2.595	-0.046
	6 O	(-1 -1 0)	5.012	2.652	-0.018
	9 O	(-1 0 0)	5.038	2.666	-0.026
	11 O	(0 -1 0)	5.048	2.671	-0.030
15 O	1 W	(0 0 1)	3.096	1.638	-0.360
	2 W	(0 0 0)	4.789	2.534	0.025
	8 O	(0 0 1)	4.984	2.637	0.003
	12 O	(0 0 1)	5.003	2.647	-0.016
	13 O	(0 0 0)	5.293	2.801	-0.014
	7 O	(0 0 0)	5.339	2.825	-0.009

Phase 7 - tetragonal:

Band Gap = 0.0966177 Hartrees

LATTICE PARAMETERS (BOHR AND DEGREES) - PRIMITIVE CELL

A	B	C	α	β	γ	Volume $Bohr^3$
9.75224	9.75224	8.47259	90.0000	90.0000	90.0000	805.79506

N. OF ATOMS PER CELL	8	NUMBER OF SHELLS	38
NUMBER OF AO	144	N. OF ELECTRONS PER CELL	60
CORE ELECTRONS PER CELL	12		
N. OF SYMMETRY OPERATORS	16	CORE PSEUDO POTENTIAL	
TOTAL ENERGY	-4.6704088148299E+02		
ENERGY per FORMULA UNIT		-233.520440741 Hartrees	

This tetragonal phase is much more regular. It still consists of alternating planes parallel to $(0\,1\,0)$ within which all the W atoms are displaced down, towards $(-Z)$ or up, towards $(+Z)$, but now the corresponding O_6 octahedra are inverted, congruent, and elongated but not otherwise deformed.

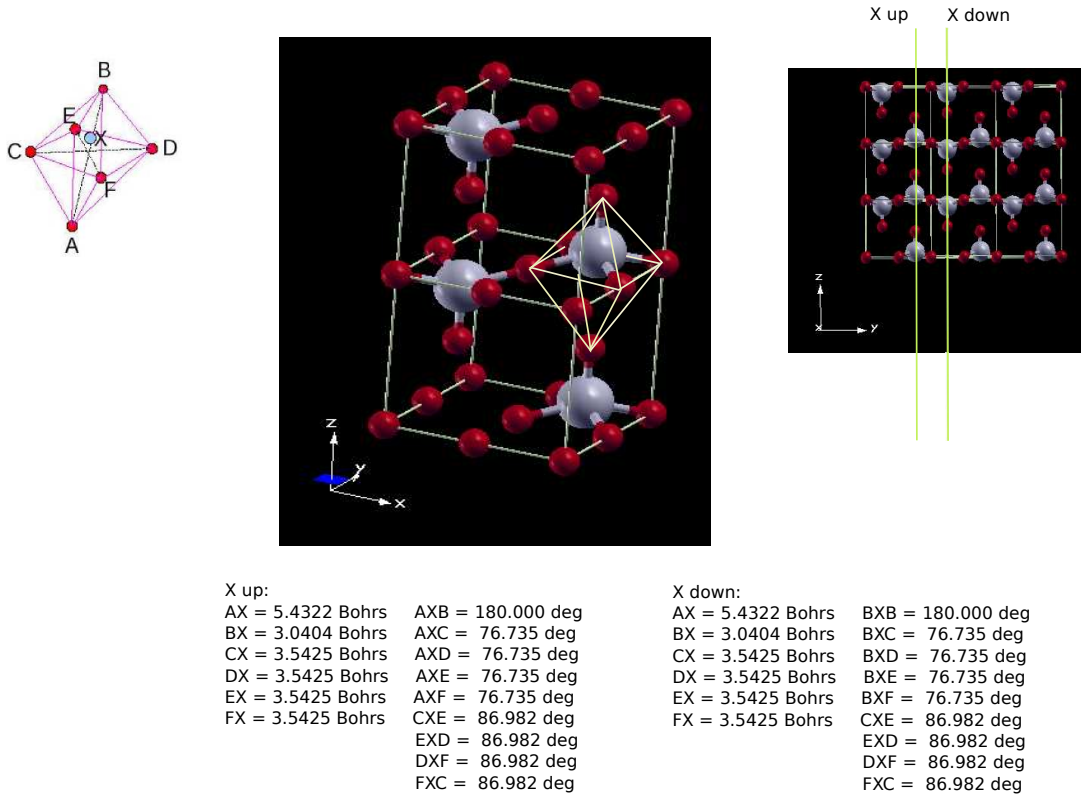

Figure A.6: Geometry of phase 7 tetragonal WO_3 with measurements according to the scheme outlined in 1.4.3.

WO3-tetragonal ALPHA+BETA ELECTRONS
MULLIKEN POPULATION ANALYSIS - NO. OF ELECTRONS 60.000000

ATOM	Z	CHARGE	A.O. POPULATION
1 W	274	2.086	-0.040 0.001 0.001 -0.002 -0.153 -0.194 -0.194 -0.152 0.853 0.645 0.645 0.479 0.710 -0.251 -0.067 -0.067 -0.002 -0.125
2 W	274	2.086	-0.040 0.001 0.001 -0.002 -0.153 -0.194 -0.194 -0.152 0.853 0.645 0.645 0.479 0.710 -0.251 -0.067 -0.067 -0.002 -0.125
3 O	8	9.320	1.997 0.541 0.710 0.710 0.735 1.121 0.605 0.605 0.635 0.527 0.341 0.341 0.404 0.009 0.019 0.019 0.001 0.001
4 O	8	9.320	1.997 0.541 0.710 0.710 0.735 1.121 0.605 0.605 0.635 0.527 0.341 0.341 0.404 0.009 0.019 0.019 0.001 0.001
5 O	8	9.297	1.998 0.512 0.721 0.721 0.771 1.062 0.651 0.651 0.658 0.465 0.333 0.333 0.402 0.002 0.003 0.003 0.007 0.006
6 O	8	9.297	1.998 0.512 0.721 0.721 0.771 1.062 0.651 0.651 0.658 0.465 0.333 0.333 0.402 0.002 0.003 0.003 0.007 0.006
7 O	8	9.297	1.998 0.512 0.721 0.721 0.771 1.062 0.651 0.651 0.658 0.465 0.333 0.333 0.402 0.002 0.003 0.003 0.007 0.006
8 O	8	9.297	1.998 0.512 0.721 0.721 0.771 1.062 0.651 0.651 0.658 0.465 0.333 0.333 0.402 0.002 0.003 0.003 0.007 0.006

ATOM	Z	CHARGE	SHELL POPULATION
1 W	274	2.086	-0.041 -0.692 3.331 -0.512
2 W	274	2.086	-0.041 -0.692 3.331 -0.512
3 O	8	9.320	1.997 2.695 2.966 1.613 0.049
4 O	8	9.320	1.997 2.695 2.966 1.613 0.049
5 O	8	9.297	1.998 2.725 3.022 1.532 0.020
6 O	8	9.297	1.998 2.725 3.022 1.532 0.020
7 O	8	9.297	1.998 2.725 3.022 1.532 0.020
8 O	8	9.297	1.998 2.725 3.022 1.532 0.020

OVERLAP POPULATION CONDENSED TO ATOMS FOR FIRST 6 NEIGHBORS

ATOM A	ATOM B	CELL	R(AB)/AU	R(AB)/ANG	OVPOP(AB)
1 W	3 O	(0 0 -1)	3.040	1.609	-0.404
	5 O	(0 0 0)	3.542	1.875	0.014
	3 O	(0 0 0)	5.432	2.875	0.009
	2 W	(0 0 0)	7.085	3.749	-0.001
	5 O	(1 0 0)	7.753	4.102	-0.001
	4 O	(0 0 0)	7.877	4.168	0.000

ATOM A	ATOM B	CELL	R(AB)/AU	R(AB)/ANG	OVPOP(AB)
3 O	1 W	(0 0 1)	3.040	1.609	-0.404
	5 O	(0 0 1)	5.171	2.736	0.003
	1 W	(0 0 0)	5.432	2.875	0.009
	5 O	(0 0 0)	5.764	3.050	-0.004
	4 O	(0 0 1)	6.938	3.672	0.000
	2 W	(0 0 0)	7.877	4.168	0.000

ATOM A	ATOM B	CELL	R(AB)/AU	R(AB)/ANG	OVPOP(AB)
5 O	1 W	(0 0 0)	3.542	1.875	0.014
	7 O	(0 0 0)	4.876	2.580	-0.059
	3 O	(0 0 -1)	5.171	2.736	0.003
	3 O	0 0 0)	5.764	3.050	-0.004
	6 O	0 0 0)	6.896	3.649	-0.011
	1 W	(-1 0 0)	7.753	4.102	-0.001

A.1.2 Rhenium trioxide $\mathrm{ReO_3}$

Even though it has an extra (5^d) electron, $\mathrm{ReO_3}$ is much simpler and more regular in its crystalline form, At ambient pressure for all temperatures it is a stable cubic, $Pm3m$ metal with very good electrical conductivity of the same order as copper [132]. At $0.52\,GPa$ it is tetragonal, $P4/mbm$, and from $0.73\,GPa$ and higher pressures it is cubic, $Im3$. A single order parameter, the rotation angle of the $\mathrm{ReO_6}$ octahedra, describes the distortion in the high pressure phases [133]. In its crystal structure, metallic character and mechanical behaviour it has parallels in the sodium tungstate bronzes. The mechanical behaviour is also similar to that of $\mathrm{SiO_2}$ and other covalently bonded framework structures (Ibid).

Here is the Bader atom picture and electronic charge distribution profiles showing the high Crystalline bridge index of the six equal $\mathrm{Re}-\mathrm{O}$ bonds. Notice that there are no maxima normal to the $\mathrm{O}-\mathrm{O}$ or $\mathrm{Re}-\mathrm{Re}$ paths, so there is no (3, -1) critical point or Bond Critical Point (BCP) - therefore no Crystalline Bond between the atoms - along these paths. This explains why the $\mathrm{O_6}$ octahedra can rotate without destroying the perovskite structure.

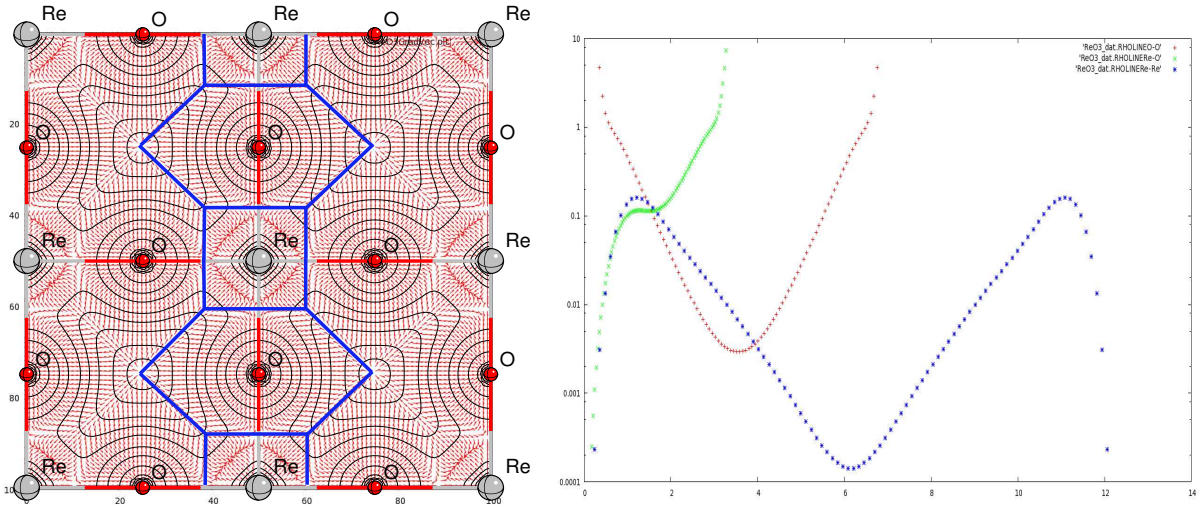

Figure A.7: Bader atoms in $\mathrm{ReO_3}$ and associated electronic charge density profiles. The electronic charge density map and the overlying Bader atoms are in the $(1\,\bar{1}\,0)$ plane.

The band structure and density of states are shown below:

A.1.2.1 Measurements

Band Gap = not present

Electrostatic Potential at $\mathrm{Re}-\mathrm{O}$ BCP 6.12086E-01 a.u.

LATTICE PARAMETERS (BOHR AND DEGREES) - PRIMITIVE CELL

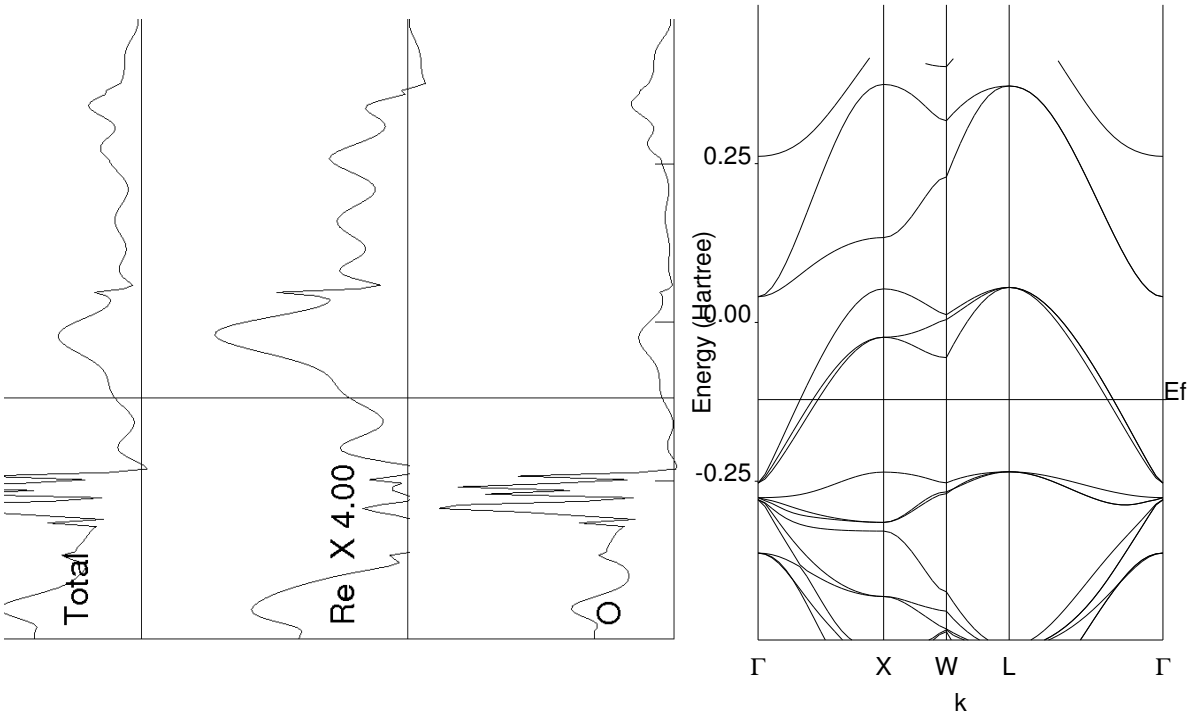

Figure A.8: Density of states and band structure of $\mathrm{ReO_3}$.

A	B	C	α	β	γ	Volume $Bohr^3$
6.96348	6.96348	6.96348	90.0000	90.0000	90.0000	337.65894

N. OF ATOMS PER CELL	4	NUMBER OF SHELLS	19
NUMBER OF AO	72	N. OF ELECTRONS PER CELL	31
CORE ELECTRONS PER CELL	6		
N. OF SYMMETRY OPERATORS	48	CORE PSEUDO POTENTIAL	
TOTAL ENERGY	-2.3687710635034E+02		
ENERGY per FORMULA UNIT		-236.8771063503 Hartrees	

The single cubic phase is completely regular with a square equatorial section, with equatorial and axial bond lengths all the same, and bond angles are all 90.

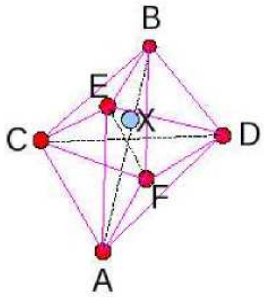

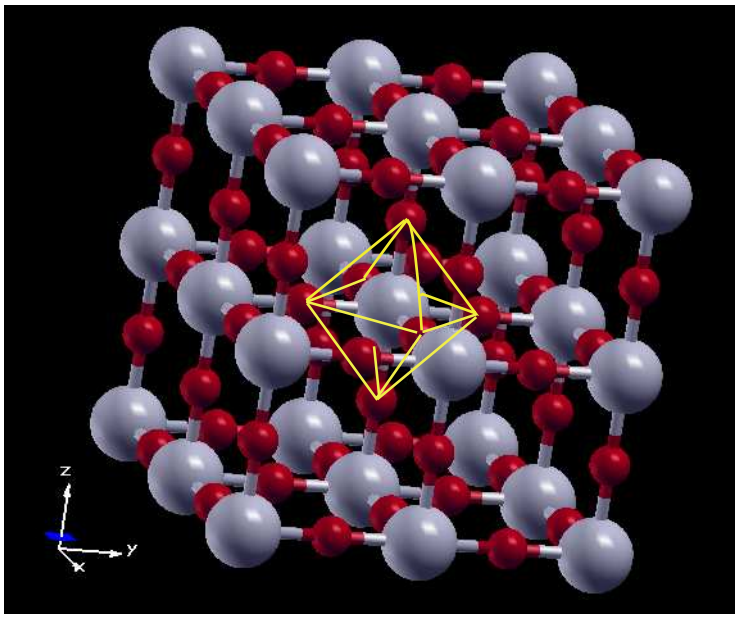

AX = 3.4817Bohrs	AXB = 180.000 deg
BX = 3.4817 Bohrs	AXC = 90.000 deg
CX = 3.4817 Bohrs	AXD = 90.000 deg
DX = 3.4817 Bohrs	AXE = 90.000 deg
EX = 3.4817 Bohrs	AXF = 90.000deg
FX = 3.4817 Bohrs	CXE = 90.000 deg
	EXD = 90.000 deg
	DXF = 90.000 deg
	FXC = 90.000 deg

Figure A.9: Geometry of ReO_3 with measurements according to the scheme outlined in 1.4.3.

ReO3-cubic ALPHA+BETA ELECTRONS
MULLIKEN POPULATION ANALYSIS - NO. OF ELECTRONS 30.998911

ATOM	Z	CHARGE	A.O. POPULATION
1 O	8	9.042	1.998 0.498 0.730 0.723 0.723 0.954 0.590 0.517
			0.517 0.552 0.361 0.427 0.427 0.002 0.011 0.001
			0.003 0.011
2 O	8	9.042	1.998 0.498 0.723 0.730 0.723 0.954 0.517 0.590
			0.517 0.552 0.427 0.361 0.427 0.002 0.001 0.011
			0.003 0.011
3 O	8	9.042	1.998 0.498 0.723 0.723 0.730 0.954 0.517 0.517
			0.590 0.552 0.427 0.427 0.361 0.003 0.011 0.011
			0.002 0.001
4 RE	275	3.874	-0.065 -0.002 -0.002 -0.002 0.128 -0.228 -0.228 -0.228
			0.693 0.944 0.944 0.693 0.944 0.119 0.015 0.015
			0.119 0.015

ATOM	Z	CHARGE	SHELL POPULATION
1 O	8	9.042	1.998 2.673 2.577 1.766 0.028
2 O	8	9.042	1.998 2.673 2.577 1.766 0.028
3 O	8	9.042	1.998 2.673 2.577 1.766 0.028
4 RE	275	3.874	-0.071 -0.554 4.216 0.283

OVERLAP POPULATION CONDENSED TO ATOMS FOR FIRST 6 NEIGHBORS

ATOM A	ATOM B	CELL	R(AB)/AU	R(AB)/ANG	OVPOP(AB)
1 O	4 RE	(0 0 0)	3.482	1.842	-0.045
	2 O	(0 0 0)	4.924	2.606	-0.039
	1 O	(-1 0 0)	6.963	3.685	-0.031
	4 RE	(0 1 0)	7.785	4.120	-0.001
	2 O	(0 0 1)	8.528	4.513	0.000
	1 O	(-1 -1 0)	9.848	5.211	0.000

ATOM A	ATOM B	CELL	R(AB)/AU	R(AB)/ANG	OVPOP(AB)
4 RE	1 O	(0 0 0)	3.482	1.842	-0.045
	4 RE	(-1 0 0)	6.963	3.685	-0.024
	1 O	(0 -1 0)	7.785	4.120	-0.001
	4 RE	(-1 -1 0)	9.848	5.211	0.000
	1 O	(1 0 0)	10.445	5.527	0.000
	4 RE	(-1 -1 -1)	12.061	6.382	0.000

A.2 The Alkaline Earth Titanates

Three examples are studied here, $\mathrm{CaTiO_3}$, $\mathrm{SrTiO_3}$ and $\mathrm{BaTiO_3}$. These Alkaline Earth Titanates have been extensively studied in pure and mixed forms because of their useful dielectric and ferroelectric properties, which are tunable by mixing and doping, and their suitability for immobilization of high-level radioactive wastes [135], [134], [136], [139], [26], [137] . The structural phase behaviour shows no trend - $\mathrm{CaTiO_3}$ has three phases, $\mathrm{SrTiO_3}$ has two and $\mathrm{BaTiO_3}$ has four. The A ion plays a role here which will be discussed in the next chapter. In this study all three cubic phases, and the orthorhombic and tetragonal phases of $\mathrm{CaTiO_3}$ and $\mathrm{BaTiO_3}$ were examined. Interestingly, of the many references used in this section, only [138] mentions that " Previous studies have shown that CaTiO3 orthorhombic perovskite is characterized by an enormous deformation from the cubic symmetry." This deformation is partly a distortion of the oxygen octahedral cage, but is mainly a rather pronounced tilting of the cages at an oxygen corner in two planes.

A.2.1 Calcium Titanate - the original perovskite $\mathrm{CaTiO_3}$

$\mathrm{CaTiO_3}$ occurs in nature as was mentioned in the opening section of this thesis. It is another example of phase stability incurring loss of symmetry. There are three phases [140] :

1. $0 - 1512\,K$ - orthorhombic $Pbnm$
2. $1512 - 1636\,K$ - tetragonal $I4/mcm$
3. $1636\,K - upwards$ - cubic $Pm\bar{3}m$

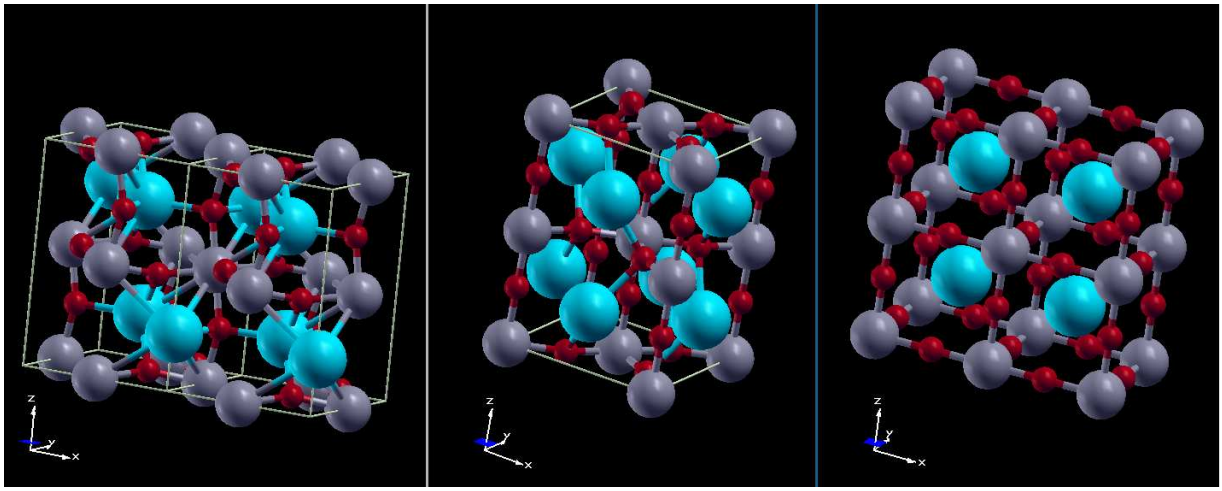

Figure A.10: The three phases of $CaTiO_3$

Phase 1 - orthorhombic.

The band structure is quite crowded as there are 432 Atomic orbitals in the primitive cell. Only the uppermost valence bands and the lower few virtual bands are displayed on a slightly expanded energy scale to illustrate the flattish bands and the band gap. Notice that the $Ti - O$ "covalency" occurs quite close to the top of the valence bands.

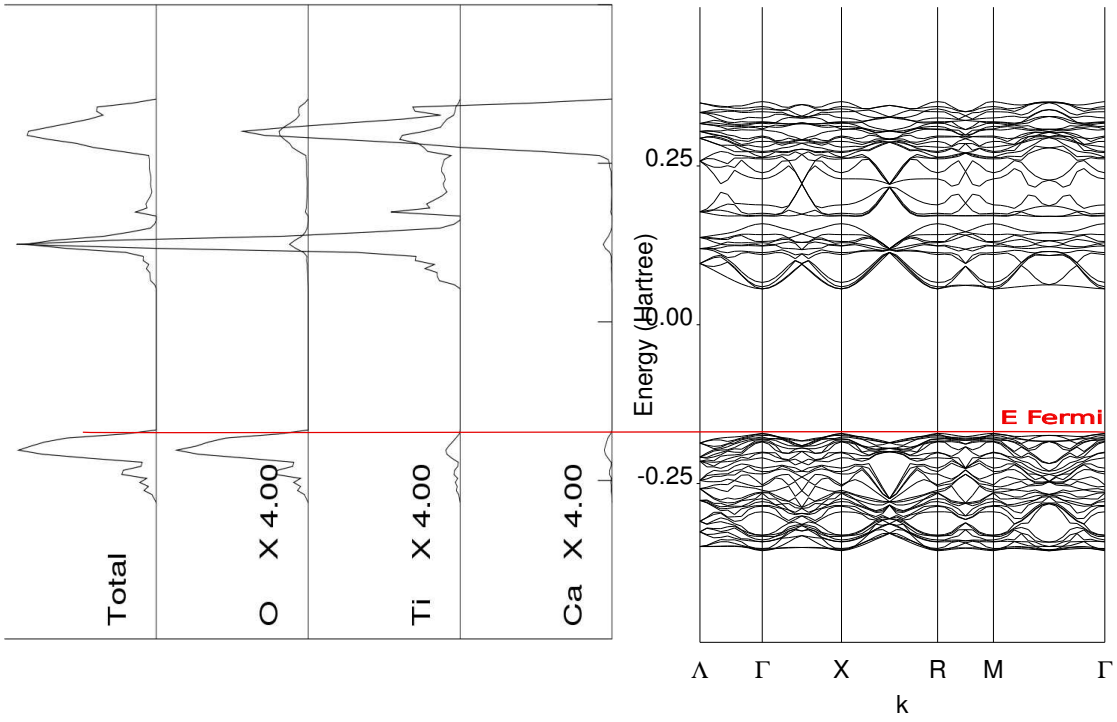

Figure A.11: $CaTiO_3$ orthorhombic phase band structure and density of states.

Measurements

Band Gap = 0.227472 Hartrees

LATTICE PARAMETERS (BOHR AND DEGREES) - PRIMITIVE CELL

A	B	C	α	β	γ	Volume $Bohr^3$
10.19020	10.32175	14.46266	90.0000	90.0000	90.0000	1521.1925

N. OF ATOMS PER CELL	20	NUMBER OF SHELLS	116
NUMBER OF AO	432	N. OF ELECTRONS PER CELL	264
CORE ELECTRONS PER CELL	168	N. OF SYMMETRY OPERATORS	8
TOTAL ENERGY	-7.0123793638616E+03		
ENERGY per FORMULA UNIT		-1753.094840965 Hartrees	
VOLUME per FORMULA UNIT		380.298125 $Bohr^3$	

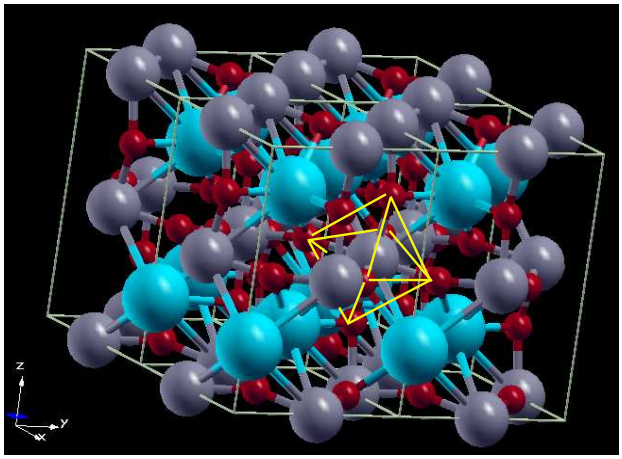

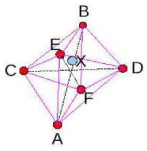

AX = 3.6972 Bohrs
BX = 3.6972 Bohrs
CX = 3.7128 Bohrs
DX = 3.7128 Bohrs
EX = 3.7070 Bohrs
FX = 3.7070 Bohrs

AXB = 180.000 deg
AXC = 89.332 deg
AXD = 90.668 deg
AXE = 90.871 deg
AXF = 89.129 deg
CXE = 89.422 deg
EXD = 90.578 deg
DXF = 89.422 deg
FXC = 90.578 deg

Tilt angle at B = 116.833 deg
Tilt angle at D = 155.596 deg

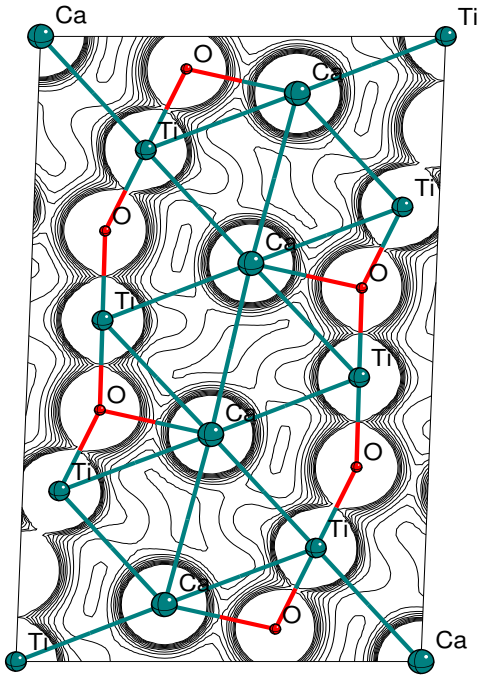

Figure A.12: Geometry of orthorhombic $CaTiO_3$ with measurements according to the scheme outlined in 1.4.3 and contour map of the electronic charge density in the (010) plane.

CaTiO3orthorhombic ALPHA+BETA ELECTRONS
MULLIKEN POPULATION ANALYSIS - NO. OF ELECTRONS 264.000000

ATOM	Z	CHARGE	A.O. POPULATION
1 CA	20	18.243	2.000 1.975 2.032 2.032 2.032 0.945 1.246 1.244 1.244 0.844 0.358 0.355 0.356 0.258 0.363 0.370 0.370 0.009 0.011 0.013 0.012 0.010 0.025 0.034 0.038 0.037 0.027
2 CA	20	18.243	2.000 1.975 2.032 2.032 2.032 0.945 1.246 1.244 1.244 0.844 0.358 0.355 0.356 0.258 0.363 0.370 0.370 0.009 0.011 0.013 0.012 0.010 0.025 0.034 0.038 0.037 0.027
3 CA	20	18.243	2.000 1.975 2.032 2.032 2.032 0.945 1.246 1.244 1.244 0.844 0.358 0.355 0.356 0.258 0.363 0.370 0.370 0.009 0.011 0.013 0.012 0.010 0.025 0.034 0.038 0.037 0.027
4 CA	20	18.243	2.000 1.975 2.032 2.032 2.032 0.945 1.246 1.244 1.244 0.844 0.358 0.355 0.356 0.258 0.363 0.370 0.370 0.009 0.011 0.013 0.012 0.010 0.025 0.034 0.038 0.037 0.027
5 TI	22	19.493	2.000 1.912 2.048 2.048 2.048 0.456 0.752 0.751 0.752 1.359 0.968 0.968 0.968 0.332 0.271 0.272 0.271 0.398 0.188 0.177 0.182 0.395 -0.028 0.010 0.014 0.011 -0.029
6 TI	22	19.493	2.000 1.912 2.048 2.048 2.048 0.456 0.752 0.751 0.752 1.359 0.968 0.968 0.968 0.332 0.271 0.272 0.271 0.398 0.188 0.177 0.182 0.395 -0.028 0.010 0.014 0.011 -0.029
7 TI	22	19.493	2.000 1.912 2.048 2.048 2.048 0.456 0.752 0.751 0.752 1.359 0.968 0.968 0.968 0.332 0.271 0.272 0.271 0.398 0.188 0.177 0.182 0.395 -0.028 0.010 0.014 0.011 -0.029
8 TI	22	19.493	2.000 1.912 2.048 2.048 2.048 0.456 0.752 0.751 0.752 1.359 0.968 0.968 0.968 0.332 0.271 0.272 0.271 0.398 0.188 0.177 0.182 0.395 -0.028 0.010 0.014 0.011 -0.029
9 O	8	9.417	1.998 0.496 0.743 0.738 0.714 0.891 0.505 0.503 0.533 0.585 0.610 0.616 0.475 0.003 0.002 0.002 0.002 0.002
10 O	8	9.417	1.998 0.496 0.743 0.738 0.714 0.891 0.505 0.503 0.533 0.585 0.610 0.616 0.475 0.003 0.002 0.002 0.002 0.002
11 O	8	9.417	1.998 0.496 0.743 0.738 0.714 0.891 0.505 0.503 0.533 0.585 0.610 0.616 0.475 0.003 0.002 0.002 0.002 0.002
12 O	8	9.417	1.998 0.496 0.743 0.738 0.714 0.891 0.505 0.503 0.533 0.585 0.610 0.616 0.475 0.003 0.002 0.002 0.002 0.002
13 O	8	9.424	1.998 0.496 0.726 0.727 0.740 0.888 0.515 0.517 0.501 0.587 0.551 0.547 0.618 0.002 0.002 0.002 0.002 0.003
14 O	8	9.424	1.998 0.496 0.726 0.727 0.740 0.888 0.515 0.517 0.501 0.587 0.551 0.547 0.618 0.002 0.002 0.002 0.002 0.003
15 O	8	9.424	1.998 0.496 0.726 0.727 0.740 0.888 0.515 0.517 0.501 0.587 0.551 0.547 0.618 0.002 0.002 0.002 0.002 0.003
16 O	8	9.424	1.998 0.496 0.726 0.727 0.740 0.888 0.515 0.517 0.501 0.587 0.551 0.547 0.618 0.002 0.002 0.002 0.002 0.003
17 O	8	9.424	1.998 0.496 0.726 0.727 0.740 0.888 0.515 0.517 0.501 0.587 0.551 0.547 0.618 0.002 0.002 0.002 0.002 0.003
18 O	8	9.424	1.998 0.496 0.726 0.727 0.740 0.888 0.515 0.517

			0.501	0.587	0.551	0.547	0.618	0.002	0.002	0.002	
			0.002	0.003							
19 O	8	9.424	1.998	0.496	0.726	0.727	0.740	0.888	0.515	0.517	
			0.501	0.587	0.551	0.547	0.618	0.002	0.002	0.002	
			0.002	0.003							
20 O	8	9.424	1.998	0.496	0.726	0.727	0.740	0.888	0.515	0.517	
			0.501	0.587	0.551	0.547	0.618	0.002	0.002	0.002	
			0.002	0.003							

ATOM	Z	CHARGE	SHELL POPULATION						
1 CA	20	18.243	2.000	8.073	4.679	1.913	1.361	0.055	0.162
2 CA	20	18.243	2.000	8.073	4.679	1.913	1.361	0.055	0.162
3 CA	20	18.243	2.000	8.073	4.679	1.913	1.361	0.055	0.162
4 CA	20	18.243	2.000	8.073	4.679	1.913	1.361	0.055	0.162
5 TI	22	19.493	2.000	8.055	2.711	4.262	1.146	1.340	-0.022
6 TI	22	19.493	2.000	8.055	2.711	4.262	1.146	1.340	-0.022
7 TI	22	19.493	2.000	8.055	2.711	4.262	1.146	1.340	-0.022
8 TI	22	19.493	2.000	8.055	2.711	4.262	1.146	1.340	-0.022
9 O	8	9.417	1.998	2.691	2.432	2.285	0.011		
10 O	8	9.417	1.998	2.691	2.432	2.285	0.011		
11 O	8	9.417	1.998	2.691	2.432	2.285	0.011		
12 O	8	9.417	1.998	2.691	2.432	2.285	0.011		
13 O	8	9.424	1.998	2.690	2.422	2.303	0.011		
14 O	8	9.424	1.998	2.690	2.422	2.303	0.011		
15 O	8	9.424	1.998	2.690	2.422	2.303	0.011		
16 O	8	9.424	1.998	2.690	2.422	2.303	0.011		
17 O	8	9.424	1.998	2.690	2.422	2.303	0.011		
18 O	8	9.424	1.998	2.690	2.422	2.303	0.011		
19 O	8	9.424	1.998	2.690	2.422	2.303	0.011		
20 O	8	9.424	1.998	2.690	2.422	2.303	0.011		

OVERLAP POPULATION CONDENSED TO ATOMS FOR FIRST 6 NEIGHBORS

ATOM A		ATOM B	CELL	R(AB)/AU	R(AB)/ANG	OVPOP(AB)
1 CA		12 O	(0 0 0)	4.452	2.356	-0.004
		16 O	(0 0 0)	4.502	2.382	-0.004
		9 O	(0 0 0)	4.676	2.474	0.003
		13 O	(0 0 0)	4.934	2.611	0.008
		15 O	(0 0 0)	5.065	2.680	0.007
		9 O	(0 -1 0)	5.777	3.057	0.005
ATOM A		ATOM B	CELL	R(AB)/AU	R(AB)/ANG	OVPOP(AB)
5 TI		9 O	(0 0 0)	3.697	1.956	0.029
		13 O	(0 0 0)	3.707	1.962	0.029
		15 O	(0 0 0)	3.713	1.965	0.030
		1 CA	(0 0 0)	6.001	3.175	0.001
		3 CA	(0 0 0)	6.200	3.281	0.000
		3 CA	(-1 0 0)	6.317	3.343	0.000
ATOM A		ATOM B	CELL	R(AB)/AU	R(AB)/ANG	OVPOP(AB)
9 O		5 TI	(0 0 0)	3.697	1.956	0.029
		4 CA	(1 1 0)	4.452	2.356	-0.004
		1 CA	(0 0 0)	4.676	2.474	0.003
		13 O	(0 0 0)	5.196	2.749	-0.029
		15 O	(0 0 0)	5.209	2.757	-0.027
		16 O	(0 1 0)	5.270	2.789	-0.019
ATOM A		ATOM B	CELL	R(AB)/AU	R(AB)/ANG	OVPOP(AB)
13 O		5 TI	(0 0 0)	3.707	1.962	0.029
		7 TI	(-1 0 0)	3.713	1.965	0.030
		4 CA	(0 1 0)	4.502	2.382	-0.004
		1 CA	(0 0 0)	4.934	2.611	0.008
		3 CA	(-1 0 0)	5.065	2.680	0.007
		9 O	(0 0 0)	5.196	2.749	-0.029

Phase 2 - tetragonal.

The band structure is simpler than the orthorhombic phase. Again only the uppermost valence bands and the lower few virtual bands are displayed on a slightly expanded energy scale to illustrate the flattish bands and the band gap, which is similar, but the density of states plot reveals that the $\mathrm{Ti}-\mathrm{O}$ "covalency" occurs further down from the top of the valence bands.

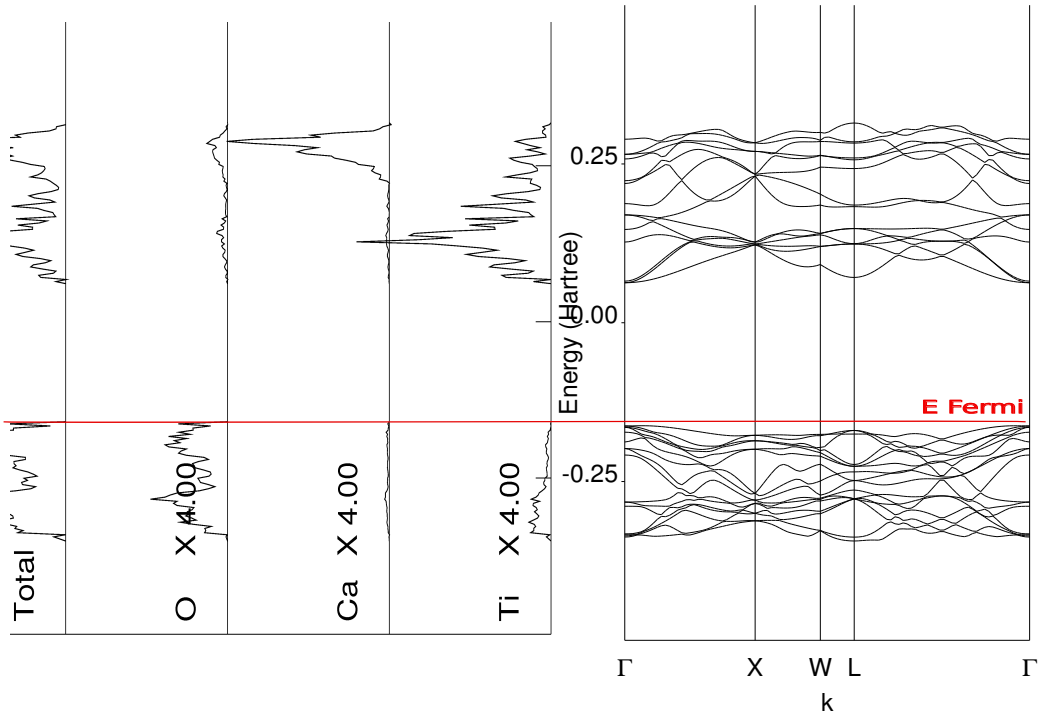

Figure A.13: $\mathrm{CaTiO_3}$ tetragonal phase band structure and density of states.

Measurements

Band Gap = 0.2233189 Hartrees

LATTICE PARAMETERS (BOHR AND DEGREES) - PRIMITIVE CELL

A	B	C	α	β	γ	Volume $Bohr^3$
10.30021	10.30021	10.30021	120.6982	120.6982	88.7948	764.38247

N. OF ATOMS PER CELL	10	NUMBER OF SHELLS	58
NUMBER OF AO	216	N. OF ELECTRONS PER CELL	132
CORE ELECTRONS PER CELL	84	N. OF SYMMETRY OPERATORS	16
TOTAL ENERGY	-3.5061822436011E+03		
ENERGY per FORMULA UNIT		-1753.091121801 Hartrees	
VOLUME per FORMULA UNIT		382.1912 $Bohr^3$	

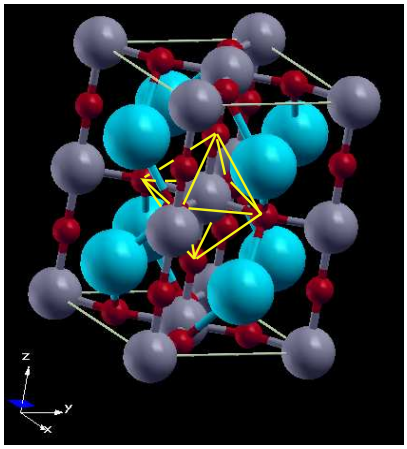

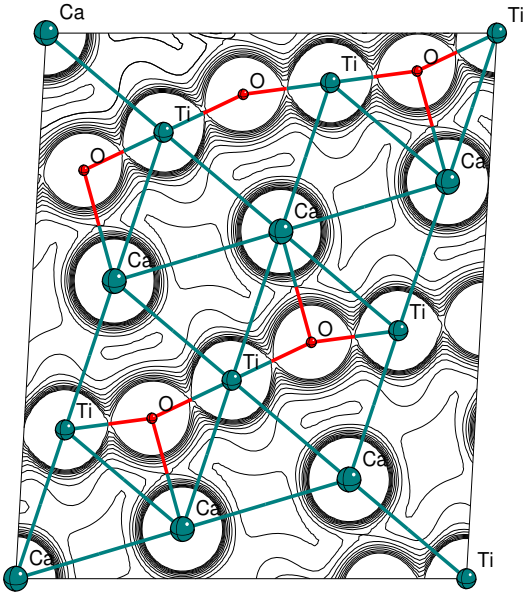

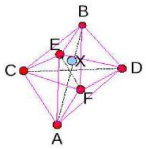

AX = 3.6798 Bohrs
BX = 3.6798 Bohrs
CX = 3.6868 Bohrs
DX = 3.6868 Bohrs
EX = 3.6868 Bohrs
FX = 3.6868 Bohrs

AXB = 180.000 deg
AXC = 90.000 deg
AXD = 90.000 deg
AXE = 90.000 deg
AXF = 90.000 deg
CXE = 90.000 deg
EXD = 90.000 deg
DXF = 90.000 deg
FXC = 90.000 deg

Tilt angle at D = 155.544 deg

Figure A.14: Geometry of tetragonal $CaTiO_3$ with measurements according to the scheme outlined in 1.4.3 and contour map of the electronic charge density in the $(1\,1\,\bar{1}\,)$ plane.

CaTiO3tetragonal ALPHA+BETA ELECTRONS
MULLIKEN POPULATION ANALYSIS - NO. OF ELECTRONS 132.000000

ATOM	Z	CHARGE	A.O. POPULATION
1 TI	22	19.498	2.000 1.911 2.048 2.048 2.048 0.456 0.752 0.752
			0.752 1.359 0.968 0.968 0.968 0.330 0.271 0.271
			0.269 0.417 0.166 0.166 0.203 0.394 -0.029 0.013
			0.013 0.010 -0.026
2 TI	22	19.498	2.000 1.911 2.048 2.048 2.048 0.456 0.752 0.752
			0.752 1.359 0.968 0.968 0.968 0.330 0.271 0.271
			0.269 0.417 0.166 0.166 0.203 0.394 -0.029 0.013
			0.013 0.010 -0.026
3 CA	20	18.238	2.000 1.976 2.033 2.033 2.032 0.945 1.241 1.241
			1.252 0.840 0.356 0.356 0.359 0.267 0.374 0.374
			0.361 0.011 0.012 0.012 0.009 0.006 0.029 0.036
			0.036 0.031 0.018
4 CA	20	18.	238 2.000 1.976 2.033 2.033 2.032 0.945 1.241 1.241
			1.252 0.840 0.356 0.356 0.359 0.267 0.374 0.374
			0.361 0.011 0.012 0.012 0.009 0.006 0.029 0.036
			0.036 0.031 0.018
5 O	8	9.433	1.998 0.499 0.736 0.736 0.721 0.876 0.496 0.496
			0.538 0.610 0.632 0.632 0.452 0.003 0.002 0.002
			0.001 0.001
6 O	8	9.433	1.998 0.499 0.736 0.736 0.721 0.876 0.496 0.496
			0.538 0.610 0.632 0.632 0.452 0.003 0.002 0.002
			0.001 0.001
7 O	8	9.416	1.998 0.496 0.730 0.730 0.736 0.889 0.520 0.520
			0.497 0.587 0.536 0.536 0.628 0.002 0.002 0.002
			0.002 0.003
8 O	8	9.416	1.998 0.496 0.730 0.730 0.736 0.889 0.520 0.520
			0.497 0.587 0.536 0.536 0.628 0.002 0.002 0.002
			0.002 0.003
9 O	8	9.416	1.998 0.496 0.730 0.730 0.736 0.889 0.520 0.520
		0.497	0.587 0.536 0.536 0.628 0.002 0.002 0.002
			0.002 0.003
10 O	8	9.416	1.998 0.496 0.730 0.730 0.736 0.889 0.520 0.520
			0.497 0.587 0.536 0.536 0.628 0.002 0.002 0.002
			0.002 0.003

ATOM	Z	CHARGE	SHELL POPULATION
1 TI	22	19.498	2.000 8.055 2.713 4.262 1.141 1.347 -0.019
2 TI	22	19.498	2.000 8.055 2.713 4.262 1.141 1.347 -0.019
3 CA	20	18.238	2.000 8.073 4.679 1.910 1.376 0.050 0.151
4 CA	20	18.238	2.000 8.073 4.679 1.910 1.376 0.050 0.151
5 O	8	9.433	1.998 2.692 2.406 2.326 0.011
6 O	8	9.433	1.998 2.692 2.406 2.326 0.011
7 O	8	9.416	1.998 2.692 2.426 2.288 0.011
8 O	8	9.416	1.998 2.692 2.426 2.288 0.011
9 O	8	9.416	1.998 2.692 2.426 2.288 0.011
10 O	8	9.416	1.998 2.692 2.426 2.288 0.011

OVERLAP POPULATION CONDENSED TO ATOMS FOR FIRST 6 NEIGHBORS

ATOM A	1 TI	ATOM B	CELL	R(AB)/AU	R(AB)/ANG	OVPOP(AB)
		5 O	(0 0 0)	3.680	1.947	0.024
		7 O	(0 0 0)	3.687	1.951	0.028
		3 CA	(0 1 0)	6.285	3.326	0.000
		2 TI	(-1 -1 0)	7.206	3.813	0.000
		2 TI	(0 0 1)	7.360	3.895	0.000
		7 O	(1 0 1)	7.367	3.898	0.000

ATOM A	3 CA	ATOM B	CELL	R(AB)/AU	R(AB)/ANG	OVPOP(AB)
		7 O	(0 -1 1)	4.637	2.454	0.003
		5 O	(-1 -1 0)	5.096	2.697	0.008
		7 O	(0 -1 0)	5.724	3.029	0.006
		1 TI	(0 -1 0)	6.285	3.326	0.000
		4 CA	(0 0 0)	7.206	3.813	0.000
		4 CA	(1 0 0)	7.360	3.895	0.000

ATOM A	5 O	ATOM B	CELL	R(AB)/AU	R(AB)/ANG	OVPOP(AB)
		1 TI	(0 0 0)	3.680	1.947	0.024
		3 CA	(1 1 0)	5.096	2.697	0.008
		7 O	(0 0 0)	5.209	2.756	-0.023
		6 O	(1 1 1)	7.206	3.813	0.001
		6 O	(0 0 0)	7.360	3.895	-0.003
		1 TI	(1 1 1)	8.091	4.282	0.000

ATOM A	7 O	ATOM B	CELL	R(AB)/AU	R(AB)/ANG	OVPOP(AB)
		1 TI	(0 0 0)	3.687	1.951	0.028
		3 CA	(0 1 -1)	4.637	2.454	0.003
		5 O	(0 0 0)	5.209	2.756	-0.023
		9 O	(0 1 0)	5.214	2.759	-0.023
		8 O	(-1 0 -1)	5.645	2.987	-0.013
		3 CA	(0 1 0)	5.724	3.029	0.006

Phase 3 - cubic.

The band structure is again simpler than the lower temperature phases, but there is more relief in the bands. The density of states plot reveals that the $\mathrm{Ti}-\mathrm{O}$ "covalency" also occurs further down from the top of the valence bands with almost no involvement of the Ca atoms.

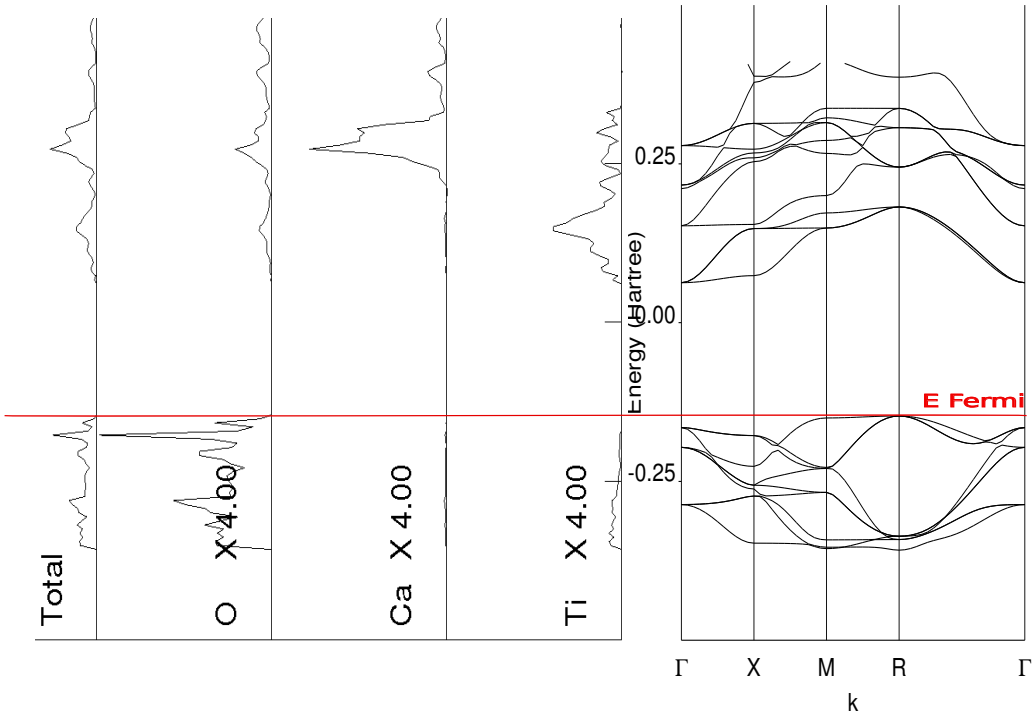

Figure A.15: $\mathrm{CaTiO_3}$ cubic phase band structure and density of states.

Measurements

Band Gap = 0.20984052 Hartrees

LATTICE PARAMETERS (BOHR AND DEGREES) - PRIMITIVE CELL

A	B	C	α	β	γ	Volume $Bohr^3$
7.29891	7.29891	7.29891	90.000	90.0000	90.0000	388.84298

N. OF ATOMS PER CELL	5	NUMBER OF SHELLS	29
NUMBER OF AO	108	N. OF ELECTRONS PER CELL	66
CORE ELECTRONS PER CELL	42	N. OF SYMMETRY OPERATORS	48
TOTAL ENERGY	-1.7530832126191E+03		
ENERGY per FORMULA UNIT		-1753.0832126191 Hartrees	
VOLUME per FORMULA UNIT		388.84298 $Bohr^3$	

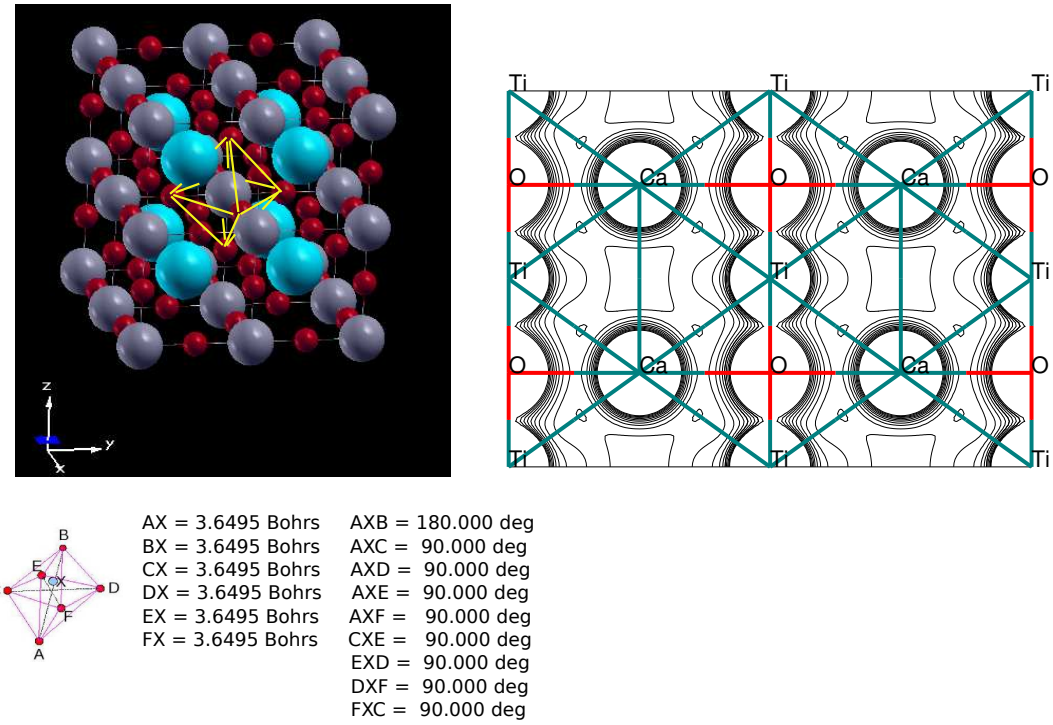

Figure A.16: Geometry of cubic $CaTiO_3$ with measurements according to the scheme outlined in 1.4.3 and contour map of the electronic charge density in the $(1\,\bar{1}\,0)$ plane.

CaTiO3-cubic ALPHA+BETA ELECTRONS
MULLIKEN POPULATION ANALYSIS - NO. OF ELECTRONS 66.000000

ATOM	Z	CHARGE	A.O. POPULATION
1 TI	22	19.515	2.000 1.911 2.048 2.048 2.048 0.456 0.753 0.753
			0.753 1.360 0.967 0.967 0.967 0.328 0.269 0.269
			0.269 0.420 0.171 0.171 0.420 0.171 -0.025 0.015
			0.015 -0.025 0.015
2 CA	20	18.222	2.000 1.976 2.033 2.033 2.033 0.945 1.245 1.245
			1.245 0.838 0.360 0.360 0.360 0.272 0.369 0.369
			0.369 0.006 0.009 0.009 0.006 0.009 0.019 0.031
			0.031 0.019 0.031
3 O	8	9.421	1.998 0.498 0.735 0.735 0.725 0.877 0.498 0.498
			0.540 0.611 0.628 0.628 0.438 0.003 0.002 0.002
			0.002 0.001
4 O	8	9.421	1.998 0.498 0.725 0.735 0.735 0.877 0.540 0.498
			0.498 0.611 0.438 0.628 0.628 0.002 0.002 0.001
			0.003 0.002
5 O	8	9.421	1.998 0.498 0.735 0.725 0.735 0.877 0.498 0.540
			0.498 0.611 0.628 0.438 0.628 0.002 0.001 0.002
			0.003 0.002

ATOM	Z	CHARGE	SHELL POPULATION
1 TI	22	19.515	2.000 8.055 2.717 4.261 1.135 1.353 -0.005
2 CA	20	18.222	2.000 8.073 4.680 1.918 1.379 0.039 0.132
3 O	8	9.421	1.998 2.694 2.413 2.305 0.011
4 O	8	9.421	1.998 2.694 2.413 2.305 0.011
5 O	8	9.421	1.998 2.694 2.413 2.305 0.011

OVERLAP POPULATION CONDENSED TO ATOMS FOR FIRST 6 NEIGHBORS

ATOM A	ATOM B	CELL	R(AB)/AU	R(AB)/ANG	OVPOP(AB)
1 TI	3 O	(0 0 0)	3.649	1.931	0.023
	2 CA	(0 0 0)	6.321	3.345	0.000
	1 TI	(-1 0 0)	7.299	3.862	0.000
	3 O	(1 0 0)	8.160	4.318	0.000
	1 TI	(-1 -1 0)	10.322	5.462	0.000
	3 O	(0 0 1)	10.948	5.794	0.000

ATOM A	ATOM B	CELL	R(AB)/AU	R(AB)/ANG	OVPOP(AB)
2 CA	3 O	(0 0 0)	5.161	2.731	0.009
	1 TI	(0 0 0)	6.321	3.345	0.000
	2 CA	(-1 0 0)	7.299	3.862	0.000
	3 O	(0 0 1)	8.939	4.730	0.000
	2 CA	(-1 -1 0)	10.322	5.462	0.000
	3 O	(-1 0 0)	11.541	6.107	0.000

ATOM A	ATOM B	CELL	R(AB)/AU	R(AB)/ANG	OVPOP(AB)
3 O	1 TI	(0 0 0)	3.649	1.931	0.023
	2 CA	(0 0 0)	5.161	2.731	0.009
	4 O	(0 0 0)	5.161	2.731	-0.024
	3 O	(-1 0 0)	7.299	3.862	0.001
	1 TI	(-1 0 0)	8.160	4.318	0.000
	2 CA	(0 0 -1)	8.939	4.730	0.000

A.2.2 Strontium Titanate $SrTiO_3$

Until 1964 Strontium Titanate $SrTiO_3$ had been described as an example of the ideal, temperature-invariant, cubic perovskite structure. However in that year Lytle published results of very detailed single crystal X-ray diffractometry augmented by optical birefringence that confirmed earlier evidence of a phase transformation near $110\,K$ [82]. He reported three, possibly four phases, as follows:

1. $0 - 10\,K$ - Possibly rhombohedral
2. $35 - 65\,K$ - Orthorhombic
3. $65 - 110\,K$ - Tetragonal $I4/mcm$.
4. $110\,K -$ upwards - Cubic $Pm3m$.

The measured departures from the cubic structure were small. The latter two phases were studied in this work.

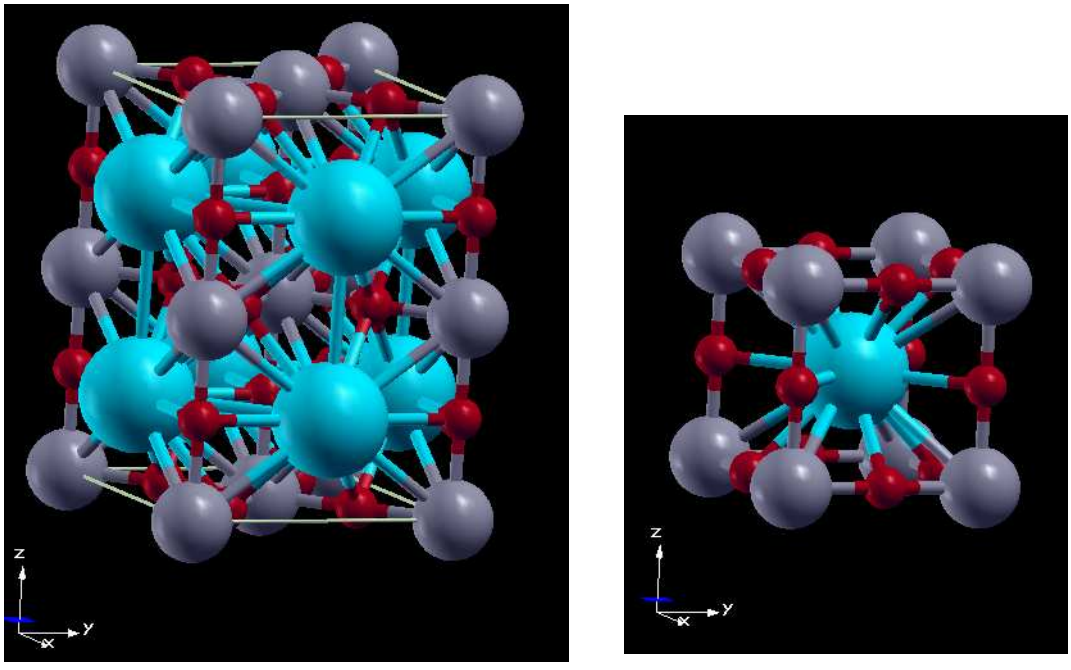

Figure A.17: The two higher temperature phases of $SrTiO_3$

Phase 3 - tetragonal.

In this phase the Ti atom remains central but there is slight elongation along the polar axis (in the Z direction).There is no tilting. There is covalency from both cations at the top of the valence band, but that between Ti and O is more significant

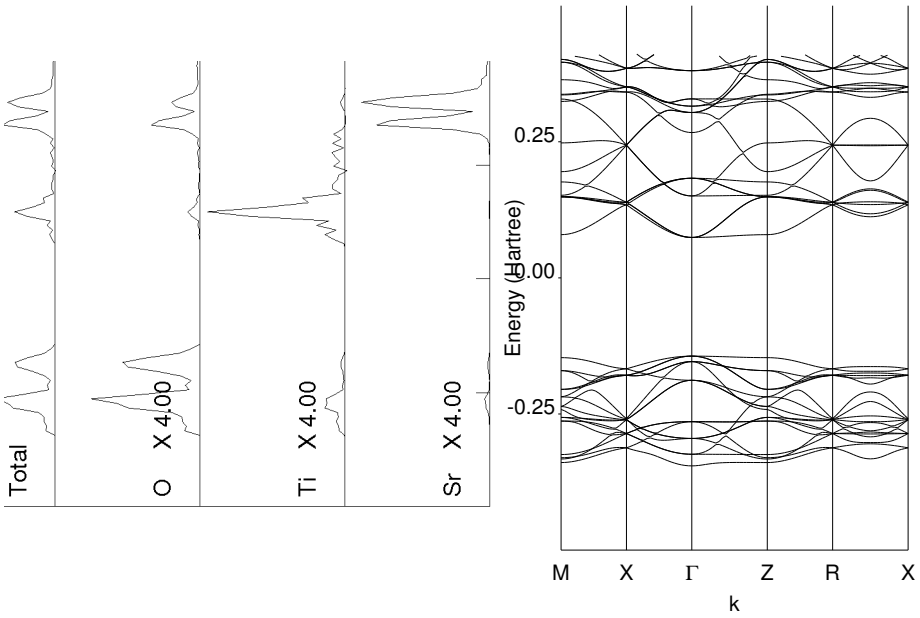

Figure A.18: $\mathrm{SrTiO_3}$ tetragonal phase band structure and density of states.

Measurements

Band Gap = 0.21791275 Hartrees

LATTICE PARAMETERS (BOHR AND DEGREES) - PRIMITIVE CELL

A	B	C	α	β	γ	Volume $Bohr^3$
10.46265	10.46265	10.46265	120.0073	120.0073	89.9874	809.77146

N. OF ATOMS PER CELL	10	NUMBER OF SHELLS	52
NUMBER OF AO	196	N. OF ELECTRONS PER CELL	112
CORE ELECTRONS PER CELL	48	N. OF SYMMETRY OPERATORS	16
TOTAL ENERGY	-2.2118376603094E+03		
ENERGY per FORMULA UNIT		-1105.918830155 Hartrees	
VOLUME per FORMULA UNIT		404.88573 $Bohr^3$	

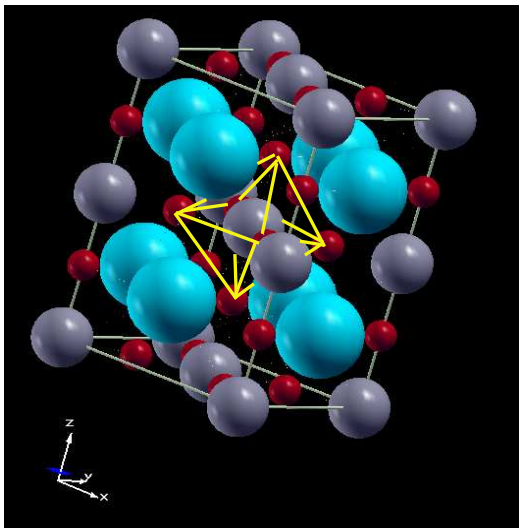

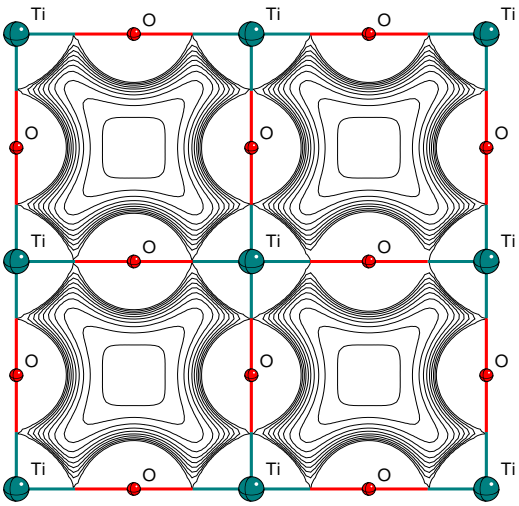

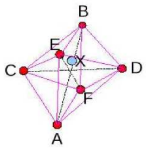

AX = 3.6995 Bohrs
BX = 3.6995 Bohrs
CX = 3.6987 Bohrs
DX = 3.6987 Bohrs
EX = 3.6987 Bohrs
FX = 3.6987 Bohrs

AXB = 180.000 deg
AXC = 90.000 deg
AXD = 90.000 deg
AXE = 90.000 deg
AXF = 90.000 deg
CXE = 90.000 deg
EXD = 90.000 deg
DXF = 90.000 deg
FXC = 90.000 deg

Figure A.19: Geometry of tetragonal $SrTiO_3$ with measurements according to the scheme outlined in 1.4.3 and contour map of the electronic charge density in the $(1\,1\,0)$ plane.

Phase 4 - cubic.

The band structure is simpler than the tetragonal phases, being less populous in the energies at the top of the valence range. The density of states plot reveals that the $\mathrm{Ti}-\mathrm{O}$ "covalency" also occurs further down from the top of the valence bands with less involvement of the Sr atoms.

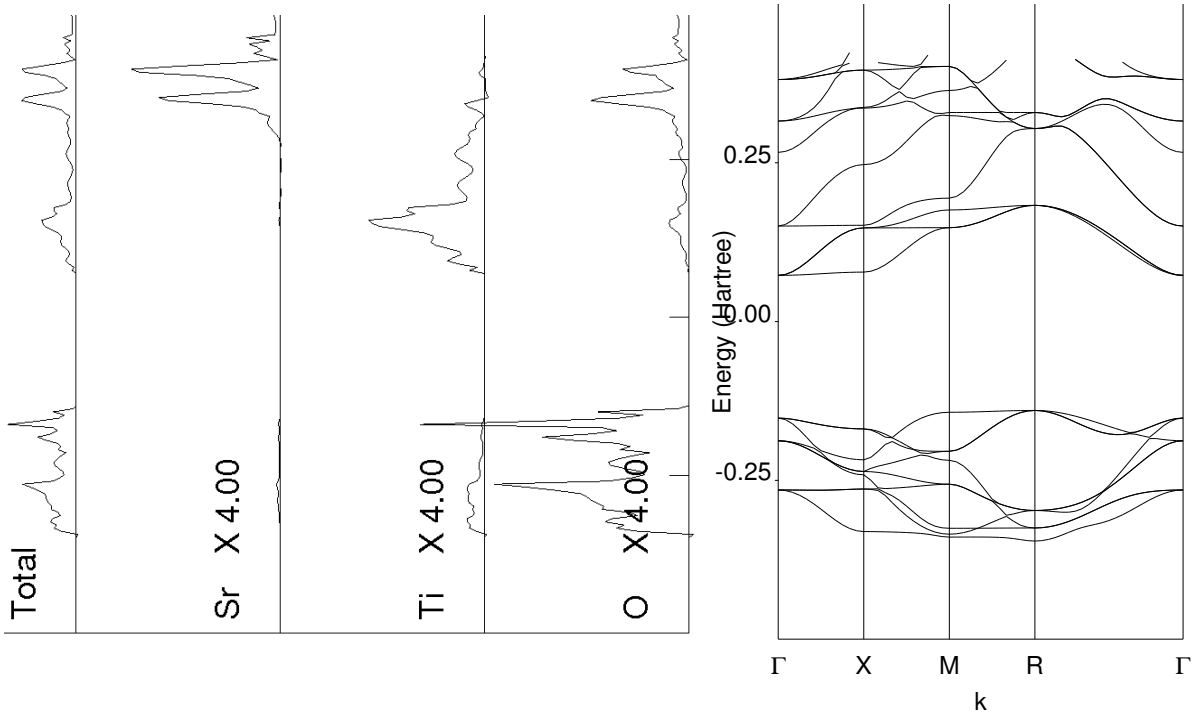

Figure A.20: $\mathrm{SrTiO_3}$ cubic phase band structure and density of states.

Measurements

Band Gap = 0.1398971 Hartrees

LATTICE PARAMETERS (BOHR AND DEGREES) - PRIMITIVE CELL

A	B	C	α	β	γ	Volume $Bohr^3$
7.39780	7.39780	7.39780	90.000	90.0000	90.0000	404.86249

N. OF ATOMS PER CELL	5	NUMBER OF SHELLS	26
NUMBER OF AO	98	N. OF ELECTRONS PER CELL	56
CORE ELECTRONS PER CELL	24	N. OF SYMMETRY OPERATORS	48
TOTAL ENERGY	-1.1059163327346E+03		
ENERGY per FORMULA UNIT		-1105.9163327346 Hartrees	
VOLUME per FORMULA UNIT		404.86249 $Bohr^3$	

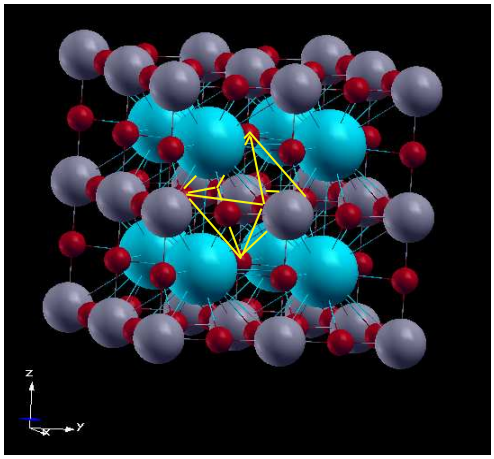

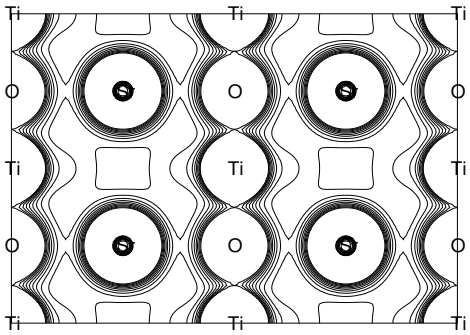

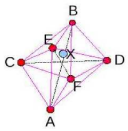

AX = 3.6989 Bohrs
BX = 3.6989 Bohrs
CX = 3.6989 Bohrs
DX = 3.6989 Bohrs
EX = 3.6989 Bohrs
FX = 3.6989 Bohrs

AXB = 180.000 deg
AXC = 90.000 deg
AXD = 90.000 deg
AXE = 90.000 deg
AXF = 90.000 deg
CXE = 90.000 deg
EXD = 90.000 deg
DXF = 90.000 deg
FXC = 90.000 deg

Figure A.21: Geometry of cubic $SrTiO_3$ with measurements according to the scheme outlined in 1.4.3 and contour map of the electronic charge density in the $(1\,\bar{1}\,0)$ plane.

A.2.3 **Barium Titanate** $\mathrm{BaTiO3}$

Barium Titanate $\mathrm{BaTiO3}$ may well be the most studied perovskite, its ferroelectric and piezoelectric properties receiving much experimental and theoretical attention since the discovery of its ferroelectricity in 1945 by Wul and Goldman (see references in [137]). It it can also be doped to create multiferroic compounds (displaying useful ferroelectric and ferromagnetic properties) [141] and tunable dielectric ceramics [142] It has four phases [137]:

1. $0 - 183\,K$ - rhombohedral $R3m$
2. $183 - 278\,K$ - orthorhombic $Amm2$
3. $278 - 393\,K$ - tetragonal $P4/mmm$
4. $393\,K - upwards$ - cubic $Pm3m$

The latter three phases were studied in this work.

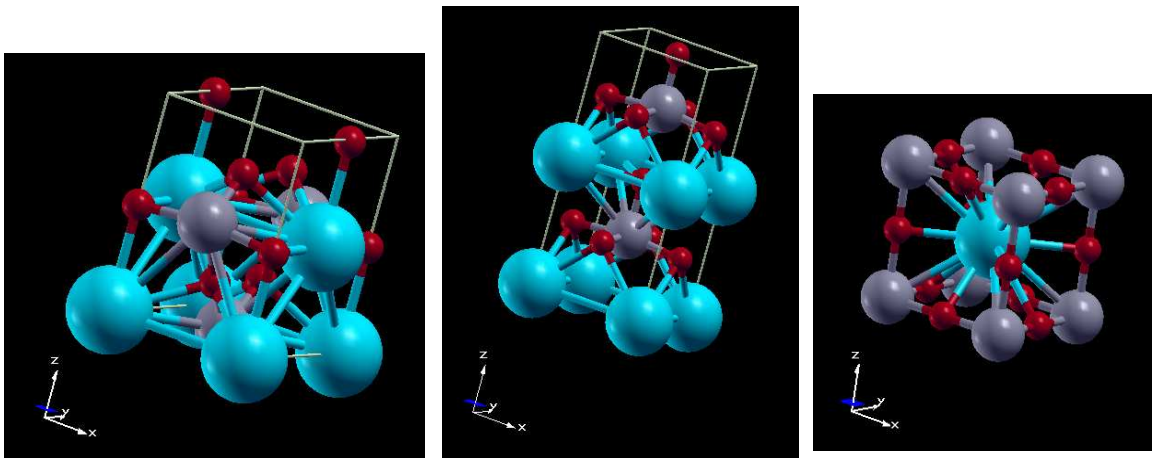

Figure A.22: The three higher temperature phases of $\mathrm{BaTiO_3}$

Phase 2 - orthorhombic. The band structure is simpler than that of the orthorhombic phase of $CaTiO_3$, and the covalency between the metal atoms and oxygen is over a wide range of states. The covalency involves both cations but is stronger between Ti and O, and this is also evident from the Crystalline bridge index data.

Notice in Fig. 5.16, two pages overleaf, that in the equatorial cross section the Ti atom is offset from the central position by two more covalent bonds opposite two less covalent bonds. The polar bonds (along X in this phase) are of equal intermediate strength.

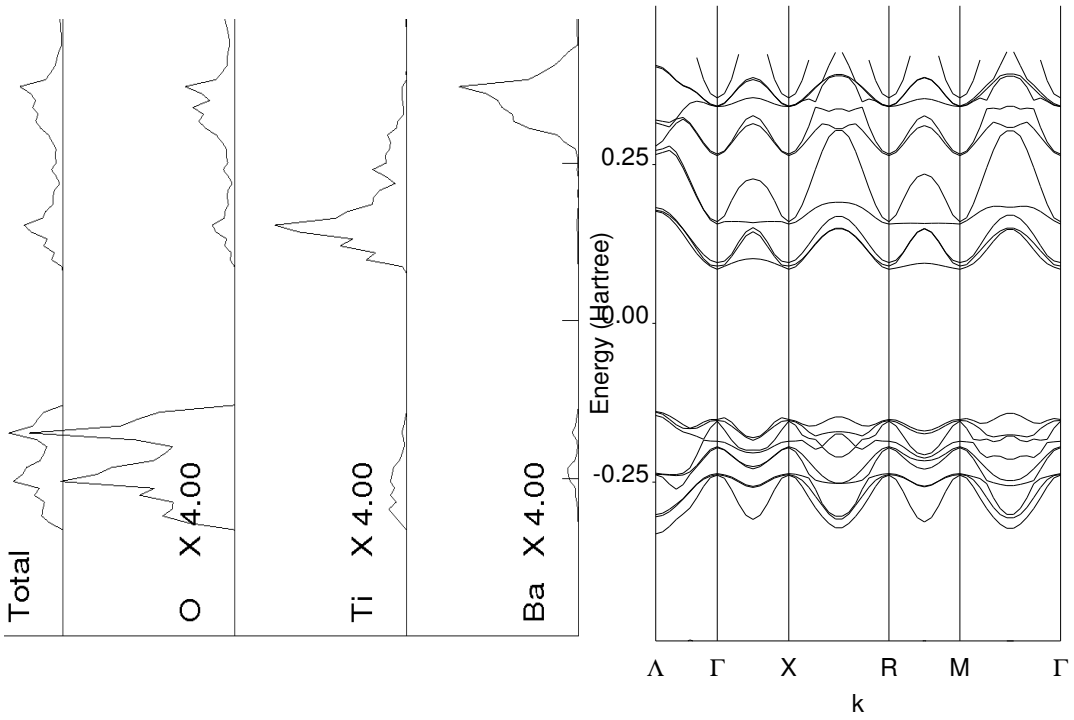

Figure A.23: $BaTiO_3$ orthorhombic phase band structure and density of states.

Measurements

Band Gap = 0.23644628 Hartrees

LATTICE PARAMETERS (BOHR AND DEGREES) - PRIMITIVE CELL

A	B	C	α	β	γ	Volume $Bohr^3$
7.53150	7.59258	7.59258	89.8336	90.0000	90.0000	434.16880

N. OF ATOMS PER CELL	5	NUMBER OF SHELLS	25
NUMBER OF AO	94	N. OF ELECTRONS PER CELL	56
CORE ELECTRONS PER CELL	28	N. OF SYMMETRY OPERATORS	4
TOTAL ENERGY	-1.1006594009214E+03		
ENERGY per FORMULA UNIT		-1100.659400921 Hartrees	
VOLUME per FORMULA UNIT		434.16880 $Bohr^3$	

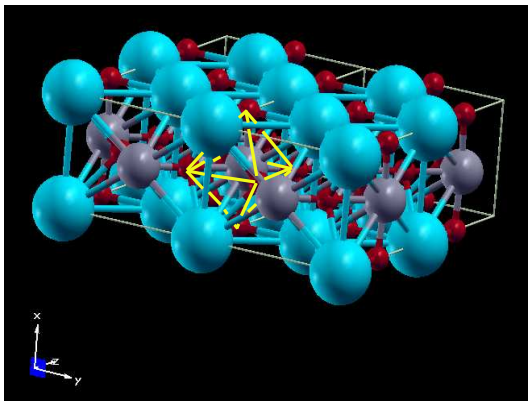

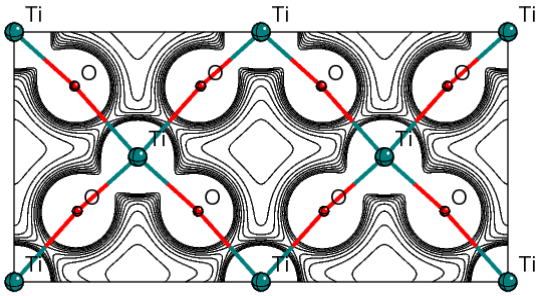

Note that A-B is now along X axis, not Z

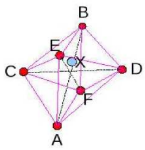

AX = 3.7790 Bohrs
BX = 3.7790 Bohrs
CX = 4.0980 Bohrs
DX = 3.5063 Bohrs
EX = 3.5063 Bohrs
FX = 4.0980 Bohrs

AXB = 170.390 deg
AXC = 86.430 deg
AXD = 93.191 deg
AXE = 93.191 deg
AXF = 86.430 deg
CXE = 89.669 deg
EXD = 96.714 deg
DXF = 89.669 deg
FXC = 83.948 deg

Tilt angle at B = 170.390 deg
Tilt angle at D = 173.617 deg

Figure A.24: Geometry of orthorhombic $\mathrm{BaTiO_3}$ with measurements according to the scheme outlined in 1.4.3 and contour map of the electronic charge density in the (200) plane. The latter shows the ”equatorial plane of the oxygen octahedra, in which the Ti atom is drawn off-centre by two “tighter” bonds juxtaposed against two weaker longer bonds.

Phase 3 - tetragonal.

In this phase the Ti atom is offset, but markedly so, only along the polar axis which is now again in the Z direction. There is covalency from both cations towards the top of the valence band (contrary to the findings of [**?**]), but that between Ti and O is more significant.

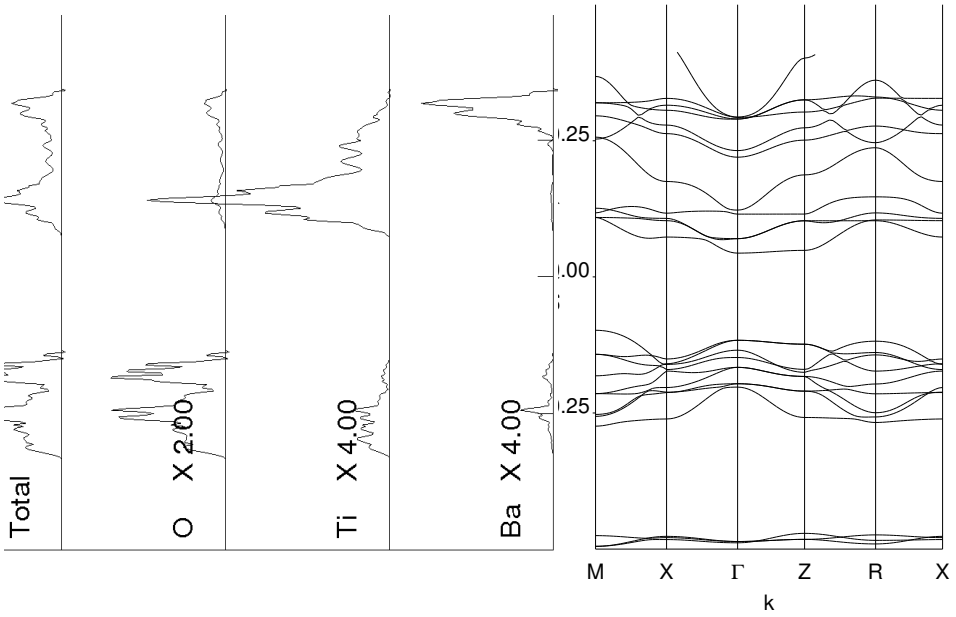

Figure A.25: $BaTiO_3$ tetragonal phase band structure and density of states.

Measurements

Band Gap = 0.21059762 Hartrees

LATTICE PARAMETERS (BOHR AND DEGREES) - PRIMITIVE CELL

A	B	C	α	β	γ	Volume $Bohr^3$
7.51733	7.51733	7.90181	90.0000	90.0000	90.0000	446.53386

N. OF ATOMS PER CELL	5	NUMBER OF SHELLS	25
NUMBER OF AO	94	N. OF ELECTRONS PER CELL	56
CORE ELECTRONS PER CELL	24	N. OF SYMMETRY OPERATORS	8
TOTAL ENERGY	-1.1006613639595E+03		
ENERGY per FORMULA UNIT		-1100.6613639595 Hartrees	
VOLUME per FORMULA UNIT		446.53386 $Bohr^3$	

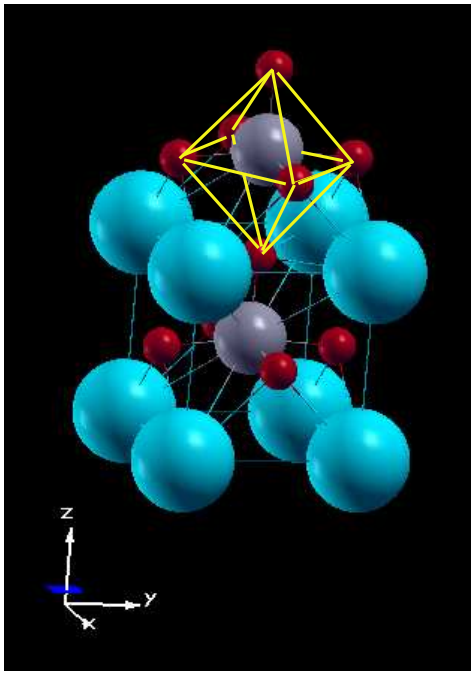

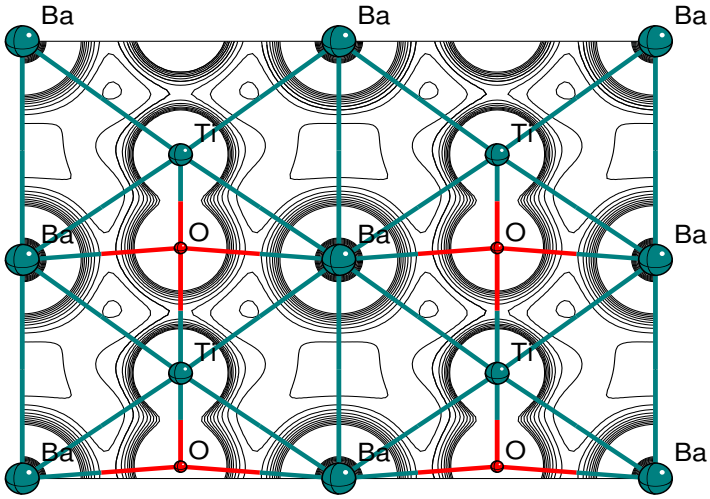

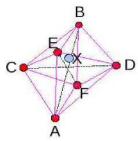

AX = 4.4935 Bohrs
BX = 3.4083 Bohrs
CX = 3.7751 Bohrs
DX = 3.7751 Bohrs
EX = 3.7751 Bohrs
FX = 3.7751 Bohrs

AXB = 180.000 deg
AXC = 84.645 deg
AXD = 84.645 deg
AXE = 84.645 deg
AXF = 84.645 deg
CXE = 89.501 deg
EXD = 89.501 deg
DXF = 89.501 deg
FXC = 89.501 deg

Figure A.26: Geometry of tetragonal $\mathrm{BaTiO_3}$ with measurements according to the scheme outlined in 1.4.3 and contour map of the electronic charge density in the $(1\bar{1}0)$ plane. The measurements reveal an offset of the Ti atom of more than one half of a Bohr from the central position.

BaTiO3_tetragonal0110
ALPHA+BETA ELECTRONS
MULLIKEN POPULATION ANALYSIS - NO. OF ELECTRONS 56.000000

ATOM Z CHARGE A.O. POPULATION

1 BA 256 8.200 1.692 0.444 0.444 0.445 0.303 1.557 1.557 1.558
0.031 0.046 0.046 0.030 0.047
2 TI 22 19.566 2.000 1.915 2.048 2.048 2.048 0.452 0.747 0.747
0.742 1.343 0.957 0.957 0.955 0.337 0.282 0.282
0.273 0.451 0.234 0.234 0.419 0.196 -0.050 0.001
0.001 -0.060 0.010
3 O 8 9.383 1.999 0.509 0.738 0.738 0.715 0.884 0.461 0.461
0.489 0.599 0.631 0.631 0.511 0.005 0.005 0.005
0.002 0.001
4 O 8 9.426 1.999 0.505 0.704 0.751 0.740 0.875 0.497 0.467
0.456 0.601 0.520 0.638 0.661 0.002 0.003 0.001
0.003 0.003
5 O 8 9.426 1.999 0.505 0.751 0.704 0.740 0.875 0.467 0.497
0.456 0.601 0.638 0.520 0.661 0.002 0.001 0.003
0.003 0.003

ATOM Z CHARGE SHELL POPULATION

1 BA 256 8.200 3.025 4.975 0.199
2 TI 22 19.566 2.000 8.059 2.689 4.211 1.174 1.533 -0.099
3 O 8 9.383 1.999 2.700 2.295 2.372 0.018
4 O 8 9.426 1.999 2.699 2.296 2.420 0.011
5 O 8 9.426 1.999 2.699 2.296 2.420 0.011

OVERLAP POPULATION CONDENSED TO ATOMS FOR FIRST 6 NEIGHBORS

ATOM A	1 BA	ATOM B	CELL	R(AB)/AU	R(AB)/ANG	OVPOP(AB)
	4 O	(0 0 0)	5.339	2.825	-0.024	
	3 O	(0 0 0)	5.362	2.837	-0.023	
	4 O	(0 0 -1)	5.681	3.006	-0.009	
	2 TI	(0 0 0)	6.591	3.488	0.000	
	2 TI	(0 0 1)	6.770	3.582	0.000	
	1 BA	(-1 0 0)	7.558	3.999	0.000	

ATOM A	2 TI	ATOM B	CELL	R(AB)/AU	R(AB)/ANG	OVPOP(AB)
	3 O	(0 0 0)	3.421	1.810	0.019	
	4 O	(0 0 -1)	3.798	2.010	0.028	
	3 O	(0 0 -1)	4.592	2.430	0.020	
	1 BA	(0 0 0)	6.591	3.488	0.000	
	1 BA	(0 0 -1)	6.770	3.582	0.000	
	2 TI	(-1 0 0)	7.558	3.999	0.000	

ATOM A	3 O	ATOM B	CELL	R(AB)/AU	R(AB)/ANG	OVPOP(AB)
	2 TI	(0 0 0)	3.421	1.810	0.019	
	2 TI	(0 0 1)	4.592	2.430	0.020	
	1 BA	(0 0 0)	5.362	2.837	-0.023	
	4 O	(0 0 -1)	5.363	2.838	-0.009	
	4 O	(0 0 0)	5.656	2.993	-0.004	
	3 O	(-1 0 0)	7.558	3.999	0.001	

ATOM A	4 O	ATOM B	CELL	R(AB)/AU	R(AB)/ANG	OVPOP(AB)
	2 TI	(0 0 1)	3.798	2.010	0.028	
	1 BA	(0 0 0)	5.339	2.825	-0.024	
	5 O	(0 0 0)	5.344	2.828	-0.017	
	3 O	(0 0 1)	5.363	2.838	-0.009	
	3 O	(0 0 0)	5.656	2.993	-0.004	
	1 BA	(0 0 1)	5.681	3.006	-0.009	

Phase 4 - cubic.

The band structure is simpler than the tetragonal phases, being less populous in the energies at the top of the valence range. The density of states plot reveals that “covalency” with oxygen also occurs from both cations.

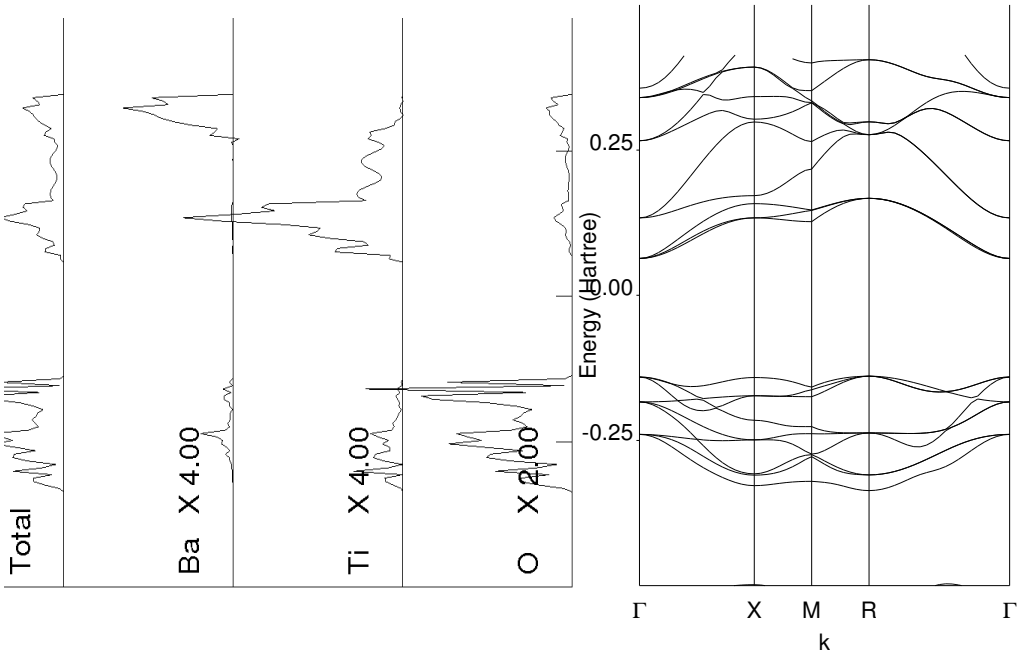

Figure A.27: $BaTiO_3$ cubic phase band structure and density of states.

Measurements

Band Gap = 0.1407499 Hartrees

LATTICE PARAMETERS (BOHR AND DEGREES) - PRIMITIVE CELL

A	B	C	α	β	γ	Volume $Bohr^3$
7.57680	7.57680	7.57680	90.000	90.0000	90.0000	434.96760

N. OF ATOMS PER CELL	5	NUMBER OF SHELLS	25
NUMBER OF AO	94	N. OF ELECTRONS PER CELL	56
CORE ELECTRONS PER CELL	24	N. OF SYMMETRY OPERATORS	48
TOTAL ENERGY	-1.1006569895032E+03		
ENERGY per FORMULA UNIT		-1100.6569895032 Hartrees	
VOLUME per FORMULA UNIT		434.96760 $Bohr^3$	

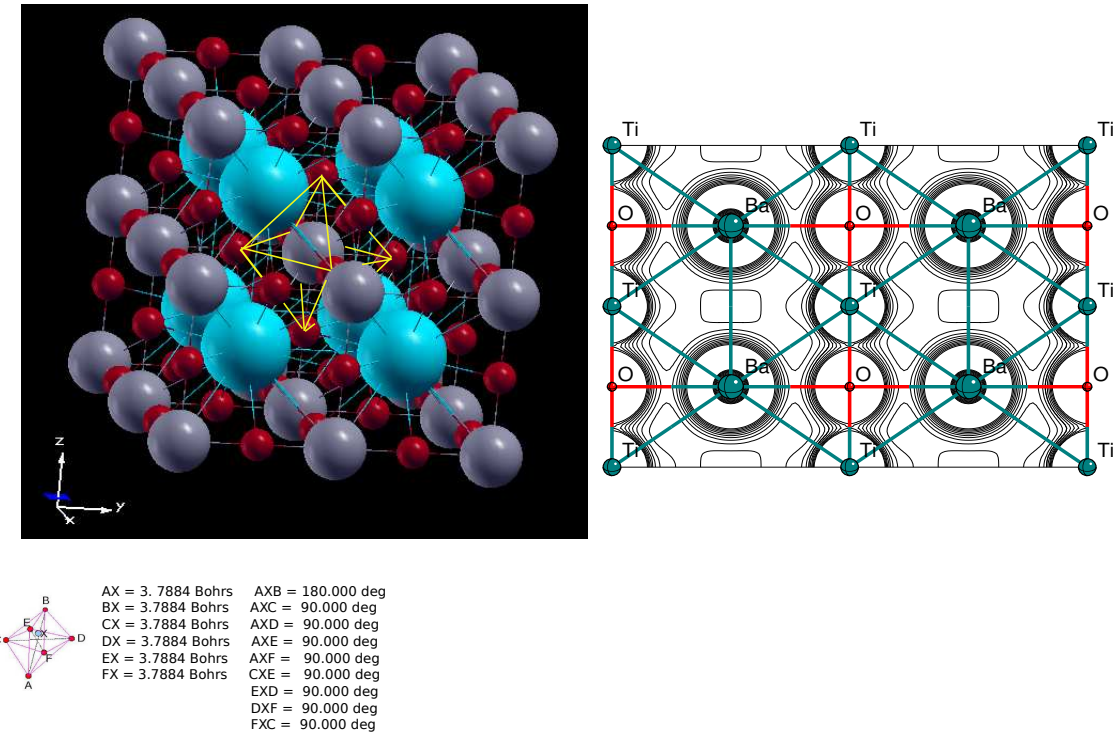

AX = 3. 7884 Bohrs AXB = 180.000 deg
BX = 3.7884 Bohrs AXC = 90.000 deg
CX = 3.7884 Bohrs AXD = 90.000 deg
DX = 3.7884 Bohrs AXE = 90.000 deg
EX = 3.7884 Bohrs AXF = 90.000 deg
FX = 3.7884 Bohrs CXE = 90.000 deg
EXD = 90.000 deg
DXF = 90.000 deg
FXC = 90.000 deg

Figure A.28: Geometry of cubic $BaTiO_3$ with measurements according to the scheme outlined in 1.4.3 and contour map of the electronic charge density in the $(1\,\bar{1}\,0)$ plane.

A.3 The Alkaline Earth Zirconates

In comparison with the Titanates of the previous section, $\mathrm{AZrO3}$ - based perovskites, which exhibit much lower permittivities than their titanate analogs, have received less attention [143]. However they are currently gaining considerable importance in the field of electrical ceramics, refractories and heterogeneous catalysis. Additionally, they have received great attention as high temperature proton conductors with the possibility of applications in fuel cells or hydrogen sensors [144]. As with the Alkaline Earth Titanates, the phase behaviour is varied: $\mathrm{CaZrO_3}$ has two phases, $\mathrm{SrZrO_3}$ has four phases and $\mathrm{BaZrO_3}$ essentially has one cubic phase, but at very low temperatures, $< 15\,K$, exhibits a dielectric anomaly which has been interpreted theoretically to be due to tilting, hence a triclinic phase [148].

A.3.1 Calcium Zirconate $\mathrm{CaZrO_3}$

Calcium Zirconate occurs in nature as the mineral Lakargiite, reported as a new mineral in 2008 [145], in which variable minor amounts of Ti and Sn occupy between 7% and 20% of the Zr sites.

The pure $\mathrm{CaZrO_3}$ material has two phases [146]:

1. $0 - 2023\,K$ - orthorhombic $Pbnm$
2. $2023\,K\ - upwards$ - cubic $Pm3m$

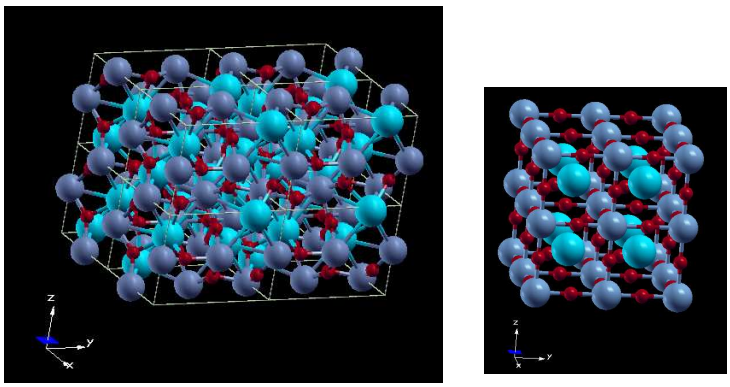

1 2

Figure A.29: The two phases of $\mathrm{CaZrO_3}$

Phase 1 - orthorhombic.

The band structure even more crowded than in the case of Calcium Titanate as there are now 452 Atomic orbitals in the primitive cell. Only the uppermost valence bands and the lower few virtual bands are displayed to illustrate the flattish bands and the band gap. There is some $\mathrm{Ca}-\mathrm{O}$ covalency close to the top of the valence bands. The oxygen octahedra are not excessively deformed and the Zirconium atom remains central, but the octahedra are tilted at every corner connection, thus considerably distorting the ideal cubic perovskite structure.

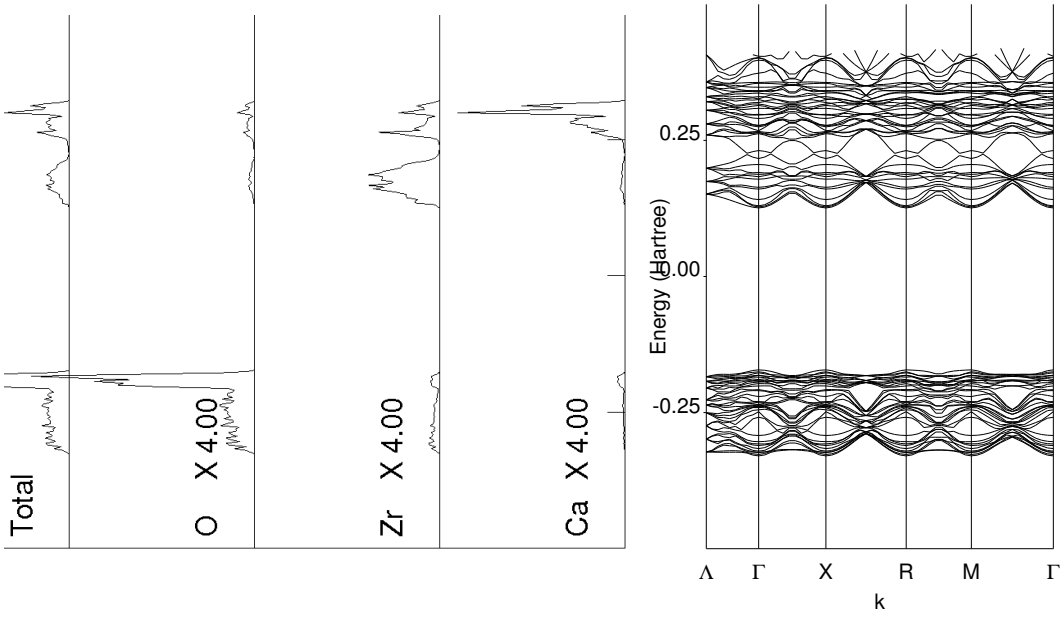

Figure A.30: $\mathrm{CaZrO_3}$ orthorhombic phase band structure and density of states.

Measurements

Band Gap 0.2973993 Hartrees

LATTICE PARAMETERS (BOHR AND DEGREES) - PRIMITIVE CELL

A	B	C	α	β	γ	Volume $Bohr^3$
10.63081	15.25780	10.96721	90.0000	90.0000	90.0000	1778.91100

N. OF ATOMS PER CELL	20	NUMBER OF SHELLS	120
NUMBER OF AO	452	N. OF ELECTRONS PER CELL	336
CORE ELECTRONS PER CELL	240	N. OF SYMMETRY OPERATORS	8
TOTAL ENERGY	-1.7779077362616E+04		
ENERGY per FORMULA UNIT		-4444.769340654 Hartrees	
VOLUME per FORMULA UNIT		444.72775 $Bohr^3$	

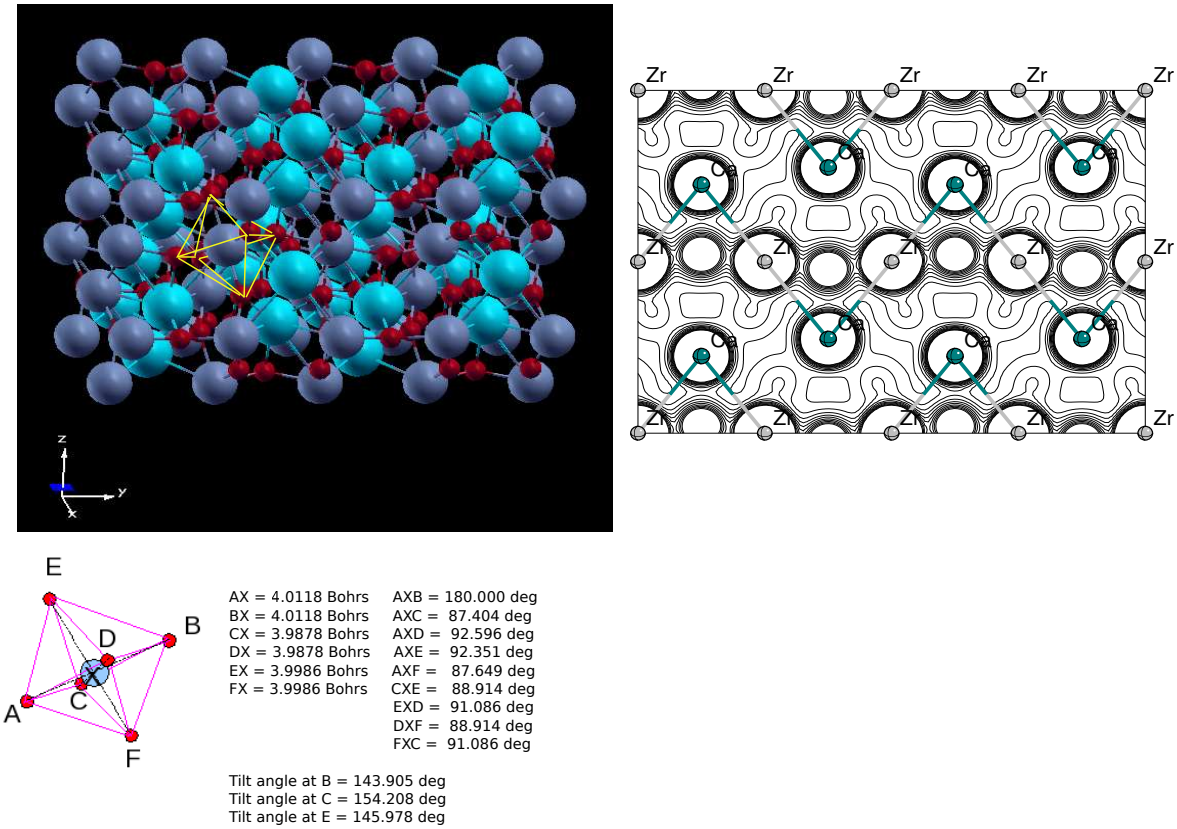

Figure A.31: Geometry of orthorhombic $CaZrO_3$ with measurements according to the scheme outlined in 1.4.3. The longest dimension of the oxygen octahedron was chosen for the AXB direction. The octahedron is inclined to all crystallographic axes. Due to the pronounced tilting at every corner connection, a rather deceptive perspective was required to reveal all six oxygen atoms - AXB is somewhat longer than EXF, contrary to the appearance of the graphic. The contour map of the electronic charge density in the (200) plane. Note that all of the oxygen atoms are out of plane, again due to the pronounced tilting.

Phase 2 - cubic.

The band structure is again yet simpler than the lower temperature phase, but there is more relief in the bands. The density of states plot reveals that the covalency has almost no involvement of the Ca atoms.

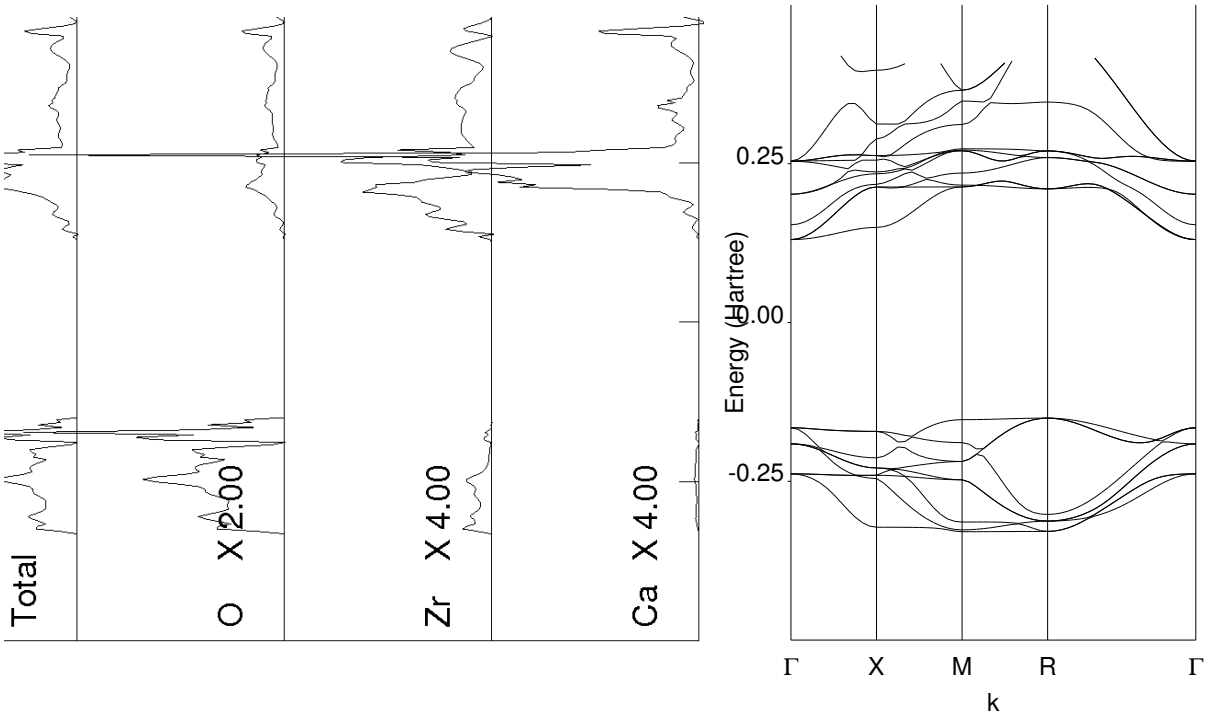

Figure A.32: $\mathrm{CaZrO_3}$ cubic phase band structure and density of states.

Measurements

Band Gap 0.2810266 Hartrees

LATTICE PARAMETERS (BOHR AND DEGREES) - PRIMITIVE CELL

A	B	C	α	β	γ	Volume $Bohr^3$
7.81970	7.81970	7.81970	90.000	90.0000	90.0000	478.15606

N. OF ATOMS PER CELL	5	NUMBER OF SHELLS	30
NUMBER OF AO	113	N. OF ELECTRONS PER CELL	84
CORE ELECTRONS PER CELL	60	N. OF SYMMETRY OPERATORS	48
TOTAL ENERGY	-4.4447290459499E+03		
ENERGY per FORMULA UNIT		-4444.7290459499 Hartrees	
VOLUME per FORMULA UNIT		478.15606 $Bohr^3$	

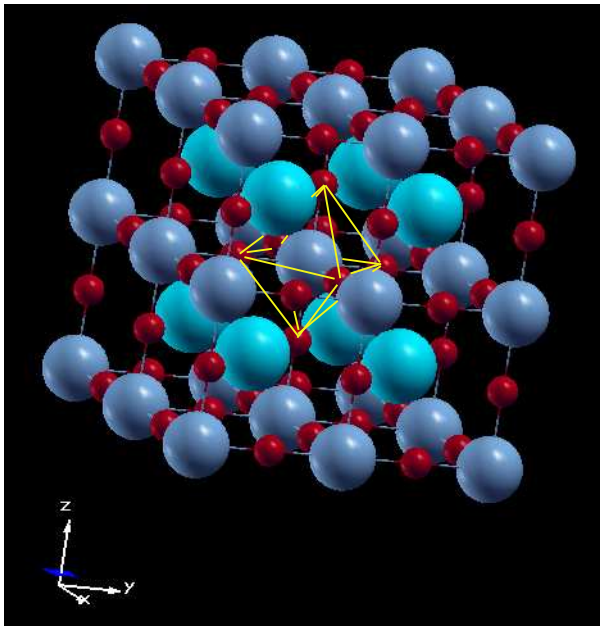

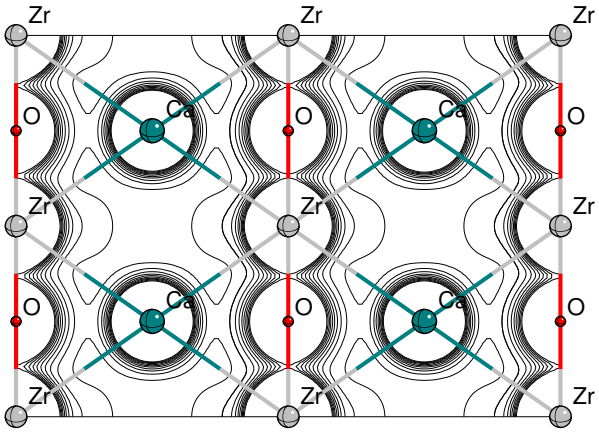

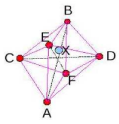

AX = 3.9098 Bohrs
BX = 3.9098 Bohrs
CX = 3.9098 Bohrs
DX = 3.9098 Bohrs
EX = 3.9098 Bohrs
FX = 3.9098 Bohrs

AXB = 180.000 deg
AXC = 90.000 deg
AXD = 90.000 deg
AXE = 90.000 deg
AXF = 90.000 deg
CXE = 90.000 deg
EXD = 90.000 deg
DXF = 90.000 deg
FXC = 90.000 deg

Figure A.33: Geometry of cubic $CaZrO_3$ with measurements according to the scheme outlined in 1.4.3 and contour map of the electronic charge density in the $(1\,1\,0)$ plane.

A.3.2 Strontium Zirconate $SrZrO_3$

Four phases are reported for $SrZrO_3$ [147]:

1. $0 - 970\,K$ - orthorhombic $Pnma$
2. $970 - 1100\,K$ - orthorhombic $Cmcm$
3. $1100 - 1440\,K$ - tetragonal $I4/mcm$
4. $1440\,K\ - upwards$ - cubic $Pm\bar{3}m$

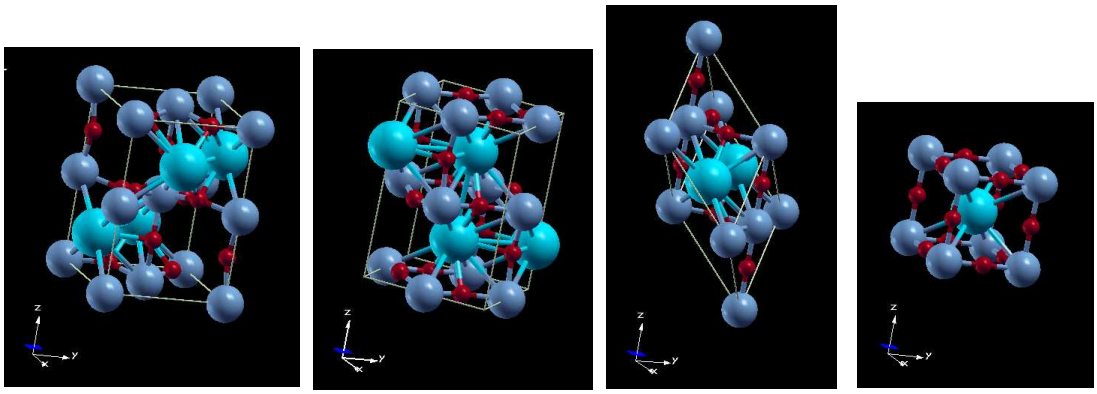

1 2 3 4

Figure A.34: The four phases of $SrZrO_3$

Phase 1 - orthorhombic $Pnma$.

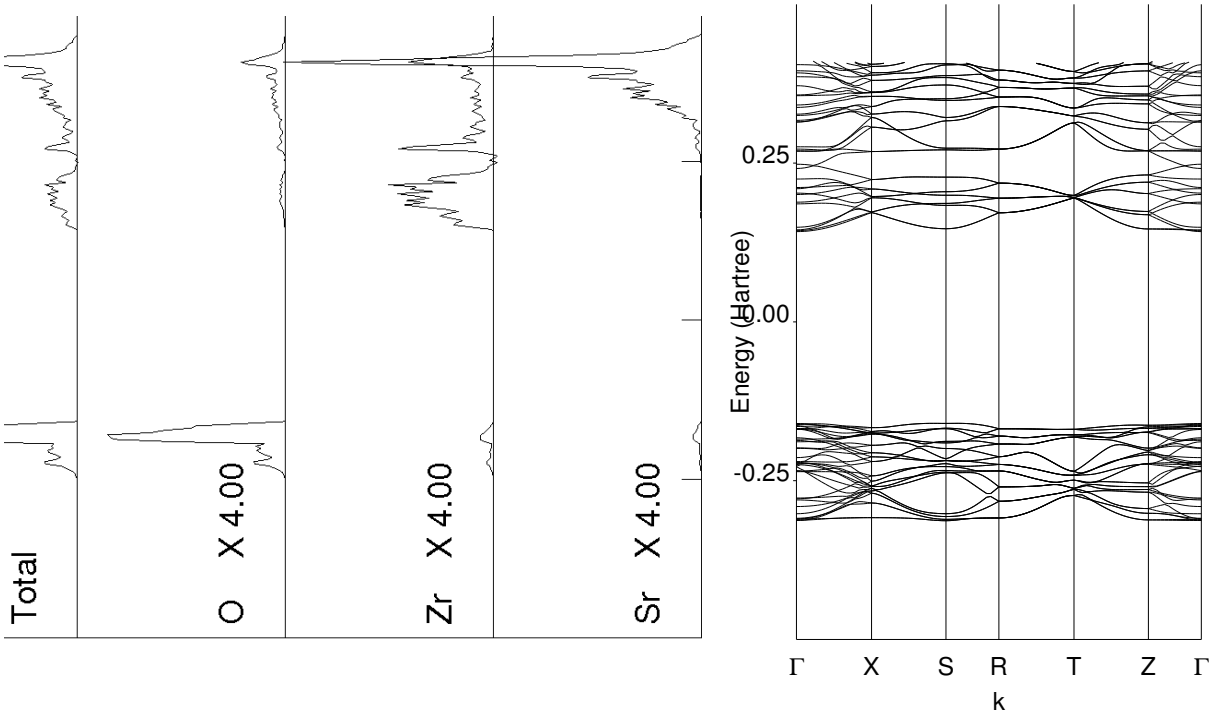

Figure A.35: $SrZrO_3$ orthorhombic $Pnma$ phase band structure and density of states.

Measurements

Band Gap 0.3019678 Hartrees

LATTICE PARAMETERS (BOHR AND DEGREES) - PRIMITIVE CELL

A	B	C	α	β	γ	Volume $Bohr^3$
11.00177	11.10285	15.61262	90.000	90.0000	90.0000	1907.09681

N. OF ATOMS PER CELL	20	NUMBER OF SHELLS	108
NUMBER OF AO	412	N. OF ELECTRONS PER CELL	296
CORE ELECTRONS PER CELL	168	N. OF SYMMETRY OPERATORS	8
TOTAL ENERGY	-1.5190353759905E+04		
ENERGY per FORMULA UNIT		-3797.588439976 Hartrees	
VOLUME per FORMULA UNIT		476.7742025 $Bohr^3$	

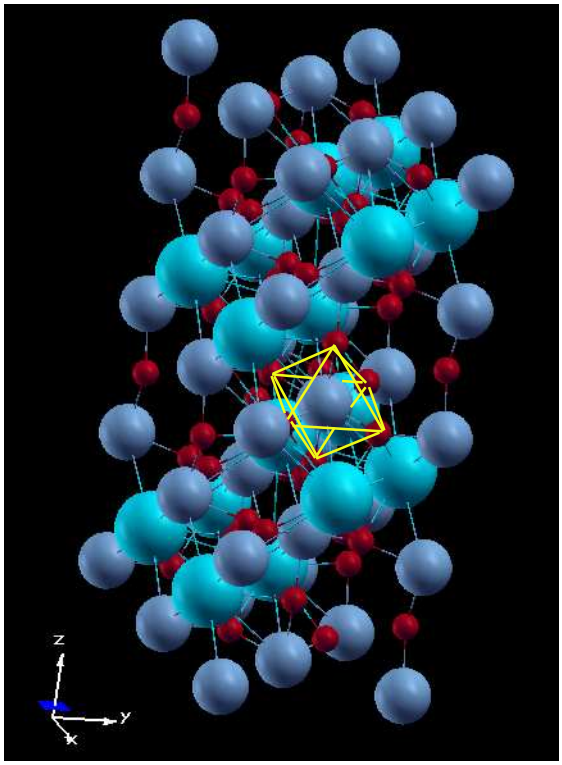

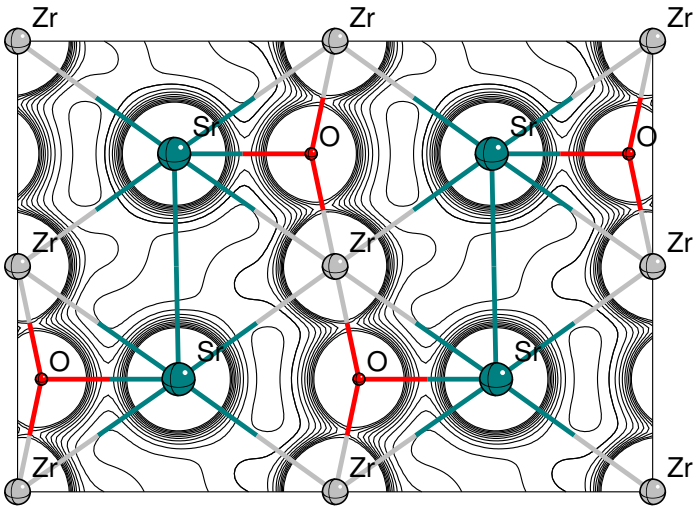

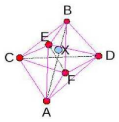

AX = 3.9962 Bohrs
BX = 3.9962 Bohrs
CX = 3.9977 Bohrs
DX = 3.9977 Bohrs
EX = 4.0014 Bohrs
FX = 4.0014 Bohrs

AXB = 180.000 deg
AXC = 91.188 deg
AXD = 88.812 deg
AXE = 89.133 deg
AXF = 90.867 deg
CXE = 89.135 deg
EXD = 90.865 deg
DXF = 89.135 deg
FXC = 90.865 deg

Tilt angle at B = 155.227 deg
Tilt angle at D = 155.386 deg
Tilt angle at F = 155.386 deg

Figure A.36: Geometry of $SrZrO_3$ orthorhombic $Pnma$ with measurements according to the scheme outlined in 1.4.3 and contour map of the electronic charge density in the $(1\,0\,0)$ plane.

Phase 2 - orthorhombic $Cmcm$.

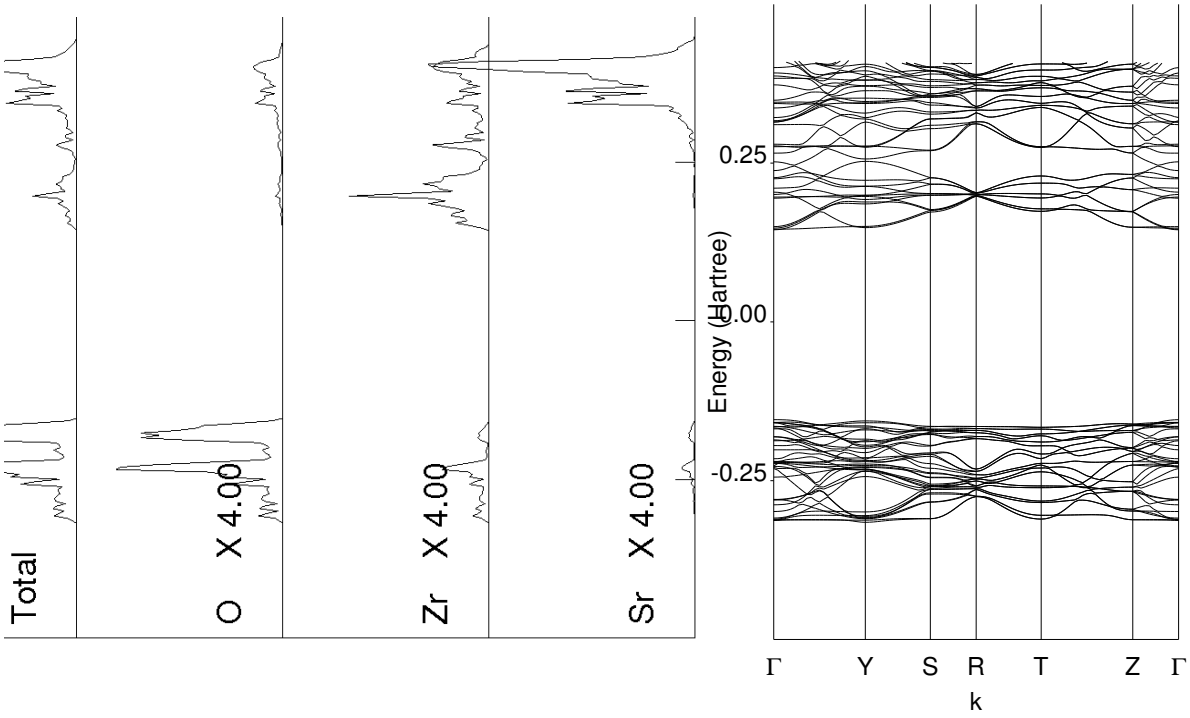

Figure A.37: $SrZrO_3$ orthorhombic $Cmcm$ phase band structure and density of states.

Measurements

Band Gap 0.2989548 Hartrees

LATTICE PARAMETERS (BOHR AND DEGREES) - PRIMITIVE CELL

A	B	C	α	β	γ	Volume $Bohr^3$
11.04632	11.04632	15.67249	90.000	90.0000	89.5245	1912.30914

N. OF ATOMS PER CELL	20	NUMBER OF SHELLS	108
NUMBER OF AO	412	N. OF ELECTRONS PER CELL	296
CORE ELECTRONS PER CELL	168	N. OF SYMMETRY OPERATORS	8
TOTAL ENERGY	-1.5190346346423E+04		
ENERGY per FORMULA UNIT		-3797.586586606 Hartrees	
VOLUME per FORMULA UNIT		478.077285 $Bohr^3$	

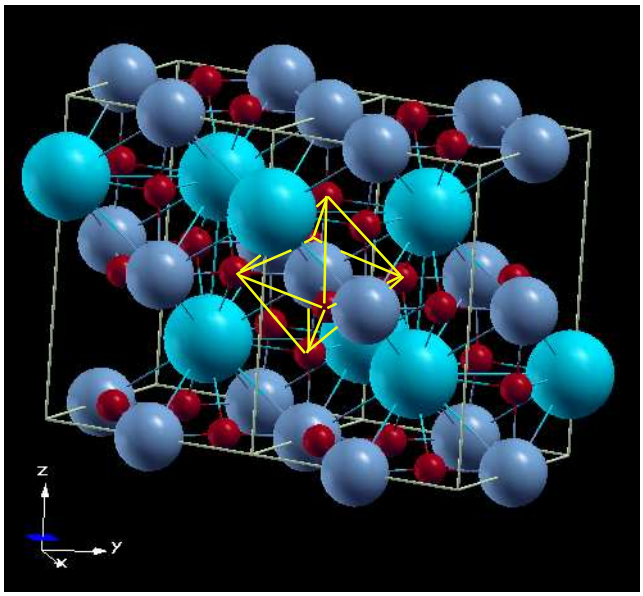

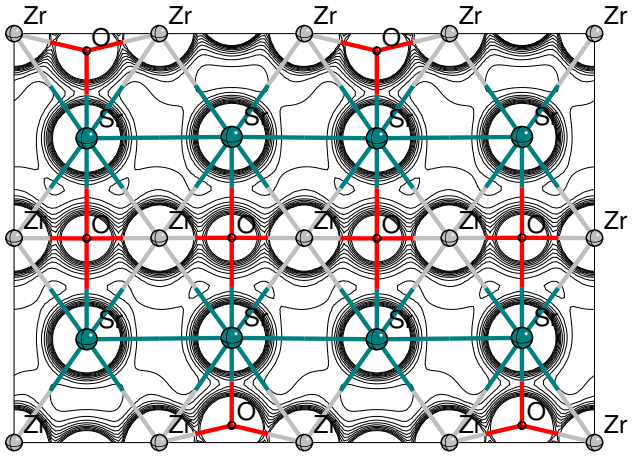

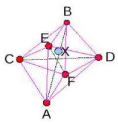

AX = 3.9821 Bohrs
BX = 3.9821 Bohrs
CX = 3.9798 Bohrs
DX = 3.9798 Bohrs
EX = 3.9989 Bohrs
FX = 3.9989 Bohrs

AXB = 180.000 deg
AXC = 89.386 deg
AXD = 90.614 deg
AXE = 89.395 deg
AXF = 90.605 deg
CXE = 89.595 deg
EXD = 90.405 deg
DXF = 89.595 deg
FXC = 90.405 deg

Tilt angle at B = 159.437 deg
Tilt angle at D = 160.378 deg
Tilt angle at F = 153.101 deg

Figure A.38: Geometry of $SrZrO_3$ orthorhombic $Cmcm$ with measurements according to the scheme outlined in 1.4.3 and contour map of the electronic charge density in the $(0\,1\,1)$ plane.

Phase 3 - tetragonal.

In this phase the oxygen octahedral cage is almost uniform, but slightly compressed along the polar (C) axis, and rotated alternately left and right about this axis so that some $\mathrm{Sr}-\mathrm{O}$ bonds are shorter than others.

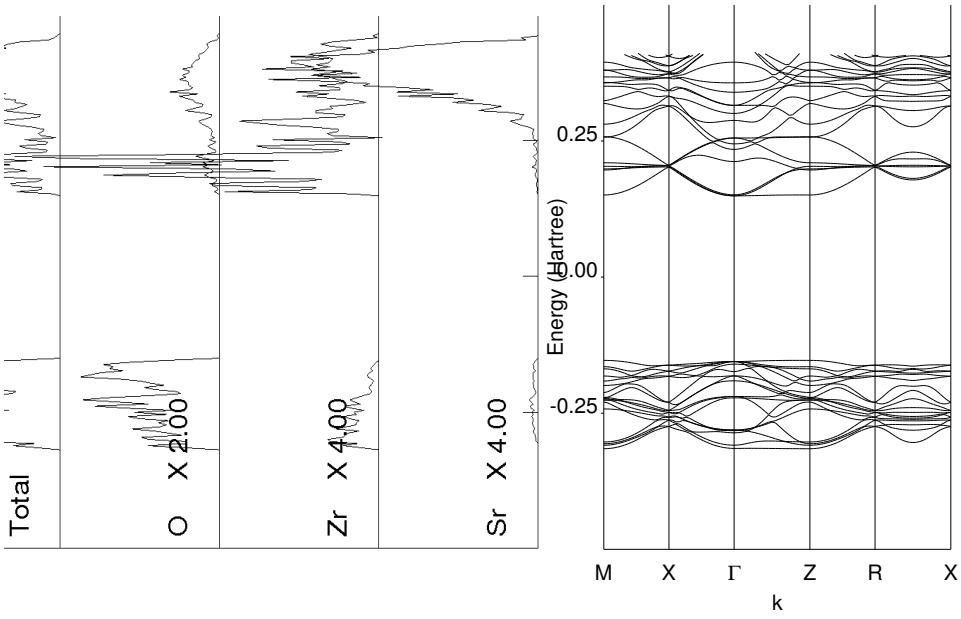

Figure A.39: $\mathrm{SrZrO_3}$ tetragonal phase band structure and density of states.

Measurements

Band Gap = 0.3022386 Hartrees.

LATTICE PARAMETERS (BOHR AND DEGREES) - PRIMITIVE CELL

A	B	C	α	β	γ	Volume $Bohr^3$
11.09868	11.09868	11.09868	120.7078	120.7078	88.7783	956.13762

N. OF ATOMS PER CELL	10	NUMBER OF SHELLS	54
NUMBER OF AO	206	N. OF ELECTRONS PER CELL	146
CORE ELECTRONS PER CELL	84	N. OF SYMMETRY OPERATORS	16
TOTAL ENERGY	-7.5951704148967E+03		
ENERGY per FORMULA UNIT		-3797.585207448 Hartrees	
VOLUME per FORMULA UNIT		478.06881 $Bohr^3$	

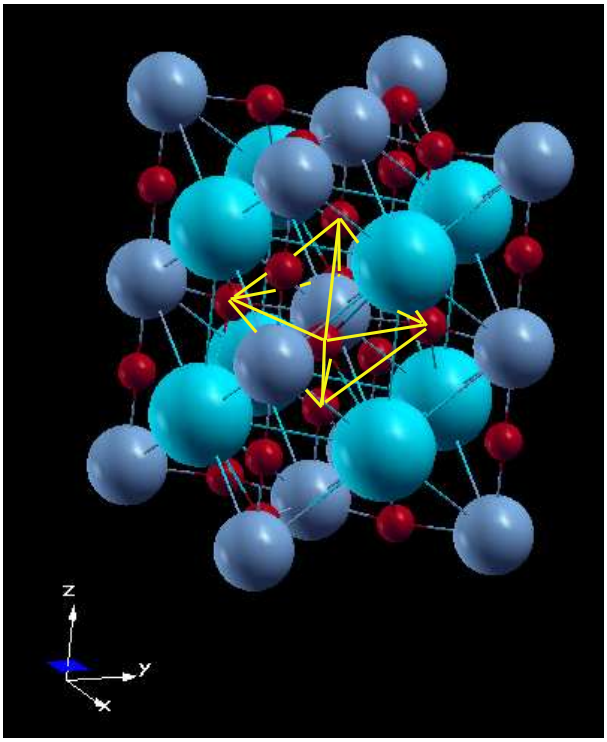

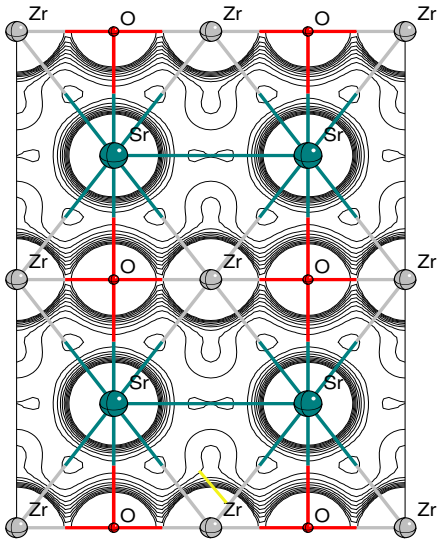

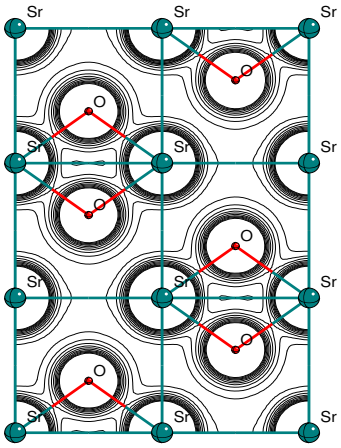

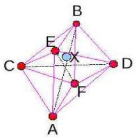

AX = 3.9656 Bohrs
BX = 3.9656 Bohrs
CX = 3.9831 Bohrs
DX = 3.9831 Bohrs
EX = 3.9831 Bohrs
FX = 3.9831 Bohrs

AXB = 180.000 deg
AXC = 90.000 deg
AXD = 90.000 deg
AXE = 90.000 deg
AXF = 90.000 deg
CXE = 90.000 deg
EXD = 90.000 deg
DXF = 90.000 deg
FXC = 90.000 deg

Tilt angle at D = 154.116 deg
Tilt angle at F = 154.116 deg

Figure A.40: Geometry of tetragonal $SrZrO_3$ with measurements according to the scheme outlined in 1.4.3 and contour map of the electronic charge density in the (010) plane (upper), and the (111) plane (lower), the latter displaying the slight covalency as a “saddle” between Sr and O atoms.

Phase 4 - cubic.

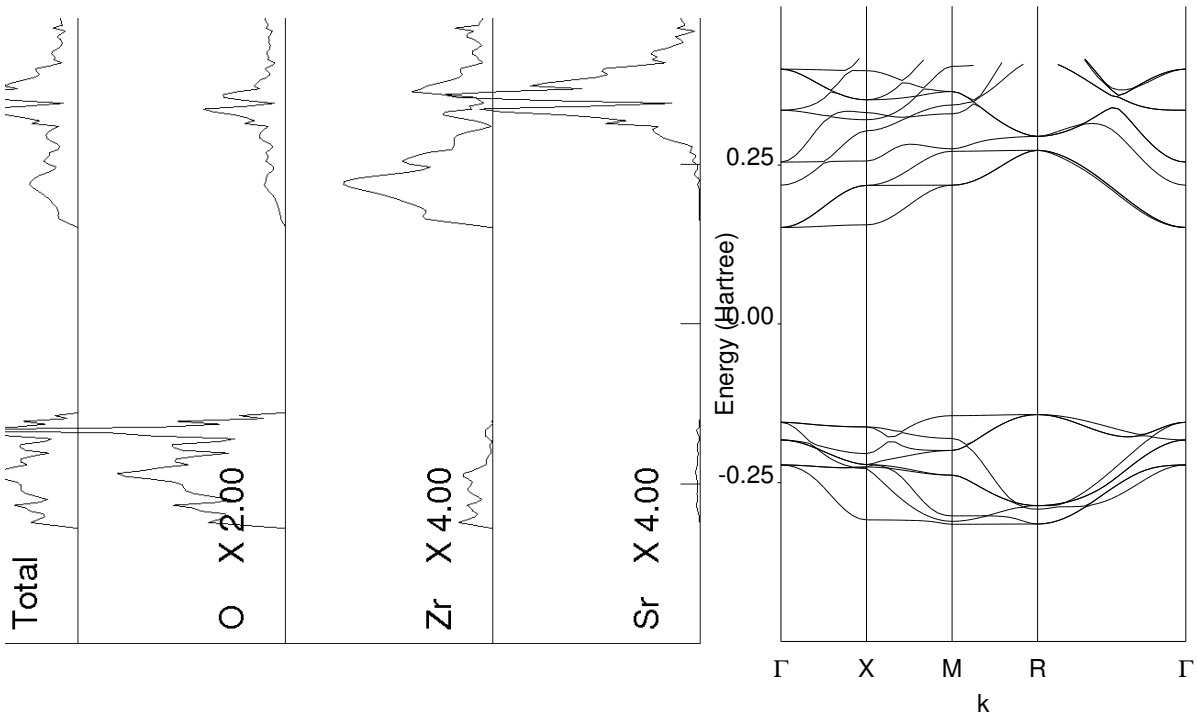

Figure A.41: $SrZrO_3$ cubic phase band structure and density of states.

Measurements

Band Gap = 0.2944933 Hartrees

LATTICE PARAMETERS (BOHR AND DEGREES) - PRIMITIVE CELL

A	B	C	α	β	γ	Volume $Bohr^3$
7.876482745	7.876482745	7.876482745	90.000	90.0000	90.0000	488.648959459

N. OF ATOMS PER CELL	5	NUMBER OF SHELLS	29
NUMBER OF AO	108	N. OF ELECTRONS PER CELL	66
CORE ELECTRONS PER CELL	42	N. OF SYMMETRY OPERATORS	48
TOTAL ENERGY	-3.7975763682695E+03		
ENERGY per FORMULA UNIT		-3797.5763682695E Hartrees	
VOLUME per FORMULA UNIT		488.648959459 $Bohr^3$	

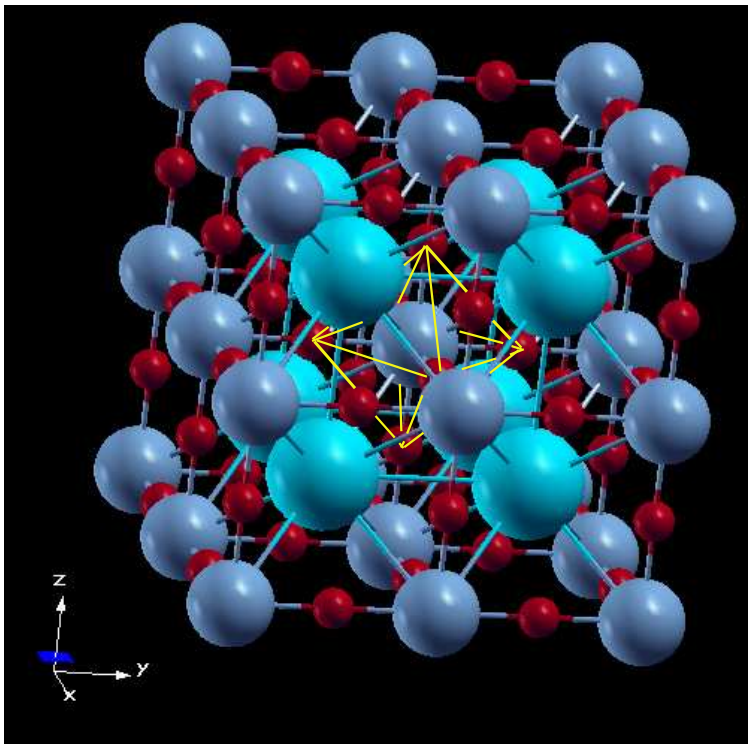

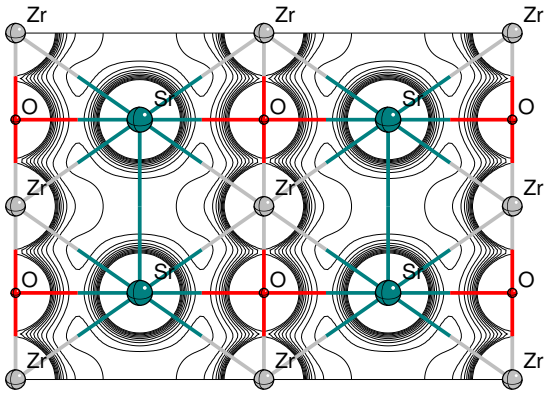

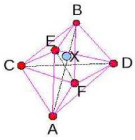

AX = 3. 9382 Bohrs	AXB = 180.000 deg
BX = 3.9382 Bohrs	AXC = 90.000 deg
CX = 3.9382 Bohrs	AXD = 90.000 deg
DX = 3.9382 Bohrs	AXE = 90.000 deg
EX = 3.9382 Bohrs	AXF = 90.000 deg
FX = 3.9382 Bohrs	CXE = 90.000 deg
	EXD = 90.000 deg
	DXF = 90.000 deg
	FXC = 90.000 deg

Figure A.42: Geometry of cubic $SrZrO_3$ with measurements according to the scheme outlined in 1.4.3 and contour map of the electronic charge density in the $(1\,1\,0)$ plane.

A.3.3 Barium Zirconate $BaZrO_3$

Although there may be a very low temperature lower symmetry phase, crystallographic data is only available for cubic $BaZrO_3$:

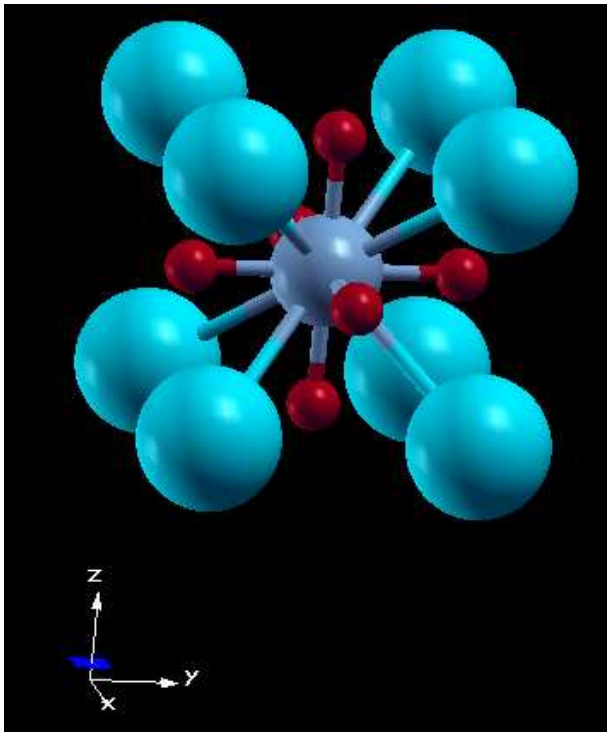

Figure A.43: Cubic $BaZrO_3$

Phase 1 - cubic.

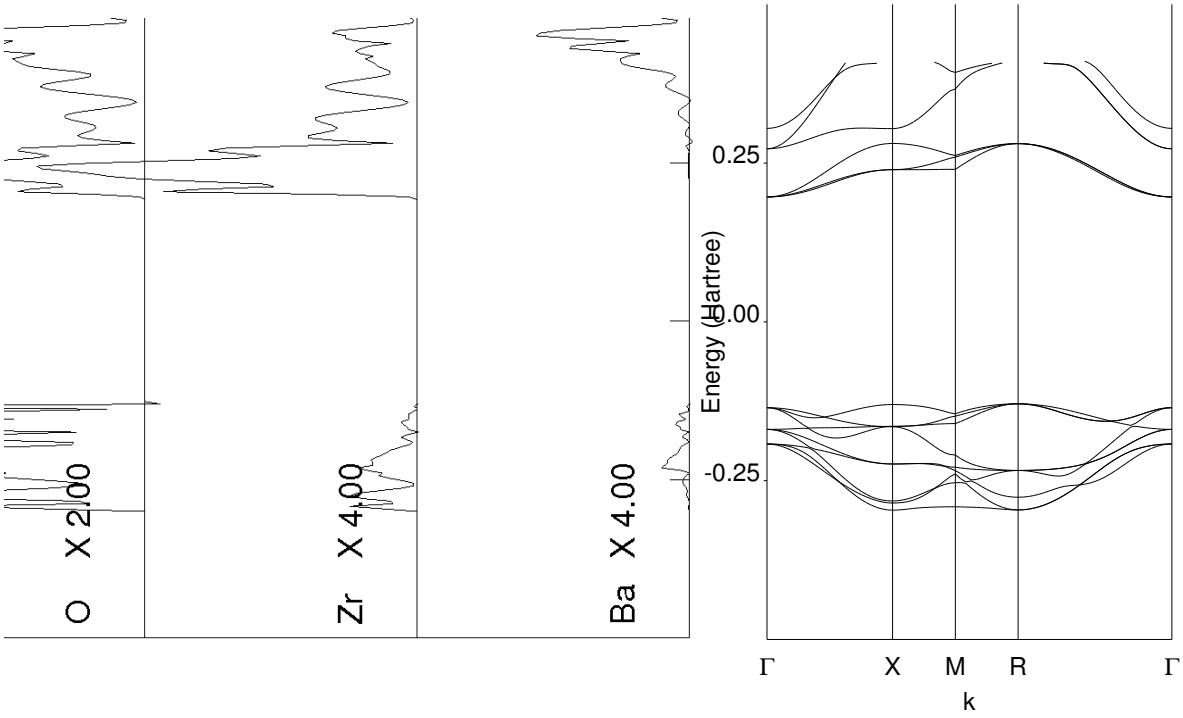

Figure A.44: $BaZrO_3$ cubic phase band structure and density of states.

Measurements

Band Gap = 0.3275056 Hartrees

LATTICE PARAMETERS (BOHR AND DEGREES) - PRIMITIVE CELL

A	B	C	α	β	γ	Volume $Bohr^3$
8.00050	8.00050	8.00050	90.000	90.0000	90.0000	512.09561

N. OF ATOMS PER CELL	5	NUMBER OF SHELLS	30
NUMBER OF AO	111	N. OF ELECTRONS PER CELL	120
CORE ELECTRONS PER CELL	96	N. OF SYMMETRY OPERATORS	48

TOTAL ENERGY -1.1653445597819E+04

ENERGY per FORMULA UNIT -1.1653445597819E+04 Hartrees

VOLUME per FORMULA UNIT 512.09561 $Bohr^3$

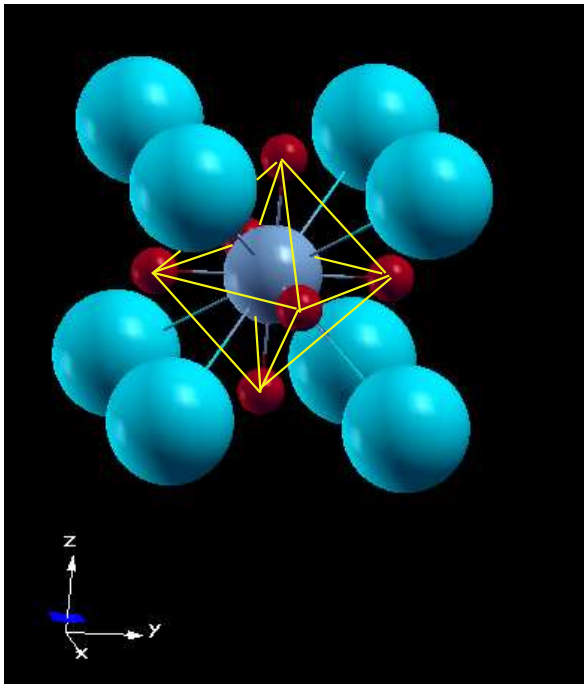

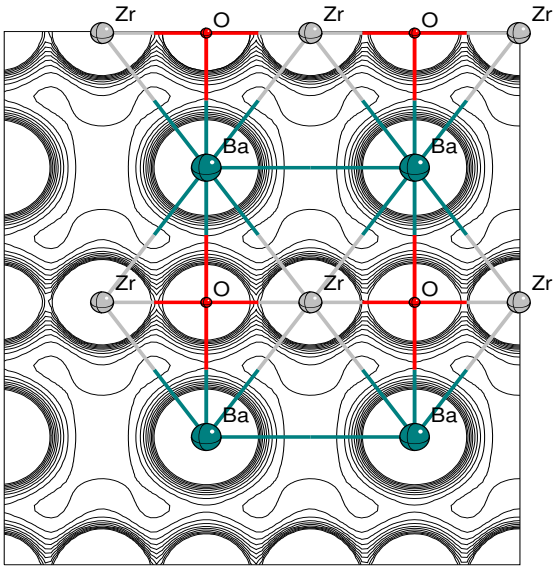

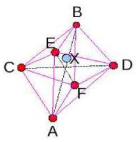

AX = 4.0003 Bohrs	AXB = 180.000 deg
BX = 4.0003 Bohrs	AXC = 90.000 deg
CX = 4.0003 Bohrs	AXD = 90.000 deg
DX = 4.0003 Bohrs	AXE = 90.000 deg
EX = 4.0003 Bohrs	AXF = 90.000 deg
FX = 4.0003 Bohrs	CXE = 90.000 deg
	EXD = 90.000 deg
	DXF = 90.000 deg
	FXC = 90.000 deg

Figure A.45: Geometry of cubic $BaZrO_3$ with measurements according to the scheme outlined in 1.4.3 and contour map of the electronic charge density in the $(1\,1\,1)$ plane.

A.4 Some other Perovskites

A.4.1 Lead Titanate $PbTiO_3$

Lead Titanate $PbTiO_3$ was chosen for study partly because, along with Barium Titanate $BaTiO_3$, it is the subject of the important letter to Nature by R. E. Cohen [**?**], partly because it is one of the most distorted perovskites, exhibiting a high degree of covalency in one bond in the low temperature ferroelectric phase and also because it illustrates (along with $BaTiO_3$) how the A cation will contribute to the covalent bond strength if its valence/conduction electrons are suitably near the O $2p$ electrons in (free atom) orbital energy.
There are two phases [**?**] [149]:

1. $0 - 766\,K$ - tetragonal $P4mm$
2. $766\,K\ - upwards$ - cubic $Pm3m$

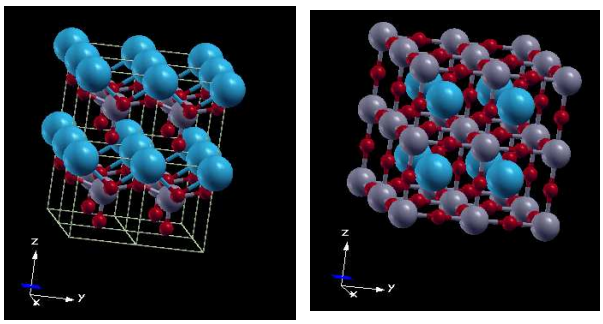

1 2

Figure A.46: The two phases of $PbTiO_3$

Phase 1 - tetragonal.

In this phase the Ti atom is displaced markedly, more than in any other perovskite studied, only along the polar axis in the Z direction. There is covalency from both cations towards the top of the valence band (in this case, in agreement with the findings of [**?**]), but that between Ti and O is more significant.

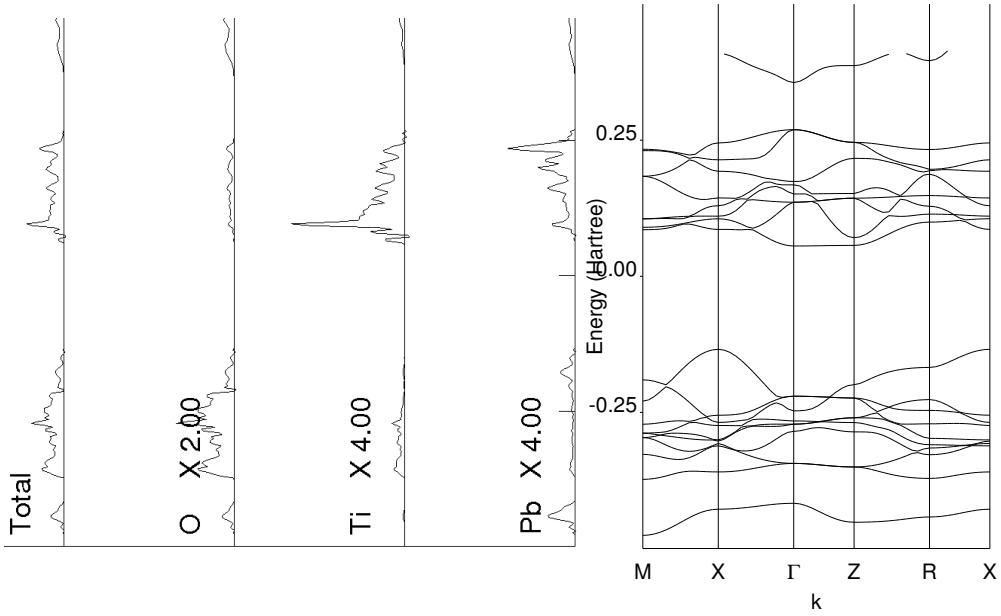

Figure A.47: $\mathrm{PbTiO_3}$ tetragonal phase band structure and density of states.

Measurements

Band Gap = 0.134082 Hartrees

LATTICE PARAMETERS (BOHR AND DEGREES) - PRIMITIVE CELL

A	B	C	α	β	γ	Volume $Bohr^3$
7.19034	7.19034	8.98661	90.0000	90.0000	90.0000	464.61691

N. OF ATOMS PER CELL	5	NUMBER OF SHELLS	26
NUMBER OF AO	98	N. OF ELECTRONS PER CELL	50
CORE ELECTRONS PER CELL	24	N. OF SYMMETRY OPERATORS	8
TOTAL ENERGY	-1.0788325493525E+03		
ENERGY per FORMULA UNIT		-1078.8325493525 Hartrees	
VOLUME per FORMULA UNIT		464.61691 $Bohr^3$	

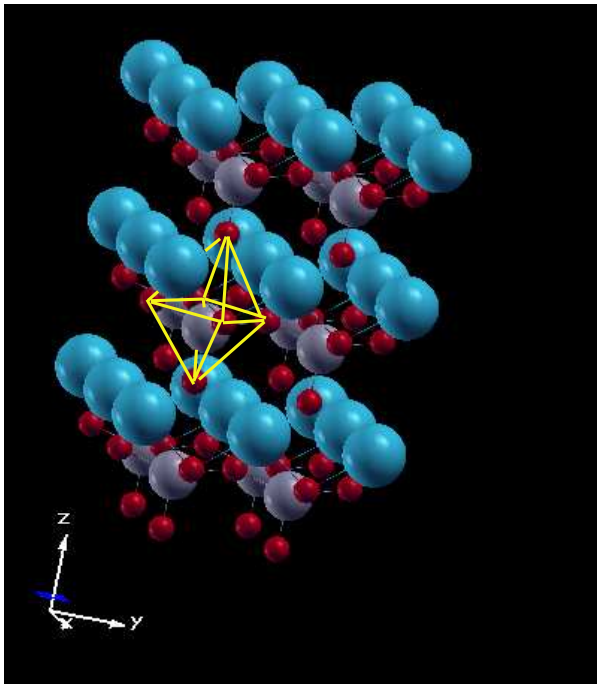

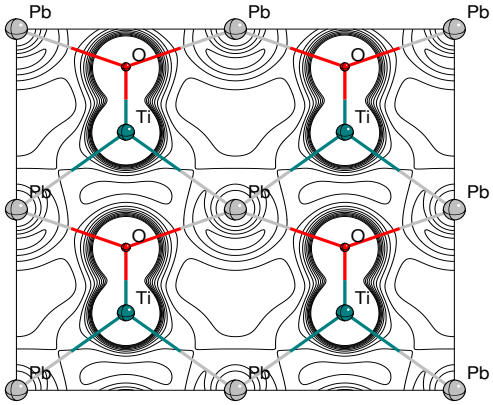

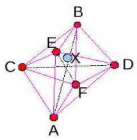

AX = 3.2545 Bohrs
BX = 5.7321 Bohrs
CX = 3.7513 Bohrs
DX = 3.7513 Bohrs
EX = 3.7513 Bohrs
FX = 3.7513 Bohrs

AXB = 180.000 deg
AXC = 106.586 deg
AXD = 106.586 deg
AXE = 106.586 deg
AXF = 106.586 deg
CXE = 85.326 deg
EXD = 85.326 deg
DXF = 85.326 deg
FXC = 85.326 deg

Figure A.48: Geometry of tetragonal $PbTiO_3$ with measurements according to the scheme outlined in 1.4.3 and contour map of the electronic charge density in the (110) plane. The measurements reveal an offset of the Ti atom of more than a Bohr from the central position.

Phase 2 - cubic.

The band structure is simpler than the tetragonal phases, being less populous in the energies at the top of the valence range. The density of states plot reveals that the "covalency" with O also occurs from both cations.

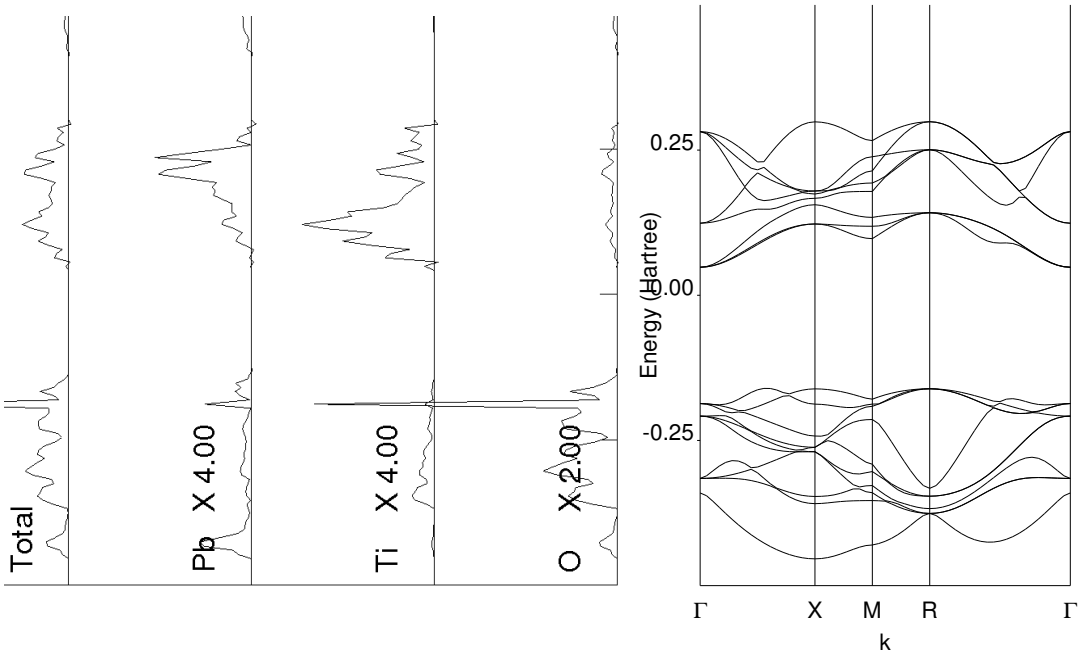

Figure A.49: $PbTiO_3$ cubic phase band structure and density of states.

Measurements

Band Gap 0.17467749 Hartree

LATTICE PARAMETERS (BOHR AND DEGREES) - PRIMITIVE CELL

A	B	C	α	β	γ	Volume $Bohr^3$
7.43495	7.43495	7.43495	90.000	90.0000	90.0000	410.99291

N. OF ATOMS PER CELL	5	NUMBER OF SHELLS	26
NUMBER OF AO	98	N. OF ELECTRONS PER CELL	50
CORE ELECTRONS PER CELL	24	N. OF SYMMETRY OPERATORS	48
TOTAL ENERGY	-1.0788168710467E+03		
ENERGY per FORMULA UNIT		-1078.8168710467 Hartrees	
VOLUME per FORMULA UNIT		410.99291 $Bohr^3$	

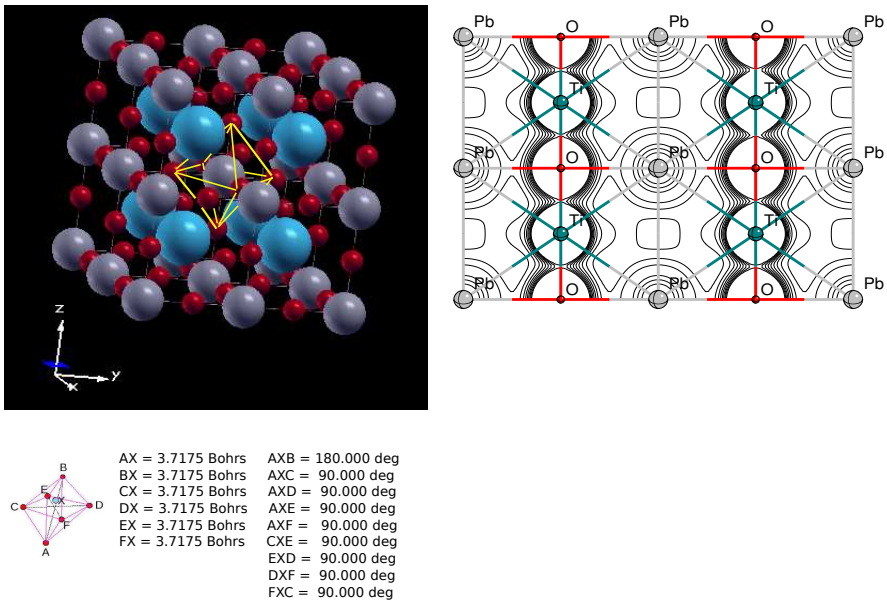

Figure A.50: Geometry of cubic $\mathrm{PbTiO_3}$ with measurements according to the scheme outlined in 1.4.3 and contour map of the electronic charge density in the $(1\,\bar{1}\,0)$ plane.

A.4.2 Lanthanum Aluminate $\mathrm{LaAlO_3}$

Lanthanum Aluminate $\mathrm{LaAlO_3}$ is of considerable modern research interest because of its role as one component of layered two dimensional superconducting systems. It is also of interest in this work because of the unique character of its A and B cations. La is the first of the Lanthanide or Rare Earth series which are characterised by their $4f$ orbitals, but its $4f^1$ electron is replaced by a $5d^1$ electron. On the other hand Al is not a transition metal, but it is sufficiently "small" to be the B cation and its $3p^1$ electron behaves like the d electrons of the transition metals in contributing to the bonding electron congregation, but in conventional terms the bonding is π bonding rather than hybridisation. The result is a small oxygen octahedron and short $\mathrm{Al-O}$ bonds despite a low electron charge density at the BCP. In this material, the oxygen octahedra are not characterised by strong $\mathrm{B-O}$ bonds. These are rather weak with the lowest Crystalline Bond Indices of all the studied perovskites. In fact the electronic charge density at the BCP is slightly lower than the average for the unit cell, which is atypical. The robustness of the oxygen octahedron is brought about by the fact that the $\mathrm{A-O}$ bonds are even weaker by a factor of about five. This will be mentioned again in the discussion.
There are two phases [150]

1. $0 - 800 \pm 10\,K$ - trigonal $R\bar{3}c$
2. $800 \pm 10\,K\ - upwards$ - cubic $Pm\bar{3}m$

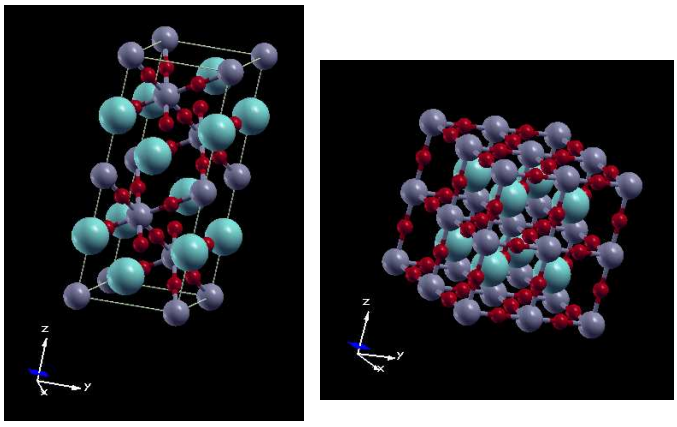

Figure A.51: The two phases of $\mathrm{LaAlO_3}$

Phase 1 - trigonal This is different from the Alkaline Earth perovskites in that the oxygen octahedron is somewhat smaller, and although equilateral, is tilted strongly from all the crystalline axes, and the internal angles are slightly distorted from the right-angle. The band structure is rich about the band gap as would be expected with 188 electrons in the primitive cell. The weak covalency involves both cations but is stronger and peaked between Al and O. Notice that the top of the valence band is higher, and the band gap somewhat wider than for the Alkaline Earth perovskites.

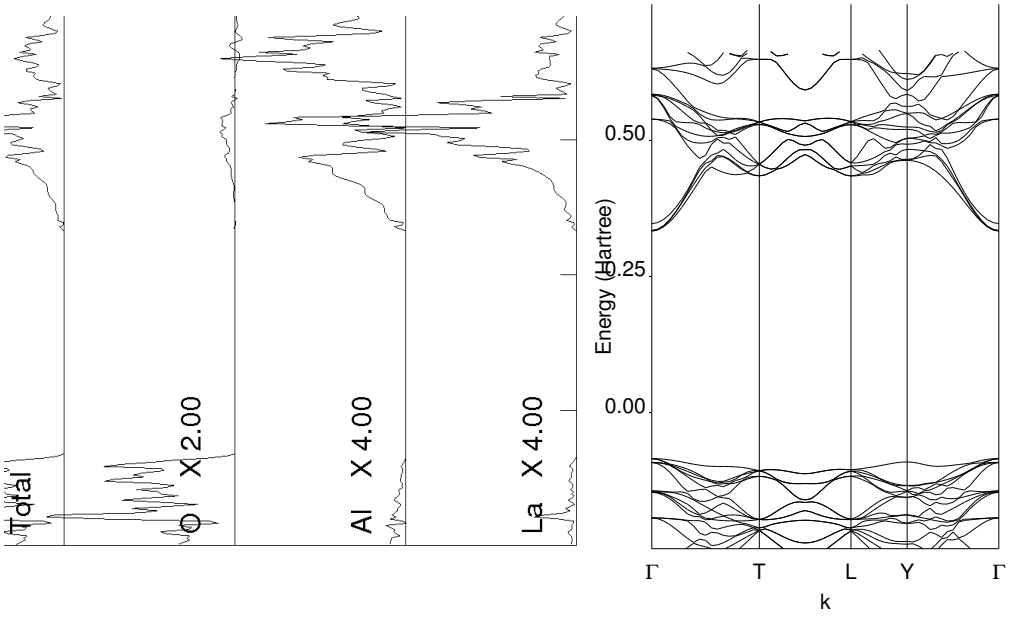

Figure A.52: $LaAlO_3$ trigonal phase band structure and density of states.

Measurements

Band Gap = 0.41763716 Hartrees

LATTICE PARAMETERS (BOHR AND DEGREES) - PRIMITIVE CELL

A	B	C	α	β	γ	Volume $Bohr^3$
10.07687	10.07687	10.07687	60.0375	60.0375	60.0375	724.15289

N. OF ATOMS PER CELL	10	NUMBER OF SHELLS	60
NUMBER OF AO	224	N. OF ELECTRONS PER CELL	188
CORE ELECTRONS PER CELL	140	N. OF SYMMETRY OPERATORS	12
TOTAL ENERGY	-1.7384983143715E+04		
ENERGY per FORMULA UNIT		-8692.491571857 Hartrees	
VOLUME per FORMULA UNIT		362.076445 $Bohr^3$	

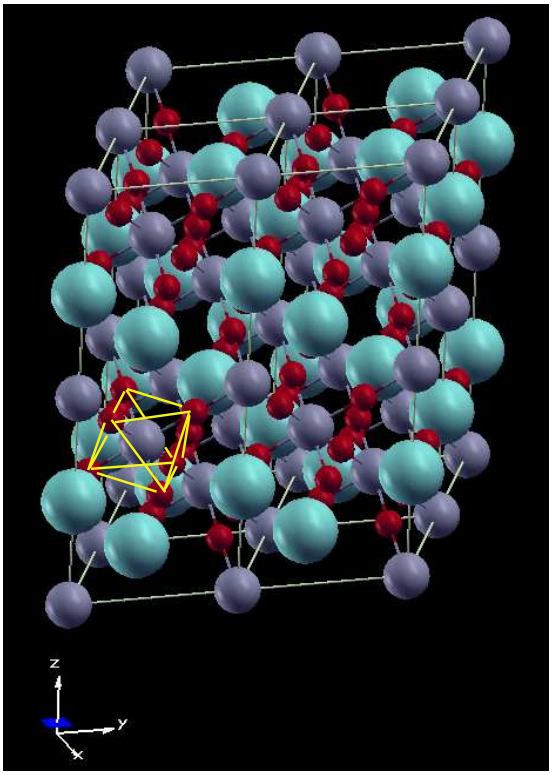

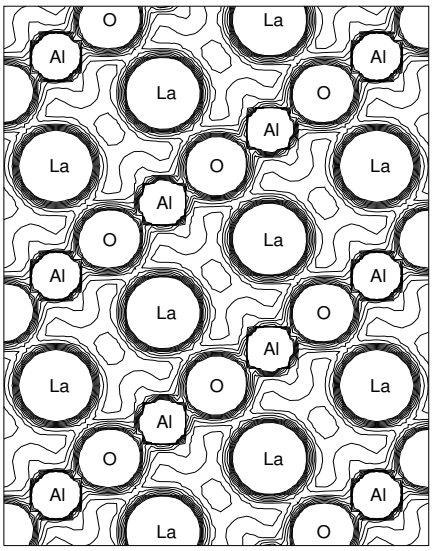

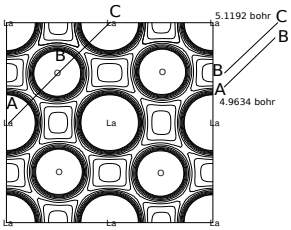

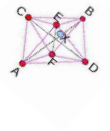

AX = 3.5646 Bohrs
BX = 3.5646 Bohrs
CX = 3.5646 Bohrs
DX = 3.5646 Bohrs
EX = 3.5646 Bohrs
FX = 3.5646 Bohrs

AXB = 180.000 deg
AXC = 89.954 deg
AXD = 90.046 deg
AXE = 89.954 deg
AXF = 90.046 deg
CXE = 90.046 deg
EXD = 89.954 deg
DXF = 90.046 deg
FXC = 89.954 deg

Tilt angle at B = 177.496 deg
Tilt angle at D = 177.496 deg

Figure A.53: Geometry of trigonal $LaAlO_3$ with measurements according to the scheme outlined in 1.4.3 and contour map of the electronic charge density in the (110) plane. The smaller map normal to this shows the slight variation in the $La - O$ bond lengths. The oxygen octahedral cages are oblique to all three crystallographic axes as well as being slightly tilted between themselves.

Notice in the above figure that the electronic charge density between Al and O is about five times greater than that between La and O.

Phase 2 - cubic In this phase the oxygen octahedron is again somewhat smaller, but is no longer tilted and parallels the crystalline axes. It is similar to cubic $BaTiO_3$ but the top of the valence band is higher, and the band gap somewhat wider.

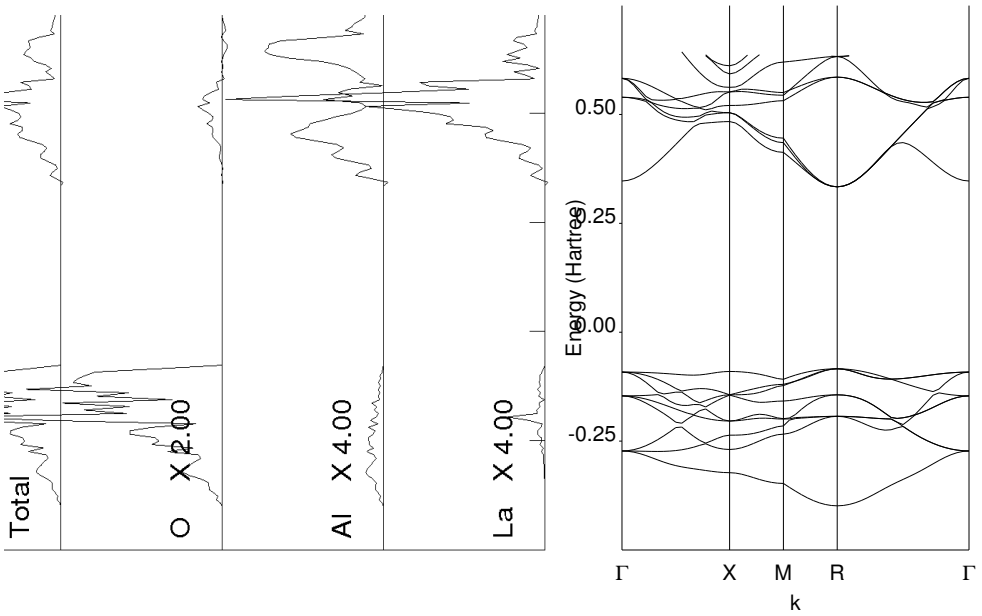

Figure A.54: $LaAlO_3$ cubic phase band structure and density of states.

Measurements

Band Gap = 0.43863784 Hartrees

LATTICE PARAMETERS (BOHR AND DEGREES) - PRIMITIVE CELL

A	B	C	α	β	γ	Volume $Bohr^3$
7.12483	7.12483	7.12483	90.0000	90.0000	90.0000	361.67888

N. OF ATOMS PER CELL	5	NUMBER OF SHELLS	30
NUMBER OF AO	112	N. OF ELECTRONS PER CELL	94
CORE ELECTRONS PER CELL	70	N. OF SYMMETRY OPERATORS	48
TOTAL ENERGY	-8.6924920829313E+03		
ENERGY per FORMULA UNIT		-8692.4920829313 Hartrees	
VOLUME per FORMULA UNIT		361.67888 $Bohr^3$	

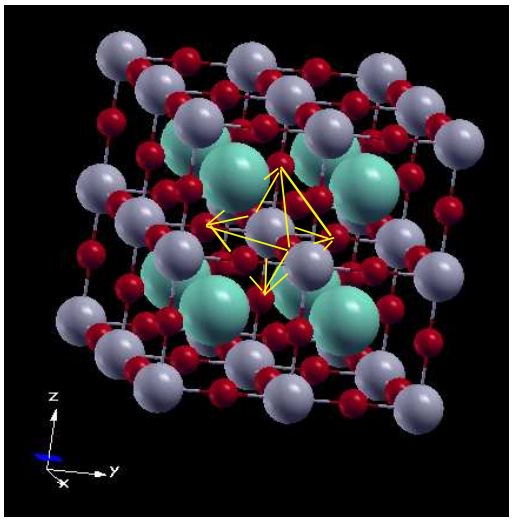

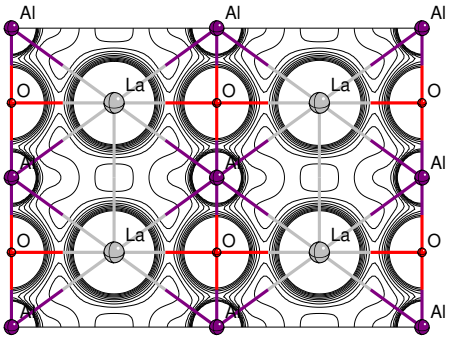

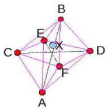

AX = 3. 5624 Bohrs
BX = 3.5624 Bohrs
CX = 3.5624 Bohrs
DX = 3.5624 Bohrs
EX = 3.5624 Bohrs
FX = 3.5624 Bohrs

AXB = 180.000 deg
AXC = 90.000 deg
AXD = 90.000 deg
AXE = 90.000 deg
AXF = 90.000 deg
CXE = 90.000 deg
EXD = 90.000 deg
DXF = 90.000 deg
FXC = 90.000 deg

Figure A.55: Geometry of cubic $LaAlO_3$ with measurements according to the scheme outlined in 1.4.3 and contour map of the electronic charge density in the (110) plane.

LaAlO3-cubic ALPHA+BETA ELECTRONS
MULLIKEN POPULATION ANALYSIS - NO. OF ELECTRONS 94.000000

ATOM	Z	CHARGE	A.O. POPULATION
1 LA	57	54.224	1.999 2.057 1.999 1.999 1.999 1.735 1.996 1.996
			1.996 1.999 1.999 1.999 1.999 1.999 0.070 0.919
			0.919 0.919 1.940 1.941 1.941 1.940 1.941 0.088
			0.102 0.102 0.088 0.102 2.166 1.092 1.092 1.092
			0.743 1.045 1.045 1.045 1.260 0.953 0.953 0.953
2 AL	13	11.188	2.000 1.966 1.988 1.988 1.988 0.016 0.085 0.085
			0.085 0.464 0.125 0.125 0.125 0.052 0.014 0.014
			0.052 0.014
3 O	8	9.529	1.084 0.910 0.315 0.339 0.339 0.924 0.664 0.645
		0.645	1.019 0.752 0.945 0.945 0.000 0.000 0.000
		0.000	0.000
4 O	8	9.529	1.084 0.910 0.339 0.315 0.339 0.924 0.645 0.664
		0.645	1.019 0.945 0.752 0.945 0.000 0.000 0.000
		0.000	0.000
5 O	8	9.529	1.084 0.910 0.339 0.339 0.315 0.924 0.645 0.645
		0.664	1.019 0.945 0.945 0.752 0.000 0.000 0.000
		0.000	0.000

ATOM	Z	CHARGE	SHELL POPULATION
1 LA	57	54.224	1.999 8.054 7.723 9.996 2.827 9.702 0.483 5.443
			3.877 4.118
2 AL	13	11.188	2.000 7.930 0.272 0.839 0.146
3 O	8	9.529	1.084 1.903 2.878 3.662 0.002
4 O	8	9.529	1.084 1.903 2.878 3.662 0.002
5 O	8	9.529	1.084 1.903 2.878 3.662 0.002

OVERLAP POPULATION CONDENSED TO ATOMS FOR FIRST 6 NEIGHBORS

ATOM A	ATOM B	CELL	R(AB)/AU	R(AB)/ANG	OVPOP(AB)
1 LA	3 O	(0 0 0)	5.038	2.666	-0.016
	2 AL	(0 0 0)	6.170	3.265	-0.001
	1 LA	(-1 0 0)	7.125	3.770	0.000
	3 O	(1 0 0)	8.726	4.618	0.000
	1 LA	(-1 -1 0)	10.076	5.332	0.000
	3 O	(0 -1 0)	11.265	5.961	0.000

ATOM A	ATOM B	CELL	R(AB)/AU	R(AB)/ANG	OVPOP(AB)
2 AL	3 O	(0 0 0)	3.562	1.885	0.123
	1 LA	(0 0 0)	6.170	3.265	-0.001
	2 AL	(-1 0 0)	7.125	3.770	-0.003
	3 O	(0 1 0)	7.966	4.215	0.000
	2 AL	(-1 -1 0)	10.076	5.332	0.000
	3 O	(1 0 0)	10.687	5.655	0.000

ATOM A	ATOM B	CELL	R(AB)/AU	R(AB)/ANG	OVPOP(AB)
3 O	2 AL	(0 0 0)	3.562	1.885	0.123
	1 LA	(0 0 0)	5.038	2.666	-0.016
	4 O	(0 0 0)	5.038	2.666	-0.031
	3 O	(-1 0 0)	7.125	3.770	0.000
	2 AL	(0 -1 0)	7.966	4.215	0.000
	1 LA	(-1 0 0)	8.726	4.618	0.000

Bibliography

[1] Hoffman R. *Solids and Surfaces: A Chemist's View of Bonding in Extended Structures.* 1st Edition Wiley-VCH ISBN 978-0-471-18710-3 - John Wiley Sons 1989.

[2] Megaw H. D. Crystal structure of double oxides of the perovskite type. *Proceedings of the Physical Society* 58:2 p133 1946.

[3] Joint Press Release, Semiconductor Research Corporation (SRC) and Yale University. 20 August 2009

[4] Kim Chang Huan, Qi Gongshin, Dahlberg Kevin and Li Wei Strontium-Doped Perovskites Rival Platinum Catalysts for Treating NO_x in Simulated Diesel Exhaust *Science* 327 pp 1624-1627 26 March 2010.

[5] Johnsson,Mats and Lemmens, Peter, Perovskites and thin filmscrystallography and chemistry. *J. Phys.: Condens. Matter* 20 264001 (6pp) 2008.

[6] R. Dovesi, V. R. Saunders, C. Roetti, R. Orlando, C. M. Zicovich-Wilson, F. Pascale, B. Civalleri, K. Doll, N. M. Harrison, I. J. Bush, Ph. DArco, M. Llunell *CRYSTAL06 User's Manual*, University of Torino, Torino, 2006

[7] Kokalj, A. *Comp. Mater. Sci.*, Vol. 28, p. 155, 2003. Code available from http://www.xcrysden.org/.

[8] Bader Richard F. W. *Atoms In Molecules - A Quantum Theory* Oxford University Press, 1990.

[9] Bader R. F. W. Bond Paths Are Not Chemical Bonds *J. Phys. Chem. A,* 113 (38), 2009 pp 1039110396, 2009.

[10] Lavers, Philip S. The Mobility of Large Anions in Crystals with the Fluorite Structure, Thesis (M.Sc.(Hons)) - University of Wollongong, 2002.

[11] Watson, Richard E. Analytic Hartree-Fock solutions for O^{--}, *Physical Review,* 111(4):1108 - 1110, August 1958.

[12] Slater John C. *Quantum Theory of Atomic Structure* (2 Vols), McGraw-Hill Book Company Inc., New York 1960. p182 and appendix

[13] Pauling, Linus *The Nature of the Chemical Bond and the Structure of Molecules and Crystals* Cornell University Press, Ithaca, New York. 1960. pp 128, 505

[14] Dovesi, R. Pisani, C. Roetti, C. and Saunders, V. Treatment of Coulomb interactions in Hartree-Fock calculations of Periodic systems *Physical Review B.* 28:10 p5781 1983.

[15] Saunders V.R., Freyria-Fava C., Dovesi R., Salasco L. and Roetti C. On the electrostatic potential in crystalline systems where the charge density is expanded in Gaussian functions. *Molecular Physics* 77:4 1992 629-665.

[16] Bader Richard F. W. et al Quantum topology of molecular charge distributions. II. Molecular structure and its change *J. Chem. Phys.* 70(9): 4316 May 1979 and references therein and numerous articles and two books thereafter

[17] Zou P. F. and Bader R. F. W. A Topological Definition of a Wigner-Seitz Cell and the Atomic Scattering Factor. *Acta Cryst. A* 50:6 714-725, 1994

[18] Tsirelson V.G., Zou P. F., Tang T. -H. and Bader R. F. W. Topological definition of crystal structure: determination of the bonded interactions in solid molecular chlorine. *Acta Cryst. A* 51:2 143-153, 1995.

[19] Aray A. and Bader R. F. W. Requirements for activation of surface oxygen atoms in MgO using the Laplacian of the electron density. *Surface Science* 351: 233-249, 1996.

[20] Mori-Sánchez P., Martín Pendás A. and Luaña V. A Classification of Covalent, Ionic, and Metallic Solids Based on the Electron Density. *J. AM. CHEM. SOC.* 124, 14721-14723, 2002.

[21] Tsirelson V. G. and Ozerov R.P. *Electron Density and Bonding in Crystals* Taylor and French 1996, and references therein.

[22] Herzig P. and Zemann J. AB_3 nets built from corner-connected octahedra: geometries, electrostatic lattice energies, and stereochemical discussion. *Zeitschrift für Krystallographie* 205,1993 85-97.

[23] Wells A. F. *Structural Inorganic Chemistry,* 5th Edition. Oxford: Clarendon Press, 1984.

[24] Shannon, R.D. Revised Effective Ionic Radii and Systematic Studies of Interatomie Distances in Halides and Chaleogenides *Acta Cryst.* A32, 751 1976.

[25] Kour P., Kumar Pawan, Sinha S.K, Kar Manoranjan. *Electrical properties of calcium modified PZT (52/48) ceramics* Solid State Communications 190 pp 3339 2014.

[26] Cohen Ronald E. Origin of Ferroelectricity in Perovskite Oxides. *Nature* 358 p136 9 July 1992.

[27] Slater J. C. The Lorentz Correction in Barium Titanate. *Physical Review* 78:6 p748 June 15 1950.

[28] Chang J, Eremin I and Thalmeier P Cooper-pair formation by anharmonic rattling modes in the -pyrochlore superconductor KOs2O6 *New Journal of Physics* 11 055068 May 2009.

[29] Schoenes J., Racu A., Doll K., Bukowski Z. and Karpinski J. Phonons and crystal structures of the -pyrochlore superconductors KOs2O6 and RbOs2O6 from micro-Raman spectroscopy *PHYSICAL REVIEW B* 77, 134515 2008.

[30] Warren M. C. and Ackland G.J. Ab initio studies of structural instabilities in magnesium silicate perovskite. *Phys. Chem. Minerals* 23 pp 107-118 1996 and references therein.

[31] Woodward P. M. Octahedral Tilting in Perovskites. II. Structure Stabilising Forces. *Acta Cryst.B* 53 pp 44-66 1997.

[32] Cowley R. A. Lattice Dynamics and Phase Transitions of Strontium Titanate *Physical Review* 134(4A):A981 May 1964.

[33] Successive structural phase transitions in $\mathrm{Na_xWO_3}$ *Physical Review B* 25(11) :6876 June 1982.

[34] The classification of tilted octahedra in perovskites *Acta Cryst.B*28 pp 33843392 1972.

[35] Woodward P. M. Octahedral Tilting in Perovskites. I. Geometrical Considerations. *Acta Cryst.B* 53 pp 3243 1997.

[36] Howard C. J. and Stokes H. T. Group-Theoretical Analysis of Octahedral Tilting in Perovskites *Acta Cryst. B* 54 pp 782-789 1998.

[37] Goodenough J. B. Metallic Oxides *Progress In Solid State Chemistry* 5 pp 145-399 1971.

[38] Harrison Walter A. *Electronic Structure and the Properties of Solids - THE PHYSICS OF THE CHEMICAL BOND* W. H. Freeman and Company San Francisco 1980.

[39] Enzonga Yoca S. et al Radiative properties and core-polarization effects in the W5+ ion. *J. Phys. B: At. Mol. Opt. Phys.* 45 No.3 035002 6pp 2012.

[40] Orchin Milton, Macomber R.S., Pinhas A. and Wilson R.M. *The Vocabulary and Concepts of Organic Chemistry* 2nd Ed. John Wiley & Sons, Inc. 2005.

[41] Mulliken Robert S. *Spectroscopy, molecular orbitals, and chemical bonding* Nobel Lecture, December 12, 1966

[42] Battye F.L., Höchst H. and Goldmann A. *Photoelectron Studies Of The* $\mathrm{BaTiO_3}$ *and* $\mathrm{SrTiO_3}$ *Valence States* Solid State Communications Vol 19 pp 269-271 1976.

[43] Tsirelson V.G., Avilov A.S., Lepeshov G.G., Kulygin A.K., Stahn J., Pietsch U., Spence J.C.H., Quantitative analysis of the inner-crystal electrostatic potential in rock-salt crystals using accurate electron diffraction data, *J. Phys. Chem. A,* B105 2001, 5068-5074.

[44] Zhurova E.A., Zuo J.M., Tsirelson V.G., Topological analysis of electrostatic potential in $\mathrm{SrTiO_3}$ *J. Phys. Chem. B*, 105:21, 2001, 5068-5074.

[45] Gatti, Carlo Chemical bonding in crystals : new directions. *Zeitschrift fr Kristallographie* 220:5-6 pp. 399-457 2005.

[46] Murrell John N., KettleSydney F. A. and Tedder John M. *The Chemical Bond* John Wiley and Sons Ltd. 1978.

[47] Dirac P 1929 Quantum Mechanics of Many-Electron Systems Proc.R.Soc.Lond. A123 714-733.

[48] New developments in molecular orbital theory. *Reviews of Modern Physics,* 23(2):69-89, April 1951.

[49] Euwema, R. N. Whilhite, D. L. and Surratt, D. T. General Crystalline Hartree-Fock Formalism: Diamond Results. *Physical Review B* 7:2 1973.

[50] Goodstein David L. *States Of Matter* esp. ch3 *Solids* Dover Publications , Inc. New York 1985.

[51] Fedor Juraj *Statistical Thermodynamics - Condensed Script* University of Fribourg Department of Chemistry. homeweb.unifr.ch/fedorj/pub/docs/std_thermo_jf.pdf 2013

[52] Seitz F. *The Modern Theory of Solids* McGraw-Hill Book Company Inc., New York 1940. pp 447 - 450.

[53] Slater J. C. and Shockley W. Optical Absorption by the Alkali Halides *Physical Review* 50:705 October 1936.

[54] Hodby J. W. Electronic Properties. In *Crystals with the Fluorite Structure*. Ed. Hayes W. Oxford University Press Belfast 1974.

[55] Kahn A. H. and Leyedecker A. J. Electronic energy bands in Strontium Titanate *Physical Review* 135(5A):A1321 August 1964.

[56] Linus Pauling "Valence and Molecular Structure," Lectures 1 and 2. Produced for the Institutes Program of the National Science Foundation. Robert and Jane Chapin, producers. 1957. http://scarc.library.oregonstate.edu/coll/pauling/bond/narrative/page1.html

[57] Visscher L. and Dyall K. G. Dirac-Fock atomic electronic structure calculations using different nuclear charge distributions *Atom. Data Nucl. Data Tabl.* 67 p. 207 1997. Also at http://www.chem.vu.nl/ visscher/FiniteNuclei/FiniteNuclei.htm .

[58] Harrison N. M An Introduction to Density Functional Theory *CRYSTAL03 Workshop Department of Chemistry* Imperial College of Science Technology and Medicine, London SW7 2AY, 2003.

[59] Hartree, D.R. Hartree, W. and Swirles, Bertha Self-consistent field, including exchange and super-position of configurations, with some results for oxygen. *Phil. Trans. A,* 238: 1939 229-247.

[60] Allan, M.C. and Mackrodt, W.C. Density functional theory and interionic potentials. *Philosophical Magazine B,* 69:5 1994 871-878.

[61] Cheetham A. K. and Day P. *Solid State Chemistry: Compounds* Oxford University Press, 1992 p.6

[62] Megaw H.D. *"Ferroelectricity in Crystals"* Methuen & Co Ltd London 1957.

[63] Bersuker, I. B. *The Jahn-Teller effect and vibronic interactions in modern chemistry.* Plenum Press, New York, 1984.

[64] Englman R. *The Jahn-Teller Effect in Molecules and Crystals* Wiley-Interscience, London, 1972.

[65] Becke, A.D. Density-functional exchange-energy approximation with correct asymptotic behaviour. *Physical Review A* 38:6 pp 3098-3100 1988.

[66] Lee, C. Yang, W. and Parr R. Development of the Colle-Salvetti correlation-energy formula into a functional of the electron density. *Physical Review B* 37:2 pp 785-789 1988.

[67] Pisani, C. Dovesi, R. and Roetti, C. *Hartree-Fock Ab Initio Treatment of Crystalline Systems.* Lecture Notes in Chemistry 48 Springer-Verlag Berlin Heidelberg 1988.

[68] Pisani, C. (Ed.) *Quantum-Mechanical Ab-initio Calculation of the Properties of Crystalline Materials.* Lecture Notes in Chemistry 67 Springer-Verlag Berlin Heidelberg 1996.

[69] Georges A., Kotliar G., Krauth W. and Rozenberg M. Dynamical mean-field theory of strongly correlated fermion systems and the limit of infinite dimensions. *Reviews of Modern Physics*, Vol. 68, No. 1, January 1996

[70] Jacob D., Haule K. and Kotliar G. Combining the hybrid functional method with dynamical mean-field theory. *EPL*, 84 (2008) 57009.

[71] Tsirelson Vladimir and Stash Adam Determination of the electron localization function from electron density. *Chemical Physics Letters* 351 pp142-148 2002.

[72] Yu Min and Trinkle Dallas R. Accurate and efficient algorithm for Bader charge integration. *THE JOURNAL OF CHEMICAL PHYSICS* 134 064111-1 2011

[73] Refer to http://www.gnuplot.info/.

[74] Tsirelson V. G., Avilov A. S., Lepeshov G. G., Kulygin A. K., Stahn J., Pietsch U. and Spence J. C. H. Quantitative Analysis of the Electrostatic Potential in Rock-Salt Crystals Using Accurate Electron Diffraction Data *J. Phys. Chem. B* 105, 5068-5074, 2001.

[75] Ageev M.V. Experimental Determination of Electron Density in Crystals *Russian Chemical Bulletin* Volume 3, Number 1 January, 1954, Springer New York

[76] Gatti C., Saunders V. R. and Roetti C. Crystal field effects on the topological properties of the electron density in molecular crystals: The case of urea. *J. Chem. Phys.* 101 (12),pp 10686-10696 15 December 1994.

[77] Perrin Charles L. Atomic Size Dependence of Bader Electron Populations: Significance for Questions of Resonance Stabilization *J. Am. Chem. Soc.* 113, pp 2865-2868 1991.

[78] Gatti C. and Piercarlo Fantucci Are Bader Electron Populations Atomic Size Dependent? *J. Phys. Chem.* 97, pp 11677-11680 1993.

[79] Martín Pendás A., Costales Aurora, and Luaña Víctor Ions in crystals:The topology of the electron density in ionic materials. 1. Fundamentals *Physical Review B* 55:7 pp 4275-4284 1997.

[80] Wysin G.M. *Probability Current and Current Operators in Quantum Mechanics* Department of Physics, Kansas State University, Manhattan, KS 66506-2601 2011.

[81] Griffiths David J. *Introduction to Electrodynamics* page 68, Prentice Hall International, Inc. 1999.

[82] Lytle, F. W. X-Ray Diffractometry of Low-Temperature Phase Transformations in Strontium Titanate. *Journal of applied Physics* 35:7 pp 2212-2215 July,1964.

[83] http://bifrost.cwru.edu/personal/collins/virial/

[84] Keith T.A., Bader R.F.W. and Aray Y. Structural Homeomorphism Between the Electron Density and the Virial Field *International Journal of Quantum Chemistry* 57 pp. 183-198 1996.

[85] Lewis G. N. The Atom and the Molecule J. Am. Chem. Soc. 1916, 38, 762.

[86] Becke A. D. and Edgecombe K. E.A simple measure of electron localisation in atomic and molecular systems. *J. Chem. Phys.* 92(9) May 1990.

[87] Calatayud M., Andrés J., Beltran A. and Silvi B. The hierarchy of localization basins: a tool for the understanding of chemical bonding exemplified by the analysis of the $\mathrm{VO_x and VO_x^+ (x = 1 - 4)}$ systems *Theor Chem Acc* 105 299-308 2001.

[88] Wannier G. H. The Structure of Electronic Excitation Levels in Insulating Crystals. *Physical Review* 52:191 August 1937

[89] Frenkel J. On the transformation of light into heat in solids. *Physical Review* 37:17 January 1931.

[90] Hopfield, J.J. Theory of the Contribution of Excitons to the Complex Dielectric Constant of Crystals. *Physical Review* 112:5 1958.

[91] Towler M., Caus M. and Zupan A. Density functional theory in periodic systems using local Gaussian basis sets. *Computer Physics Communications* 98, pp. 181-205 (1996)

[92] Special Issue: “90 Years of Chemical Bonding” *Journal of Computational Chemistry* Volume 28 Issue 1 1-466 January 2007.

[93] Brown, I. D. Chemical and Steric Constraints In Inorganic Solids. *Acta Cryst.* B48 553-572 1992.

[94] *The Quantum Theory of Atoms in Molecules* Edited by C.F. Matta and R. J. Boyd WILEY-VCH Gerlag GmbH & Co. KGaA Weinheim.

[95] Shannon R. D. and Prewitt C. T. Effective ionic radii in oxides and fluorides. *Acta Cryst.* B25 925 - 946 1969.

[96] Hoffmann Roald How Chemistry and Physics Meet in the Solid State. *Angew. Chem. Int. Ed. Engl.* 26 846 - 878 1987.

[97] Bader, R. F. W. A Bond Path: A Universal Indicator of Bonded Interactions. *J. Phys. Chem. A* 102 7314-7323 1998.

[98] Grimme, Stefan, Mück-Lichtenfeld, Christian, Erker, Gerhard, Keh,r Gerald, Wang, Huadong, Beckers, Helmut and Willner, Helge When Do Interacting Atoms Form a Chemical Bond? Spectroscopic Measurements and Theoretical Analyses of Dideuteriophenanthrene *Angew. Chem. Int. Ed.* 48 2592 2595 2009.

[99] Hunt Patricia Molecular Orbitals and Population Analysis www.huntresearchgroup.org.uk/teaching/...chem.../L7$_b onding.pdf$ 2008.

[100] Gillespie, R. J. *Molecular Geometry* Van Nostrand Reinhold, London 1972.

[101] Gillespie, Ronald J. Improving our understanding of molecular geometry and the VSEPR model through the ligand close-packing model and the analysis of electron density distributions. *Coordination Chemistry Reviews* 197 pp. 51 69 2000.

[102] Popelier, P. L. A. On the full topology of the Laplacian of the electron density. *Coordination Chemistry Reviews* 197 pp. 169 189 2000.

[103] Malcolm, Nathaniel O. J. and Popelier, Paul L. A. On the Full Topology of the Laplacian of the Electron Density II: Umbrella Inversion of the Ammonia Molecule. *J. Phys. Chem. A* 105 pp. 7638-7645 2001.

[104] Savin A., Jepsen O., Flad J., Andersen O. K., Heinzwerner Preuss H. and von Schnering H.G Electron Localization in Solid-state Structures of the Elements: the Diamond Structure *Angew. Chem. Int. Ed. Engl.* 31 No. 2 1992.

[105] Silvi B. and Savin A. Classification of chemical bonds based on topological analysis of electron localization functions. *Nature* 371-20 pp. 683 - 686 October 1994.

[106] Savin A., Nesper R., Wengert S. and Fässler T.E. ELF: The Electron Localization Function *Angew. Chem. Int. Ed. Engl.* 36 pp. 1808 - 1832 1997.

[107] Contreras-Garca J. and Recio J.M. On Bonding in Ionic Crystals *J. Phys. Chem. C* 115 pp. 257263 2011.

[108] Schmider, H.L. and Becke, A. D. Chemical content of the kinetic energy density *Journal of Molecular Structure (Theochem)* 527 pp.51 - 61 2000.

[109] Miedema, A. R. Energy effects and charge transfer in metal physics; modelling in real space *Physica B: Condensed Matter* 182:1 pp 1-17 Sept 1992.

[110] Ashcroft, N.W. and Mermin, N.D. *Solid State Physics* Saunders College Publishing 1976.

[111] http://www.tcm.phy.cam.ac.uk/ mdt26/crystal.html .

[112] Geneste, G. et al. Ab initio study of Mg adatom and MgO molecule adsorption and diffusion on the MgO (0 0 1) surface *Applied Surface Science* 188 pp 122-127 2002.

[113] Cohen, A.J. and Gordon, R.G. Modified electron-gas study of the stability, elastic properties and high-pressure behaviour of MgO and CaO crystals. *Physical Review B* 14:10 p. 4593 1976.

[114] Pyper, N.C. The Cohesion of Solid Magnesium and Calcium Oxide: The Role of in-Crystal Modification of the Oxide ion and Electron Correlation *Phil. Trans. R. Soc. Lond. A* 352:1698 pp 89-123 15 July 1995.

[115] Doll, K, Dolg, M. Fulde, P. and Stoll, H. Correlation effects in ionic crystals: The cohesive energy of MgO. *Physical Review B* 52:7 4842 1995.

[116] Doll, K, Dolg, M. and Stoll, H. Correlation effects in MgO and CaO: The cohesive energies and lattice constants. *Physical Review B* 54:19 13529 1996.

[117] Zhang, X.D. and Sauthoff, G. Analysis of relationships between cohesive energy, elastic moduli and lattice parameter of some high temperature intermetallics. *Intermetallics* 3 pp 137-140 1995.

[118] Verma, A.S. An empirical model for bulk modulus and cohesive energy of rocksalt-, zincblende- and chalcopyrite-structured solids. *Phys. Status Solidi B* 246, No. 2, pp 345353 2009.

[119] Gordon Roy G. and Kim Y.S. Theory for the Forces between Closed-Shell Atoms and Molecules *THE JOURNAL OF CHEMICAL PHYSICS* Vol. 56 No.6 1972.

[120] Tanner, Brian K. *Introduction to the Physics of Electrons in Solids* Cambridge University Press, 1995. pp. 46, 47.

[121] Lpez, J. M.and Alonso, J.A. Volume Dependence of the Bulk Modulus in Alkali Metals *physica status solidi (b)* 104:1 Pp.307 - 312 1981.

[122] Parr Robert G. and Yang Weitao *Density Functional Theory of Atoms and Molecules* Oxford University Press, 1989.

[123] Tsirelson, V.G. Avilov, A.S. Lepeshov, G.G. Kulygin, A.K Stahn J. Pietsch, U. and Spence J.C.H. Quantitative Analysis of the Electrostatic Potential in Rock-Salt Crystals Using Accurate Electron Diffraction Data *J. Phys. Chem. B* 105, 5068-5074 2001.

[124] Griffiths David J. *Introduction to Quantum Mechanics* Prentice-Hall Inc. 1995.

[125] Slater John C. *Quantum Theory of Atomic Structure*, volume 2. appendix 22. McGraw-Hill Book Company Inc. 1960

[126] Tull, V.F.G. The calculation of the inner potential of a crystal. *Proc. Roy. Saoc. Lon.* 206:1065 April 1951

[127] Causà M., Dovesi R., Pisani C. and Roetti C. Electronic structure and stability of different crystal phases of magnesium oxide. *Physical Review B* 33:2 January 1986 1308-1316

[128] Cora F., Patel A., Harrison N., Dovesi R. and Catlow C. An ab Initio Hartree-Fock Study of the Cubic and Tetragonal Phases of Bulk Tungsten Trioxide *J. Am. Chem. Soc.* 118:48 1996 12174-12182.

[129] Salje E., Rehmann S., Pobell F. and Dove M. Crystal structure and paramagnetic behaviour of $\epsilon - WO_{3-x}$. *J. Phys.:Condens. Matter* 9 1997 65636577.

[130] Howard C., Luca V. and Knight K. High-temperature phase transitions in tungsten trioxidethe last word? *J. Phys.:Condens. Matter* 14 2002 377387.

[131] Crichton W., Bouvier P. and Grzechnik A. The first bulk synthesis of $\mathrm{ReO_3}$-type tungsten trioxide, $\mathrm{WO_3}$, from nanometric precursors. *Materials Research Bulletin* 38 2003 289-296.

[132] Myron H., Gupta R. and Liu S. Study of the Electronic Structure of $\mathrm{ReO_3}$ and its Pressure Dependence by the Korringa-Kohn-Rostoker Method. *Physical Review B* 8:4 1293-1295 August 1973.

[133] Jørgensen J.-E, Jørgensen J. D., Batlogg B, Remeika J and Axe J. Order parameter and critical exponent for the pressure-induced phase transitions in ReO_3.

[134] Samara G Pressure and Temperature Dependences and Dielectric Properties of the Perovskites $BaTiO_3$ and SrTiO3 *Physical Review* 151:2 p 378 Nov. 1966.

[135] Harada J., Pedersen T. and Barnea Z. X-ray and Neutron Diffraction Study of Tetragonal Barium Titanate *Acta Cryst* A26 p 336 1970.

[136] Michel-Calendini F and Mesnard G Band structure and optical properties of tetragonal $BaTiO_3$ *J.Phys. C:Solid State Phys.*, 6 p 1709 1973.

[137] Kwei G, Lawson A and Billings S. Structures of the Ferroelectric Phases of Barium Titanate. *J. Phys. Chem.* 97 pp 2368-2377 1993.

[138] Yamanaka T, Hirai N and Komatsu Y. Structure change of $Ca_{1x}Sr_xTiO_3$ perovskite with composition and pressure. *American Mineralogist*, Volume 87, pages 11831189, 2002

[139] Salehi H, Shahtahmasebi N and Hosseini S. Band structure of tetragonal BaTiO3 *Eur. Phys. J. B* 32, 177-180 (2003)

[140] Yashima M and Roushown A. Structural phase transition and octahedral tilting in the calcium titanate perovskite CaTiO3. *Solid State Ionics* 180 120-126 2009.

[141] Lin Fanting and Shi Wangzhou Magnetic properties of transition-metal-codoped BaTiO3 systems *Journal of Alloys and Compounds* 475 pp 64-69 2009

[142] Cernea M and Manea A $Ba(Ti_{1-x}Sn_x)O_3$ (x = 0.13) Dielectric Ceramics Prepared by Coprecipitation *J. Am. Ceram. Soc.* 90:6 pp 1728-1732 2007.

[143] Levin I. et al. Phase equilibria, crystal structures, and dielectric anomaly in the $BaZrO_3CaZrO_3$ system. *Journal of Solid State Chemistry* 175 pp 170-181 2003.

[144] TerkiR., Feraoun H., Bertrand G. and Aourag H. Full potential calculation of structural, elastic and electronic properties of $BaZrO_3$ and $SrZrO_3$ *phys. stat. sol. (b)* 242:5 pp 1054-1062 2005.

[145] Galuskin et al., Lakargiite CaZrO3: A new mineral of the perovskite group from the North Caucasus, Kabardino-Balkaria, Russia. *American Mineralogist* 93:11-12 pp 1903 - 1910, Nov-Dec 2008.

[146] Ianos R. and Barvinschi P. Solution combustion synthesis of calcium zirconate, $CaZrO_3$, powders. *Journal of Solid State Chemistry* 183 pp 491496 2010.

[147] Kennedy B. J. and Howard C. J. High-temperature phase transitions in $\mathrm{SrZrO_3}$. *PHYSICAL REVIEW B* 59:6 Feb. 1999

[148] Bennett J. W., Grinberg I., and Rappe A. M. Effect of symmetry lowering on the dielectric response of $\mathrm{BaZr_O}3$. *PHYSICAL REVIEW B* 73, 180102 (R) 2006.

[149] Chou Chen-Chia and Hou Chun-Shou Structural Instability during CubicTetragonal Transformation in Lead Titanate Single Crystals *J. Am. Ceram. Soc.* 82:5 pp 129498 1999.

[150] Howard C.J., Kennedy B.J. and Chakoumakos B.C. Neutron powder diffraction study of rhombohedral rare-earth aluminates and the rhombohedral to cubic phase transition. *J. Phys.: Condens. Matter* 12 pp 349365 2000.

[151] Clementi E. Atomic Negative Ions: The Iron Series *Physical Review* 135:4A August 1964.